Internal Fluid Mechanics of an Effervescent Atomizer

by

Miguel A. Balzán

A thesis submitted in partial fulfillment of the requirements for the degree of

Doctor of Philosophy

Mechanical Engineering
University of Alberta

Abstract

An experimental investigation was conducted with the purpose of studying the effects of selected operating and design variables in the flow inside an effervescent atomizer. A series of tests were performed in a horizontally oriented, square conduit of 12.7 mm in diameter which constituted the mixing chamber of the effervescent atomizer. The operating fluids were water and air. The air was injected perpendicularly into a fully developed, turbulent water flow, whose bulk water velocity values ranged between 1.1 and 4.3 m/s. The gas mass flow rate values were in the range between 8 and 60×10^{-3} g/s. Three different gas injectors, with diameters of 0.27 mm, 0.52 mm and 1.59 mm were used. The combination of variables allowed the operation of the atomizer within the limits of what constitutes a bubbly flow in pipes. High-speed shadowgraphy was the technique used to investigate thoroughly the dynamics between the gas and liquid phases near the gas injection region as well as upstream the discharge nozzle.

A set of original, empirical expressions used to estimate the incipient centerline and borderline trajectories of the gas phase, during its initial interaction with the liquid and based on dimensionless parameters, were introduced. The assessment of the correlations gave a strong prediction of the initial centerline and borderline trajectories of the gas jet in the flowing liquid.

The effects that the gas injection velocity, liquid mean velocity and injection gas injection diameter have on the process of bubble generation were investigated. Four distinct regimes were identified: Single Bubbling (*SB*), Pulse (*P*), Elongated Jetting (*EJ*) and Atomizing Jetting (*AJ*). It was observed that the shift between regimes occurs gradually, producing the need to identify

transitional regions: *SBP* and *PTJ*. Sets of independent dimensionless variables were used to categorize the proposed regimes in bubble formation maps. Empirical correlations that delimit the boundaries between ordered and chaotic bubble generation were determined.

An introductory description of the forces involved in the bubbling process was conducted. The results indicated that the form-induced drag and added mass force were dominant detaching and cohesive force respectively. While there was agreement with previous works regarding the dominant breakup effect, the results obtained for the main attaching force were unique. Also, a novel methodology for the estimation of dynamic shape based drag and added mass coefficient was included.

The morphological features of the gas jet were described through empirical correlations based on relevant dimensionless numbers associated to the variations of three fundamental design parameters: liquid cross-flow velocity, gas mass flow rate and the nozzle dimensions. The gas jet features were compared with representative statistical diameters from the population distribution, resulting in an estimation of the averaged Sauter mean diameter and maximum bubble diameter as a function of the gas jet dimensions. It was determined that the gas injection conditions play a fundamental role in the internal flow characteristics for an effervescent atomizer.

Nomenclature

Standard

A_C	channel cross-sectional area (m^2)
A_G	projected area occupied by the gas phase (mm^2, m^2)
A_L	projected area occupied by the liquid phase (mm^2, m^2)
A_P	projected area of the gas jet/bubble (mm^2)
A_{inj}	injection cross-sectional area (m^2)
C_D	drag coefficient
C_L	lift coefficient
C_M	Added mass coefficient
D_{32}	Sauter mean diameter of the detached bubbles (mm)
D_{99}	bubble diameter equal to 0.99 times the maximum diameter found in a distribution (mm)
D_B	bubble diameter (mm)
D_{equiv}	jet equivalent diameter (mm)
D_{inj}	gas injector diameter (m)
D_H	channel hydraulic diameter (m)
D_{ratio}	gas injector diameter/channel hydraulic diameter ($= D_{inj}/D_H$)
D_W	gas jet width (mm, pixels)
Eo_G	gas Eotvos number
F_B	buoyancy force (N)
F_D	combined drag force (N)
F_I	added mass or inertial force (N)
F_M	momentum force (N)
F_P	contact pressure force (N)
F_{SL}	lift-induced force (N)
F_σ	surface tension force (N)
F_τ	turbulence-induced force (N)
Fr_G	Froude number of the gas phase
Fr_α	Critical Froude number delimiting the maximum stable bubbling point
G	Baker map Gas-Liquid mass flux (kg/cm^2-hr)
GLR	Gas-to-Liquid ratio
I	turbulence intensity
K	total number of bubbles measured
L	generic gas jet length (mm, m)
L_H	channel length (m)
M_G	gas mass flow rate (g/s)
M_L	liquid mass flow rate (kg/s)
M_R	momentum ratio
M_R''	momentum flux ratio
MF_G''	gas momentum flux $\left(= \rho_G U_G^2\right)$ (kg/ms^2)
MF_L''	liquid momentum flux $\left(= \rho_L U_L^2\right)$ (kg/ms^2)
N_{inj}	number of injector ports
P_L	channel pressure (kPa)

P_G	gas injection pressure (kPa)
P_{ER}	perimeter of the projected gas jet area (mm, pixels)
$\dot{\varsigma}$, Q_A	volumetric gas flow rate (cm^3/s)
$\dot{\varsigma}$	volumetric liquid flow rate (LPS)
Re_B	bubble Reynolds number
Re_{eff}	effective Reynolds number
Re_L	liquid phase Reynolds number
S	point within the image with (x, y) coordinates (mm, mm) (pixels, pixels)
S_{URF}	surface of the projected particle
St	Stokes number
St_Λ	turbulence Stokes number
T_G	mean gas temperature (K)
U_{eff}	effective velocity (m/s)
U_G	gas injection velocity (m/s)
U_L	bulk liquid cross-flow velocity (m/s)
U_R	gas to liquid velocity ratio (U_G/U_L)
U_{SG}	gas superficial velocity (m/s)
U_{SL}	liquid superficial velocity (m/s)
V_C	gas chamber volume (m^3)
V_G	volume occupied by the gas phase (mm^3, m^3)
V_L	volume occupied by the liquid phase (mm^3, m^3)
We_{aero}	Aerodynamic Weber number (Ragucci et al., 2006)
We_G	gas Weber number
We_L	liquid Weber number
X_{break}	stream-wise location of the gas jet breakup location measured from the gas injection location (m)
X_{pos}	Horizontal position (mm)
Y_{pos}	Vertical position (mm)
d_i	ensemble of bubble diameters
F	friction factor
P	perimeter of the projected equivalent diameter (mm, pixels)
r_L	channel length/channel diameter ratio
t	time (s)
t_{growth}	gas jet growth time (s)
t_G	total time that the gas phase is observed at point S (s)
t_Λ	time-scale of integral scale eddies (s)
w	Dimension of the gas jet/bubbles in the plane direction (mm)
x	horizontal coordinate (mm, pixels)
y	vertical coordinate (mm, pixels)
y_{top}	vertical distance measured from the top wall (mm, pixels)

Greek letters

Λ	integral length scale (mm, μm)
λ	fluid correction factor for the Baker map defined as $(\rho_G/\rho_{air})^{0.5}(\rho_L/\rho_{water})^{0.5}$
$\bar{\alpha}$	time and area averaged void fraction
α_{area}	area averaged void fraction
α_{local}	local void fraction
Γ	dispersed phase density function
ε	turbulent energy dissipation rate (m²/s³)
$\varepsilon_{binarization}$	uncertainty associated to the image binarization (%)
$\varepsilon_{calibration}$	uncertainty associated to the calibration process (%)
$\varepsilon_{filtering}$	uncertainty associated to the filtering technique (%)
ε_{total}	total uncertainty involved in the image processing (%)
Z	circularity
H	Kolmogorov length scale (mm, μm)
Θ	inclination angle
θ_{adv}	advancing angle
θ_{long}	longitudinal angle
θ_{reced}	receding angle
K	turbulence kinetic energy (m²/s²)
Λ	Taylor length scale (mm, μm)
μ_G	gas viscosity (Pa.s)
μ_L	liquid viscosity (Pa.s)
ν_L	liquid kinematic viscosity (m²/s)
ρ_G	gas density (kg/m³)
ρ_L	liquid density (kg/m³)
τ_Λ	turbulence-induced shear stress (Pa)
ψ	fluid correction factor for the Baker map defined as $(\sigma_L/\sigma_{water})^{-1}(\mu_L/\mu_{water})^{0.33}(\rho_L/\rho_{water})^{-0.66}$

Subscripts

B	bubble
G	gas
H	hydraulic
L	liquid
W	width
Adv	advancing
Aero	aerodynamic
Area	area
break	jet breakup location
Eff	effective
equiv	equivalent
Inj	injection
Pos	position
Red	reducing

Acronyms

AJ	Atomizing Jet
C	Cavity
EJ	Elongated Jet
GJILCF	Gas Jets in Liquid Cross Flow
JICF	Jets in Cross Flow
LJIGCF	Liquid Jets in Gas Cross Flow
P	Pulse regime
PTJ	Pulse-to-Jet
SB	Single Bubbling
SBP	Single Bubbling-to-Pulse

Table of Contents

Index of Figures

Index of Tables

1. Introduction

1.1. General Background

Atomizers are a prominent technology employed in a vast array of fields and applications such as food processing, chemical and pharmaceutical industry, fuel injection technology, oil production and power generation in the form of gas turbine combustors and boilers. There are several techniques that could be used to create the sprays, although all of them involve the breakup of portions of liquid into small particles due to its interaction with streams of gas. Most atomizing techniques involve the change of mechanical or kinetic energy to produce the breakup of the liquid into droplets (Konstantinov et al., 2010) and depending on how the gas and liquid interaction occurs, they can be characterized in two main groups: external–mixing or internal–mixing.

Within the external–mixing devices, it is possible to identify the conventional air blast atomizers and air–assisted atomizers; the main idea behind this technology is to convert a mass of liquid to a fast stream, and then cutting it into small drops due to the action of a high–speed gas jet. The use of the internal mixing technique involves the interaction of gas and liquid inside the atomizer chamber in order to create a multiphase mixture (Sovani et al., 2001). In this category, some techniques such as flash atomization, dissolved gas atomization and effervescent atomization can be included. Of these three techniques, the one that provides the most advantageous atomizing technique is the effervescent atomizer, due to the fact that it does not involve the change of phase

of the liquid, needed for the flash atomization technique, nor the amount of gas contained within the liquid, an essential factor for the dissolved gas atomization.

An effervescent atomizer can be defined as an atomization method, where gas enters the mixing chamber through a port or series of them. There, it will interact with a liquid stream, allowing the creation of a two–phase current. This flow passes through a small orifice or nozzle, in order to make small droplets due to the dual effect of the mixture passing through a contraction and gas expansion when the multiphase flow exits the nozzle (Sovani et al., 2001; Chin and Lefevbre, 1993).

The fluid mechanics of an effervescent atomizer can be broken down into five clearly defined regions (Figure 1.1), whose description is given next:

Zone I.   Bubble formation, which occurs due to the injection of a gas stream into a liquid cross flow.

Zone II. Bubble transport and development in a flowing liquid; involving the possibility of deformation, coalescence and/or breakup, bubble–bubble interactions, bubble–wall interactions.

Zone III. Two–phase flow evolution inside a confined space: interaction between the gas and liquid phases, effects of the liquid phase on the bubbles and vice versa, possibility of flow pattern evolution (bubbly flow to annular or slug flow), turbulence effects.

Zone IV.   Flow of a two–phase mixture through a contraction, which involves compressibility effects in the gas, friction loses and discharge coefficient, gas and liquid interactions.

Zone V. Shred and ligament formation and disintegration, formation of small droplets from the "root–like" structures, flow of droplets through a stagnant gas, droplet collisions, droplet shape deformation and breakup due to shear effects.
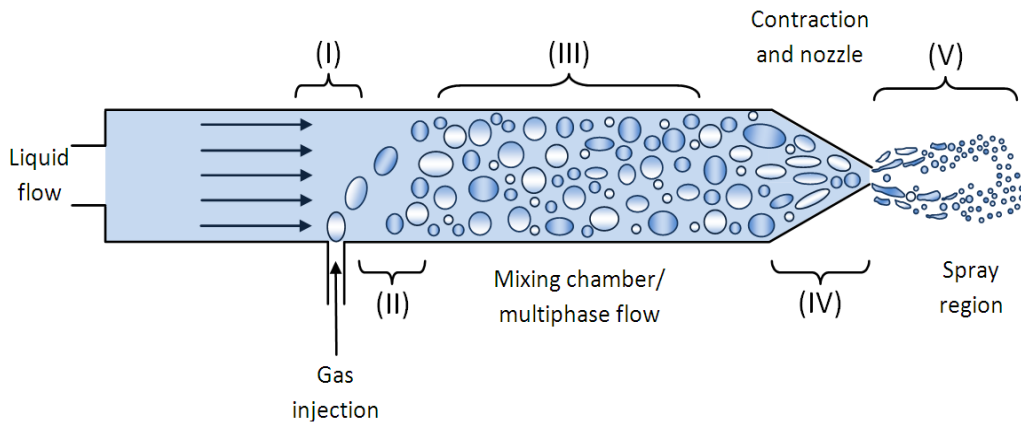
Figure 1.1. Schematic of an effervescent atomizer showing the different regions involved: Liquid entrance, gas injection, mixing chamber for the multiphase flow, flow through a nozzle and spray region

The processes occurring in the spray region have a strong dependency on the mechanisms inside the atomizer (Chin and Lefevbre, 1994; Jedelsky and Jicha, 2009; Rahman et al., 2011); hence it is clear that a meticulous analysis of the internal flow region will result in a better comprehension and control of the external flow. This leads to a better performance of the effervescent atomizer, consequently affecting the quality of the spray produced through the use of this technique (Huang et al., 2008; Jedelsky and Jicha, 2008).

According to Konstantinov et al. (2010) and Sovani et al. (2001), there are several variables, listed in Table 1.1, which can be involved in the optimum performance of effervescent atomizers. These parameters can be characterized depending on their relation to the operating

3

and initial conditions, fluid properties and atomizer internal and external geometry. The combination of this array of variables alongside the intricate dynamics of the fluids involved provides a clearer panorama of the complexity of effervescent atomizers.

Table 1.1. Categorization of the variables involved in an effervescent atomization process

Category	Independent variables	Dependent Variables
Initial and operating conditions	GLR or mass flow rates for the liquids involved (M_G, M_L). Temperature (T_G) Density (ρ_L, ρ_G) Viscosity ($\boldsymbol{\mu}_L$, $\boldsymbol{\mu}_G$) Surface tension ($\boldsymbol{\sigma}$)	Liquid and gas velocities (U_{SL}, U_{SG}, U_L, U_G) Liquid pressure (P_L), gas injection pressure (P_G) Void fraction (α)
Internal geometry	Chamber dimensions (length (L_H), hydraulic diameter (D_H), cross–sectional area (A_C), shape) Injector orifices (number (N_{inj}), diameter (D_{inj}), area (A_{inj}), and location (r_L))	Two–phase flow pattern and evolution inside the mixing chamber Two–phase flow inside a nozzle Bubble size (D_b), bubble interaction, bubble coalescence and evolution Momentum ratio
External geometry & exit conditions	Exit orifices (number of orifices, diameter, area, length) Ambient pressure	Liquid structure in the outer zone of the nozzle Spray cone angle, momentum and unsteadiness Droplet diameter, velocity and distribution

The scope of the present work will be limited to the study of the flow dynamics associated to the zones (I) to (III), as they were described in Figure 1.1, with particular emphasis on the mechanisms involved in the process of gas injection into liquid cross–flow (zone I), in order to determine the relevancy of the geometrical variables and operating conditions, the relation between them and how they affect the two-phase flow entering the discharge nozzle.

1.2. Motivation and Specific Background

1.2.1. Internal Flow in an Effervescent Atomizer

As indicated in Figure 1.2., early studies about effervescent atomizer behavior (Lund et al., 1993) inferred that the ratio between the diameters of the bubbles produced and the exit nozzle diameter have a direct influence in the morphology of the ligaments produced. It has been proven that the gas-liquid interaction at the discharge orifice controls the Sauter mean diameter (D_{32}) of the droplets produced (Chin and Lefevbre, 1995; Ferreira et al., 2001). A definition for D_{32} will be provided in Section 2.3.1. Hence the relevance of identifying the effervescent atomizer internal flow is given by the hypothesis that the quality of the two-phase flow upstream of the discharge nozzle and passing through it exerts a strong influence in the spray composition.
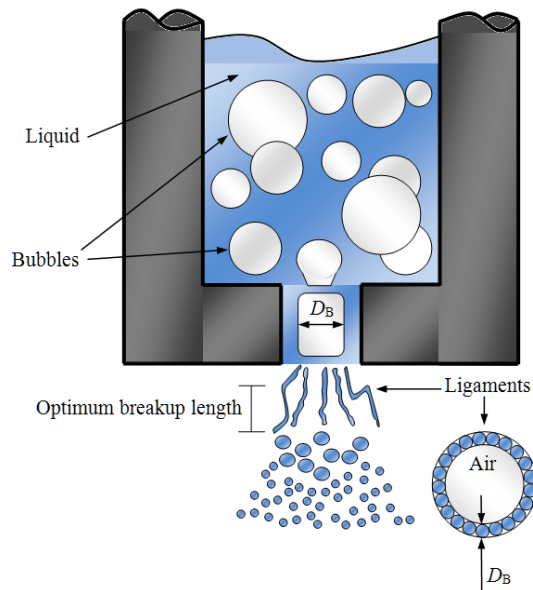
Figure 1.2.   Bubble passing through the discharge nozzle and its effects on the ligament-droplet formation in the spray region of an effervescent atomizer (Lund et al., 1993)

Despite this acknowledged fact, the nature of the flow inside an effervescent atomizer and its influence on the spray region are not fully comprehended. The research about the fluid mechanics inside an effervescent atomizer have focused primarily on the visualization of the flow conditions inside the mixing chamber and upstream the nozzle (Buckner and Sojka, 1991; Huang et al., 2008; Ghaemi et al., 2010, Sen et al., 2014) and exploring the applicability of pipe flow regime maps to the estimation of flow in the atomizer mixing chamber (Chin and Lefevbre, 1993; Chin and Lefevbre, 1995; Lorcher and Mewes, 2001; Kim and Lee., 2001). In the next two sections, some of the most relevant findings related to the aforementioned topics will be described.

1.2.2. Flow Visualization inside an Effervescent Atomizer

Although flow visualization is a technique that mainly provides results of qualitative nature, it has been proven to be an efficient method for the analysis of the internal flow behavior in an effervescent atomizer mixing chamber and the discharge nozzle. Primarily, this technique has been used to observe the behaviour of the flow passing through the discharge nozzle and relate it to the upstream conditions (Sakai et al, 1996; Kufferath et al., 1999; Kim and Lee, 2001; Lorcher et al., 2003; Ghaemi et al., 2010, Sen et al., 2014). It can also be used to analyze internal flow changes and its effects on the atomizer performance (Jagannathan et al., 2011; Rahman et al., 2012, Sen et al., 2014).

Kim and Lee (2001) used a CCD camera coupled with a Halogen Lamp as a light source to examine visually the most common two-phase flow regimes inside an effervescent atomizer:

bubbly, annular and intermittent flow. Through the use of direct observation, it is possible to correlate the effects of the internal flow with the external flow behavior. The results shown in Figure 1.3 highlight the strength of using visualization as a tool to explore the fluid behavior inside an effervescent atomizer. Also, they are a clear indication of the dependence of the spray performance on the flow inside the atomizer mixing chamber and allow the comparison of the internal flow with the behaviour at the spray region.
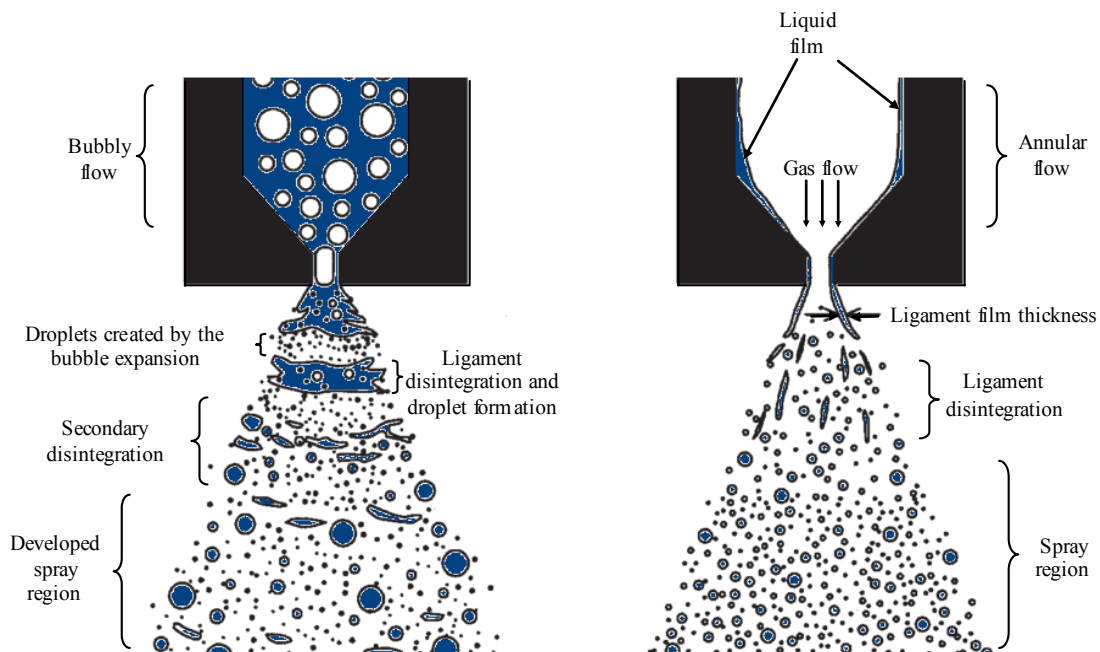
Figure 1.3.   Comparison between internal and external flow characteristics in an effervescent atomizer (Adapted from Kim and Lee, 2001)

Huang et al. (2008) used flow visualization to examine the effects of the internal flow characteristics on the droplets produced. Through direct examination via high-speed imaging, they characterized the flow regimes inside an effervescent atomizer. With this technique a clear identification of the typical flow features inside the atomizer is possible. It also provides a qualitative differentiation of the flow characteristics depending on the type of gas injector used. Ghaemi et al. (2010) determined that using a porous media injector caused a high number of

small size bubbles, while the multi-hole injector induced a smaller number of large-sized bubbles, whose diameter was comparable to that of the discharge nozzle used.

Sen et al. (2014) studied the process of bubble formation inside the mixing conduit of an effervescent atomizer through the use of flow visualization. M. Balzán was the sole responsible for the setup design, determination of the experimental conditions and obtaining the results presented in the referred article. The results shown in Figure 1.4 corroborate previous findings that indicate that relevant flow characteristics, e.g. bubble morphology and bubble deformation at the nozzle, can affect the performance of the effervescent spray. It was also observed that pressure pulses at the spray region, created by the intermittent passing of bubbles through the discharge nozzle, could affect the mechanics of gas formation inside the chamber.
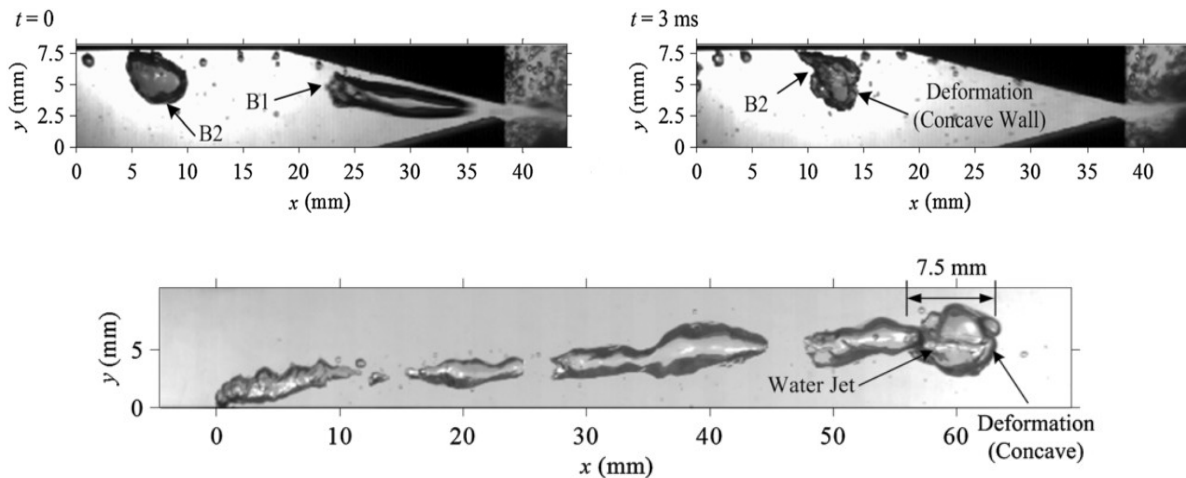
Figure 1.4. Top: Bubble interaction with the discharge nozzle, where the effects of bubble B1 passing through a nozzle cause an upstream pressure pulse, producing the deformation of the bubble B2 and of the water jet (Sen et al., 2014). Bottom: Depiction of the possible deformation of the incipient bubbles owing to the conditions of the flow passing through the nozzle.

Although most of the results obtained by the previously mentioned studies can be deemed of qualitative nature, it is undeniable that this approach has expanded the knowledge about the fluid

mechanics inside an effervescent atomizer. While the focus has been primarily on the observation of the gas-liquid interaction at the discharge nozzle and the flow pattern upstream of the nozzle, limited information exists about the mechanics of gas injection in an effervescent atomizer. However, numerous research studies have been conducted to understand the more basic problem of bubble formation, where flow visualization provides a strong approach to recognize the underlying physics of the problem (Kulkarni and Joshi, 2005). It has been argued that parallelisms between the two processes can be established (Sovani et al., 2001; Konstantinov et al., 2010), which cannot but solidify the argument about using direct observation to comprehend the internal flow inside an effervescent atomizer.

1.2.3. Flow Pattern in Effervescent Atomizers

In an effervescent atomizer, design conditions must aim to assure that there is a bubbly flow in the mixing chamber (Lefevbre, 1992; Lefevbre, 1996). Hence, the most common flow pattern inside an effervescent atomizer is the bubbly flow regime. However, it is also possible to observe flow regimes such as annular flow (Whitlow and Lefevbre, 1993; Chin and Lefevbre, 1995; Lorcher and Mewes, 2003; Rahman et al., 2012), slug flow (Chin and Lefevbre, 1995) or intermittent flow (Kim and Lee, 2001; Ramamurthi et al., 2009). While a smaller average droplet diameter can be obtained if the flow pattern is annular, there will be a trade−off in the cost required to operate under this regime, principally because of the increase in the gas volumetric flow required, as well as a less efficient use of the atomizing energy (Lefevbre, 1996; Kim and Lee, 2001; Konstantinov et al., 2010). Therefore, when compared to the other possible regimes, the bubbly flow regime is the most beneficial inside an effervescent atomizer, due to a more

efficient use of the atomizing energy and lower gas requirements/*GLR* (Gas-to-Liquid Ratio) values, and more importantly, the generation of a fine and stable spray (Jedelsky and Jicha, 2008).

In the design of effervescent atomizers, it is common to use pipe flow regime maps in order to determine the operating conditions that are most likely to generate a bubbly flow. However, the physical principles of effervescent atomizers are different from those encountered in two–phase pipe flow (Lefevbre, 1996). Pipe flow regime maps refer to fully developed flow in long pipes, with geometries of constant cross-sectional area. In twin–fluid atomizers, the mixing chamber length is short when compared to pipeline lengths, which limits the possibility of flow development and reaching equilibrium between bubble formation and coalescence. As described by Lefevbre (1996), the conditions inside an effervescent atomizer are transient and approximately similar to the flow development at a pipe entrance. Additionally, due to the interaction between the gas and liquid phases during the injection process, the flow accelerates throughout the mixing chamber length up to the nozzle exit.

Regardless of these underlying physical differences, studies based on the applicability of pipe flow regime maps to effervescent atomizers can provide practical information in the analysis of the atomizer performance. Table 1.2 presents a summary about some of the most relevant examples about the use of pipe flow pattern maps in the analysis of effervescent atomizers. Specific application examples about the use of flow pattern maps for effervescent atomizers are shown in Figure 1.5., where as described by Chin and Lefevbre (1993), the effects of the *GLR* in the flow pattern transition and its importance for the design and sizing of the atomizer chamber

could be analysed through the flow pattern maps highlighted. Similarly, the link between operational conditions and the flow pattern inside the atomizer and its effect on the atomizer performance can be studied by following a flow pattern approach, as was introduced in Figure 1.3 (Kim and Lee, 2001).
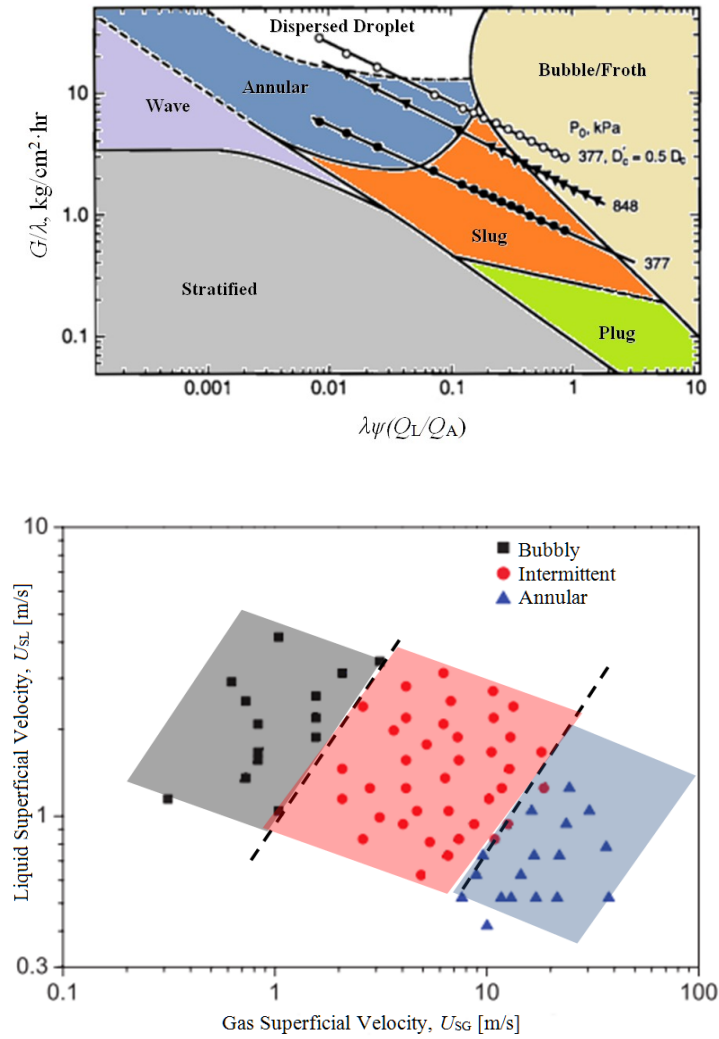
Figure 1.5. Examples about the use of pipe flow regimes in the design of effervescent atomizers. Top: Use of a standard Baker Map in the study of effervescent atomizers. Adapted from Chin and Lefevbre (1993). Bottom: Evolution of flow pattern inside the atomizer and transition criteria as a function of U_{SG} and U_{SL}. Adapted from Kim and Lee (2001)

Table 1.2.   Summary of studies resorting to the use of pipe flow regime patterns in effervescent atomizers

Authors	Main Research focus	Comments about flow regime maps
Chin and Lefevbre (1993)	Examination of flow patterns in internal-mixing, twin-fluid atomizers based on standard pipe flow regime maps	Effects of the *GLR*, chamber pressure, fluid properties and channel orientation on the flow pattern transition
Chin and Lefevbre (1995)	Present a design methodology for effervescent atomizer operation	Influence of the mixing chamber diameter on the flow pattern transition Identification of the flow regime based on Baker's map
Lefevbre (1996)	Review about developments on effervescent atomization, with particular interest on the effects of the fluid properties on the drop size	Assessment about the influence of the fluid properties, *GLR* and channel orientation on the atomizer internal flow pattern
Kim and Lee (2001)	Relation between spray behaviour and the internal flow in an effervescent atomizer	Identification of flow regimes based on the *GLR* Effect of the flow regime on the Sauter mean diameter of the droplets produced Transition criteria between flow regimes
Lorcher et al. (2003)	Prediction of the phase distribution at the atomizer discharge and its influence on the spray performance	Void fraction evaluation based on the atomizer internal flow regime Flow regime identification and calculation based on energy considerations and comparison with pipe flow maps
Rahman et al. (2012)	Study of the effects of the atomizer operating conditions on the flow regime, bubble size and droplet size distribution	Identify atomizer internal flow regimes Establish a correlation between downstream spray conditions and flow patterns inside the atomizer Correlate the frequency of slug formation with the flow regimes observed

While the use of flow pattern regime maps has proven to be a useful tool for the understanding of the internal fluid mechanics of an effervescent atomizer, most of the studies on this area focus on the discernment of the flow pattern regime in the atomizer. However, the existing flow regime maps have been created for fully developed pipe flow, an application with different acting physical mechanisms.

1.2.4. Bubbly flows and gas injection into liquid cross−flow

In applications where the mass transfer process occurs rapidly, the size of the particles produced and the degree of mixing between the phases is strongly determined by the mechanics of the gas injection into the liquid (Kulkarni and Joshi, 2005). In effervescent atomizers, where one of the main design constraints is to have a bubbly flow in the mixing chamber (Lefevbre, 1996), the two-phase flow is quickly transported from the injection area to the exit nozzle. For this type of application, a clear understanding about the nature of the bubbles produced is essential (Jedelsky et al., 2009; Konstantinov et al., 2010), because the characteristics of the spray produced are severely affected by the nature of the flow passing through the nozzle (Rahman et al., 2012).

Similarly, in bubble column reactors a homogeneous flow is desired for proper heat and mass transfer between gas and liquid, as well as optimum mixing. A bubbly flow guarantees scarce bubble-bubble interaction and little to no breakup, producing a steady, uniform bubble diameter (Kantarci et al., 2005). It has been shown that the bubble size is primarily determined by the sparger geometrical configuration (Thorat and Joshi, 2004). Hence, a thorough knowledge of the

bubble generation conditions is necessary for a proper prediction and control of bubbly flows and distinctive features such as flow pattern evolution and particle size and distribution.

The conditions of the liquid strongly affect the dynamics of bubble formation (Kulkarni and Joshi, 2005; Chakraborty et al., 2011). Kawase and Ulbretch (1981) showed that in a cross-flowing liquid during the bubble detachment phase the buoyancy and inertial forces are balanced by the interfacial tension, similar to the injection in a stagnant liquid, plus the effects of the viscous drag force. Other authors added effects such as lift forces (Tan et al., 2000; Nahra and Kamotani, 2003), an additional inertia component and a modification on the interfacial tension force (Tan et al., 2000; Nahra and Kamotani, 2003; Thorncroft et al., 2001; Liu et al., 2010). This presents different criteria and mechanisms to the process of formation when compared with stagnant liquids. Still, it has been proven that the bubbles produced from a gas injector have a smaller diameter and an increased bubbling frequency; mainly, due to the influence of the liquid momentum (Marshall et al., 1993; Zhang and Tan, 2003). Besides the influence in the bubble size, the injection into a liquid cross flow affects the process of coalescence; diminishing the possibilities of bubble-bubble interaction by transporting the bubbles away from the injection point (Tan et al., 2000) hence decreasing the chances that bubbles could merge and create bigger bubbles. Therefore, because of the advantageous effects of having a relative velocity between phases at the injection location, it is relevant to obtain a clear evaluation of the process of gas injection into a liquid cross-flow.

The vast majority of the studies about bubble injection into a cross-flow focus on the experimental evaluation or computational modeling of spherical bubble growth and uniform

detachment where the bubble experiences little to no deformation due to the effects of the liquid velocity (Table 1.3). However, there are circumstances where, due to the system configuration, the bubble detachment does not occur immediately. Instead a gas jet forms within the liquid cavity (Sada et al., 1978; Wace et al., 1987). The detachment from this gas stream occurs in a less predictable manner (Forrester and Rielly, 1998) and the assumption that round bubbles form at a quasi-periodic rate is no longer valid.

Table 1.3.   Summary of selected studies in the field of gas injection into a liquid cross-flow

Author(s)	Approach	Bubbling regimes evaluated
Silberman (1957)	E, T	*J*
Sullivan et al. (1964)	E, T	*SB*
Kawase and Ulbretch (1981)	T	*SB*
Tsuge and Hibino (1983)	E, T	*SB*
Wace et al. (1987)	E, T	*SB, J*
Marshall et al. (1993)	E, T	*SB*
Oĝuz and Prosperetti (1993)	E, N, T	*SB*
Rigby et al. (1995)	E, T	*SB, P, J*
Forrester and Rielly (1998)	E	*SB, P, J, C*
Iguchi et al. (1998)	E	*SB*
Tan et al. (2000)	T	*SB*
Sovani (2001)	E, N (*SB* only), T	*SB, P, J*
Nahra and Kamotani (2003)	E, N, T	*SB*
Zhang and Tan (2003)	E, N, T	*SB*
Loubiere et al. (2004)	E, T	*SB*
Machniewksi et al. (2004)	E, T	*C*
Duhar and Colin (2006)	E, T	*SB*
Liu et al. (2010)	N, T	*SB*

Legend: E = Experimental, N = Numerical, T = Theoretical, *SB* = Single Bubbling, *P* = Pulse bubbling, *J* = Jetting, *C* = Cavity formation

As stated by Cai et al. (2010), due to the different experimental and theoretical methodologies followed, there are significant inconsistencies in the criteria used to identify the various bubbling regimes and their transitions. Few studies have been devoted to provide regime charts that characterize the various regimes of bubble formation in the presence of a cross-flow (Rigby et al., 1995; Forrester and Rielly, 1998). Hardly any studies have considered the use of dimensionless numbers in flowing liquids (Sovani, 2001) as an alternative to present a more general classification about the regimes of bubble formation. Consequently, due to the lack of studies dedicated to the bubbling regime characterization in a liquid cross-flow, it is considered of practical necessity to expand the existing knowledge associated to this subject. An outline of the of the hypothetical bubble formation regimes that can be present in the process of gas injection under the influence of liquid cross–flow is shown in Figure 1.6. As the gas injection velocity is increased, the bubble formation regime transitions from the single bubbling case (low gas injection velocities) towards the pulse bubbling, jetting and cavity formation (very high gas injection velocities) respectively.

Although there are few studies related to bubble formation regime characterization, no exact procedure exists for the verification of the bubble formation regime besides a balance between gas and liquid velocities or momenta. The existing studies (Rigby et al., 1995; Forrester and Rielly, 1998) only consider dimensional variables, which can be applicable to similar cases of operation only if most of the variables match, which limits their range of application. Only Sovani (2001) considers the use of dimensionless variables, although not a completely appropriate dimensional analysis was performed. Nevertheless, all findings provide a conveniently starting point to determine the appropriate regime of operation.
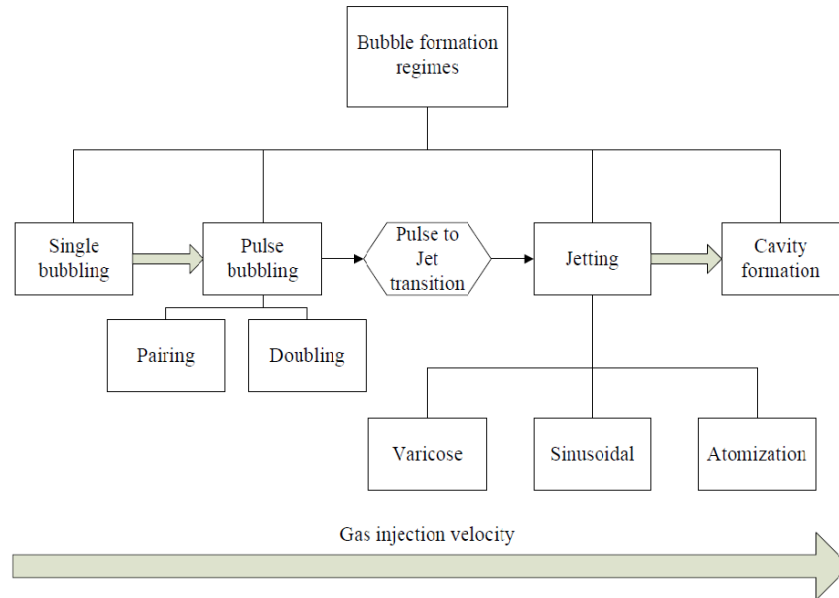
Figure 1.6.   Schematic of the possible bubble formation regimes that occur during the gas injection into the liquid–cross flow

It is desirable to operate within the single bubbling region due to the uniformity of the bubbles produced regarding their diameter and shape, as well as the homogeneous rate of detachment, desirable characteristics that are particularly beneficial for effervescent atomizers. In theory, a low gas injection velocity and a high liquid velocity will induce the formation of a single bubbling regime. Nonetheless, scarce information about clear operational limits for the discrete regime was found (Rigby et al., 1995; Forrester and Rielly, 1998; Sovani, 2001).

1.3. Hypothesis

1.3.1. Link between motivation and hypothesis

Based on the background presented, it is clear that there are fundamental questions regarding the nature of the multiphase flow inside an effervescent atomizer that need to be addressed, in order to have a clearer understanding of the physical mechanisms involved. The gap of knowledge associated to these processes can be summarized as follows:

* The specific information about gas injection mechanics in effervescent atomizers is limited. The process under which the bubbles are injected into the liquid will determine the flow pattern upstream of the nozzle. The flow pattern is one of the factors, along with the nozzle geometry, that controls the characteristics of the spray. It has been shown that there is a relation between the bubble diameter inside the conduit and the droplet diameter in the spray region (Rahman et al., 2012).

* A common misconception is that the flow pattern inside a conduit will be determined only by the volumetric/mass flow rates of the fluids involved and diameter of the chamber, without considering the method used to produce the two–phase flow. Under the same operational conditions, and different bubble creation mechanisms, it is possible to observe clear differences in the gas–liquid flow morphology (Brennen, 2005).

* Although the use of flow pattern maps created for fully developed, steady pipe flow provides an initial estimation for the flow regime inside an effervescent atomizer, the balance between geometrical and operating variables must be clarified due to the intrinsic link between atomizer performance and the flow regime inside the atomizer. When the flow regime desired is the bubbly flow, as in the case of effervescent atomizers, there are at least four possible scenarios involved, as described by Andreussi et al. (1999). Each one of these scenarios will lead to a distinct performance for a horizontally–oriented effervescent atomizer.

* There are limited correlations that outline the optimum design conditions or the magnitude of the geometrical variables needed to obtain a bubbly flow inside the mixing chamber (Chin and Lefevbre, 1995). The flow inside an effervescent atomizer is unsteady. Achieving fully developed flow conditions depends on the geometrical conditions (L_H) of the mixing conduit. There is no clear theoretical/experimental support that delimits the effect of a fully developed profile upstream of the injection point on the bubble diameter. It has been proposed that an asymmetrical array of the injector holes leads to a smaller droplet size under the same operating conditions (Sojka, 2011), although no extensive verification for this statement exists.

1.3.2. Hypothesis Formulation

The hypothesis of the present research can be stated, in such a form that it addresses a fundamental question that arises from the gap of knowledge described previously. It also sets the base for the proposed methodology to be followed, in order to present feasible and clear explanations to the questions presented. The primary hypothesis of this research is to investigate:

If through variations of distinc operating (gas mass flow rate and volumetric liquid cross flow) and geometric parameters (injection diameter) it is possible to describe quantitatively the process of gas injection into liquid cross–flow and the subsequent morphology of the detached bubbles present in the mixing chamber of an effervescent atomizer.

1.4. Objectives

With the purpose of assessing the proposed hypothesis, five independent objectives were proposed:

1.4.1. Characterize the process of gas injection into a liquid flowing in a conduit through techniques used for canonical jets in a cross-flow. The focus would be the measurement of the incipient gas jet maximum probability path line and gas jet borderline while affected by a turbulent liquid cross-flow. The results obtained from this approach will be presented in Chapter 3.

1.4.2. Describe the different forces that influence the growth of a gas plume in a liquid cross-flow based on a review of existing approaches for the case of single bubble formation. The attention would be on defining each dynamic effect acting on the growing gas jet in the presence of a liquid cross-flow following definitions and methodologies found in previous works. The findings will be shown in Chapter 4.

1.4.3. Estimate quantitatively the dominant forces during the growth of a gas plume in a strong liquid cross-flow and how they affect the gas jet breakup location. Building on the results obtained from the previous section, the dynamic analysis will differentiate the dominant forces during the process of gas injection. This will set the base for the estimation of the bubbling frequency and breakup location. The results obtained will be presented in Chapter 5.

1.4.4. Correlate the nature of the flow upstream of the nozzle with the characteristics of the bubbly flow right after the gas jet disintegration occurs. The effect that the gas jet morphology has on the void fraction and bubble diameter will be discussed. The conclusions derived from this discussion will be shown in Chapter 6.

1.4.5. Create bubble formation regime charts based on relevant dimensionless numbers that allow the identification of the bubbling regimes near the injection region. The dimensionless numbers will be based on the results from standard dimensional analysis. Even though a true variation of the dimensionless numbers would not be performed (the fluid physical properties are constant and the channel geometry is not changed), the choice of dimensionless parameters is justified on the fact that it allows for an easier comparison with other studies while simultaneously encompassing the fundamental dynamics of a GJILCF. The possible modes under which bubbling occur will be explored and categorized according to fundamental variables. Chapter 7 will elaborate on the outcome of this approach.

1.5. Expected Results

After the objectives are accomplished, important contributions in the field of gas-liquid flows will be provided. In general terms, the outcome of this research will expand the present understanding about the mechanics of gas injection in a liquid cross-flow. Since this process constitutes a key aspect of effervescent atomizers, the knowledge generated from this research would not be exclusively of theoretical interest but also of applied nature. Specifically, some of the novel expected contributions from this work will be:

* Introduce original correlations that allow the estimation of the gas phase probability distribution in a conduit under the presence of a liquid cross-flow. This is particular interest in the understanding of the initial gas-liquid interaction from an integral point of view.

* Discern the effect that selected variables, such as liquid cross-flow velocity, gas injection velocity and nozzle diameter, have on the process of perpendicular gas injection into a flowing liquid. This is of fundamental interest since the chosen variables are key design parameters for effervescent atomization. There is not complete understanding on the topic of internal flow in an effervescent atomizer.

* Present a comprehensive analysis of the forces acting on a growing gas jet/bubble attached to wall under the effects of a perpendicular liquid flow. Although there is a wealth of knowledge about discrete bubble formation, insufficient data exists about cases that extend beyond this mode. As stated by Clift *et al.* (1978), this area is essential to understand the complex process of

bubble formation, growth and detachment. This can also be used as a base for predictive computational models.

* Provide a simplified dynamic approach for the study of the mechanics of bubble formation in a horizontally oriented cross-flow.

* Correlate the effect that the gas jet morphology has on the morphology of the incipient bubbles. To the best of the author's knowledge, there are no existing studies that present a link between gas jet geometry and bubble dimensions based on relevant dimensionless numbers.

* Differentiate the bubbling regimes in a liquid cross-flow under formation regime maps. This is a new and unique approach in the field of effervescent atomizers, where the conditions under which bubbles form is fundamental to the atomizer performance.

2. Experimental Methodology

In the present chapter, the experimental setup used in the data collection process will be discussed. The methodology followed for the processing of the images will be described as well, presenting specific information about the various steps involved. It is expected that the following description provides the reader with full understanding of the research methods used in the present study, which are in agreement with a vast number of recent experimental investigative studies in the area of gas injection in liquid and bubbly flow studies (Kulkarni and Joshi, 2005; Duhar and Colin, 2006; Andersson and Andersson, 2006; Rahman et al., 2012; Weiland and Vachlos, 2013; Harby et al., 2014; Sen et al., 2014).

2.1. Equipment

An illustration of the two-phase flow channel and equipment used during the tests is presented in Figure 2.1 and a detailed description is provided next. The experimental setup shown and the range of variables tested were chosen such that the various scenarios studied remain constrained to what is as a bubbly flow regime in pipe flows (Andreussi et al., 1999). Variations of the gas mass flow rate (M_G) and liquid cross-flow velocity (U_L) were considered as the study variables that control the type of bubble generation that might occur. Several values of the gas injection diameter (D_{inj}) were evaluated as well. The fluids used were air and water, for the dispersed and continuous phase respectively.
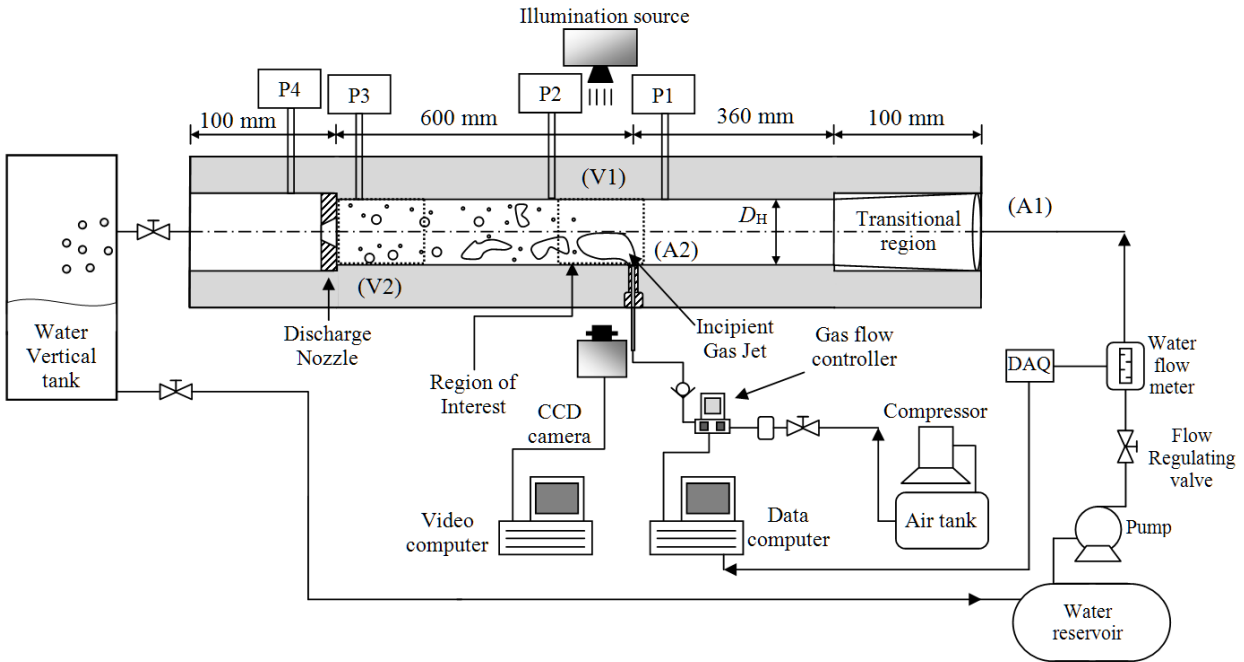
Figure 2.1.   Schematic representation of the experimental and imaging setup used

2.1.1. Two-phase flow channel assembly

This study focuses on an outside-in atomizer. It was designed considering the guidelines proposed by Chin and Lefevbre (1995). A schematic of the channel configuration is shown in Figure 2.1. The experiments were conducted with a horizontally oriented conduit that has a square cross–sectional area (A2) of 161.3 mm^2, such that D_H = 12.7 mm $\pm$ 0.1 mm. Its total length is 1160 mm $\pm$ 0.1 mm. The top and bottom walls of the channel are made of polished aluminum, while the sides are made from polycarbonate to allow observation of the interaction between phases. Flat side walls are chosen with the purpose of minimizing visual distortion throughout the channel. The surface of the channel can be considered as smooth.

A rapid prototyped transition region, of 100 mm in length, is located at the entrance of the channel to create a smooth transition from the circular cross-section (A1) of the upstream pipe,

with a diameter of 19 mm, to the square conduit. The gas injector is located 360 mm downstream of the end of the transitional region, so that the liquid flow is fully developed before interacting with the gas stream. Appendix F contains the considerations related to fully developed flow in square conduits. The mixing chamber has a length of 600 mm (L_H). The dimension ratio $L_H/D_H \approx 47$ is comparable to that of other effervescent atomizers (Huang *et al.*, 2008; Jedelski *et al.*, 2009; Ramamurthi *et al.*, 2009). At the end of the conduit, downstream of viewing section V2, a convergent nozzle was installed. The nozzle had an exit slot of $D_{nozzle} = 0.8$ mm, a length $L_{nozzle} = 10$ mm and angle $\beta_{nozzle} = 31°$.

A stainless steel hypodermic tube, with a length of 80 mm, was used to inject the gas into the channel. This tubing passed through the channel wall and mounted flush into it. Various sizes of tubing internal diameter were used to observe the effects of the injection diameter on the process of bubble generation. The values of D_{inj} used during the study are shown in Tables 2.2-2.4. The effects of nozzle orientation on the gas jet dynamics were studied by changing the injector location, which was positioned in either the top wall or the bottom wall of the channel (Figure 2.2). The tolerance associated to the internal diameter of hypodermic tubing is $\pm$ 0.01 mm.
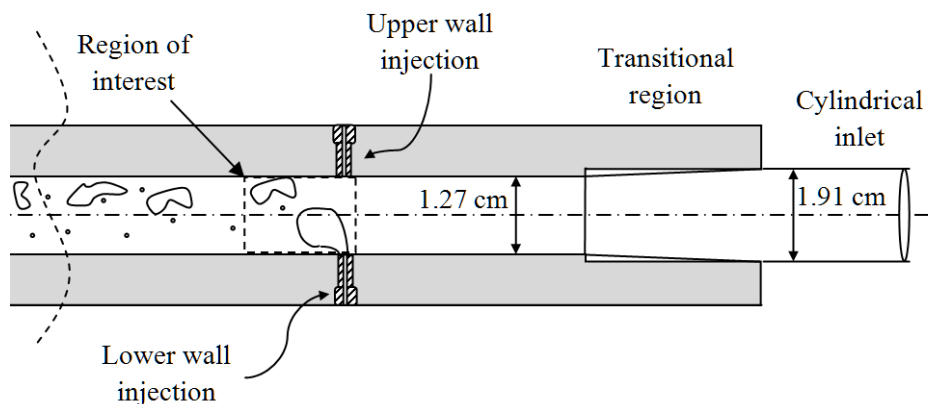
Figure 2.2.   Depiction of the gas injector location

After the liquid cross-flow interacts with the gas jet it produces a deflection in the jet trajectory. Right at the inlet port, the liquid momentum shifts the jet orientation from perpendicular, up to a stream aligned with the flow a few channel diameters downstream of the injection point. The combined distance between the smoothing section and the gas injector location gives a total development length for the flow larger than $50D_H$. As was shown in Figure 2.1, pressure transducers (Omega FLR7330) were installed at four strategic locations, P1 – P4, to observe the pressure differences along the mixing chamber. The nozzle pressure differences associated to the various test configurations were reported in Tables 2.2 to 2.4, which are introduced in Section 2.1.3.

2.1.2. Gas injection system

A 4 kW air–cooled, screw compressor (Atlas Copco GX 2-11) provides a constant flow of air to a flow controller (Alicat MC_10 SLPM D/5 M 5 IN) with a range of 0-10 SLPM and an estimated accuracy of ± 0.01 SLPM. The air flows through a filter to remove any impurities. A needle valve and a secondary 5 μm filter are installed upstream of the gas flow controller. The gas is injected into the square-shaped conduit through the injector depicted in section (A2), Figure 2.1. The M_G value to be injected into the conduit is established using a simple computational routine installed into the operational data computer. The computer records the instantaneous values of M_G, the air volumetric flow rate (Q_G), the gas injection pressure (P_G) and gas temperature (T_G). These variables were sampled at a frequency of 10 Hz and then stored. A summary of the measured parameters using this configuration can be obtained from Tables 2.2 to 2.4.

Due to the short distance between the controller exit and the gas inlet, it was assumed that the gas temperature variations were minimal and its mean value remained relatively constant, equal to T_G = 297.4 K $\pm$ 0.4 K. The air system was designed in a manner such that the gas injection into the conduit occurred under constant flow rate conditions (Tsuge and Hibino, 1983; Akagi et al., 1987, Sovani, 2001). Three injectors with different ID's were tested: 0.27 mm, 0.52 mm, 1.59 mm. To eliminate the possibility of water entering the gas injection system a check valve is installed in the line.

2.1.3. Liquid supply and flow system

The water entered the channel through inlet (A1), Figure 2.1. The liquid flow rates can be varied between 0.19 and 0.70 L/s, with an expected resolution of ΔQ_L = 0.01 L/s, which correspond to minimum and maximum velocities of 1.1 m/s and 4.4 m/s, respectively. The flow circuit operates in a closed loop, with a 1.49 kW (2 HP) high–head pump (Model A-97568304, Grundfos) producing the liquid flow. The flow rate through the channel assembly was controlled by manipulating the globe valves, whose locations are shown in Figure 2.1. Two large storage tanks (170 L and 250 L) were included in the flow circuit to ensure that the change in water temperature caused by the frictional heating during continuous recirculation was minimal. The water temperature, measured with a standard mercury thermometer inserted into the 170 L tank, varied between 295.3 K and 298.4 K, with a mean value of 296.8 K $\pm$ 0.2 K. This results in an approximately constant water viscosity of μ_L = 9.24 $\times$ 10^{-4} Pa.s, with a corresponding average variation of $\pm$ 3.6%. The water density is assumed to be constant at ρ_L = 994 kg/m^3. The

viscosity and density were obtained using the mean water temperature value and standard tables for fluid physical properties (White, 2005).

Flow rates in lines were measured with two volumetric flow transducers (Omega FLR 8340D), whose outputs were collected by means of a data acquisition card (NI DAQPad-6015) and a computer loaded with LabView 2011, which records the information at a frequency of 10 Hz. The surface tension between the phases, σ, was estimated to be a constant equal to 0.072 N/m. The difference between the mean temperatures of the fluids, led to the safe assumption that heat transfer effects between the phases could be disregarded. No mass transfer effects were considered. The definition of the relevant variables used in this study is presented in Table 2.1. Important dimensionless variables, such as the liquid Reynolds number (Re_L) and the gas Froude number (Fr_G) and their relationship with more fundamental parameters such as Q_L and M_G was introduced. A summary of the liquid related parameters using this configuration is shown in Tables 2.2 to 2.4.

Table 2.1.   Definition of important variables and dimensionless numbers used in this study

U_{L}	mean liquid cross-flow velocity (m/s)	$\left(= Q_{\mathrm{L}} \middle/ D_{\mathrm{channel}}^{2} \right)$
U_{G}	gas injection velocity (m/s)	$\left(= 4M_{\mathrm{G}} \middle/ \pi \rho_{\mathrm{G}} D_{\mathrm{inj}}^{2} \right)$
Re_{L}	liquid phase Reynolds number	$\left(= \rho_{\mathrm{L}} U_{\mathrm{L}} D_{\mathrm{channel}} \middle/ \mu_{\mathrm{L}} \right)$
Fr_{G}	Froude number based on gas injection conditions	$\left(= \rho_{\mathrm{L}} U_{\mathrm{G}} \middle/ \left(\rho_{\mathrm{L}} - \rho_{\mathrm{G}} \right) \left(g D_{\mathrm{inj}} \right)^{1/2} \right)$
U_{R}	Gas/liquid velocity ratio	$\left(= U_{\mathrm{G}} \middle/ U_{\mathrm{L}} \right)$
M_{R}''	Gas/liquid Momentum flux ratio	$\left(= \rho_{\mathrm{G}} U_{\mathrm{G}}^{2} \middle/ \rho_{\mathrm{L}} U_{\mathrm{L}}^{2} \right)$
M_{R}	Effective velocity ratio	$\left(= \left(\sqrt{\rho_{\mathrm{G}} \middle/ \rho_{\mathrm{L}}} \right) \left(U_{\mathrm{G}} \middle/ U_{\mathrm{L}} \right) \right)$
We_{aero}	Aerodynamic Weber number	$\left(= \rho_{\mathrm{G}} D_{\mathrm{channel}} U_{\mathrm{L}}^{2} \middle/ \sigma \right)$
We_{G}	Gas Weber number	$\left(= \rho_{\mathrm{G}} D_{\mathrm{inj}} U_{\mathrm{G}}^{2} \middle/ \sigma \right)$
Eo_{G}	Eötvos number	$\left(= \Delta \rho_{\mathrm{G}} D_{\mathrm{inj}}^{2} g \middle/ \sigma \right)$

Table 2.2.　　Summary of test conditions for D_{inj} = 1.59 mm

			Eo_G = 0.34				
U_L (m/s)	T_G (K)	P_G (kPa)	$M_G \times 10^{-3}$ (g/s)	U_G (m/s)	$Re_L \times 10^3$	We_G	$Fr_G \times 10^1$
1.3	298.7	146	4.9	1.5	16.7	0.08	1.2
1.2	299.2	138	9.9	3.1	15.9	0.32	2.5
1.2	299.5	138	14.8	4.6	15.6	0.72	3.7
1.1	299.0	139	19.7	6.1	14.3	1.3	4.9
1.1	299.7	136	24.7	7.8	13.7	2.0	6.3
1.1	299.2	142	29.5	9.0	14.2	2.8	7.2
1.1	299.3	147	39.5	11.7	13.9	4.9	9.4
2.1	296.6	211	9.9	2.0	27.5	0.11	1.3
2.1	297.6	214	19.7	4.0	26.9	0.42	2.5
2.1	298.1	217	29.5	5.9	26.8	0.92	3.7
2.0	298.4	220	39.4	7.7	26.5	1.6	4.9
2.2	298.7	225	49.2	9.5	27.9	2.5	6.1
2.1	297.5	231	59.1	11.0	27.0	3.5	7.2
2.0	297.8	245	78.8	13.9	26.5	5.8	8.3
2.0	298.3	260	98.5	16.4	26.4	8.6	9.4
3.1	299.1	511	9.8	1.1	40.6	0.04	0.9
3.2	299.3	512	19.7	2.2	41.2	0.17	1.8
3.1	299.4	512	29.6	3.3	40.0	0.39	2.6
3.1	299.5	513	39.4	4.4	40.6	0.70	3.5
3.3	299.6	515	49.2	5.4	42.7	1.1	4.4
3.1	299.6	513	59.1	6.5	40.1	1.5	5.2
4.4	299.4	662	14.8	1.0	56.7	0.08	0.5
4.3	299.7	660	19.7	1.3	56.4	0.13	1.0
4.3	300.2	660	29.5	1.9	56.2	0.30	1.5
4.3	299.9	661	39.4	2.6	56.2	0.53	2.0
4.3	300.3	661	49.5	3.2	56.2	0.84	2.5
4.3	300.3	661	59.1	3.8	56.2	1.2	2.9
4.3	300.4	661	69.8	4.5	56.2	1.7	3.4
4.3	299.0	663	78.6	5.0	56.2	2.1	3.7
4.3	299.3	663	98.6	6.2	56.2	3.3	4.4
± 0.1	± 0.1	± 5	± 0.1	± 0.2	± 0.03	± 0.02	± 1.6

The experiments were performed at an average $T_G \approx$ 296.8 K.

Table 2.3.　　Summary of test conditions for $D_{inj} = 0.52$ mm

			$Eo_G = 0.04$				
U_L (m/s)	T_G (K)	P_G (kPa)	$M_G \times 10^{-3}$ (g/s)	U_G (m/s)	$Re_L \times 10^3$	We_G	$Fr_G \times 10^2$
1.2	302.7	140	5.0	14.5	15.4	2.3	2.0
1.2	300.2	145	9.9	27.7	15.0	8.9	3.9
1.2	303.1	158	19.7	51.1	15.0	32.7	7.2
1.2	301.7	181	29.7	66.8	14.9	64.4	9.3
1.1	302.7	249	49.2	80.6	14.5	128.6	11.3
2.1	301.7	209	4.9	9.6	27.5	1.5	2.9
2.2	302.4	212	9.8	18.9	28.1	5.7	5.0
2.2	302.9	222	19.6	36.2	28.5	20.8	6.5
2.2	303.1	263	39.5	61.5	28.7	60.1	7.5
2.2	302.6	288	49.4	69.7	28.5	77.5	9.7
2.2	302.6	317	59.4	76.2	28.0	92.6	10.4
3.0	299.2	326	5.1	6.2	38.5	1.0	1.4
3.0	299.9	331	9.7	12.0	38.8	3.8	2.8
3.0	300.4	334	19.6	23.7	39.1	15.1	4.1
3.0	300.6	361	39.5	44.3	39.4	56.8	5.3
3.1	301.1	449	78.6	71.0	39.7	181.0	6.4
3.0	302.3	700	152.2	88.6	39.4	437.7	7.4
4.4	297.3	674	9.9	5.9	56.5	1.9	0.8
4.3	297.9	677	19.8	11.7	56.1	7.5	1.6
4.3	298.2	679	29.5	17.5	56.1	16.7	2.4
4.3	298.5	688	39.5	23.1	56.2	29.5	3.2
4.3	299.0	695	43.0	28.5	56.1	45.4	3.9
4.3	299.2	706	60.4	34.5	56.1	67.4	4.6
± 0.1	± 0.1	± 5	± 0.1	± 2	± 0.03	± 0.04	± 10

The experiments were performed at an average $T_G \approx 296.8$ K.

Table 2.4.　　　Summary of test conditions for $D_{inj} = 0.27$ mm

			$Eo_G = 0.01$				
U_L (m/s)	T_G (K)	P_G (kPa)	$M_G \times 10^{-3}$ (g/s)	U_G (m/s)	$Re_L \times 10^3$	We_G	$Fr_G \times 10^3$
1.1	297.6	154	4.8	47.9	14.6	14.6	0.94
1.1	297.9	176	9.8	86.2	14.3	53.9	1.70
1.1	298.2	220	14.8	102.7	14.2	96.0	2.01
1.1	298.3	268	19.8	113.0	13.9	141.1	2.21
1.1	298.4	365	29.7	124.6	14.2	233.5	2.44
1.1	298.6	467	39.3	128.5	14.0	319.4	2.52
1.0	298.6	573	49.3	132.1	13.5	412.2	2.59
1.9	297.2	197	5.0	38.7	24.3	12.1	0.76
1.9	297.6	214	9.9	70.3	24.7	43.8	1.40
1.9	297.8	252	14.8	89.7	24.5	83.8	1.73
1.9	297.9	294	19.6	102.2	24.5	126.8	2.00
1.9	298.0	385	29.5	117.6	24.3	219.3	2.30
1.9	298.0	480	39.5	125.8	24.3	313.1	2.50
1.9	298.0	578	49.2	130.3	23.8	404.9	2.50
1.9	298.0	684	59.1	132.1	24.0	492.7	2.60
3.3	296.3	527	9.8	28.4	43.1	17.7	0.64
3.3	299.1	534	14.8	42.6	42.3	39.8	1.20
3.4	297.2	555	19.7	54.3	43.4	67.6	1.60
3.2	297.8	598	29.5	75.5	41.1	140.6	1.90
3.2	299.3	625	34.3	84.5	41.6	183.3	2.20
3.2	298.2	659	39.9	92.7	41.7	233.3	2.30
3.2	298.5	713	46.5	99.9	41.8	293.2	2.36
4.3	297.5	668	10.1	23.2	56.2	14.7	0.42
4.3	297.9	680	14.6	32.8	56.3	30.2	0.64
4.3	298.1	699	21.1	46.2	56.2	61.5	0.64
4.3	298.1	714	25.8	55.3	56.2	89.9	1.20
4.3	298.8	721	29.5	60.7	56.2	110.4	1.40
4.3	299.3	732	31.5	66.0	56.3	131.3	1.50
± 0.1	± 0.1	± 5	± 0.1	± 3	± 0.03	± 1.8	± 22

The experiments were performed at an average $T_G \approx 296.8$ K

2.2. Image capture procedure and equipment

Similar to other studies about bubble formation regimes and bubbly flows (Sada et al., 1978; Rigby et al., 1995; Kyriakides et al., 1997; Andreussi et al., 1999; Machniewski et al., 2004, Kulkarni and Joshi, 2005; Andersson and Andersson, 2006), a high-speed imaging technique was chosen. The data were collected using a 1.2 MP, 8-bit CCD high-speed camera (Lightning RDT Redlake MotionPro) with a 35 mm lens (AF-S Nikkor) at a rate of 3,000 frames per second for at least 3.2 seconds. To assure repeatability, each video was captured three times under the same experimental conditions. The two-phase flow behaviour was measured at viewing sections (V1) and (V2) (Figure 2.1). Each section had dimensions of 168 pixels × 800 pixels in the vertical and horizontal directions respectively. The camera was connected to a computer which recorded the array of images using a commercial software package (MiDAS V 2.0). The focal plane for the images was located on the channel centerline, passing through the air injection port, which gave an approximate working distance for the camera of 25 cm.

An in-focus calibration plate was placed on the external windows of the channel to estimate an mm-to-pixel factor that allowed the conversion to physical dimensions. The averaged value for this factor was 76 µm/pixel. More information about the methodology involved in the calibration process can be found in Appendix A. This resulted in viewing areas with physical dimensions of 12.7 mm × 60 mm in the vertical and horizontal dimensions respectively. For section (V1), it allowed a full visualization of the gas phase morphology and the gas-liquid interaction near the gas injection location following a distance several hydraulic diameters downstream of this point.

For section (V2), these dimensions allow a detailed observation of the bubbly flow upstream the discharge nozzle.

An incandescent light source (2 × 400 W) was used as the illumination source. The lights were located behind a thin translucent plastic sheet that acted as a diffuser. Hence, all the images captured had clearly defined contours and there was a clear differentiation between the background (liquid phase) and the objects (gas phase). To freeze the motion of the gas particles within the channel, an exposure time of 160 μs was used. Figure 2.3 presents an example of the raw two-phase flow obtained through visualization at section (V1) and (V2) respectively.
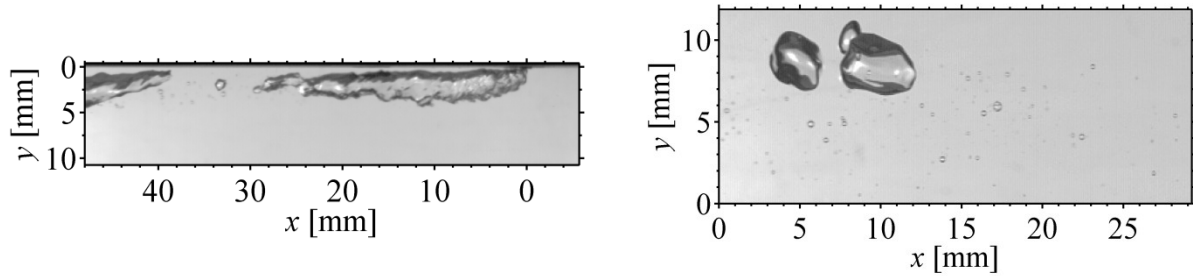
Figure 2.3.   Examples of gas-liquid interaction at the selected visualization windows. Left: injection region (V1). Right: upstream discharge nozzle (V2)

2.3.   Image Analysis Methodology

An in-house, Matlab (v. 2013a) based algorithm was developed to extract the relevant morphological features of the gas structures. The image processing steps consisted of:

a.1) Cropping of the raw image to remove non-desirable objects, such as the edge of the channel walls.

a.2) Subtract the background image to increase the contrast.

a.3) Obtain the gray level image histogram and determine an appropriate threshold level.

a.4) From the selected value, invert and binarize the image.

a.5) Perform image enhancement operations such as filtering, dilation, filling and erosion.

a.6) Identify the objects of interest within the image and conduct geometrical measurements of the features of interest such as projected area, horizontal length, perimeter and centroid coordinates.

After this process, the only objects in the image were the gas structures, which appear as white regions. The above mentioned process facilitates the unbiased delimitation and identification of the different structures present within each instantaneous image. A more detailed description of the image processing methodology can be obtained from the information provided in Appendix A, specifically Figures A.2 and A.3, and Appendix G, which contains the detailed and commented Matlab algorithms.

2.3.1. Estimation of bubble diameter and gas jet morphology

The gas features were projected as a shadow in the focal plane and were captured by the camera as a two-dimensional image. Any volumetric estimation had to be determined from the areas captured in the shadowgraph. Limitations related to the equipment configuration restricted the measurements to the side view, at a parallel level with the channel and perpendicularly oriented

to the flow. In a similar experimental configuration, Razzaque et al. (2003) determined that difference between data captured from the side position and that captured from the side is not relevant. Hence, it was inferred that an analogous situation would occur here and the results obtained were not biased based on the orientation of the visualization window.

Although three-dimensional information such as volume or depth cannot be obtained, it is possible to detect the variation of the gas jet boundaries and shape in time. This allows the estimation of key morphological features such as the gas jet equivalent diameter (D_{equiv}), the averaged jet width (D_{width}), jet axis breakup length (X_{break}) and jet perimeter (P_{ER}). The D_{equiv} of any gas object present in the image was obtained from area-based measurements performed on each still frame, as defined in Equation (2.8), where A_P is the projected area of the gas structure in the plane of the image. The bubble geometric diameter (D_B) is obtained in a similar way; through the estimation of the projected area of the bubbles in the image focal plane and can be estimated in the exact way described for gas jets. X_{break} is defined as the maximum horizontal length that the gas jet grows before bubble detachment occurs. This implies the separation of a bubble whose volume is large enough to incur in a noticeable change in the gas jet dimensions. D_{width} is defined as the maximum distance between the inner and outer boundaries of a gas jet and *Per* is the perimeter of the gas projected area on the frame.

Figure 2.4 depicts a visual description for each one of the previous definitions as well as a summarized depiction of the image analysis process, showing the cropped region of interest, the final binary image and the matching of the calculated contour with that of the original image. The gas jet interfacial positions were tracked at all times, the estimated boundaries exhibit a high

level of agreement with the experimental frame, providing an accurate method of measuring the previously defined morphological features, as can be seen in Figure 2.4.

$$\text{Gas jet equivalent diameter } D_{\text{equiv}} = \sqrt{4A_{P(\text{jet})}\Big/\pi} \qquad (2.8a)$$

$$\text{Bubble diameter } D_{\text{B}} = \sqrt{4A_{P(\text{bubble})}\Big/\pi} \qquad (2.8b)$$
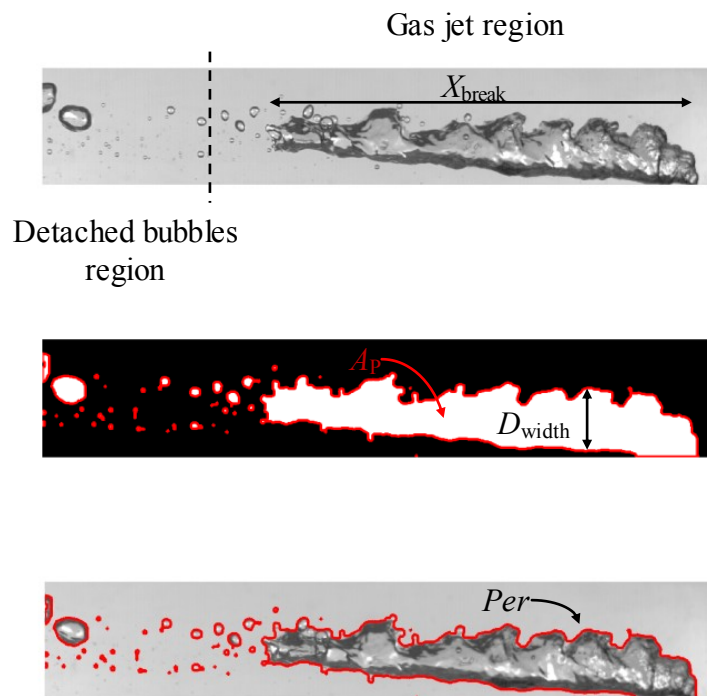
Figure 2.4.   Depiction of the image analysis process. Top: original image, cropped to capture the region of interest. Middle: final binary image, where the white region refers to the gas phase. Bottom: comparison between the outline computed from the binary image and the original image, showing an almost perfect estimation of the boundary between phases

The methodology followed to estimate the diameter of the detached bubbles is similar to that described for the calculation of the gas jet morphological features. The bubble diameter after detachment was measured at a distance of at least 30 mm downstream of the gas nozzle. After

this point, the frames captured depicted the incipient bubbly flow features. Similarly, to estimate the diameter of the bubbles before they passed the discharge nozzle, the values were measured using an interrogation window which encompasses the area 1 to 4 cm upstream of the nozzle. In each case, the physical dimensions of the region of interest where 127 mm × 360 mm in the vertical and horizontal direction respectively. This region corresponded to approximately 168 pixels × 480 pixels. Between 650 and 750 images were chosen for each test condition and analyzed using Matlab. This number of images was chosen with the purpose of ensuring the necessary and sufficient statistical independence of the data obtained.

As occurs in most practical cases of particle ensembles, particularly in bubbly flows, the distributions observed were polydisperse in nature. For the purposes of easier characterization, the use of a common single number is mandatory. Although it is possible to use simple definitions such as the median diameter or the average arithmetic diameter, the surface area and volume of the bubbles are related to the square and cube of the diameter, respectively. Therefore, it is required a more detailed parameter for an adequate characterization. The Sauter mean diameter (D_{32}) is one of such parameters and has been commonly used for the study of bubbly flows and effervescent atomizers (Chin and Lefevbre, 1995; Razzaque et al., 2003; Ghaemi et al., 2010; Rahman et al., 2012). D_{32} was estimated from the particle array using equation (2.9), where K is the total number of bubbles measured and n_i is the number of bubbles whose diameter is equal to d_i. D_{32} was determined by applying equation (2.9) to the bubble ensemble.

Although in the jetting regimes it is possible to observe the existence of multiple detached bubbles, only the diameter of the main particle separating from the gas core was considered as a

representative value of the bubble size. The effects of coalescence, secondary detachments and other effects were not considered. Appendix A explains the uncertainty associated to the estimation of the diameters from the projected area, which applies to the both D_{equiv} and D_{32} estimations. Additionally, Appendix A (Table A.4) contains information about the uncertainty associated to the estimation of volumetric quantities from a projected area approach.

$$D_{32} = \frac{\sum_{i=1}^{K} n_i d_i^3}{\sum_{i=1}^{K} n_i d_i^2}; \quad \sum_{i=1}^{K} n_i = K \tag{2.9}$$

The maximum bubble diameter (D_{99}) was defined as particle diameter value below which 99% of the bubbles in either a size-based or number-based distribution exist.

Lastly, it is important to mention that the experimental setup and imaging systems used were not designed nor selected with the purpose of achieving high definition in the vicinity of the nozzle region. While having detailed resolution in this region could be interesting for studying the formation of microbubbles, the effects of the nozzle material on the bubbling process or the estimation of the contact angle, none of these topics was withing the scope of the thesis. For the purposes of identifying the bubble diameter, the bubbling regime, the gas jet morphological features and the dispersion of the gas jet in the liquid cross-flow, the camera resolution selected is more than adequate. The region of interest selected along with the level of definition used guarantees acceptable, repeatable results. Additional information about the relevance of the nozzle dimensions with respect to the gas jet dimensions is included in Appendix A.

2.3.2. Estimation of the gas jet trajectory

The external boundaries of the objects were traced and particles whose total area were equal or less than four pixels were eliminated from the image. Owing to the changing nature of the jet, the locus of the maximum probability, as well as the borderline, were determined from a time-averaged image ensemble consisting of at least 750 individual binary frames. The image ensemble is obtained through a summation-averaging method, where each of one the independent binary frames is added and the final result is divided by the total number of frames included (averaging). The delay used in the estimation of the images was necessary and sufficient to ensure statistical independence of the results obtained. This results in a final image, with spatially varying values, which represents a time-based averaged estimation of the gas phase probability distribution in the Cartesian system represented by the image extension.

This methodology is similar to the one described and followed by Harby *et al*. (2014) for the analog case of gas jet injection in stagnant liquids. Figure 2.5 presents a review of the methodology used in the estimation of the gas jet trajectory, showing an example of the original cropped image, the resulting binary image and the array obtained from the composition of the individual frame. Following a procedure similar to the one proposed by Amighi *et al*. (2009), the mean jet centerline was characterized as the (x, y) position, along the stream wise direction, where the highest probability that gas was present occurred.

a)

b)

c)
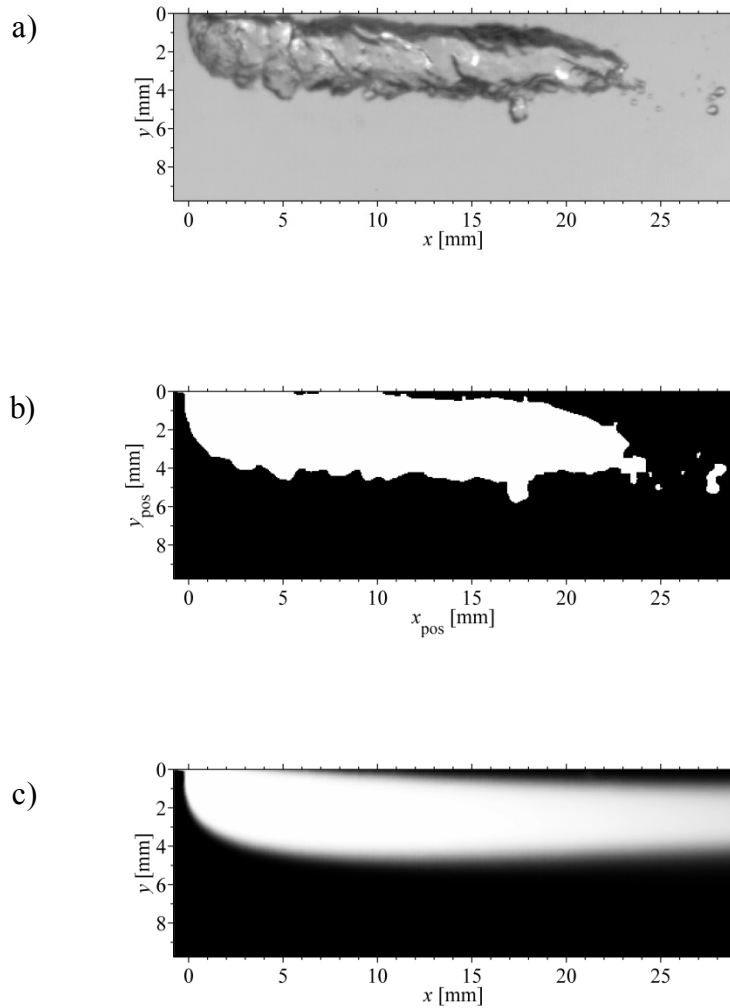
Figure 2.5.   a) Instantaneous frame of the gas plume near the injector. b) Color inverted image obtained after the use of the imaging-algorithm on the instantaneous frame. c) Image ensemble obtained from averaging a succession of at least 750 frames corresponding to the same set of geometrical and experimental conditions. The results shown were obtained for D_{inj} = 0.27 mm, M_G = 45.71 × 10^{-6} g/s, U_L = 1.1 m/s

When there was more than one local maximum at a single horizontal location, the algorithm considered the locations of the neighbouring points to determine the vertical position of the centerline. This step minimized the variability in the centerline location. The trajectory was determined from the gas inlet ($x = 0$, $y = 0$) up to a distance downstream of the inlet equal to four

times the channel diameter, which encompassed the gas jet breakup process, and in some cases, the initial path of the recently detached bubbles.

Kamotani and Graber (1974) and Muppidi and Mahesh (2005) argued that, for jets in a cross-flow, defining the trajectory near the injection is complicated due to the occurrence of multiple maximum concentration and velocity points. Although Yuan and Street (1998) recommended the use of the streamline as the best alternative for the definition of the jet trajectory, they determined that the differences between the definition of the centerline based on maximum velocity, maximum scalar concentration or streamline produced only slightly different results. However, for the purposes of gas injection in a liquid cross-flow, the use of a methodology other than maximum probability of gas presence is not applicable because of the difficulties in obtaining the velocity within the gas phase.

Harby *et al.* (2014) compared two imaging methodologies that allow the estimation of the geometrical parameters associated to a gas jet injected in liquid. The first method corresponded to the statistical approach, where the shape parameters were extracted from each individual frame and then quantified statistically. The second method was a summation technique, where each processed image is added to the last one, resulting in a final frame with intensity that varies spatially. The morphological features of the gas plume are extracted from this final image. Harby *et al.* (2014) determined that, for various Fr_G and D_{inj} values, the differences in the morphological features of a gas jet between the two image processing methods were between 2% to 5%. Based on this result, it was inferred that the use of the summation method would generate

results that reproduce reliably the physical behaviour of the gas jet and was the approach chosen in this study.

Figure 2.6 presents an array of individual frames obtained using the summation method. The succession of points represents the location where the gas maximum probability in the vertical direction can be observed. Similarly, the region where the gas probability became less than 10% of the maximum horizontal value was identified as the gas phase boundary, represented in Figure 2.6 by the continuous yellow line. The image indicates the existence of a large continuous gas region, as indicated by the maximum color bar value, present within the liquid flow.
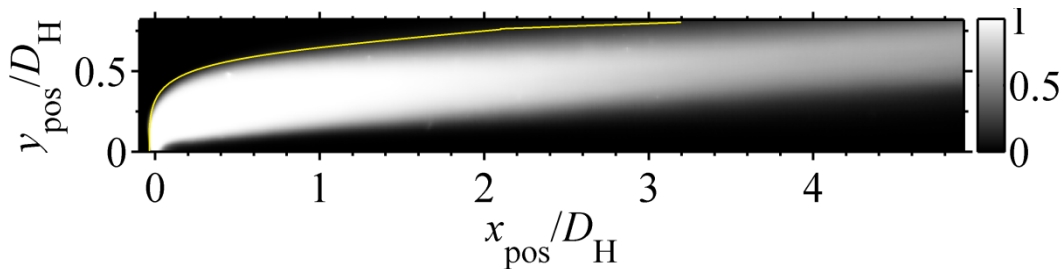
Figure 2.6.   Estimation of the gas jet trajectory from the summation of individual images

2.3.3. Void Fraction Definition and Calculation

In this study the void fraction is defined as the percentage of the channel cross-sectional area that is occupied by the gas, and as mentioned in chapter two of this manuscript, the approach followed is the use of time-averaged values. However, it must be understood that the instantaneous void fraction value is fluctuating with time, and at any given (x, y) location within the interrogation area the fluid can be either gas or liquid. Commonly, when referring to the void

fraction, it is implicitly related to the volumetric void fraction (α) defined according to equation (2.10), where V_G and V_L are the volume occupied by the gas and liquid phases respectively.

$$\alpha = \frac{V_G}{V_G + V_L} = \frac{V_G}{V} \qquad (2.10)$$

Similarly, the theoretical definition of the cross-sectional or area based void fraction (α_{area}) is given in equation (2.11), where A_G and A_L are the areas within a region of interest occupied by the gas and liquid phases respectively.

$$\alpha_{area} = \frac{A_G}{A_G + A_L} = \frac{A_G}{A} \qquad (2.11)$$

Although there are other definitions, such as the local void fraction (α_{local}) and the chordal void fraction, the area based void fraction is the most widely used in two-phase flow applications (Kocamustafaogullari et al., 1994; Coddington and Macian, 2002). It is the parameter of choice in the estimation of flow pattern transitions, two-phase pressure drops and flow boiling coefficients. Therefore, from this point on, any discussion about the void fraction will refer to the variable estimated to an area based approach, in line with the experimental method chosen.

In the combined flow of gas and liquid phases it is common to define a parameter called the dispersed-phase density function, as given in equation (2.12)

$$\gamma(\mathbf{S},t) = \begin{cases} 1 & \text{if at time } t, \text{ the point } \mathbf{S} \text{ is in gas phase} \\ 0 & \text{if at time } t, \text{ the point } \mathbf{S} \text{ is in liquid phase} \end{cases} \tag{2.12}$$

In stationary cases, the time-averaged local void fraction (α_{local}) can be defined according to equation (2.13), where t_∞ refers to a very long time.

$$\alpha_{\text{local}}(\mathbf{S},t) = \frac{1}{t_\infty} \lim_{t_\infty \to \infty} \left(\int_0^{t_\infty} \gamma(\mathbf{S},t)\,\mathrm{d}t \right) \tag{2.13}$$

Equation (2.13) can be also be expressed as equation (2.14), where t_G refers to the total time that the gas phase was observed at point $\mathbf{S}$.

$$\alpha_{\text{local}}(\mathbf{S}) = \sum t_G \big/ t_\infty \tag{2.14}$$

The void fraction can also be defined using spatial averages. One of the possible alternatives is the area-averaged void fraction (α_{area}), which is defined as the area-averaged local instantaneous void fraction, at a time t over the reference area A_P, as defined in equation (2.15).

$$\alpha_{\text{area}}(\mathbf{S},t) = \frac{1}{A_P} \iint_{A_P} \gamma(\mathbf{S},t)\,\mathrm{d}A \tag{2.15}$$

The time and area-averaged void fraction ($\overline{\alpha}$) at the section A_P, in a time interval is defined as:

$$\overline{\alpha}\left(A_{\mathrm{P}}\right)=\frac{1}{t_{\infty}}\int_{0}^{t_{\infty}}\alpha_{\mathrm{area}}\left(\mathbf{S},t\right)\mathrm{d}t \qquad (2.16)$$

The experimentally determined void fraction values were estimated from the image array, obtained following the previously described summation methodology. The resulting image, composed by at least 750 independent frames, encompassed a region of at least 127 mm × 320 mm in the horizontal and vertical dimensions, respectively. The choice of 750 independent images guarantees statistical independence. These images obtained under for a set of experimental conditions and repeated at the least three times, to assure that the results were reproducible. An example of the estimated values for the void α_{area} and α_{local} can be observed in Figure 2.7. The area void fraction is obtained by adding the time-based results for each individual point, whose values oscillate between zero (pure liquid) and unity (pure gas), and dividing them by the area of interest, resulting in a mean void fraction value that presents the ratio between the averaged probability of the liquid phase versus that of the gas phase.
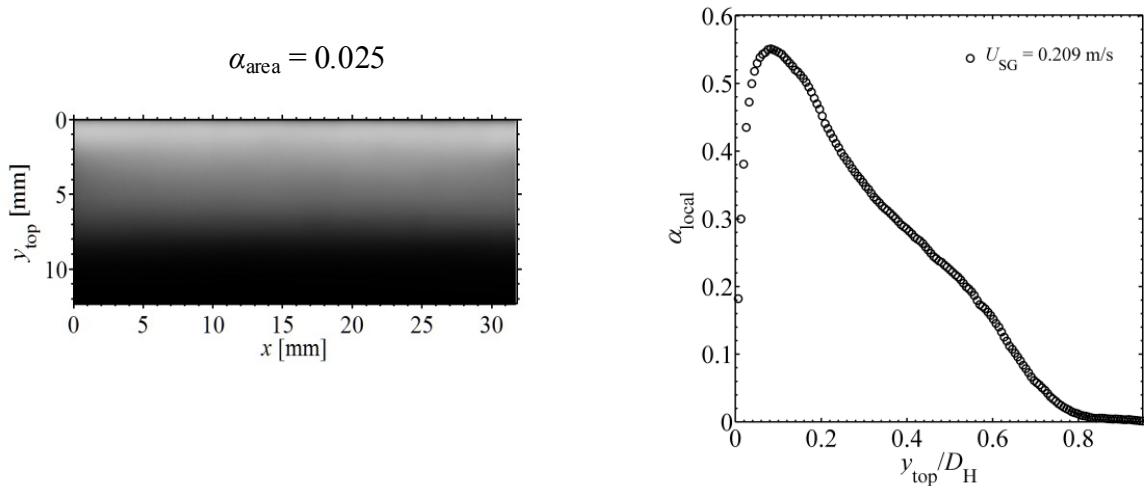
Figure 2.7.   Left: representation and estimation of the area based void fraction. Right: local void fraction as a function of the vertical distance measured from the top wall

2.3.4. Gas Jet Growth Cycle

The process of growth of a gas jet, and subsequent breakup, in the presence of a liquid cross-flow exhibits a quasi-periodical behaviour, as shown in Figure 2.8. The results depicted in this graph represent the evolution in time of the dimensionless gas jet length (χ) for a selected interval. The physics of the gas injection phenomenon in a liquid indicate that, at a fixed M_G rate, the plume experiences a continuous growth from its initial state ($t = 0$) until reaching the point of gas jet distintegration. The growth time (t_{growth}) can be defined as the time where this breakup occurs. After the bubble detachment, the gas jet experiences again an expansion process until fragmentation is observed again. This process can be defined as the gas jet growth cycle and refers to that continuous and sequential growth-breakup behaviour which is inherent to the mechanics of bubble formation in liquids.

However, because of the natural randomness involved associated to the gas injection mechanics, a perfectly periodical breakup-detachment cycle is unrealistic; particularly under turbulent flow conditions for either or both the gas and liquid and for experimental conditions that aim to simulate an industrial scenario. The results shown in Figure 2.8 are proof of this. Hence, to properly characterize the t_{growth} associated to a particular set of experimental conditions, it must be obtained from a statistically adequate number of growth-break cycles. Considering the total number of detachment scenarios encompassed within a single measurement and the repeatability approach used, it was assumed that the t_{growth} obtained for each experimental configuration was above this statistical limit.
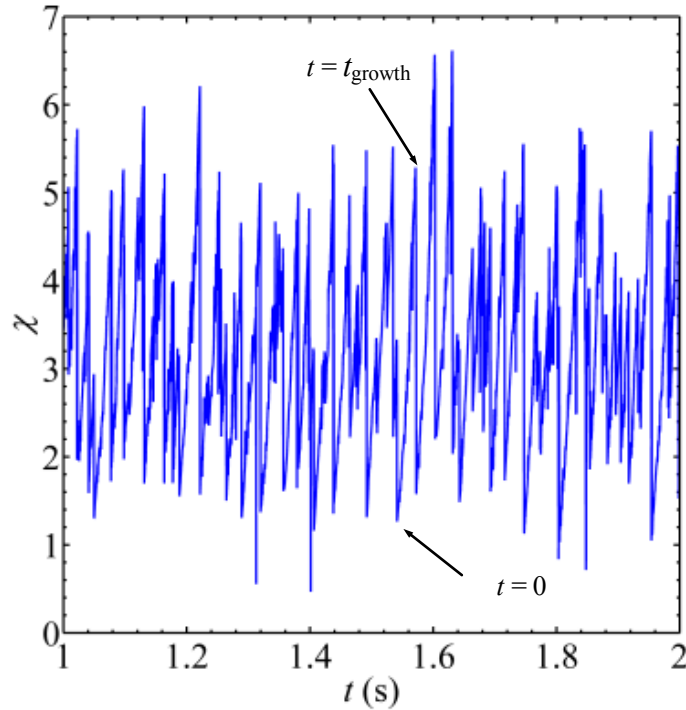
Figure 2.8.   Gas jet growth cycle as a function of time during a selected interval, where χ is the instantaneous gas jet dimensionless length. The conditions are $M_G = 39.5 \times 10^{-3}$ g/s, $D_{inj} = 0.27$ mm, $U_L = 1.9$ m/s

It is also important to mention that, as observed in Figure 2.8, the growth of the gas jet does not necessarily start from $\chi = 0$. While in most bubble formation in liquid studies it is assumed that the bubble separates almost completely from the submerged nozzle (Kulkarni and Joshi, 2005), this is not necessarily true for gas injection into a liquid cross-flow. The results depicted in Figure 2.8 indicate that after the gas jet disintegrates, a gas neck with an averaged magnitude approximately equal to $\chi = 1.7$ is present in the conduit. While this is only a representative case, for the vast majority of the scenarios tested, this phenomenon was observed.

2.3.5. Image processing error

For a comparable phenomenon, Duhar and Colin (2006) proposed that the error associated to the image processing is caused by the filtering operation, the binarisation process and due to the calibration. Hence the total error related to the image analysis process can be estimated as $\varepsilon_{total} = \varepsilon_{filtering} + \varepsilon_{calibration} + \varepsilon_{binarisation}$. The $\varepsilon_{binarisation}$ is the error introduced by the binarisation process. This error considers the inversion of the image, the adjustment of its contrast by use of a background image and a threshold to produce a black and white image.

The average $\varepsilon_{binarisation}$ obtained during this study oscillated between 0.7 and 1.1 % of the projected gas jet diameter. $\varepsilon_{filtering}$ is the error caused by the use of the dilation, filling, erosion and a structured squared filter. This was done with the purpose of filling any non-physical inner holes inside the objects and smoothing the object boundary. These holes were created by the light source reflection on the bubble surface. A value of 0.4% was determined for $\varepsilon_{filtering}$. It encompassed all the errors created by the morphological filtering operations, although the changes in the area and shape of the objects were minimal. $\varepsilon_{calibration}$ is the error value associated to the calibration process. An error of one pixel was equal to 0.07 mm, which translated into an averaged uncertainty value of 0.7%. Therefore, the maximum ε_{total} is approximately equal to 2.2% of the gas jet equivalent diameter.

Appendix A presents additional information about the uncertainty in the estimation of geometric variables through the chosen experimental method. Table A.4 provides a summary of the uncertainties associated to the geometrical quantities estimated during this study. Of fundamental

interest is the fact that the discrepancies related to D_{equiv} are approximately equal to 1.3% of the reported values while the variations associated to the estimation of any value related to the volume of the bubbles or jets is equal to 4.2% of the reported value.

2.4. Relationship between Measurements and Internal Fluid Mechanic Flow in Effervescent Atomizers

As was mentioned in Section 1.1, the extent of the present work is focused on the internal fluid mechanics inside an atomizer mixing chamber. Hence, the measurement regions defined in the previous sections (V1 and V2) were chosen as to allow the evaluation of the gas-liquid interaction within the conduit based on the zones described in Figure 1.1, with exclusive focus on zones I-II-III. The measurement window (V1), with physical dimensions of $D_H \times 5D_H$ (V $\times$ H), allows the observation of the two-phase flow in the vicinity of the gas injection nozzle.

As per the definition given in Section 1, the results obtained from the images captured at window (V1) can be associated to region I since they refer to the process of gas injection and bubble formation into a liquid cross-flow. Although the gas jet dimensions (length, equivalent diamter, width) are transient and vary in magnitude depending on the operating and geometric conditions, the extent of region (V1) is enough to guarantee a full capture of this effect.

Even though the dimensions of the gas jet are cyclical (change in time within constrained boundaries), the extent of the interrogation area (V1) allows for a detailed and complete capture of the gas-liquid characteristics desired and necessary to describe adequately the features

associated to zone I from Figure 1.1. Since region I was defined as the process of gas injection and bubble formation, the features captured in the area (V1) fully account for this. Also, considering that the process of bubble separation and initial stages of the bubbly flow are captured, the transitions between zone I and II is also captured in this region.

Similarly, the dimensions of region (V2) allow for the visualization and characterization of the conditions of the two-phase flow before it is passed through the discharge nozzle. Hence, the outcome of the analysis associated to window (V2) can be directly correlated to the description of zones II and III (Figure 1.1). It is possible to observe the flow pattern of the mixture before it is discharged, the distribution of the gas phase within the liquid and void fraction profile, features associated to zone III in an effervescent atomizer. Also the possibilities of bubble coalescence or breakup, the interactions between wall-bubbles and the diameter and distribution of the bubbles can be determined, which provides for a thorough description of the two-phase flow physics of zone II. As occurred for window (V1), the dimensions selected for window (V2) provide enough information about the bubble flow and, in this case, the variability associated to possible changes in the extent or the zones does not constitute an issue, as only a small but fundamental region of the mixing chamber was studied.

With the purpose of providing a clear understanding about how the contributions to be presented in the following chapter fit into the fluid mechanics inside an effervescent atomizer, an excerpt about the contents of each Chapter will be correlated with the respective effervescent atomizer region and measurement window. This summary is included in Table 2.5 and exemplifies how

the nature of the measurements conducted encompasses the regions associated to the internal flow in an effervescent atomizer.

Table 2.5. Relation between measurement windows, regions in an effervescent atomizer and the nature of the flow

Chapter description	Effervescent atomizer regions	Visualization window
Characterization of the gas injection process into a liquid cross-flow using JICF analogy	(I) and transition toward region (II)	(V1)
Description and estimation of the forces influencing the growth of a gas plume in a liquid cross-flow	(I)	(V1)
Recognition of the dominant dynamic forces during the growth of a gas plume in a strong liquid cross-flow	(I)	(V1)
Link between gas injection mechanics and the nature of the flow upstream of the nozzle	(II) and (III)	(V2)
Bubble formation regime charts based on dimensionless numbers	(I)	(V1)

3. Gas phase probability distribution in a liquid cross-flow

The interaction of an air jet in a liquid water cross-flow in the vicinity of a gas injector is experimentally investigated using high-speed shadowgraphy. A turbulent, fully developed water flow, with superficial water velocity values between 1.9 and 4.3 m/s, circulated through a 12.7 mm square channel of 116 cm in length. Three different gas nozzles, with diameters of 0.27 mm, 0.52 mm and 1.59 mm, were used to inject the air perpendicularly into the water flow. The gas mass flow rates ranged from 10 to 60×10^{-3} g/s. An image processing algorithm was used to estimate the incipient centerline and borderline trajectories of the gas phase during its initial interaction with the liquid. The experimental results were compared with existing correlations developed for standard jets in a cross-flow, with limited agreement between them being found. There is a substantial lack of correlations specifically developed for gas jets in a cross-flowing liquid. Therefore, a set of original empirical expressions based on dimensionless parameters was introduced. The assessment of the correlations indicated a dependable prediction of the initial centerline and borderline trajectories of the gas jet in liquid.

3.1. Background

Several authors have studied the mechanics of gas jets in a liquid cross-flow (GJILCF) and its inherent advantages over bubbling in stagnant liquids (Tan *et al*., 2000; Nahra and Kamotani, 2003; Kulkarni and Joshi, 2005, Duhar and Colin, 2006; Liu *et al*., 2010). However, most of the research focus has been devoted to studying the dynamics of bubble generation in a liquid cross-flow under an individual formation regime (Kulkarni and Joshi, 2005). Other regimes of bubble

formation, such as pulsating and jetting have been rarely studied (Rigby *et al.*, 1995; Forrester and Rielly, 1998; Sovani, 2001), even though it has been inferred that from the onset of the pulsating regime, a gas plume exhibited characteristics similar to those of a canonical jet in a cross flow (JICF) (Wace *et al.* 1987), where instead of detaching and forming close-to-spherical particles, the gas jet remained attached to the injection orifice through small necks, elongating continuously until the detachment of a gas slug occurred. A gas core constantly interacted with the liquid cross-flow, and as the gas mass flow rate (M_G) increased, the penetration of the plume of gas into the conduit had a more normal direction.

The primary focus of the abovementioned studies was on the experimental delimitation of the conditions under which the transition between bubbling regimes occur. No studies were found that attempt a quantitative description of a general characterization of GJILCF following an approach similar to JICF. The existing studies that estimate the gas jet trajectory in a liquid considered only the injection in a still liquid, and to the author's knowledge, no previous research has considered the gas jet trajectory in a cross-flowing liquid.

Therefore, the objective of the current chapter is to present an exploratory approach to the characterization of GJILCF in a square conduit, through the exploration of analogies with JICF. The focus was on the experimental measurement of the incipient gas jet boundaries, affected by a mildly turbulent, fully developed liquid cross-flow, during its development and subsequent turbulent breakup. This allowed the estimation of the maximum penetration (borderline) of the gas jet and the location of the maximum gas phase probability (centerline) during the gas phase evolution and its initial spreading near the gas injection location. The effects that the liquid

cross-flow Reynolds number (Re_L), gas injection Froude number (Fr_G), nozzle dimensions (D_{inj}) and inlet port location have on the gas jet width and gas phase probability near the inlet area were explored. The applicability of existing jet centerline trajectory JICF correlations to a GJILCF was evaluated as well. Also, based on the assessment of previous correlations, empirical equations which estimate the path of the jet centerline and the location of the gas jet outermost boundary for a GJILCF were introduced, taking into account the location of the gas injector (top or bottom wall).

For JICF, the trajectory is a good indication of the jet dynamics and its interaction with the cross-flow, the deformation of the jet column and the effects of shear and pressure forces on the jet. A parallelism can be established for GJILCF, where combining the information related to both the centerline and borderline trajectories, it is possible to have a better understanding of the gas-liquid dynamics, the possible interaction of the gas jet with the channel walls and a better knowledge of the gas jet dimensions on the projected plane. All of these are important design variables in fluid mixing applications (Amighi *et al.*, 2009; Ashgriz, 2012; Diez *et al.*, 2011; Gutmark *et al.*, 2010; Kandakure et al., 2009).

3.2. Process of Gas Injection in a Liquid Cross-flow

A JICF can be defined as the continuous injection of a high momentum current into a stream moving perpendicular to the injection nozzle. One of the most typical features in a JICF is the centerline trajectory of the jet. This is commonly defined as the trajectory of the maximum velocity magnitude locus (Diez *et al.*, 2011; Gutmark *et al.*, 2010). In some cases, it was defined

as the maxima of the concentration (Yu *et al.*, 2006; Karagozian, 2010; Ashgriz, 2012). According to New *et al.* (2006), the jet trajectory can also be defined as the streamline that emanates from the center of the jet.

Several correlations describing the jet centerline for JICF exist (Ashgriz, 2012). An extensive number of them were developed for the case where the difference between the densities of the fluids is small. A summary containing some of the pertinent correlations defining the jet trajectory, including the scaling variables considered by each author, is included in Table 3.1. Similar information can be found in the works of Amighi *et al.* (2009) and Kandakure *et al.* (2009). Generally, the expressions follow the power-law form given by equation (3.1) (Kandakure *et al.*, 2009) where α, β and γ are constants estimated for the particular conditions tested, D_{inj} refers to the nozzle diameter and Π_1 is a dimensionless number.

$$\left(\frac{y}{D_{inj}}\right) = \alpha \left(\frac{x}{D_{inj}}\right)^{\beta} \left(\Pi_1\right)^{\gamma} \tag{3.1}$$

Table 3.1. Summary of existing correlations dedicated to the estimation of the jet centerline trajectory

Author(s)	Proposed correlation	Range of parameters/coefficients	Application
Ragucci *et al* (2007)	$\left(\dfrac{y}{D_{inj}}\right) = 2.698\, M_R^{"\,0.441} We_{aero}^{-0.070}\left(\dfrac{x}{D_{inj}}\right)^{0.367}$	$D_{inj} = 0.3, 0.5$ mm; $U_{jet} = 10 - 52$ m/s; $U_\infty = 24.3\text{-}63.7$ m/s	A-1 kerosene fuel or water - air LJIGCF
Kamotani and Graber (1974)	$\left(\dfrac{y}{D_{inj}}\right) = B\left(M_R^{"\,0.47}\right)\left(\dfrac{x}{D_{inj}}\right)^{0.36}$ $\left(\dfrac{y}{D_{inj}}\right) = 2.0\left(M_R^{"\,0.28}\right)\left(\dfrac{x}{D_{inj}}\right)^{0.50}\left(1-e^{-0.07H/D_{inj}}\right)$	$B = 0.89$ (flat initial profile) $B = 0.81$ (fully developed initial profile) $D_{inj} = 0.635$ cm, $8 < M_R^" < 72$	Combustion gases - air JICF. 2D jet trajectory
Pratte and Baines (1967)	$\left(\dfrac{y}{U_{ratio}D_{inj}}\right) = A\left(\dfrac{x}{U_{ratio}D_{inj}}\right)^B$	$5 < M_R^" < 35$, $A = 2.05$, $B = 0.28$	JICF
New *et al.* (2006)	$\left(\dfrac{y}{D_{inj}}\right) = A\left(\dfrac{x}{D_{inj}}\right)^B$	Tophat jet: $A = 1.65$, $B = 0.25$ Parabolic jet: $A = 1.96$, $B = 0.31$ $2.3 < M_R^" < 5.8$, $D_{inj} = 13.5$ mm	Water – water JICF
Margason (1993)	$\left(\dfrac{y}{M_R^" D_{inj}}\right) = A\left(\dfrac{x}{M_R^" D_{inj}}\right)^B$	$1.2 < A < 2.6$; $0.28 < B < 0.34$	
Muppidi and Mahesh (2005)	$\left(\dfrac{y}{M_R^" D_{inj}}\right) = A\left(\dfrac{x}{M_R^" D_{inj}}\right)^B$	$1.45 < A < 2.39$, $0.32 < B < 0.34$ $C = 0.15$, $U_{ratio} = 1.52$, $U_{ratio} = 5.70$	DNS of laminar JICF
Diez *et al.* (2011)	$\left(\dfrac{y}{M_R^" D_{inj}}\right) = AJ^C\left(\dfrac{x}{M_R^" D_{inj}}\right)^B$	Single phase jet: $A = 0.91$, $B = 0.29$, $C = 0.3$ Part. laden jet: $A = 0.89$, $B = 0.27$, $C = 0.3$, $M_R^" = 18$, $D_{inj} = 3$ mm	JICF of water streams, seeded with glass spheres and without particles, into a cross-flowing water
Amighi *et al.* (2009)	$\left(\dfrac{y}{D_{inj}}\right)_{centerline} = 0.191\left(\dfrac{x}{D_{inj}}\right)^{0.43} M_R^{"\,0.30} Re_{channel}^{0.12} Re_{jet}^{0.14}$ $\left(\dfrac{y}{D_{inj}}\right)_{windward} = 0.167\left(\dfrac{x}{D_{inj}}\right)^{0.37} M_R^{"\,0.31} Re_{channel}^{0.11} Re_{jet}^{0.15}$	$10 < M_R^" < 80$, $D_{inj} = 0.40, 0.50$ mm	LJIGCF Water - air. Simulation of spray conditions
Yuan and Street (1998)	$\left(\dfrac{y}{U_{ratio}}\right) = A\left(\dfrac{x}{U_{ratio}}\right)^B \quad (12)$	$A = 1.2 – 1.4$; $B = 0.27\text{-}0.29$; $U_r = 2.0 – 4.0$, $Re_\infty = 2100\text{-}9066$	LES of JICF

New *et al.* (2006) argued that, despite the vast number of numerical and experimental studies devoted to the study of JICF or liquid jets in gas cross-flow (LJIGCF), no universal scaling parameter exists. As observed in Table 3.1, a common variable used in the scaling was the momentum flux ratio (M_R''). When the fluids involved had the same density, the momentum ratio was substituted by the square of the velocity ratio U_R (Yuan and Street, 1998). Diez *et al.* (2011) reasoned that the ample range of differences observed in the scaling correlations was explained by the varied definitions of what constitutes the jet centerline, as well as, the different experimental methodologies followed.

For the case of LJGICF, Ragucci *et al.* (2007) and Ashgriz (2012) suggested that besides U_R and M_R'', another parameter which can influence the jet trajectory is the aerodynamic Weber number (We_{aero}), which represents the ratio of the aerodynamic effects of the flowing current to the surface tension force of the jet. Also, the Reynolds number of the gas jet (Re_G) and the liquid cross-flow (Re_L) could be influential variables in the LJGICF trajectory.

A GJILCF can be defined as the JICF where the injected current is a gaseous phase and the cross-flow is a liquid. Owing to the density difference between the fluids, the GJILCF has similarities with a pure buoyant jet while the effects of the cross-flowing liquid caused significant bending of the jet, giving it advected jet behaviour. Examples of such resemblance are the presence of a well-defined jet-region, the occurrence of a maximum probability trajectory and the existence of multiple zones within the whole jet region.

Despite the parallels between a JICF and a GJILCF, important differences exist between the two processes. In a GJILCF there is a characteristic unsteadiness associated with the gas jet (Harby *et al.*, 2014; Loth and Faeth, 1989), resulting in oscillatory gas release which is often periodic. Also, the entire GJILCF encompasses several sub regions (Kim, 1985), as shown in Figure 3.1. Region I is located near the injector and a pure gas jet exists, where the gas injection characteristics (jet momentum, pressure difference and jet turbulence) dominate. Region II is the switchover stage, defined as the transition region where the balance between inertial forces and buoyancy forces dictates the penetration and bending of the gas jet (Kikkert, 2006). Region III is a plume, where the bubbles detach and the balance between buoyancy and surface tension versus cross-flow effects (turbulence, lift and drag) becomes relevant.
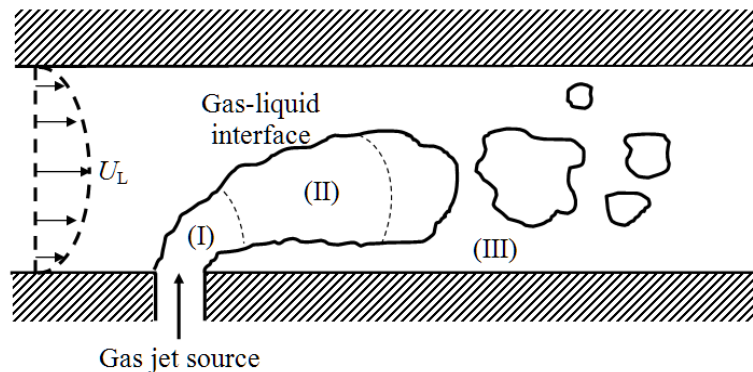
Figure 3.1.   Flow regions of a typical GJILCF scenario

When comparing Figure 3.1 with the concepts introduced in Figure 1.1, the GJLICF scenario is considered to be encompassed within Zone I of the effervescent atomizer description following a fluid mechanics point of view. The first two regions in a GJILCF

refer to the description of the bubble formation dynamics from a novel point of view. Region III (Figure 3.1) depicts the transition from the bubble formation mechanics zone towards the zones II and III inside an effervescent atomizer, as described in Figure 1.1.

Although JICF have been studied extensively, limited information in the field of GJILCF can be found. Most studies associated to the process of gas injection in a liquid focus on stagnant liquids, where the mechanics are primarily dominated by the injection characteristics near the nozzle and buoyancy forces as the jet penetrates into the liquid. Oryall and Brimacombe (1976) observed that the trajectory of a horizontally injected buoyant jet was severely influenced by the nozzle dimension and the physical properties of the injected liquid. The gas jet Froude number, as defined in Table 2.1, had an essential role in the gas jet trajectory within the liquid and its forward penetration into it.

Zhu *et al.* (1998) argued that in an air-water system, the centerline trajectory of a gas jet emanating from a horizontal injector was a function of the Fr_G and D_{inj}, although the jet cone angle also played a role in the jet path. The gas jet penetration length into the liquid, defined similarly as the outermost location of a JICF, was also a function of the Fr_G and gas density ratio. Harby *et al.* (2014) found that D_{inj}, Fr_G, M_G and M_R'' were the variables dictating the gas jet spread in a still liquid. An increase in either of these variables would result in further expansion of the gas jet.

To understand the mechanics of bubbling in a liquid cross-flow, an assessment of the different variables affecting the incipient gas jet was conducted. A simple evaluation of the variables involved indicated that, any morphological feature associated to the gas jet (L_G) would be a function of the geometrical and operational variables involved (Clift *et al.*, 1978), as expressed in equation (3.2), where L_G represents the gas jet length, gas jet equivalent diameter or any other geometrical variable.

$$L_G = f\left(g, M_G, D_{inj}, \rho_G, \mu_G, \sigma, P_G, U_L, D_{channel}, P_L, \rho_L, \mu_L, V_{cha}\right) \tag{3.2}$$

Since the gas is injected directly into the channel from a capillary tube, it was considered that M_G did not change and the bubbling occurred under constant flow rate conditions. Therefore, the volume of the gas reservoir (V_{cha}) and the orifice constant could be disregarded. Because $\mu_G \ll \mu_L$, the effect of gas viscosity was disregarded as well. Similarly, since $\rho_G \ll \rho_L$ then $\Delta\rho \approx \rho_L$ or $\Delta\rho/\rho_L \approx 1$. However when the momentum of the injected gas is relevant, the density of the gas phase must be considered.

A force balance about the forces affecting the gas jet growth indicated that for the range of variables studied (gas nozzle diameter, gas mass flow rate, and liquid velocities), the surface tension forces were very small when compared to other variables. Therefore, the inertial forces became the controlling attaching forces. The pressure force, created by the difference between P_L and P_G, was important during the first stages of gas-liquid interaction. However, as the gas jet expanded, P_G begins to approximate P_L and its

influence as a detaching force decreases. Also, this analysis led to consider that the relevant physical properties of the liquid, ρ_L, μ_L, could be simply grouped into the kinematic viscosity (ν_L). Based on these considerations, a reduced form of L_G was obtained, as indicated in equation (3.3). From the number of fundamental dimensions involved (mass, length and time), it was concluded that a dimensionless geometrical variable (L_{G0}), as given in equation (3.4), could be defined in terms of three dimensionless numbers, Eo_G, Fr_G and Re_L. The other dimensionless numbers refer to the dimensionless ratio between L_G an either D_{inj}, and the diameter ratio D_{inj}/D_H. To take into account the effects of buoyancy caused by the density difference between phases, as well as the effects of nozzle dimensions and surface tension, Eo_G was used.

$$L_G = f\left(g, M_G, D_{inj}, U_L, D_{channel}, \nu_L, \sigma\right) \tag{3.3}$$

$$L_{G0} = \left(L_G \Big/ D_{inj}\right) \text{ or } \left(L_G \Big/ D_{channel}\right) = f\left(U_G \Big/ \sqrt{gD_{inj}}, U_L D_{channel} \Big/ \nu_L, \Delta\rho g D_{inj}^2 \Big/ \sigma\right) = f\left(Fr_G, Re_L, Eo_G\right) \tag{3.4}$$

3.3. Results and Discussion

3.3.1. Evaluation of existing expressions for jet trajectory

The dispersed phase trajectory near the gas inlet location can be observed in Figure 3.2, where the (x, y) locations were made dimensionless using $D_{channel}$. Although a common approach for JICF is to use D_{inj} as a scaling parameter (Gutmark *et al*., 2011; Karagozian, 2010; Rudman, 1996), the choice of $D_{channel}$ for GJILCF is justified because it allows a

better understanding of the distribution of the gas phase along the conduit span. It also permits the evaluation of possible interactions between the gas jet with the opposite wall of the channel.

As illustrated in Figure 3.2, the location of the gas injector plays a key role in the behaviour of the GJILCF trajectory. For top wall injection, independent of the D_{inj} and the value of Re_L, the maximum probability trajectory remained relatively close to the wall, with the maximum penetration having an approximate value $y/D_{channel} < 0.28$, which occurred at $D_{inj} = 0.27$ mm and $Re_L \approx 24{,}000$. This was caused by a buoyancy-induced displacement of the gas jet towards the top channel wall. This effect was more noticeable when the injector was positioned in the top wall, since the buoyancy acted as an attaching force, opposing the penetration of the gas into the conduit.
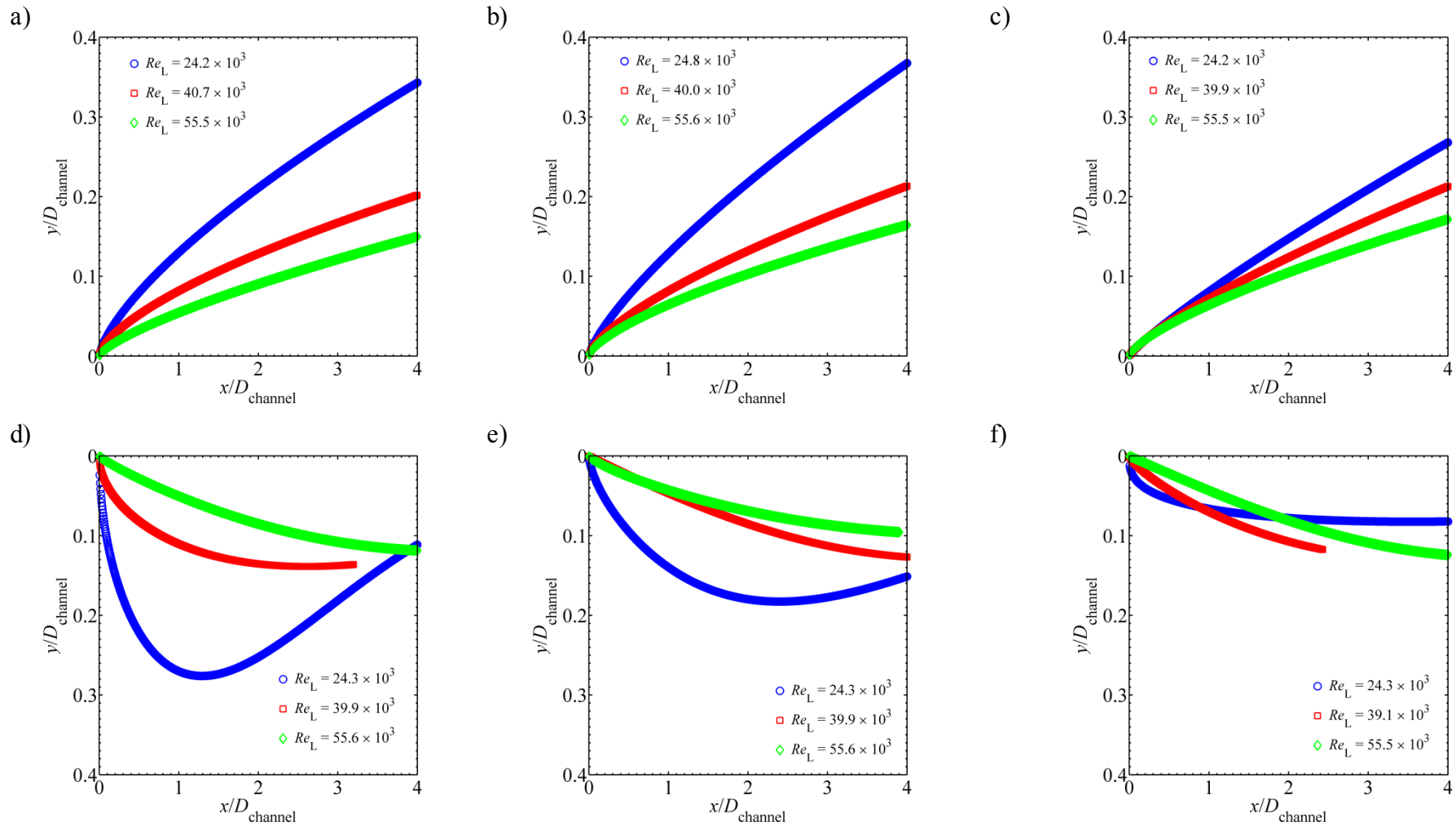
Figure 3.2. Consideration of the effects of the Re_L on the experimentally determined maximum probability of the gas phase during the injection into a liquid cross-flow. The penetration effects between top and bottom wall effects are compared. The M_G and D_{inj} for each chart are constant. Bottom wall injection: a) $M_G \approx 39.4$ g/s $\times 10^{-3}$, $D_{inj} = 0.27$ mm. b) $M_G \approx 39.4$ g/s $\times 10^{-3}$, $D_{inj} = 0.52$ mm. c) $M_G \approx 39.4$ g/s $\times 10^{-3}$, $D_{inj} = 1.59$ mm. Top wall injection: d) $M_G \approx 39.4$ g/s $\times 10^{-3}$, $D_{inj} = 0.27$ mm. e) $M_G \approx 39.4$ g/s $\times 10^{-3}$, $D_{inj} = 0.52$ mm. f) $M_G \approx 39.4$ g/s $\times 10^{-3}$, $D_{inj} = 1.59$ mm

For the bottom wall injection case, the tendencies exhibited a gradual increase in the centerline slope, with the maximum vertical location of the probability centerline always occurring at the end of the interval $x/D_{channel} = 4$. As observed in Figure 3.2, incrementing Re_L caused a slower increase of the gas jet penetration into the channel. For the smallest Re_L, the centerline trajectories exhibited further penetration into the conduit.

At the lowest Re_L, M_G and the density-difference between phases had an influential role, as indicated by the manifest variations in the centerline trajectory. Figure 3.2d exemplifies this scenario, where the gas inertial forces caused deep initial penetration of the gas jet into the conduit up until reaching a turning point at $x/D_{channel} = 1.4$. After this, the combined influence of the liquid cross-flow momentum and buoyancy induced a rapid decrease in the trajectory, which achieved a quasi-steady trend near the end of the interval. As Re_L was increased, the liquid momentum became the dominant force in the gas jet path overcoming both the buoyancy and inertial forces and causing the centerline trajectories to exhibit a smoother transition towards stable values. As observed, at the highest Re_L, the centerline trends were almost equal for all the D_{inj} values tested, which indicated an almost complete transition from a buoyancy-momentum driven regime towards a cross-flow dominated regime.

For a fixed M_G value, a small D_{inj} translated into high U_G and consequently further penetration of the gas jet into the conduit, as indicated by the results depicted in Figure 3.2. As the gas nozzle dimensions increased, the momentum and inertial forces associated to the

gas jet became less relevant when compared to the liquid cross-flow momentum, causing an overlapping of the centerline paths for different Re_L.

An assessment of the applicability of the correlations shown in Table 3.1 to the GJILCF scenario was conducted. Several expressions were selected with the purpose of obtaining a complete characterization of the several forms of the equations describing the JICF centerline trajectory. The correlations were tested for the range of parameters shown in Tables 2.2-2.4. The results from the comparison between the correlations and the experimental results from this study can be observed in Figure 3.3. In all cases, $M_G \approx 29.8 \times 10^{-3}$ g/s and $Re_L \approx 24{,}000$ remained constant.

It was observed that a change in the channel orientation created a difference in the location of the maximum probability, which was not adequately reproduced by the correlations. Even though the full extent of the results obtained could not be presented, the information shown provided a clear characterization of the general trends observed. Although not clearly defined, for all the correlations it was assumed that the injection into the cross-flow occurs in the direction opposite to the gravity.
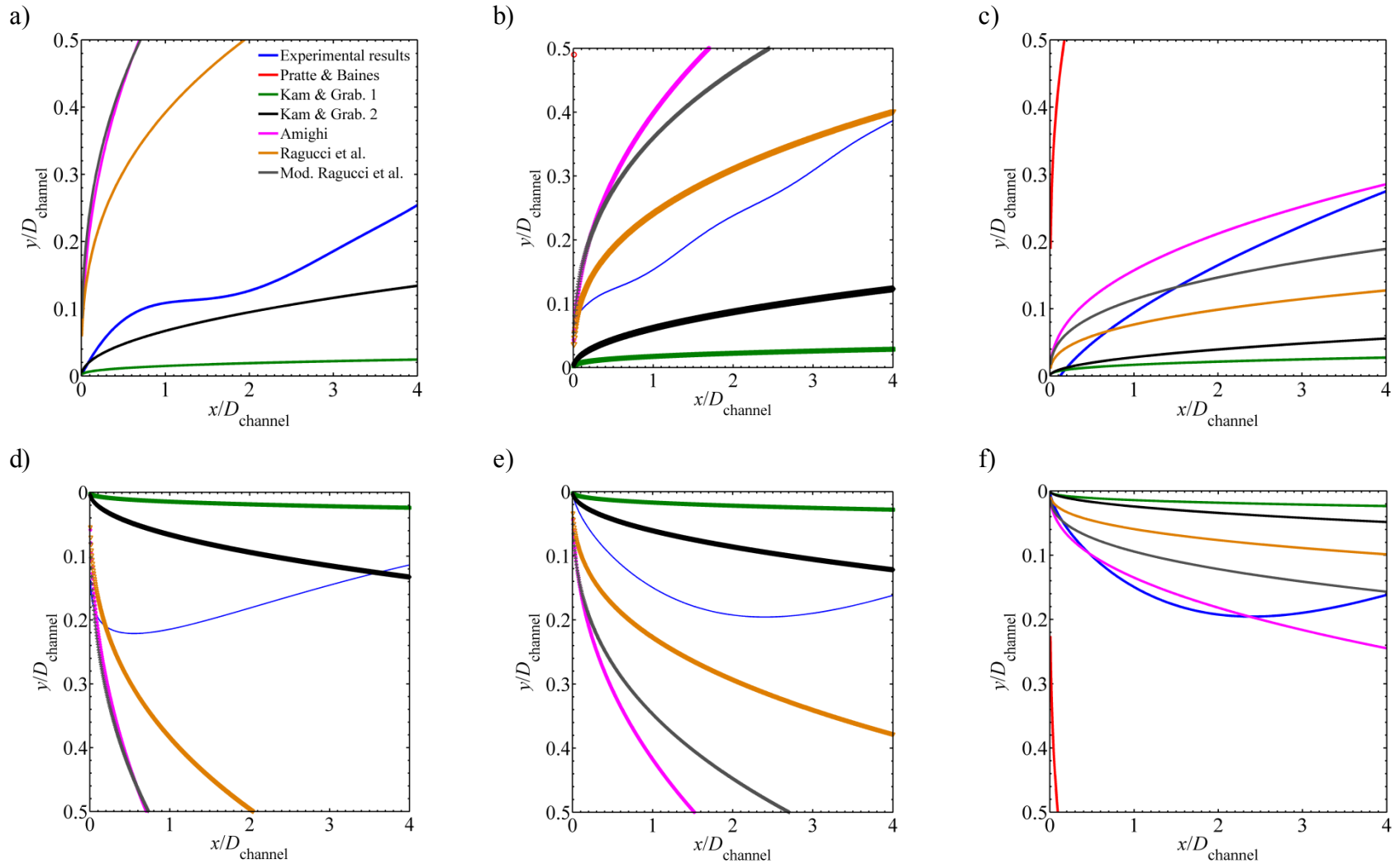
Figure 3.3. Comparison of experimental jet centerline trajectory for several D_{inj} and $Re_L \approx 24{,}000$ with selected correlations. Top row: Bottom wall injection. Bottom row: Top wall injection. a) and d) $D_{inj} = 0.27$ mm, b) and e) $D_{inj} = 0.52$ mm, c) and f) $D_{inj} = 1.59$ mm. All the results correspond to a $M_G = 29.8 \times 10\text{-}3$ g/s

The comparison of existing jet centerline mathematical equations with the experimental data proved that, in general, their applicability to GJILCF could achieve, at best, a modest level of success. The reasons for the discrepancy with the experimental results originate on the differences between the physical mechanisms affecting a GJILCF and a JICF. The density difference between the phases causes the buoyancy forces to be an important factor in GJILCF, while it is not a driving mechanism for JICF. Another factor to consider is the influence of the attaching forces in the evolution of gas jets. While being non-significant for the majority of the JICF situations discussed in previous works (see Table 3.1), the cohesive effects (inertia and surface tension) counteract the disruptive forces (liquid cross-flow), causing the presence of a continuous gas stream within the liquid. The entrapment of the gas phase occurs once the bubbles detach from the gas core.

Before the gas jet breakup occurred, the attaching forces (inertia and surface tension) facilitate the displacement of the gas jet as presented in Figure 3.4, where a gas plume having jet-like characteristics elongates up to a distance equal to several times the channel diameter. Previous researchers (Wace *et al.*, 1987; Forrester and Rielly, 1998) have reported similar characteristics for a gas jet. This type of behaviour was not observed in the general case of JICF and LJIGCF, where the jet length did not extend further than a distance equal to few times D_{inj} in the span wise and stream wise direction (Rudman, 1996; Yuan and Street, 1998; New *et al.*, 2006; Xiao *et al.*, 2011).
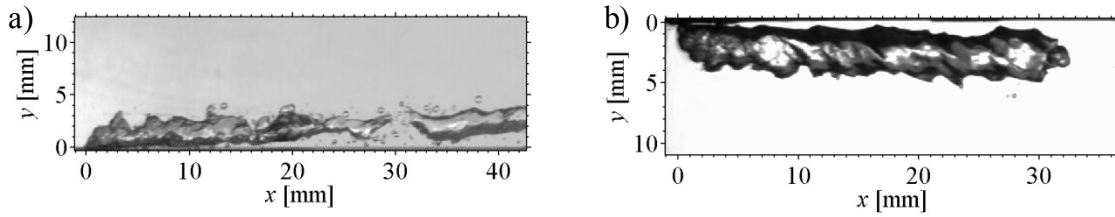
Figure 3.4. Still images showing the expansion characteristics of a GJILCF instantaneous representations of a GJILCF scenario where $M_G \approx 35 \times 10^{-3}$ g/s, $U_L \approx 4.3$ m/s and $D_{inj} = 0.27$ mm

A common assumption for gas injection in a liquid is that individual bubble formation occurs. Varied regimes of bubbling have been observed (Forrester and Rielly, 1998; Kulkarni and Joshi, 2005). The single bubbling regime was observed only at very low Fr_G and was more likely to occur at the highest D_{inj}. As Fr_G increased, the gas plume evolved from a core present continuously in the cross-flow, passing through a small pulsating regime, to a disordered jetting regime; following a set of formation scenarios similar to those described by Forrester and Rielly (1998) and Sovani (2001).

For the majority of the experiments conducted in this study, the gas jets showed a growth that spanned distances downstream of the injection point that could be at least one order of magnitude higher than those generally observed in a JICF. For the cases where discrete bubble formation occurs, the mean probability centerline describes the path followed by the succession of bubbles right after detachment and in the vicinity of the gas injector. The shortest jet length observed during the experiments was equal to $x/D_{channel} \approx 0.24$, which corresponded to the formation of single bubbles, while the longest length could be equal, if not superior, to $x/D_{channel} \approx 4.0$.

3.3.2. Estimation of the maximum probability trajectory

The comparison between modified jet centerline correlations and the experimental data proved that, for the set of conditions tested, there was no correlation that provided universal prediction of the GJILCF trajectory in the near injector region. It was deemed necessary to perform a preliminary examination into how the geometrical and operational variables affect the behaviour of the maximum probability path. Owing to the observed influence of the buoyancy and injector position, combined with the dimensional analysis of variables involved, Fr_G was the variable used, because it relates the kinematic gas momentum and buoyancy forces. Other authors have also determined that Fr_G is the adequate parameter for the characterization of the influence of the gas momentum on the jet trajectory (Oryall and Brimacombe, 1976; Zhu *et al.*, 1998; Bashitialshaaer *et al.*, 2012; Harby *et al.*, 2014).

Since the liquid cross-flow had an essential effect on regulating the gas jet penetration into the conduit, the addition of an associated control variable was required. The dimensional analysis indicated that Re_L was the adequate choice, because it represents the magnitude of the momentum cross-flow, provides information about the physical properties of the fluid and describes the level of cross-flow induced mixing caused by the turbulence. Although the momentum ratio between the phases was considered, Re_L provides an important measure of the detaching effects of the liquid on the gas plume, which is one of the primary forces controlling the gas jet breakup and subsequent bubble detachment, while scaling

with the turbulence in the fully developed conduit flow, which has contributions to the gas disintegration.

Following an approach similar to those observed in the other JICF studies, a power law correlation based on the Re_L, Eo_G, Fr_G and $x/D_{channel}$ was developed. Using these variables, along with the Cartesian coordinates (x, y), as the control parameters, two correlations were empirically determined. Each expression, equations (3.5) and (3.6), predict the maximum probability trajectory within the region of interest, taking into consideration the location of the gas injector. The coefficients associated to the variables were calculated from a nonlinear regression analysis (Amighi *et al.*, 2009). The results obtained valid within the range of parameters used in this study. Further exploration for different conditions needs to be tested.

$$\left(\frac{y}{D_{channel}}\right)_{\substack{Centreline \\ Bottom\ wall}} = 3.88 \left(Eo_G\right)^{0.18} \left(\frac{x}{D_{channel}}\right)^{3.10 Re_L^{-0.14}} \left(Fr_G\right)^{0.16} \left(Re_L\right)^{-0.38} \tag{3.5}$$

$$\left(\frac{y}{D_{channel}}\right)_{\substack{Centreline \\ Top\ wall}} = 0.32 \left(Eo_G\right)^{0.25} \left(\frac{x}{D_{channel}}\right)^{3.4 \times 10^{-6} Re_L^{1.1}} \left(Fr_G\right)^{0.26} \left(Re_L\right)^{-0.19} \tag{3.6}$$

While the functional form of the correlations presented is straightforward, each dimensionless number elevated to a simple power, the coefficient used for the $(x/D_{channel})$ is presented as a function of the liquid phase Reynolds number. It was observed that the trend exhibited by the pathlines varied as a function of the Re_L. For bottom wall injection and low

Re_L values, the gas jet centerline exhibited a quasi-linear form; fast growth of the pathline trend with a very small curvature. It was inferred that this was caused by a high ratio of the buoyancy versus liquid cross-flow momentum forces. As Re_L increased, the effect of the buoyancy decreased and the liquid cross-flow caused a curved shape of the gas jet centerline. A similar behaviour was observed for top wall injection; a low Re_L number caused a sudden penetration of the gas jet and then a flattened centerline trend. At high Re_L values, the liquid cross-flow momentum counteracts the buoyancy force and causes further dispersion of the gas phase along the conduit spanwise direction.

Physically, the term $(x/D_{channel})$ is the one that determines the shape of the gas jet centerline. Hence, the power associated to this term was expressed as a function of Re_L. This same physical behaviour occurs at all gas jet dispersion levels, hence the equations for the gas jet borderline were expressed in a similar manner, with the exponent for the term $(x/D_{channel})$ being also a function of Re_L. Further information explaining the changes in the magnitude of the exponent associated to the streamwise location can be found in Appendix B, where data associated to the estimation of the penetration and buoyancy lengths is also included. Both lengths provided the preliminary estimations for the proposal of the correlations for the centerline and borderline trajectories presented in this Chapter.

At low D_{inj} values, high penetration of the gas jet into the conduit was observed, which was explained from the high Fr_G values. It was expected that as Re_L increased, the probability trajectory would tend to be located closer to the wall. Both phenomena were captured in the correlations, which ascribed an increase in $y/D_{channel}$ with an increase in Fr_G, and an inverse

effect as Re_L was increased. It was determined that besides changing the magnitude of y/D_{inj}, Re_L also affected the trend exhibited by the $y/D_{channel}$ curves. Hence, the power coefficient of the term $(x/D_{channel})$ was adjusted to this fact and defined as a function of the Re_L. For equal operational and geometrical conditions, there was a difference in the centerline path, based on whether the gas injection was located in the top or bottom wall. These discrepancies were attributed to the gravity effects.

Figure 3.5 shows the contrast between the experimentally determined jet centerline and the predictive correlations. It was observed that when compared with the modified versions of existing centerline correlations, equations (3.5) and (3.6) provided a significant improvement in the description of the GJILCF centerline trajectory over any JICF correlation. For the bottom wall injection, correlation (3.5) had a mean R^2 equal to 0.94, which indicated a strong correlation with the experimental data. The assessment of results obtained from equation (3.6) gave comparably robust results, with a mean $R^2 = 0.82$. The results depicted in Figures 3.5a and 3.5b had mean R^2 values equal to 0.94 and 0.87 respectively. For the results shown in Figures 3.5c to 3.5d, the mean R^2 was equal to 0.93 and 0.96 respectively.
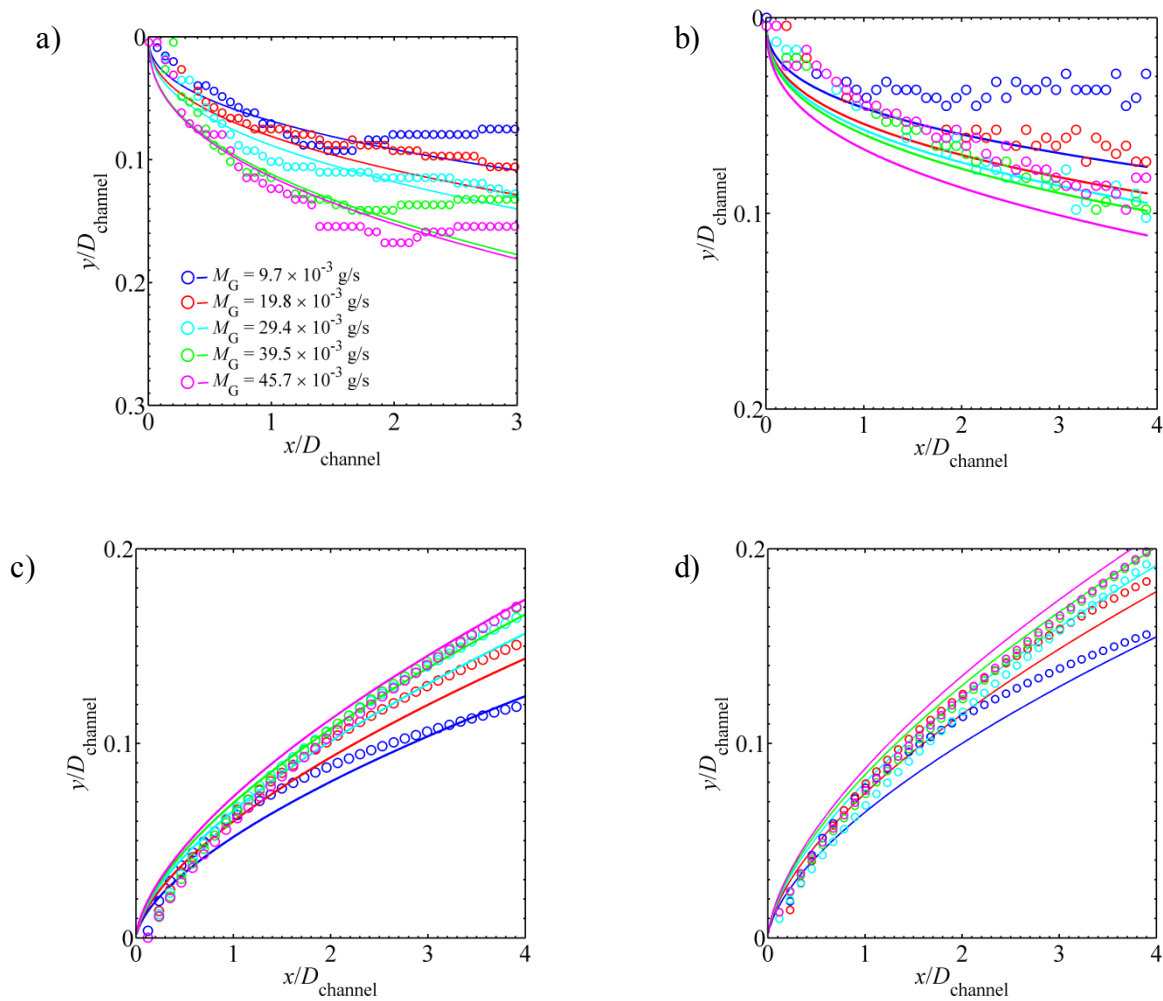
Figure 3.5.   Experimental gas phase probability centerline versus the proposed correlations at different operational conditions: a) $Re_L \approx 40,000$, $D_{inj} = 0.27$ mm, top wall. b) $Re_L \approx 40,000$, $D_{inj} = 1.59$ mm, top wall. c) $Re_L \approx 24,000$, $D_{inj} = 0.27$ mm, bottom wall. d) $Re_L \approx 40,000$, $D_{inj} = 0.52$ mm, bottom wall

A special scenario was observed for top wall injection and the following experimental conditions $Re_L \approx 24{,}000$, $Eo_G \leq 0.04$ and $M_G \geq 40 \times 10^{-3}$ g/s, which is similar to that depicted in Figure 3.3d. For this case the jet experiences an enhanced penetration when compared to the other scenarios, causing a variation in the trend line. Equation (3.6) provided a satisfactory estimation of the probability maxima location at $x/D_{channel} = 4$, but was not capable of reproducing the penetration distance near the injector at high U_G, which is where the highest discrepancies between predictions and results were observed. For top wall injection, the maximum level of divergence was obtained for $D_{inj} = 0.27$ mm and when Fr_G was higher than 2100. The correlation underestimated the jet trajectory by an average value of 41%. Similar results were obtained for $D_{inj} = 0.52$ mm, when $Fr_G \geq 970$, where the discrepancies were in the order of 37%. Hence, the ($x/D_{channel}$), Fr_G and Re_L power coefficients used in equation (3.6) were modified to have values 0.10, 0.55 and -0.32 respectively in order to provide a better representation of this particular case, decreasing the differences between predictions and experiments to an average value of 11%.

It was determined that, the maximum variation between experiments and predicted results occurred near the injection point, which is restricted not only to the close proximity of the gas nozzle, but for $x/D_H < 0.5$ and encompassing the spanwise extent of the channel. An increase in Fr_G produced a higher penetration and distribution of the trajectory throughout the interest region. This caused the probability trajectory to displace towards the center of the channel, near the injector as well as at the end of the interval. Trajectories that showed sudden penetration near the inlet, generally maintained the tendency of having higher a vertical location at the end of the interval. As Re_L increased, the differences in the

centerline path were less significant, independent of the magnitude of Fr_G and D_{inj}. When $D_{inj} = 1.59$ mm, the trajectories became very similar for all the mass flow rates considered. At $Re_L \approx 56,000$, independent of D_{inj}, the differences in the centerline path were not significant. Similar behaviour was observed for the top wall injection, which was considered as an indication that for larger injection diameters the maximum probability path might exhibit an independence of D_{inj} and Fr_G.

3.3.3. Estimation of the gas phase distribution boundaries

The centerline of a GJILCF referred to the maximum probability location of the gas phase. However, it did not permit the evaluation of the gas jet growth or the extent of its boundaries. It was inferred that a thorough characterization of the GJILCF behaviour could be obtained with the inclusion of its outermost or borderline trajectory. This parameter could be used to identify possible scenarios like contact of the GJILCF with the top wall or interaction between the gas jet with pre-existent bubbles in the conduit. The summary of correlations presented in Table 3.1, showed that little attention has been given to this particular topic. Amighi *et al.* (2009) provided the only set of expressions that presented a clear difference in the estimation of both trajectories. Building upon this, a set of expressions that could predict the location of the GJILCF outermost location was introduced. The power-law correlations, equations (3.7) and (3.8), were obtained following the same methodology used for the centerline correlations.

$$\left(\frac{y}{D_{\text{channel}}}\right)_{\substack{\text{Borderline}\\ \text{Top wall}}} = 1.27\left(Eo_{\text{G}}\right)^{0.24}\left(\frac{x}{D_{\text{channel}}}\right)^{2.50\,Re_{\text{L}}^{-0.14}}\left(Fr_{\text{G}}\right)^{0.16}\left(Re_{\text{L}}\right)^{-0.23} \tag{3.7}$$

$$\left(\frac{y}{D_{\text{channel}}}\right)_{\substack{\text{Borderline}\\ \text{Bottom wall}}} = 0.19\left(Eo_{\text{G}}\right)^{0.20}\left(\frac{x}{D_{\text{channel}}}\right)^{5.9\times10^{-4}\,Re_{\text{L}}^{0.59}}\left(Fr_{\text{G}}\right)^{0.30}\left(Re_{\text{L}}\right)^{-0.11} \tag{3.8}$$

Clear guidelines or criteria about the definition of the jet boundary, particularly for an estimation based on probability, were not found in previous works. With the purpose of establishing a coherent criterion for the outermost location, it was considered that the outermost location would consist of the position in the span wise direction, where the probability became lower than 0.10. Taking this into consideration along with the approximations used by the imaging algorithm, it was concluded that the chosen criteria provided a satisfactory margin for the estimation and description of the borderline trajectory.

Typical outermost trajectory data, which encompassed the cases where $Re_{\text{L}} \approx 24{,}000$ and $M_{\text{G}} = 19.7 \times 10^{-3}$ g/s and $Re_{\text{L}} \approx 40{,}000$ and $M_{\text{G}} = 29.4 \times 10^{-3}$ g/s were included in Figure 3.6. This chart contrasted the experimentally determined trajectory versus the correlation-determined outermost path. The correlations predicted with considerable accuracy the location of the GJILCF boundary, particularly near the injector, $x/D_{\text{channel}} \leq 2$. The highest divergence was observed for $D_{\text{inj}} = 1.59$ mm and $Re_{\text{L}} \approx 24{,}000$ where, independent of the nozzle position, the calculated trajectories underestimated the experimentally determined path. As D_{inj} decreased, the differences between experiments and predictions minimized.

For high Re_{L}, the gas border curves became increasingly similar, exhibiting decreased dependence from D_{inj} and M_{G}. The coefficients of determination indicated similarly strong correspondence between data and predictions as those obtained for the centreline correlations. The mean values for R^2 were 0.84 and 0.95, for the top and bottom wall injection cases respectively. The maximum discrepancy occurred at low $Re_{\mathrm{L}} \approx 24{,}000$ and $D_{\mathrm{inj}} = 1.59$ mm (not shown). For this case, R^2 had a value equal to 0.77. For top wall injection the averaged relative error was 0.05, 0.03 and 0.02 y/D_{channel} for $D_{\mathrm{inj}} = 0.27$, 0.52 and 1.59 mm respectively, resulting in an averaged value approximately equal to $0.04y/D_{\mathrm{channel}}$. For bottom wall injection, the averaged relative error was 0.03 y/D_{channel} uniform for all D_{inj} used. For both injector location cases, the minimum observed error was $0.01y/D_{\mathrm{channel}}$.
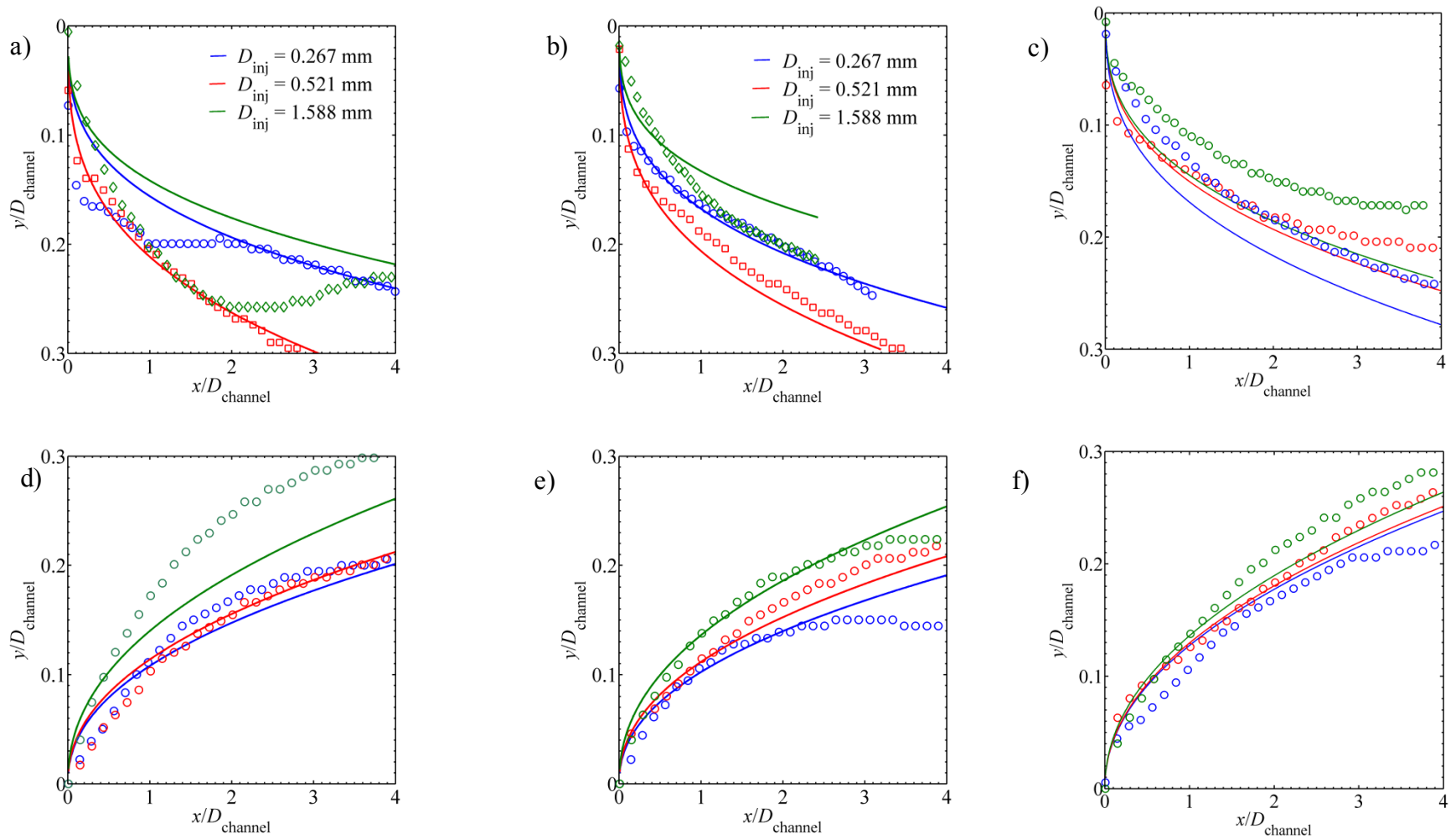
Figure 3.6. Experimental gas phase probability borderline versus the proposed correlations at different operational conditions: a) $Re_L \approx 24{,}000$, $M_G = 19.7 \times 10^{-3}$ g/s, top wall. b) $Re_L \approx 40{,}000$, $M_G = 29.4 \times 10^{-3}$ g/s, top wall. c) $Re_L \approx 56{,}000$, $M_G = 39.4 \times 10^{-3}$ g/s, top wall d) $Re_L \approx 24{,}000$, $M_G = 19.7 \times 10^{-3}$ g/s, bottom wall. e) $Re_L \approx 40{,}000$, $M_G = 29.4 \times 10^{-3}$ g/s, bottom wall. f) $Re_L \approx 56{,}000$, $M_G = 39.4 \times 10^{-3}$ g/s, bottom wall

When combining the results from the proposed centerline and borderline trajectories, it is possible to obtain a thorough characterization of the gas jet in the vicinity of the injector. Both instantaneous (Figure 3.7a) and time-averaged estimations (Figure 3.7b) are considered as valuable tools for the understanding of the gas phase behavior in the vicinity of the gas injector, which is of fundamental interest for the design of effervescent atomizers.
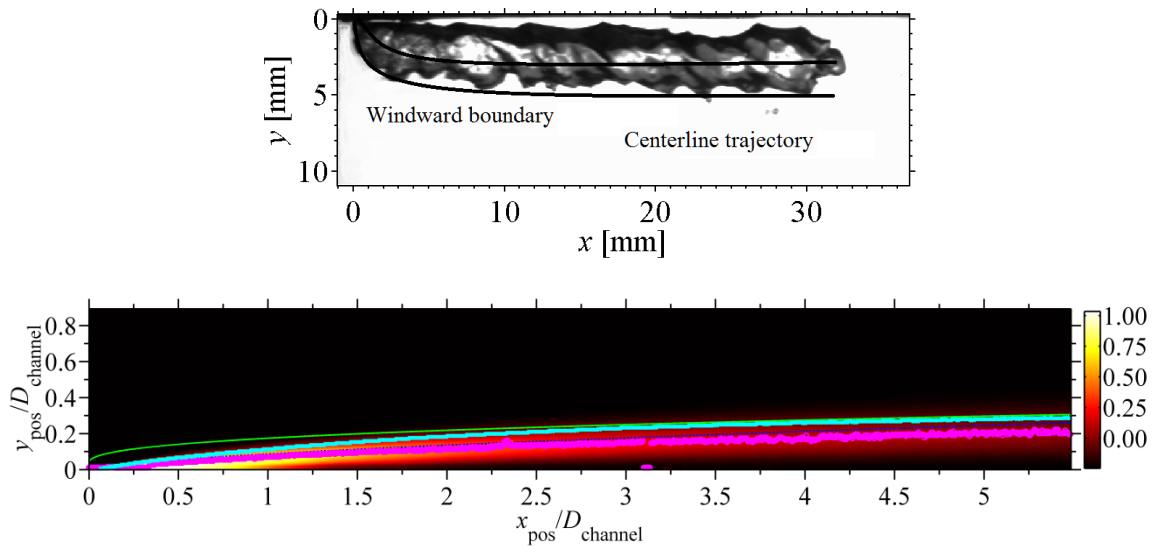
Figure 3.7. Practical application of the combined centerline and borderline trajectories for an instantaneous (a) and time-averaged (b) estimation of the gas phase distribution in the injector area

3.4. Conclusions

High-speed shadowgraphy tests near the gas injection nozzle into a square channel liquid cross-flow were performed. The experimental conditions were confined to simulate bubbly flow in a conduit and were carefully controlled to ensure repeatability. Using image processing algorithms, it was possible to identify relevant features of the initial interaction between the gas and liquid phases, such as the centerline and borderline trajectory. The results presented here are of great interest since no previous research was found that considered the use of a JICF approach

to the evaluation of gas plumes in a perpendicular liquid stream. The most relevant findings are summarized below:

* The use of existing correlations developed for canonical JICF did not provide satisfactory results for the estimation of the incipient GJILCF probability centerline. Several JICF correlations were evaluated, which did not yield a universally accurate prediction of the gas maximum probability position along the streamwise location. It was known beforehand that each correlation is valid within the range of parameters for which it was developed. However, the evaluation of their applicability to the analog scenario of gas injection into a traverse liquid current provided the base for the development of correlations valid for the range of conditions tested.

* The effects that important design paramaters, represented in dimensionless form by Fr_G, Re_L, D_{inj}, as well as the gas inlet location have on the process of gas injection were studied. For small Re_L values, the gas injection parameters had a more influential role in the gas jet trajectory, whereas the liquid cross-flow effects had a more relevant effect in the behaviour of the GJILCF probability centerline as Re_L increased. This is due to the combined effect of enhanced momentum and increased turbulent mixing with Re_L, causing more stochastic motion of the gas plume compared to a trajectory influenced by injection momentum or buoyancy. From the data shown (Figure 3.2), it can be inferred that at $Re_L \approx 56000$ was the point where the gas jet dynamics were mostly controlled by the liquid cross-flow momentum.

* The use of smaller D_{inj} increased the penetration of the gas plume, caused by an increase in Fr_G. The location of the gas nozzle, top or bottom wall, affected considerably the GJILCF centerline trajectory, mainly due to the influence of the buoyancy as either an attaching or detaching effect. For similar values of Fr_G and Re_L, placing the injector in the top wall caused a decrease in the vertical penetration when compared to the use of gas injector in the bottom wall. This trend was observed for all the operational configurations tested, and was a fairly predictable outcome of buoyancy effects.

* The assessment of the variables involved in the gas injection process, together with the evaluation of the JICF expressions, led to the proposal of empirical expressions that predict the centerline and borderline locations for GJILCF. The mean R^2 for the centerline generally had a value above 0.8, which indicated a reasonable relationship between experimental results and predictions.

* For high Fr_G, the dependability of the equations in reproducing the penetration near the gas injection region was reduced, although it was possible to observe an agreement after the probability maxima reached a stable point. At high Re_L, the cross-flow effects and turbulence dictated the dynamics of gas dispersal in the conduit, independent of the inlet conditions.

4. Forces involved in the process of bubbling and jetting into a cross flow

4.1. Background

Kulkarni and Joshi (2005) stated that there are at least forty-six assumptions commonly used during the modeling of bubble formation. Some of these considerations included, but were not restricted to: the liquid was assumed isothermal, inviscid, uniform and its circulation was negligible; the physical properties of the liquid had no effect on the dynamics of bubble formation; the gas injection rate was considered constant; the gas was incompressible or its density was neglected; bubble detachment occurred when the neck dimensions reduced to zero during the bubble formation; bubble formation frequency was constant; the gas pressure inside the bubble was uniform and the conduit geometry had no effect on the formation of bubbles.

Various analytical models have been developed to characterize the bubble expansion from an orifice in a cross flow (Oguz and Prosperetti, 1993; Bhunia *et al.*, 1998; Loubiere *et al.*, 2004; Duhar and Colin, 2006; Liu *et al.*, 2010). However, owing to the complexity of the bubble formation process, most of these models center solely on simplified scenarios, focusing on the formation of single bubbles, which grow in an ideal spherical manner, despite the distortion and inclination imposed by the liquid cross-flow.

Although discrete bubble approaches are undoubtedly relevant to understand bubble formation physics, the assumption of perfectly spherical bubble formation is realistic only under low gas mass flow rates (M_G). For large M_G values, which are of particular interest for industrial applications, these methods can result in considerable miscalculations (Clift *et al*., 1978).

Although the aim of the present study is not to develop a predictive theoretical model about the process of bubble growth and detachment, a preliminary description of the forces involved in the bubbling process, based on an assessment of previous works, was deemed necessary. Therefore, the objective of this chapter was to describe and illustrate the different forces that influence the growth of a gas plume in a cross flow. Each dynamic effect was defined based on existing concepts, mainly adapted from single bubble formation and applied to the case of gas jet formation. When multiple definitions were found, contrasts of the proposed alternatives were conducted, with the idea of identifying possible sources of discrepancy between them and select an adequate alternative to the present case.

Following a common methodology, the forces affecting the process of bubble generation were categorized as horizontal and vertical forces. The $\hat{\mathbf{x}}$ and $\hat{\mathbf{y}}$ axes were oriented in the flow direction and perpendicular to the wall respectively, as shown in Figure 4.1a, where key gas jet parameters, such as the gas jet equivalent diameter (D_{equiv}), estimated width (D_W) and inclination angles are depicted. It was considered that the physical properties of the liquid remained unchanged. Figure 4.1b depicts the component of the dynamic effects acting on the incipient gas jet. The geometrical definitions D_{equiv} and D_W were included in Section 2.3.
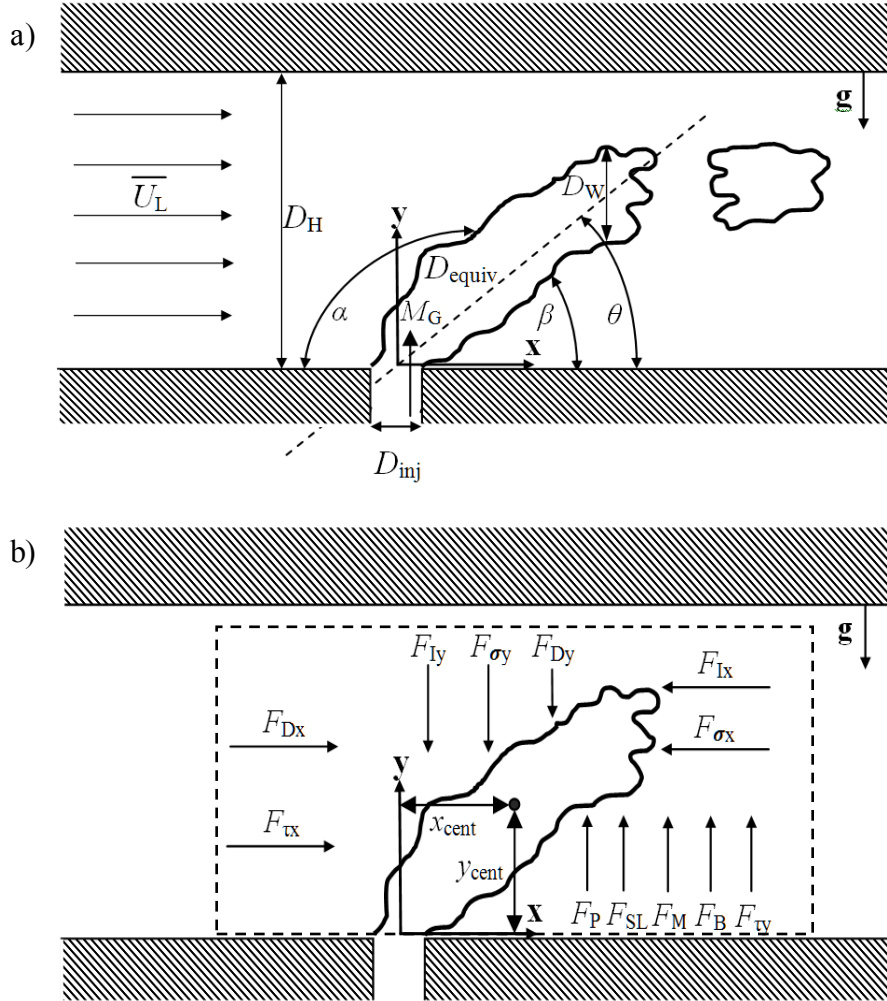
Figure 4.1.   a) Gas jet geometry, variables and coordinates. b) Forces acting on a growing gas jet in the horizontal and vertical dimensions

4.2.   Forces in the vertical direction

The balance of forces in the $\hat{\mathbf{y}}$ direction considered the attaching and detaching effects acting on the gas core during the process of formation. The attaching forces are represented by the drag (F_D), added mass (F_I) and surface tension forces (F_σ), while the detaching effects included the, lift (F_{SL}), momentum force (F_M) and pressure forces (F_P). The buoyancy (F_B) force can be either

an attaching or detaching effect depending on the gravity direction. Each one of these forces will be described next.

4.2.1. Buoyancy Force

The buoyancy force (F_B) is defined similarly to the buoyancy effects in still liquids (Loubiere *et al.*, 2004; Duhar and Colin, 2006). Since the experimental technique employed does not allow the direct calculation of the volume variations as a function of time, any estimation of the volume requires the extrapolation from the gas core projected area (A_P), which can be obtained from the instantaneous shadowgraphs. Based on this limitation, the approach used consisted in obtaining V_G (volume of a gas object within the image) was based on A_P, which allows the calculation of the volume from the shape of the gas plume. To determine V_G, w, which is the dimension of the gas jet in the $\mathbf{z}$ direction, was assumed equal to D_w. F_B can be estimated from equation 4.1.

$$F_B = (\rho_L - \rho_G) g A_P D_w \hat{\mathbf{y}}$$

(4.1)

It was considered that equation (4.1) provides a clear delimitation of the volume, because the imaging algorithm allowed an accurate estimation of A_P. This was considered as an advantageous feature, because the use of empiricisms was limited. The only assumption was that of a symmetric growth in the perpendicular direction, $w \approx D_w$. Appendix C.1 presents a detailed description of the various approaches found in the literature for the estimation of F_B.

4.2.2. Gas momentum force

The force associated to the effects of the gas momentum flux (F_M), defined according to equation (4.2), is a detaching force. Although the bubbles formed are generally inclined due to the cross flow effects, it was found that, for horizontally oriented injectors, F_M was defined as acting only on the vertical direction. When a vertical injector is used, Sovani (2001) considered that F_M had components in both directions due to the inclination of the gas structure. When small D_{inj} are used, the magnitude of F_M becomes relevant (Nahra and Kamotani, 2003). Liu *et al.* (2010) considered that the contributions of F_M can usually be neglected unless U_G exceeds a limit of 5 m/s. In the current study this limit was surpassed for a vast number of experiments, hence it was not initially disregarded.

As occurred with F_B, F_M is defined in a way similar as for stagnant liquids. Considering the gas density (ρ_G) as constant, the volumetric gas flow rate, Q_G, provided the main contribution for the expansion of the gas structure. Each one of the possible definitions can be considered as equivalent, if it is considered that Q_G remains constant and that V_G can be directly related to it through $dV_G = Q_G dt$. Equation (4.2) presents some of the approaches found in the literature for the definition of F_M, where each one of them is considered equivalent and valid for the estimation of F_M magnitude.

$$F_M = \iint_{A_{inj}} \mathbf{U}\left(\rho_G \mathbf{U}.d\mathbf{A}\right) = \rho_G U_G^2 A_{inj}\hat{\mathbf{y}} = \frac{\pi}{4}\rho_G U_G^2 D_{inj}^2\hat{\mathbf{y}} = \frac{4\rho_G Q_G^2}{(\pi)\left(D_{inj}^2\right)}\hat{\mathbf{y}} = \frac{4\rho_G\left(\dfrac{dV_G}{dt}\right)^2}{(\pi)\left(D_{inj}^2\right)}\hat{\mathbf{y}} \qquad (4.2)$$

4.2.3. Added mass force

The force that the gas exerted into the liquid with the purpose of displacing a volume equal to the gas core is defined as the added mass or inertial force (F_I). Owing to the growth of the gas plume and continuous bubble detachment, a supplementary weight effect was imparted to the flowing liquid system by the gas phase. Since an unsteady motion of the gas structure occurred and the gas plume experienced continuous growth, F_I was considered as an evolving force.

The accelerated (or decelerated) unsteady gas volume is characterized by the added mass coefficient (C_M). In gas jet formation, the use of $C_M = \frac{1}{2}$, value corresponding to a perfectly spherical bubble at finite Re, would be inadequate due to the elongated, non-symmetric and developing nature displayed by the gas jet, as well as the irregular shape of the detached bubbles. Commonly, the added mass coefficient is defined as $C_M = 11/16$ (Sovani, 2001; Liu *et al.*, 2010).

However, Loubiere *et al.* (2004) stated that this is not the best choice for a non-spherical growing bubble attached to a wall and under the effects of a liquid cross flow. Ohl *et al.* (2003) proved that the process of bubble growth, hence of any generic gas plume, affects significantly the added mass interaction. The effects of a high Re_L and a turbulent flow field would undoubtedly modify the value of C_M, but the influence of these conditions on C_M or F_I has not been reported.

Kendoush (2007) developed one of the few existing correlations that provide a link between the bubble growth process and the changes in the virtual mass coefficient. The general version is shown in Equation (4.3). Even though the expression was developed for a perfectly spherical growing bubble, considering as well potential flow around the particle and linear movement in

one direction, it provides a better physical description of C_M than the assumption of a constant value.

$$C_M = \frac{3\left(\dfrac{dD_B}{dt}\right)^2}{U_B^2} + \frac{1}{2}$$

(4.3)

Defining $\mathbf{S}(x, y) = x\,\hat{\mathbf{x}} + y\,\hat{\mathbf{y}}$ as the position vector that represented the position of the gas core center of mass, where x and y vary with time as the gas jet expands, F_I was defined as

$$F_I = \frac{d}{dt}\left(\rho_G V_G \frac{d\mathbf{S}}{dt}\right) + \frac{d}{dt}\left[\rho_L C_M V_G\left(\frac{d\mathbf{S}}{dt} - U_I \mathbf{x}\right)\right]$$

$$\underbrace{\phantom{\frac{d}{dt}\left(\rho_G V_G \frac{d\mathbf{S}}{dt}\right)}}_{\text{Inertia due to the gas mass}} \quad \underbrace{\phantom{\frac{d}{dt}\left[\rho_L C_M V_G\left(\frac{d\mathbf{S}}{dt} - U_I \mathbf{x}\right)\right]}}_{\text{inertia due to the displaced liquid}}$$

(4.4)

Substituting $\mathbf{S}(x, y)$ in equation (4.4), it was possible to define the inertia force in the vertical direction as given in equation (4.5). Nahra and Kamotani (2003) estimated that when the bubbling process occurs under constant flow rate conditions, the bubble volume evolved based on $V_G = Q_G t$, which yielded the alternative expression on the right hand side of equation (4.5).

$$F_{Iy} = \frac{d}{dt}\left[\left(\rho_G + \rho_L C_M\right)V_G\left(\frac{dy}{dt}\right)\right] = \frac{d}{dt}\left[\left(\rho_G + \rho_L C_M\right)\left(Q_G t\right)\left(\frac{dy}{dt}\right)\right]$$

$$F_{Iy} = \left(\rho_G + \rho_L C_M\right)\left[\frac{dV_G}{dt}\left(\frac{dy}{dt}\right) + V_G \frac{d^2 y}{dt^2}\right]$$

(4.5)

Because of the lack of proper correlations estimating the evolution of the inertial effects of the jet, a methodology was devised to include the effects of the gas core expansion. Equation (4.6)

was used to approximate the volumetric variation of the gas jet as a function of time. Combining equations (4.5) and (4.6) led to an expression that allows the computation of the inertial force experienced by the gas structure as a function of time (Equation 4.7). The force can be estimated within the time interval that characterizes the mean growth of the gas core until detachment occurs.

$$\frac{dV_G}{dt} = D_w(t)\left(\frac{dA_P(t)}{dt}\right) + A_P(t)\left(\frac{dD_w(t)}{dt}\right) \tag{4.6}$$

$$F_{Iy} = (\rho_G + \rho_L C_M)\left[\left(D_w(t)\left(\frac{dA_P(t)}{dt}\right) + A_P(t)\left(\frac{dD_w(t)}{dt}\right)\right)\left(\frac{dy}{dt}\right) + (D_w(t)A_P(t))\frac{d^2y}{dt^2}\right] \tag{4.7}$$

4.2.4. Surface tension force

The surface tension or capillary force (F_σ) constitutes one of the main effects that opposed the gas jet breakup. A variety of approaches about the description of the capillary force exist: some involve a definition of the inclination angle of the gas plume (θ) (Tan *et al.*, 2000; Sovani, 2001; Liu *et al.*, 2010) while others use the general contact angle (γ), which takes into consideration the influence of the advancing (θ_{adv}) and receding (θ_{red}) angles, as a method of defining F_σ (Klausner *et al.*, 1993; Loubiere *et al.*, 2004; Duhar and Colin, 2006). Nahra and Kamotani (2003) used the longitudinal angle (θ_{long}) to define a function that describes the bubble local inclination. F_σ can be calculated according to equation (4.8). Appendix C.2 presents a detailed description of the different forms used to estimate F_σ, as well as a more detailed description about the neck formation mechanics.

$$F_{\sigma y} = \pi \sigma D_{\text{inj}} \sin(\theta)$$

(4.8)

Before a bubble separated from the gas column, the formation and evolution of a gas neck was noticed. The surface tension counteracted the influence of the detaching forces, giving rise to the appearance of a neck. A typical scenario which shows a neck formation in the gas jet is presented in Figure 4.2. As can be observed, the dimensions of the gas stem that linked the main core to the incipient, separating bubble were smaller than the width of the gas structure.
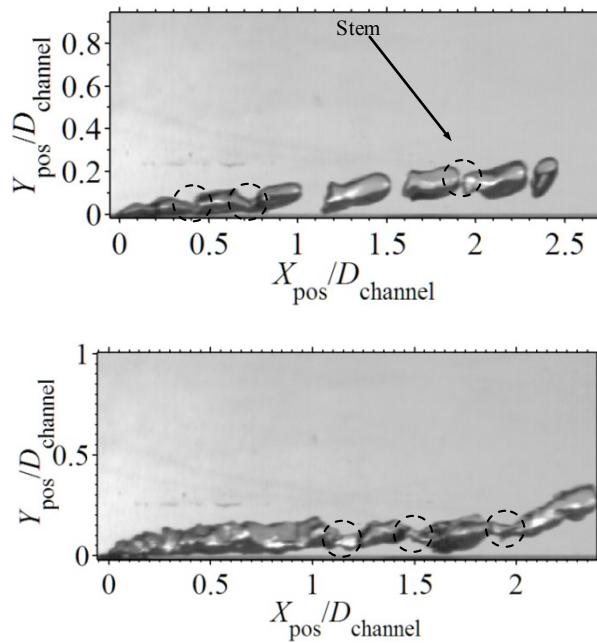
Figure 4.2.   Stem dimensions linking consecutive gas structures before detachment. In many cases, the separation of the gas lumps from the main structure was observed at a distance equal to several D_{inj} downstream of the gas inlet. The experimental conditions for the images are: Top) $D_{\text{inj}} = 1.59$ mm, $U_G = 2.2$ m/s, $U_L = 3.0$ m/s. Bottom) $D_{\text{inj}} = 0.52$ mm, $U_G = 27.8$ m/s, $U_L = 4.3$ m/s

4.2.5. Drag force

The drag force (F_D) is defined as the effect generated by the liquid on the gas plume due to the relative velocity existing between them. F_D is commonly estimated from the general expression given in equation (4.9). Since the liquid velocity acts primarily in the streamwise direction, the drag force in the vertical direction was caused by relative velocity of the gas jet (Equation 4.10). Despite the apparent simplicity in the estimation of the drag coefficient, little consistency was found amongst the varied number of approaches existing to estimate the drag coefficient (C_D), as indicated in Table 4.1. See Section 4.2.3 for the definition of S.

$$F_D = \frac{1}{2} \rho_L C_D A_G \sqrt{\left(\frac{dS}{dt} - U_L \mathbf{x}\right)^2} \left(\frac{dS}{dt} - U_L \mathbf{x}\right) \tag{4.9}$$

$$F_{Dy} = \frac{1}{2} \rho_L C_D A_G \sqrt{\left(\frac{dS}{dt} - U_L \mathbf{x}\right)^2} \frac{dy}{dt} \hat{\mathbf{y}} \tag{4.10}$$

Table 4.1. Review of correlations used to define the drag coefficient of objects submerged in liquids

Author(s)	Definition of C_D
Bhunia *et al.* (1998) Liu *et al.* (2010)	$$U_{\text{eff}} = \sqrt{\left(U_L - \frac{dx}{dt}\right)^2 + \left(\frac{dy}{dt}\right)^2} \quad (4.11)$$ $$Re_{\text{eff}} = \frac{U_{\text{eff}} D_B}{\nu} \quad (4.12)$$ $$C_D = \begin{cases} 24/Re_{\text{eff}} & Re_{\text{eff}} \le 2 \\ 18.5/Re_{\text{eff}} & 2 \le Re_{\text{eff}} \le 500 \\ 0.44 & 500 \le Re_{\text{eff}} \end{cases} \quad (4.13)$$
Klausner *et al.* (1993)	$$Re_B = \frac{U_L D_B}{\nu} \quad (3.25)$$ $$C_D = \frac{2}{3} + \left[\left(\frac{12}{Re_B}\right)^n + 0.796^n\right]^{-1/n}, \, n = 0.65 \quad (4.14)$$
Loubiere *et al.* (2004)	$$C_D = \begin{cases} \dfrac{24}{Re_{\text{eff}}}\left(1 + 0.15 Re_{\text{eff}}^{0.687}\right) & 1000 \le Re_{\text{eff}} \\ 0.44 & Re_{\text{eff}} > 1000 \end{cases} \quad (4.15)$$
Duhar and Colin (2006)	$$C_D \approx \frac{16}{Re_{\text{eff}}}\left[1 - \frac{3}{4}\left(\frac{D_B}{2y}\right) - \frac{9}{64}\left(\frac{D_B}{2y}\right)^4\right] \quad (4.16)$$
Haider and Levenspiel (1989)	$$C_D = \frac{24}{Re_B}\left[1 + 8.1716\left(e^{-4.0655\phi}\right)Re_B^{(0.0694+0.5565\phi)} + \frac{73.7 Re_B\left(e^{-5.0748\phi}\right)}{Re_B + 5.378\left(e^{6.2182\phi}\right)}\right] \quad (4.17)$$
Thorncroft *et al.* (2001)	$$C_D = \frac{2}{3} + \left[\left(\frac{12}{Re_B}\right) + 0.75\left(1 + \frac{3.315}{Re_B^{1/2}}\right)\right]^{-1} \quad (4.18)$$
Legendre and Magnaudet (1998)	$$C_D = \frac{15.34}{Re_{\text{eff}}} + \frac{2.163}{Re_{\text{eff}}^{0.6}} \quad (4.19)$$
Chow (1980)	$$C_D = \begin{cases} \dfrac{24}{Re_{\text{eff}}^{0.646}} & 1 \le Re_{\text{eff}} \le 400 \\ 0.44 & 400 < Re_{\text{eff}} < 3 \times 10^5 \end{cases} \quad (4.20)$$
Ishii and Hibiki (2010)	$$C_D = \frac{\sqrt{2}}{3}\frac{\mu_L}{\left(\rho_L \sigma \sqrt{\dfrac{\sigma}{g\Delta\rho}}\right)} Re_B \quad (4.21)$$

A common assumption in the estimation of the drag force for forming bubbles is that the particles remain spherical throughout the growth and detachment process. The presence of a liquid cross-flow alters significantly the shape of the gas jet and the bubbles formed, giving them an unsteady elongated profile which undoubtedly modifies the magnitude of the drag force. Limited correlations were found for the calculation of the drag coefficient of non-spherical particles, as was shown in Table 4.1.

Haider and Levenspiel (1989) introduced one of the few existing correlations on this topic, which allowed the estimation of the drag coefficient for irregularly shaped particles, using the concept of particle sphericity (φ). It related the actual surface of the particle (S_{URF}) to that of a sphere with the same volume (s). The sphericity was defined according to equation (4.22). As a result of the difficulties associated in obtaining the actual volume of the gas jet, the sphericity was replaced by the analog concept of circularity (ξ), as defined by equation (4.23). ξ was defined as the ratio between the perimeter of the projected equivalent diameter (p) and the projected perimeter of the gas core (P_{ER}). The circularity was easily obtained from the still shadowgraphs and provided a way of introducing a shape factor into the drag force while limiting the use of empiricisms.

$$\phi = \frac{s}{S_{URF}} \qquad (4.22) \qquad \xi = \frac{p}{P_{ER}} = \frac{\pi D_{equiv}}{P_{ER}} \qquad (4.23)$$

The change in the particle circularity as a function of time was shown in Figure 4.3. Selected scenarios representing the evolution of the gas jet circularity are depicted. This evolution goes from its initial growing stage until breakup occurs. P_{ER} and D_{equiv} were calculated for each data

point following the methodology described in Section 2.3.1. This allowed the estimation of the circularity variation as a function of time. For the chosen cases, all the formation times were approximately equal to 1.9 ms, which accounted for the moment right after which the gas lump detached, corresponding to a minimum P_{ER}, passing through the growth stage, up to the point where it achieved its maximum P_{ER}, just before the next breakup event occurred. The gas plume exhibited its maximum circularity at the beginning of the formation stage, which related to minimum values of the projected perimeter.
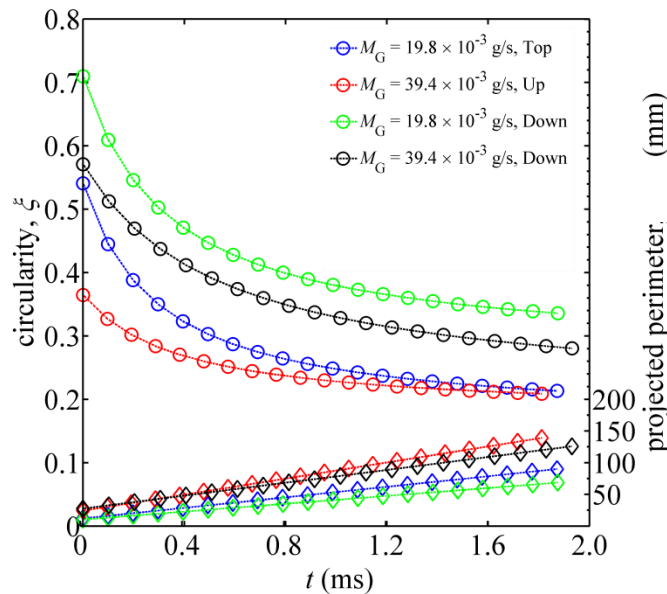
Figure 4.3.   Variation in the circularity (circle) and projected perimeter (diamond) of the gas plume during the formation stage as a function of time ($D_{inj} = 0.52$ mm, $U_L = 4.3$ m/s)

As the gas flow inlet increased the dimensions of the core, ξ gradually decreased until achieving a relatively constant value near the middle of the formation interval, close to 0.9 ms. Even though P_{ER} kept growing, φ remained relatively constant, which indicated that the gas plume attained a steady shape before the breakup occurred. The trend was similar for all the cases

tested, independent of U_G or the channel orientation. It was observed that the injection of gas from the lower port produced gas plumes that had a higher sphericity than the ones produced from the top wall injector.

Bhunia *et al.* (1998) determined that the use of a constant D_{equiv} would not reproduce adequately the physics of bubble generation, thanks to the variations in the plume geometry. It was inferred that an increase in the dimensions associated to the gas column, due to the constant influx of gas mass from the inlet, must produce values of Re_{eff} that increase with t_{growth}. This fact was verified in the results shown in Figure 4.4, where the changes in Re_{eff} are directly proportional to the D_{equiv}. t_{growth} refers to the time that it takes for a gas jet to expand from its minimum point until breakup occurs, which is considered as the point of maximum dimensions (length, D_{equiv}). After this occurs, the gas jet growth cycle starts anew. t_{growth} could be interpreted as quasi-periodic in nature, although the breakup frequency of the gas jet is not perfectly cyclical because of the effects associated to the inherent randomness of the gas jet and the turbulent nature of the liquid cross-flow.

Even though the formation time was relatively short, Re_{eff} showed marked variations within the formation interval. Initially, as a result of the smaller dimensions of the gas plume, the form (thinner, slender body) and skin (decreased surface) drag experienced by the gas structure were minimal. As V_G increased, the jet resembled a bluff body, which increased the pressure drag while simultaneously increasing the wetted surface, which translated into an increased friction resistance. It was deduced that this would have an important impact on the magnitude of C_D, and inherently on F_D.
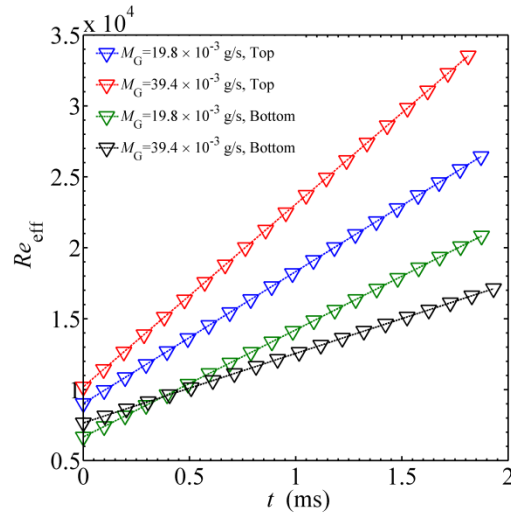
Figure 4.4.   Effects of the gas mass flow rate and injector location on the effective Reynolds number as a function of time. $D_{inj} = 0.52$ mm, $U_L = 4.3$ m/s

The C_D, as obtained from equations (4.14, 4.17 – 4.19), was assessed under the experimental conditions $M_G = 36.5 \times 10^{-3}$ g/s, $U_L = 3.0$ m/s and the gas injector was located in the bottom wall. The results obtained are shown in Figure 4.5 and exhibited a high degree of variability based on the equation used.   The correlation developed by Legendre and Magnaudet (1998), gave a $C_D \approx 0.1$, comparable to the one corresponding to a streamlined body; which clearly did not adhere to the physics of a gas plume interacting with a cross flow in a conduit. The drag coefficients obtained from equations (4.17) and (4.19) gave a high C_D value, exhibiting a trend that indicated independence of the gas jet morphology during the growth period.
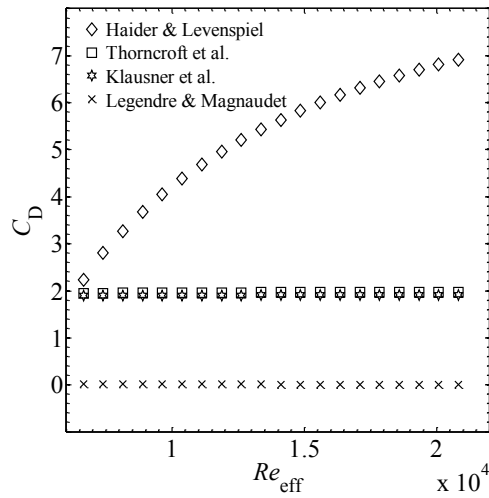
Figure 4.5. Estimation of the drag coefficient versus the effective Reynolds number using selected correlations. $D_{inj} = 0.52$ mm, $M_G = 36.5 \times 10^{-3}$ g/s, $U_L = 4.3$ m/s

It was inferred that neither expression reproduced properly the variations in time of the gas structure volume. Also, since both equations were developed for perfectly spherical particles, they did not take into account the elongated nature of the gas core, which as shown in Figure 4.4 changed dramatically during t_{growth}. The expression introduced by Haider and Levenspiel (1989) proved to be capable of providing an accurate link between the drag coefficient and the evolution of the gas jet morphology, while including the changes in time experienced by the gas core, which certainly enhanced the drag effects, hence the drag coefficient, experienced by the gas jet as it grew. Supplemental information on the form-induced drag is presented in Appendix C.3.

4.2.6. Lift Force

Similarly to the drag force, the lift force (F_{SL}) occurs due to the velocity difference between the gas and liquid phases. Duhar and Colin (2006) considered the lift force as part of a general definition of migration forces, which consisted of two lift effects: one associated to the slip and

the other associated to the shear in the flow. It is commonly reported that the lift occurs only due to the shear induced force (Klausner *et al.*, 1993; Nahra and Kamotani, 2003; Liu *et al.*, 2010). F_{SL} is determined according to equation (4.24), where C_L represents the lift coefficient and is obtained from equation (4.25).

$$F_{SL} = \frac{1}{2}\rho_L C_L A_P |U_{eff}|(U_{eff})\hat{\mathbf{y}} \tag{4.24}$$

$$C_L = \frac{1}{2}\left(\frac{1+16Re_B^{-1}}{1+29Re_B^{-1}}\right), \quad 5 < Re_B < 500 \tag{4.25}$$

No correlations were found for the estimation of C_L during the interaction of non-spherical gas plumes with a liquid crossflow; hence the methodology followed in this study was similar to the scenario for single rounded bubbles. It was noticed that, similar to the observations for C_D, C_L also varied with time, because of the change in dimensions experienced by the gas plume during its development. In the vertical direction, the lift force exerts an opposite effect to the drag: The drag force opposes the displacement of gas plume centroid, delaying the detachment in the spanwise direction, while F_{SL} helps in the separation of the gas plume from the wall. Klausner *et al.* (1993) determined that both effects were within a comparable order of magnitude; the lift force had a slightly higher magnitude than the drag force. Liu *et al.* (2010) determined that F_{SL} was the main detaching effect in the vertical direction while the drag force becomes negligible. Thus, C_L was determined based on the instantaneous geometry of the gas jet and was not considered as a constant. Appendix C.4 expands on the findings of C_L for a growing gas jet in a flowing liquid.

4.2.7. Pressure force

The injection of the gas phase into the liquid cross-flow occurred because of the pressure difference between the phases at the injection orifice, $P_G - P_L$. This was defined as the pressure force (F_P). The pressure force could be interpreted as a reaction force that acted on the control volume associated to the bubble. Liu *et al.* (2010) defined the pressure force as acting only at the injection orifice, as indicated in equation (4.26). If the gas flow rate is slow or the pressure difference between phases is very small, the pressure force can be considered as negligible (Badam *et al.*, 2007).

$$F_P = \left(P_G - P_L \right) A_{inj} \tag{4.26}$$

Klausner *et al.* (1993) defined F_P as the combination of three effects: the hydrodynamic pressure acting on the bubble, the contact pressure at the injection orifice (equation 4.27) and the buoyancy force, which was defined in section 4.2.1. Nahra and Kamotani (2003) defined F_P as the sum of two components: the first component was the pressure difference between the gas at the orifice and the liquid pressure of the hydrodynamic forces, defined as interfacial tension pressure. The second component is attributed to the contact pressure.

Duhar and Colin (2006) defined F_P simply as the effect of the contact pressure, while considering that the hydrodynamic forces contributed on the drag, migration and unsteady forces. Nahra and Kamotani (2003) inferred that the contact pressure force contributed to the stagnation effects near the injector area, which caused a high pressure region that helped elongation and

consecutive detachment of the gas core. In the present study, the pressure force was calculated according to equation (4.27). . Although the ideal scenario would be to know the pressure right at the injection location, this is not generally a known variable. In this case it is not possible to measure the magnitude of P_G right at the injector because the experimental setup does not allow for this. It is understood that the physical implications of the gas injection problem require that P_G must be higher than P_L, hence P_G can only be estimated by knowledge from the conditions given by the gas mass flow controller and the knowledge of the pressure in the conduit. Accompanying information on the pressure force is included in Appendix C.5.

$$F_P = \left(P_G - P_L \right) A_{\text{inj}} = \frac{\pi D_{\text{inj}}^2}{4} \frac{\sigma}{D_{\text{equiv}}} \hat{\mathbf{y}} \qquad (4.27)$$

4.2.8. History force

Duhar and Colin (2006) defined the history force as part of a general unsteady force term, which plays an important part only at the initial stage of the bubble growth and after the breakup occurs. This unsteady term accounts for the variations of the shear stress acting on the surface of the growing bubble exposed to the liquid cross flow. It was inferred that during these stages the gas jet experienced strong accelerations and the history forces could be important. Mazzitelli (2003) considered that the existence of a tangential velocity at the gas-liquid interface diminished the boundary layer delay and that for $Re_B \sim 1$, the F_H could be neglected. Klausner et al. (1993) considered that since the amplitude of history forces oscillated with time scaled by u_τ, their contribution to the diameter at breakup is insignificant. Clift et al. (1978) commented that neglecting the history term greatly simplifies the estimation of the effects acting on particles,

although it could result in substantial errors in the estimation of the unsteady motion of fluid particles in liquids. However, as the Re_B increases, the errors caused by disregarding the history term effects are less significant. For the purposes of the current study, Re_B was relatively large and the history force effects were not considered.

4.2.9. Turbulent induced force

To evaluate the influence of the turbulence effects on the gas jet growth dynamics, an appraisal of the scales associated to the turbulence and bubble growth time was conducted. The experiments were performed under liquid conditions that corresponded to a fully developed turbulent flow, which required the evaluation of the various eddy length scales, more explicitly the Kolmogorov scale (η), the Taylor scale (λ), and the integral scale (Λ). A semi-theoretical, exploratory assessment of the turbulence parameters indicated that the energy containing eddies were the only structures whose length scale was constantly within an order of magnitude comparable to that of the gas plume. A detailed explanation about the findings that led to this statement can be found in Appendix C.6.

To include the effects of the turbulent flow in the mechanics of formation, the dynamic pressure fluctuations were considered as the disruptive turbulent effect inducing disintegration. These fluctuations were characterized by Hinze (1955), Hesketh (1987) and Andersson and Andersson (2006) according to equation (4.28). In this work, this shear stress was called the turbulent-induced shear stress (τ_Λ). To estimate its effect on a growing jet, it was considered that τ_Λ acted on the jet surface, defined by the product ($D_W\ P_{ER}$). The turbulence induced force (F_τ) was

defined in equation (4.29). Appendix C.6 provides further clarification about how the turbulence energy dissipation rate (ε) can be approximated.

$$\tau_\Lambda \approx 2\rho_L \left(\varepsilon\Lambda\right)^{2/3} \qquad (4.28) \qquad F_\tau = 2\rho_L \left(\varepsilon\Lambda\right)^{2/3}\left(D_W P_{ER}\right) \qquad (4.29)$$

4.3. Forces in the horizontal direction

The essential forces in the $\hat{\mathbf{x}}$ direction are the surface tension, which was an attaching force; the drag force, which acted as the main detaching force in the streamwise direction, contrary to the effect that had for the vertical direction; and the added mass or inertial force, which could be an attaching or detaching force, depending on the relative velocity between the phases.

4.3.1. Added mass force

Similarly to the methodology introduced in section 4.2.3, an expression for the added mass force in the streamwise direction was obtained. Equation (4.30) is very similar to equation (4.7), the only difference is the inclusion of a term that included the effects of the cross-flow velocity on the inertial effects experienced by the growing gas jet.

$$
\begin{aligned}
F_{Ix} = \left(\rho_G + \rho_L C_M\right) &\left[\left[D_w\left(t\right)\left(\frac{dA_P\left(t\right)}{dt}\right) + A_P\left(t\right)\left(\frac{dD_w\left(t\right)}{dt}\right)\right]\left(\frac{dx}{dt}\right) + \left(D_w\left(t\right)A_P\left(t\right)\right)\frac{d^2x}{dt^2}\right] \\
&- \rho_L C_M U_L \left(D_w\left(t\right)\frac{dA_P\left(t\right)}{dt} + A_P\left(t\right)\left(\frac{dD_w\left(t\right)}{dt}\right)\right)\right\}\hat{\mathbf{x}}
\end{aligned}
$$

(4.30)

4.3.2. Surface tension force

As expressed in section 4.2.4, the surface tension force is defined as a function of the D_{inj}. However, under non-idealized scenarios, the breakup of the bubbles occurs at the end of the gas plume. Hence, defining the attaching force as a function of D_{inj} would not provide an adequate characterization of the bubble separation dynamics. A depiction of the hypothetical mechanisms opposing the breakup of the gas core is included in Figure 4.6. The dotted area describes the surface tension effect opposing the separation of bubbles from the gas core, which was considered to be a function of the width of the jet instead of D_{inj}.
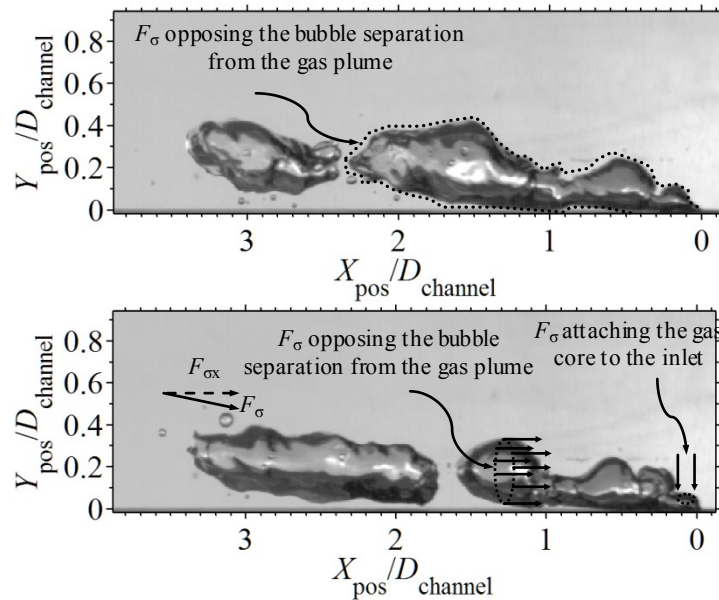
Figure 4.6.   Sketch depicting the surface tension force opposing the separation of bubbles from the gas core. The conditions under which the images were taken were: $Fr_G \approx 460$, $D_{inj} = 0.52$ mm, $Re_L \approx 56000$

Contrary to what was observed in the present study, none of the previous works estimated the possibility of a gas core permanently attached to the injection. It was commonly assumed that bubbles form individually, and in some cases a small neck remained attached to D_{inj} (Kulkarni

and Joshi, 2005). As indicated by the images, which represented the scenario immediately after bubble detachment, the breakup did not occur near the orifice but at the end of the plume.

It was inferred that only when the bubbling process consisted on the growth and full separation of a bubble from the orifice, the surface tension force could be defined as a function of the gas port dimensions. Otherwise, the gas core dimensions provided a better assessment of the forces opposing the breakup of the gas structure. This was taken into consideration and the surface tension force was defined using two alternative approaches. The first one, defined in equation (4.31), is similar to the one followed by Tan *et al.* (2000), Sovani (2001) and Liu *et al.* (2010), with the added difference that D_{inj} has been substituted by D_W. The inclination angle determined the effects on the horizontal and vertical direction.

The second approach is included in equation (4.32), and is analog to bubble breakup dynamics. It was inferred that the surface tension does not oppose detachment exclusively on A_{inj}, instead along the whole shell of the gas plume. Therefore, P_{ER} was used to estimate the cohesive effects. A comparison between the surface tension forces defined using equations (4.31) and (4.32) is shown in Figure 4.7.

$$F_{\sigma x} = \sigma \pi D_W \cos(\theta)\hat{\mathbf{x}} \qquad (4.31) \qquad F_{\sigma x} = \sigma \pi P_{ER} \cos(\theta)\hat{\mathbf{x}} \qquad (4.32)$$
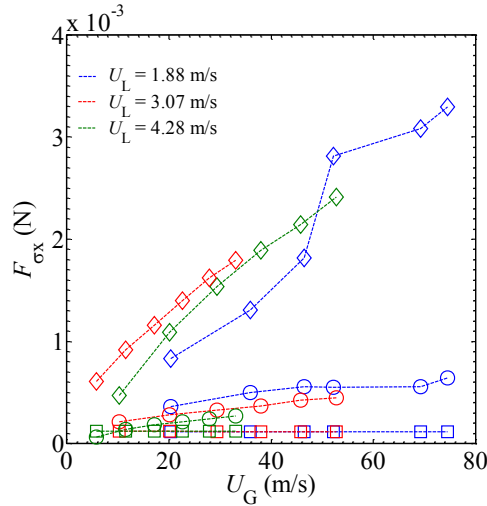
Figure 4.7. Comparison of the surface tension force magnitude defined as a function of D_{inj} (square), D_{W} (circle), P_{ER} (diamond). The conditions corresponded to $D_{\text{inj}} = 0.52$ mm

When compared to the simpler approach obtained from utilizing D_{inj}, the use of D_{W} and P_{ER} in the surface tension force resulted in a stronger attaching effect. When $F_{\sigma x}$ was defined as a function of D_{inj}, it gave an almost constant value. As U_{G} increased, the gas core dimensions grew and the influence of the forces opposing detachment increased as well, since the width of the gas core could grow up to several times D_{inj} downstream of the inlet location. Also, the enlargement of the jet caused a direct increment in P_{ER}.

Similarly, when U_{L} was increased, D_{W} and P_{ER} decreased; diminishing the resistance offered by the gas phase to the detachment of bubbles. It was concluded that, even though the surface tension force was commonly defined as a function of D_{inj}, this parameter did not represent accurately the cohesive forces in the gas jet formation and disintegration process. Using P_{ER} in the definition of F_{σ} gave results that followed more closely the physics of breakup, as they resemble better to the well-know phenomenon of bubble separation in flowing liquids, which are associated to the whole extent of the bubble. Contrary to the common assumption of taking only

D_{inj} as the dimension associated, P_{ER} would be a more representative dimension of the surface of the jet opposing the breakup.

4.3.3. Drag force

The drag force on the horizontal direction is defined according to equation (4.33). Since the main component of the liquid cross flow velocity acts in the streamwise direction, it was expected to observe a dominant effect of the horizontal component over the vertical one, as shown in Figure 4.8, which includes the variations of F_{Dx} during the growth time of a gas jet for several values of M_{G}. The results correspond to selected cases related to the experimental conditions chosen which describe a typical gas jet growth cycle. The initial points for each curve correspond to $t \approx 0$, which is the point where the gas jets starts is growth cycle anew. Near the start of the formation process, the drag force in the horizontal direction was dominant over the vertical component. As the gas core volume grew, the slip velocity in the spanwise direction increased, causing F_{Dy} to exert a more relevant contribution. The ratio $F_{\text{Dy}}/F_{\text{Dx}}$ grew rapidly until it reached ratios that varied from 0.10 to 0.19 near the end of the interval. This behaviour occurred for all the M_{G} values tested.

$$F_{\text{Dx}} = \frac{1}{2} \rho_{\text{L}} C_{\text{D}} A_{\text{G}} \sqrt{\left(\frac{d\mathbf{S}}{dt} - U_{\text{L}} \right)^2} \left(\frac{dx}{dt} - U_{\text{L}} \right) \hat{\mathbf{x}} \tag{4.33}$$
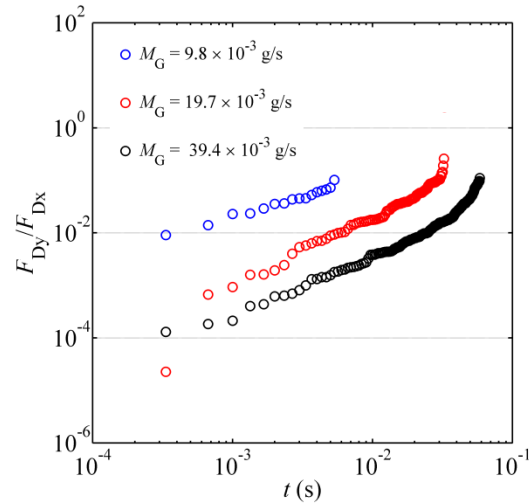
Figure 4.8.   Ratio of the vertical (F_{Dy}) to horizontal (F_{Dx}) drag force versus time up until the bubble separation occurs. The conditions correspond to $D_{inj} = 0.27$ mm and $Re_L \approx 24000$

4.4.   Concluding remarks

The dynamic effects acting on a gas jet during its injection into a liquid cross flow were thoroughly categorized and evaluated. Although the single bubble formation process has immense applicability, no definitive agreement on the definition of many of the forces involved during the gas jet growth was found. Because there is no clear theory developed for the jetting scenario, the majority of the definitions were adapted from the single bubbling formation. Theoretically, all bubble formation modes occur under markedly similar physical principles. The conclusions obtained from the theoretical-empirical analysis conducted were:

* Many numerical models rely on the supposition of a non-deformed, symmetrical sphere to reproduce the growth and detachment development, limiting their applicability to quasi-ideal scenarios. Based on the results obtained from the experiments, it is very unlikely that this could occur in the presence of a strong U_L, especially if the values are similar to those found in

109

industrial applications. The results obtained indicate that the initial circularity of the incipient gas jet is between ξ = 0.6-0.7 for bottom wall injection and ξ = 0.5-0.4 for top wall injection. Independent of the injector location, as the gas jet grows, the circularity decreases. For bottom wall injection, ξ decreases to a value approximately equal to 0.34, while for top wall injection $\xi \approx 0.2$.

* Important hydrodynamic effects, like the drag and lift forces, varied significantly based on the correlation used to obtain to estimate their associated coefficients. This limits severely most of the existing models, because generally they were validated for a specific correlation. Depending on the correlation used, the magnitude of either F_D or F_{SL} could have differences in the order of at least 150% in some cases.

* The coefficients C_D, C_L and C_M were commonly assumed as constants, disregarding the growth and deformation of the bubble/gas jet. Owing to the dependence of these coefficients on the geometry of the developing gas structure, it was concluded that an instantaneous approach was preferred over the use of constant values. The correlations developed by Haider and Levenspiel (1989) and Ishii and Hibiki (2010) were the only expressions capable of take into account the deformation of the gas jet and/or growth mechanics in the calculation of C_D. However, the correlation of Haider and Levenspiel (1989) yields C_D values that could require further testing due to the relatively high magnitude ($C_D \approx 2$ -5). Despite representing key forces during the bubble growth and development, limited data was found for C_M and C_L; hence the methodology proposed by Kendoush (2007) and Legendre and Magnaudet (1998) was followed. It was obvious that further development in this topic is necessary.

* It was considered that the cohesive effects acted along the plume surface instead of exclusively at D_{inj}, which was more in line with the physical implications of the gas stream. It was expected that the evaluation presented could serve as a base for an all-inclusive dynamic study of the developing gas jet. Using P_{ER} over D_{inj} or D_W in the estimation of the surface tension forces, gives results that could be between 1.2 to 3 times higher.

5. Wall Gas Jet Dynamics and Bubble Detachment in a Strong Liquid Cross Flow

5.1. Introduction

The purpose of the present chapter is to discern the dominant forces during the growth of a gas plume in a strong liquid cross flow and how they affect gas jet breakup location. The analysis focused on observing the evolution of the gas stream from its incipient state until the point where detachment occurs. All the information was obtained through time-averaged shadowgraphs. After the dynamics assessment, the effects of the gas injection velocity (U_G), liquid velocity (U_L) and injection diameter (D_{inj}) on the gas jet growth and bubbling frequency were studied. This analysis allowed the estimation of obtain empirical correlations that estimate the averaged gas stream breakup location (x_{break}) and bubble detachment frequency (f_B) as a function of important dimensionless numbers.

5.2. Gas jet breakup and bubble departure conditions

A commonly accepted criterion is that bubble detachment occurs immediately after the detaching forces overcome the connecting forces. While the bubble remains attached to the nozzle, the equilibrium conditions require that:

$$\sum F_x \leq 0 \qquad (5.1a) \qquad \qquad \sum F_y \leq 0 \qquad (5.1b)$$

In case either condition does not hold, bubble departure occurs. If the condition (5.1a) is violated first, then the bubble slides along the wall before lift takes place. Should condition (5.1b) be broken first, then no sliding occurs and lift off occurs first (Klausner *et al.*, 1993). The conditions presented in equation (5.1) constituted the base for the models found in the literature that predict single bubble detachment (Sovani, 2001; Thorncroft *et al.*, 2001; Nahra and Kamotani, 2003; Duhar and Colin, 2006). However, the validity of these predictive approaches was not explored for other bubbling regimes, such as pulse bubbling or jetting, as defined by Rigby *et al.* (1995), Forrester and Rielly (1998) and Sovani (2001). This point will be further expanded in Chapter 7.

Under the pulsating bubble regime, bubble elongation and chaining occurred. Even though the bubbles still detached as individual entities, they remained linked together and to the injection area (A_{inj}). Hence, they were categorized as a single plume (Forrester and Rielly, 1998). Similarly, under the jetting regimes multiple breakup scenarios were observed. Although the detachment of a larger bubble from the gas core still occurred, the separation of bubbles of varied volume from the main gas plume was increased. Predicting the detachment through numerical modelling for regimes beyond single bubbling becomes increasingly challenging due to the difficulties in the calculation of the viscous forces as well as the deformation experienced by the bubbles (Nahra and Kamotani, 2003).

The force balance in the **x** and **y** directions were calculated from equations (5.2a) and (5.2b). The equations encompassed the forces defined in Chapter 4 and were grouped based on whether they contributed to the breakup of the gas plume or exerted a cohesive effect.

$$\underbrace{}_{\text{Detaching}} \quad \underbrace{}_{\text{Attaching}} \qquad (5.2a)$$

$$\underbrace{}_{\text{Detaching}} \quad \underbrace{}_{\text{Attaching}} \qquad (5.2b)$$

A summary of the force analysis conducted by previous researchers is presented in Table 5.1. This review included the forces studied along with the dynamic parameters that were found to be dominant in their studies. As observed, there were manifest differences between authors about the governing forces during the bubble formation process. Although the studies shown in Table 5.1 refer to comparable physical phenomena (single bubbling), varied conclusions regarding the dominant force balance were obtained. Also, discrepancies were found concerning the direction on which the dominant force balance was observed. Even in the presence of a liquid cross-flow, some researchers concluded that the vertical force balance had comparable magnitudes to the ones observed in the streamwise direction.

Table 5.1.   Summary of forces considered by previous authors in the field of bubble formation into a liquid cross-flow

Author(s)	F_y	Dominant F_y balance for bubble detachment	F_x	Dominant F_x balance for bubble detachment	Governing direction
Klausner *et al.* (1993)	$F_{\sigma y}, F_{SL}, F_B, F_P, F_{Dy}, F_{Iy}, F_{hyd}$	$F_{SL} - F_{Iy} - F_{\sigma y} \approx 0$	$F_{\sigma x}, F_{Dx}, F_{Ix}$	$F_{Dx} - F_{Ix} \approx 0$	V
Sovani (2001)	$F_{\sigma y}, F_B, F_M, F_{Dy}$	$F_{Dy} - F_{\sigma y} \approx 0$	---	---	V
Nahra and Kamotani (2003)	$F_{\sigma y}, F_{SL}, F_B, F_P, F_{Dy}, F_{Iy}, F_M$	$F_{Iy} = F_B + F_M + F_{SL} + F_P - F_{Dy}$	$F_{\sigma x}, F_{Dx}, F_{Ix}$	$F_{Ix} = F_{Dx} - F_{\sigma x}$	V - H
Loubiere *et al.* (2004)	$F_{\sigma y}, F_B, F_{Dy}, F_{Iy}, F_M$	$F_{Iy} + F_{\sigma y} + F_{Dy} = F_B + F_M$	$F_{\sigma x}, F_{Dx}, F_{Ix}$	$F_{Dx} - F_{\sigma x} \approx 0$	V - H
Duhar and Colin (2006)	$F_{\sigma y}, F_{SL}, F_B, F_P, F_{Dy}, F_{Iy}$	$F_B + F_P - F_{\sigma y} \approx 0$	$F_{\sigma x}, F_{Dx}, F_{Ix}$	$F_{Dx} - F_{\sigma x} \approx 0$	V
Liu *et al.* (2010)	$F_{\sigma y}, F_{SL}, F_B, F_P, F_{Dy}, F_{Iy}, F_M$	$F_{Iy} = F_B + F_{SL}$	$F_{\sigma x}, F_{Dx}, F_{Ix}$	$F_{Ix} + F_{\sigma x} = 0$	H

In this study, a comprehensive force analysis similar to the ones conducted in previous works was performed. The only difference was the inclusion of a turbulence induced detaching force (section 4.2.9) in both directions. The evaluation contrasted the different forces, with the subsequent order of magnitude evaluation. After this, it was determined which dynamic effects had a dominant contribution in the morphological features of the gas jet, as well as the detachment of bubbles from the main gas structure.

The analysis was divided in two categories: First, a brief evaluation of the differences between the possible gas injector locations, top or bottom wall, was performed. Second, the effect that the operational and geometric variables had on the forces acting on a growing gas jet was considered. For every one of the studied scenarios, the results represented an individual gas jet growth-detachment case for the conditions reported. Each occurrence gave a distinctive characterization of the gas jet evolution phenomena and provided a discerning evaluation of the gas-liquid interaction dynamics and how they affect the development of the gas jet.

5.3. Effect of the gas inlet location on the forces acting on a developing gas jet

The influence of the nozzle location on the gas plume growth was evaluated under the following conditions: $U_L \approx 2.0$ m/s, $M_G = 29.5 \times 10^{-3}$ g/s and $D_{inj} = 0.27$ mm. The forces were considered as positive if they applied a detaching effect over the gas jet and negative if they opposed the gas jet breakup. A comparison of the forces that acted on a growing gas jet, when the gas was injected from the top wall versus the bottom wall injection case was presented in Figure 5.1.
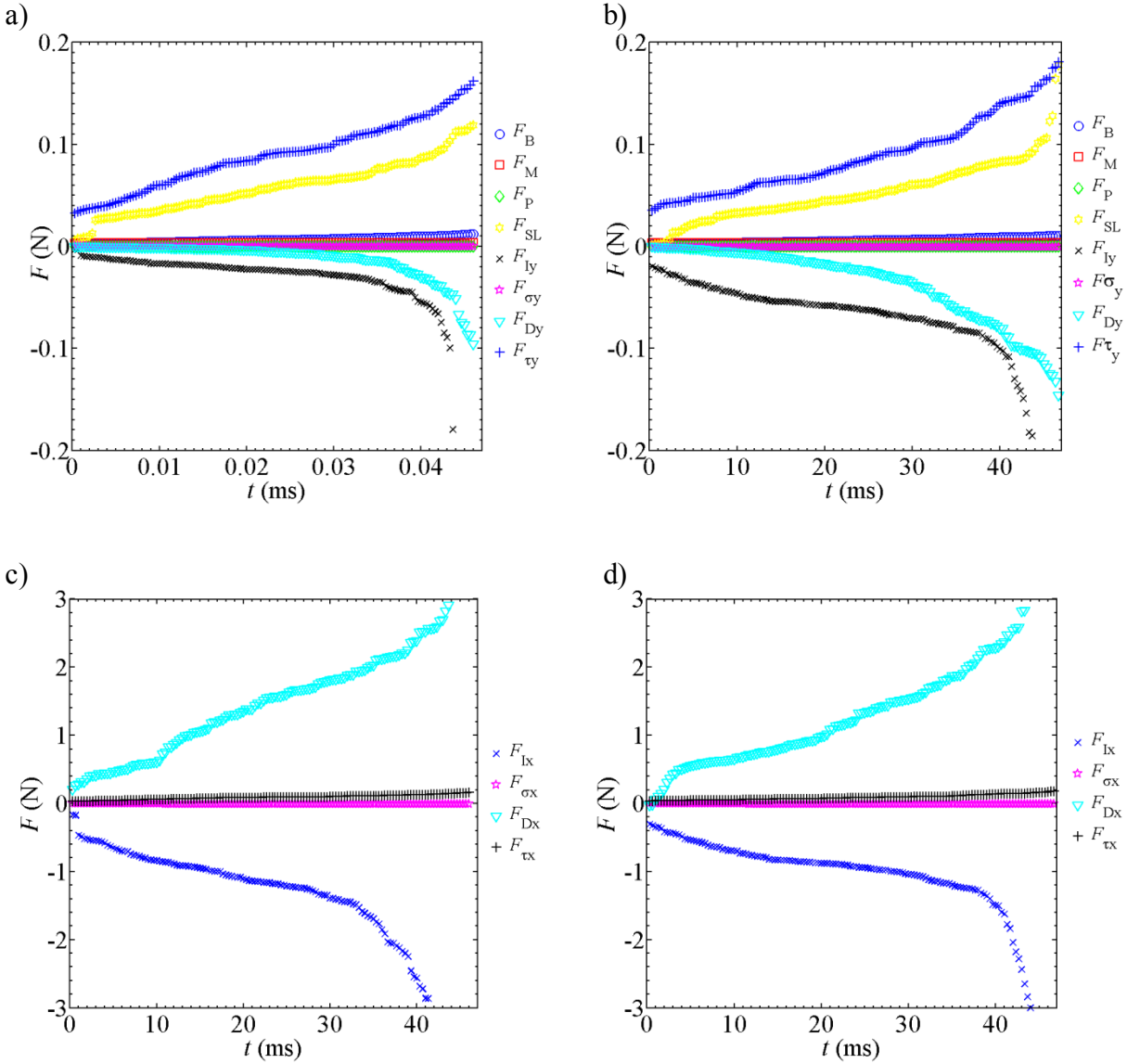
Figure 5.1. Estimation of the forces acting on a growing gas jet in a cross flow: a) F_y, Far wall injection. b) F_y, Near wall injection. c) F_x, Far wall injection. d) F_x, Near wall injection. The results depicted correspond to the conditions $D_{inj} = 0.27$ mm, $M_G = 29.5 \times 10^{-3}$ g/s, $U_L \approx 2.0$ m/s

In the vertical direction, Figures 5.1a and 5.1b, the results exhibited a high degree of similarity

between them. In both cases the dominant detaching forces were the shear lift force and the

turbulence force, while the prevailing attaching forces were the inertial and drag forces. These

results resembled the observations of Liu *et al.* (2010), who found that the F_{SL}, F_B and F_{Iy} were

the dominant effects in the $\hat{y}$ direction. The buoyancy force had a minimal effect during the

earlier stages of the gas jet growth. Close to bubble detachment, the contribution of F_B was approximately equal to 12% of the magnitude of F_{SL}. The other forces, such as F_M, F_P and $F_{\sigma y}$ had a negligible effect.

The results presented in Figure 5.1 also showed that for the selected case, the nozzle position did not produce significant variations in the magnitude of the vertical detaching forces involved. The dominant forces, $F_{\tau y}$ and F_{SL}, exhibited similar trends and scales for both top and bottom wall injection. Conversely, the vertical cohesive forces showed small magnitude differences. As indicated in Figure 5.1, for the top wall injection case the inertial and drag forces had slightly smaller values than those estimated for the bottom wall injection. It was inferred that when the nozzle was in the top wall, the presence of a boundary restricted the natural tendency of the gas jet to displace contrary to the gravity. This limited the growth, velocity and acceleration of the gas jet in the $\hat{y}$ direction, which produced smaller values for F_{Iy} and F_{Dy} than those observed for bottom wall injection. The results are in agreement with the findings discussed in Chapter 3 and 4.

Figures 5.1c and 5.1d showed that the magnitude of the forces in the $\hat{x}$ direction had a larger value than those in the $\hat{y}$ direction. F_{Dx} was the dominant effect contributing to the fragmentation of the gas jet, while F_{Ix} was the dominant cohesive force in this direction. $F_{\tau x}$ and $F_{\sigma x}$ played smaller roles in the gas plume dynamics. These findings differed from the observations presented by other authors. Duhar and Colin (2006) determined that F_D had a small but non negligible contribution in the bubble detachment mechanics, while Liu et al. (2010) considered that the drag

force was negligible in the $\hat{x}$ direction. Klausner *et al.* (1993) determined that F_{Dx} was important but had a smaller magnitude than F_{Dy}.

The differences were attributed to the fact that the previous works focused on the formation of microbubbles, whose dimensions were much smaller than the gas jets considered here and had an almost spherical shape. This resulted in a decrease on the contribution of the combined form and shear drag. Also, it was observed that for previous studies the relative velocity $U_L - dx/dt$ was smaller, leading both to a smaller contribution of F_{Dx} and F_{Ix}.

In general terms, the results indicated that the position of the gas injector did not induce significant variations in the magnitude of the forces affecting the gas jet. However, when the gas nozzle was located in the top channel wall, the presence of a boundary restricted the expected displacement of the jet in the positive $\hat{y}$ direction. As discussed, under this configuration, the values for U_{eff} were smaller than when the injector was located in the bottom wall, causing the aforementioned differences in the values of the inertial and drag forces. Independent of the position of the gas injector, F_{Dx} was the dominant detaching effect, while F_{Ix} was the most important force opposing the disintegration of the gas jet.

5.4. Influence of the operating conditions on the forces acting on a developing gas jet

5.4.1. Influence of the liquid cross flow velocity

For fixed values of M_G and D_{inj}, the magnitude of U_L was varied with the intention of studying its influence on the dynamics of an evolving gas jet. A force balance assessment for three liquid crossflow velocity values, U_L = 2.1 m/s, 3.0 m/s and 4.3 m/s, was conducted. A D_{inj} = 1.59 mm was used, while the gas mass flow rate was held constant at M_G = 29.5 × 10^{-3} g/s. The results obtained were reported in Figure 5.2, where the forces were categorized according to the direction upon which they acted.

An increase in the U_L magnitude will undoubtedly cause a decrease in the time it takes for the gas jet to expand and disintegrate, which was defined as t_{growth} in section 4.2.5. The gas jet dimensions (diameter, width, length) shortened as well. Both results exhibited great similarity with the conclusions presented by Sovani (2001), Nahra and Kamotani (2003), Duhar and Colin (2006) and Liu *et al.* (2010). Since the inertial force depends primarily on the volume of liquid displaced by the gas, i.e. gas jet size, it was expected to create a decline in the value of the F_I with an increase in U_L. This caused F_{Dy} to overcome F_{Iy} as the dominant attaching effect in the vertical direction. When U_L = 2.1 m/s, the inertial force was approximately 1.7 times higher than the drag effect, and was the prevailing connecting effect under these conditions. As was shown in Figure 5.2, the estimated magnitude of F_{Ix} and F_{Iy} decreased when U_L increased from 2.1 to

4.3 m/s. For all the cases studied, F_{Ix} constituted the main force in the horizontal direction delaying the gas jet breakup.

Independent of U_L, F_{SL} and $F_{\tau y}$ were the dominant detaching effects in the vertical direction. Its influence as breakup forces strengthened as the liquid crossflow was accelerated. Although the slip and shear exerted over the gas jet increased with an increase in U_L, the surface area of the jet diminished, which caused the magnitude of these forces to be encompassed within similar ranges for varied values of U_L. The detaching influence of F_{SL} and $F_{\tau y}$ was balanced by the combined effects of F_{Dy} and F_{Iy}. The other forces, F_P, F_M, F_B and F_σ, had a very small magnitude and its influence on the gas jet growth was considered as negligible.

Lastly, it was observed that for all D_{inj} tested the forces in $\hat{x}$ were an order of magnitude higher than those in $\hat{y}$. Hence it was deduced that, while the vertical force balance had an important influence in the tilting and deformation of the gas jet, the horizontal forces were dominant in the control on the gas jet breakup. F_{Dx} and $F_{\tau x}$ were the effects causing the disintegration of the plume into bubbles. The ratio $F_{\tau x}/F_{Dx}$ was encompassed between 0.088, 0.104 and 0.127 for $U_L = 2.1$, 3.1 and 4.3 m/s respectively, which indicated that F_{Dx} was the leading detaching force. The turbulence effects had a magnitude of up to $0.25F_{Dx}$ at the beginning of the formation stage, but this role decreased significantly before bubble detachment occurred. It was conjectured that F_τ contributed to the irregular bubble detachment, as well as the deformation of the gas jet.
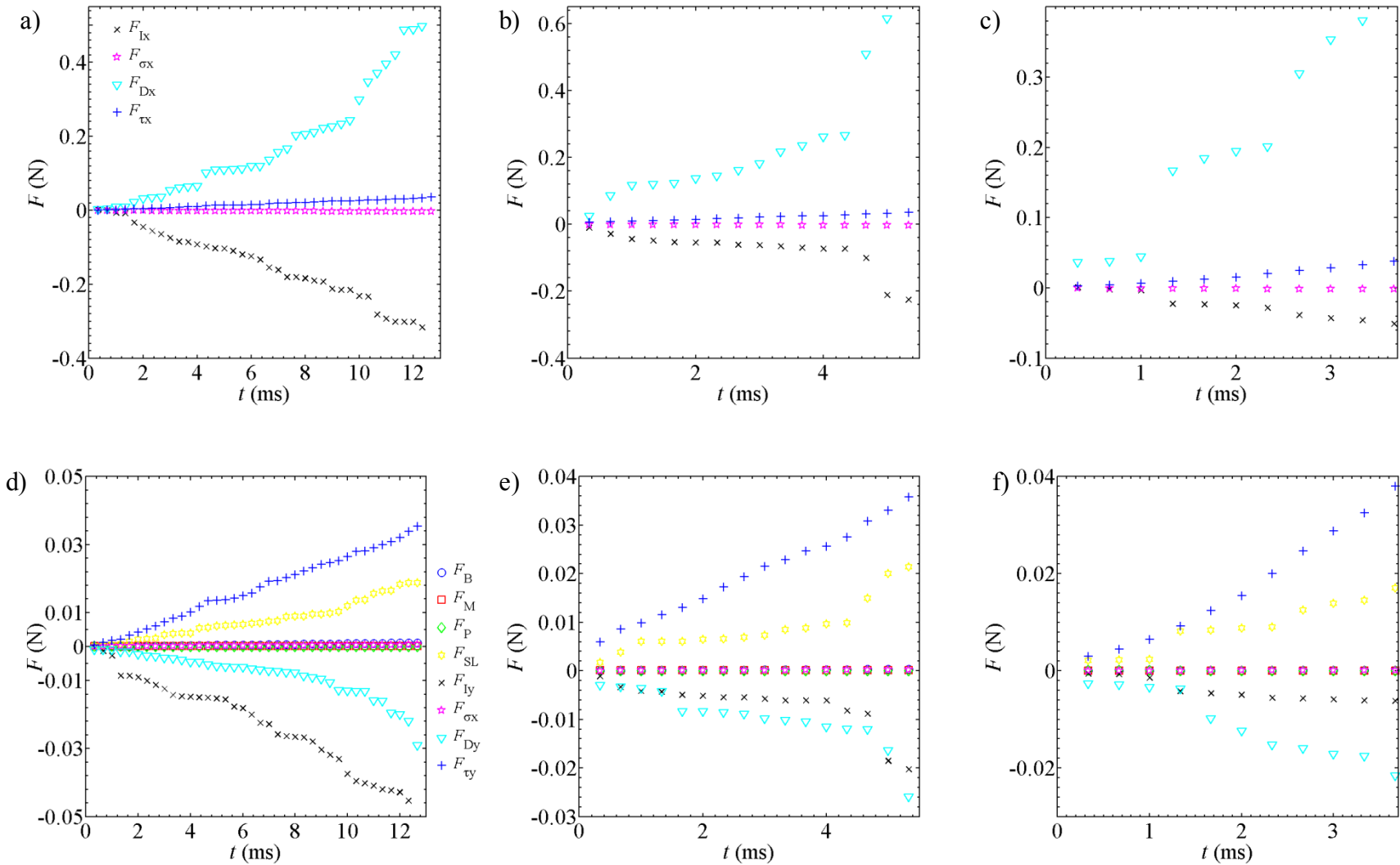
Figure 5.2.   Influence of U_L on the dynamics of a growing gas jet in a liquid crossflow: a) F_x, U_L = 2.1 m/s. b) F_x, U_L = 3.0 m/s. c) F_x, U_L = 4.3 m/s. d) F_y, U_L = 2.1 m/s. e) F_y, U_L = 3.0 m/s. f) F_y, U_L = 4.3 m/s. The results were obtained under the conditions: D_{inj} = 1.59 mm, M_G = 29.5 × 10^{-3} g/s, bottom wall injection

5.4.2. Influence of the gas mass flow rate

The effects of the gas mass flow rate on the dynamics of an evolving gas jet were evaluated. The liquid cross flow velocity and gas injector diameter values were held constant, at $U_L = 3.1$ m/s and $D_{inj} = 0.52$ mm respectively. Six variations of M_G were considered, following the range of values defined in the Experimental Setup chapter. The results are presented in Figure 5.3. Independent of the value of M_G, it was determined that the magnitude of the buoyancy, pressure, momentum and surface tension forces were negligible; whereas the lift, drag, inertial forces and turbulent fluctuations were the dominant effects. These results did not fully adhere to the observations presented by previous authors, where different forces were reported as the governing ones during the bubbling process, as was shown in Table 5.1.
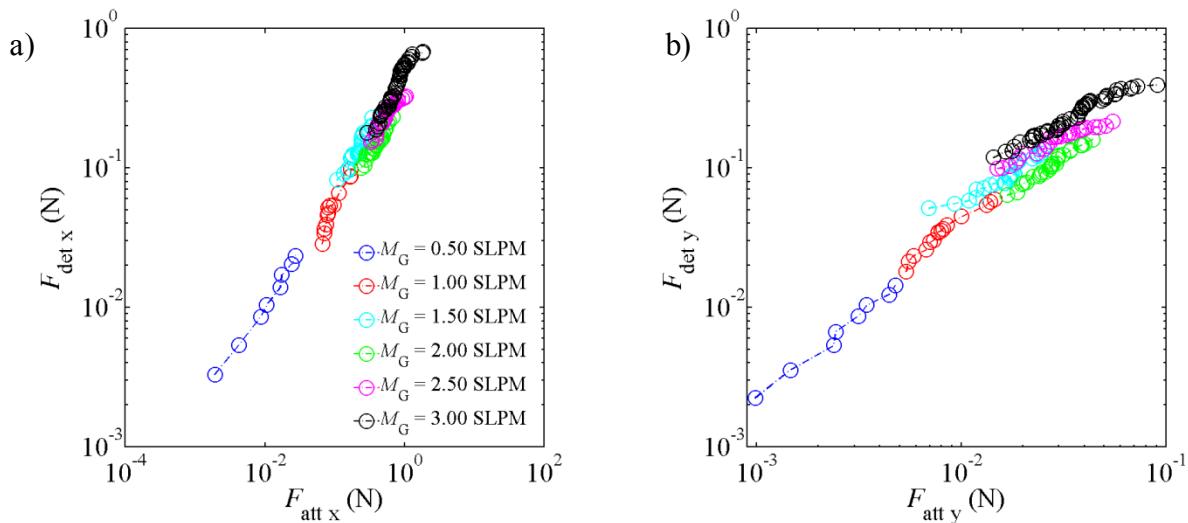
Figure 5.3.   Ratio of the dominant detaching force versus dominant attaching force as a function of time: a) horizontal forces. b) vertical forces. The graph depicts typical gas jet growth scenarios. The conditions corresponded to $D_{inj} = 0.52$ mm and $U_L \approx 3.1$ m/s. Bottom wall injection

As was shown in Figure 5.3a, for low M_G values, the values of F_{detx} and F_{attx} were lower than those observed for higher M_G values. As the gas jet evolved, both forces increased in magnitude. This was an expected result because according to the results explained in the previous chapter, a vast majority of the forces affecting the gas jet growth have a directly proportional relation with M_G.

The number of detaching forces exhibiting direct relationship with the continuous mass influx into the channel is higher than the number of forces opposing the gas jet disintegration, causing the eventual disparity between the two effects and the subsequent breakup. Near the instant when bubble detachment occurred, it was found that the ratio F_{detx}/F_{attx} had minimum and maximum values located between 1.5 and 3. Theoretically, the force ratio should have not exceeded unity, according to the criteria presented in equation (5.1a). It was inferred that the attaching forces near detachment where possibly underestimated, most likely F_σ. At the beginning of the gas jet expansion cycle (time), F_{detx}/F_{attx} had its lowest value, which never reached a value equal to zero. Physically, this implied that full detachment of the whole gas plume did not occur.

The force evaluation in the vertical direction was performed using all the effects involved, although the ratio $(F_{SL} + F_{\tau y})/(F_{Dy} + F_{Iy})$ was the mechanism controlling the gas jet dynamics in this direction. Although F_{Iy} had a significant contribution as an attaching force, particularly in the early stages of the gas jet enlargement, its strength decreased as the jet evolved. The drag force became the principal effect opposing detachment from the mid to final instants of gas jet development. F_{SL} and $F_{\tau y}$ were several orders of magnitude stronger than the other possible

detaching forces. Independent of M_G, $F_{\tau y}$ was the dominant force in the $\hat{y}$ direction and was approximately 2.1 times higher than F_{SL} throughout the growth interval.

Finally, it was observed that the assessment of forces in both directions was similar. An increase in M_G caused an increase in the scale of both F_{det} and F_{att}. However, the growth slope for the $\hat{y}$ forces had a less pronounced rate than the slope for the $\hat{x}$ forces, which became more noticeable at high M_G values. This occurred because F_{Dy} grew at a faster rate than the detachment forces. It was inferred that the form drag effects became more relevant for higher M_G. For all the M_G scenarios tested, the horizontal forces had a much higher magnitude than those observed in the vertical direction. Hence, in the presence of a strong liquid crossflow and independent of the M_G magnitude, the force balance in the horizontal dimension controlled the bubble breakup detachment.

5.4.3. Influence of the injection diameter

The influence of the D_{inj} on the dynamics of gas jet formation was evaluated as well. The M_G and U_L values were held constant, at 40.0×10^{-3} g/s and 3.1 m/s respectively. D_{inj} was varied, allowing the evaluation of its effects on the forces acting on the jet. Similar to the results presented in Sections 5.4.1 and 5.4.2., the governing forces were F_{SL}, F_D and F_I. The force ratio F_{Dx}/F_{SL} had a mean value approximately equal to 25.9, 22.7 and 17.2, while the ratio between connecting forces F_{Ix}/F_{Iy} was 12.2, 7.8 and 5.5 for D_{inj} = 0.27, 0.52 and 1.59 mm respectively. Hence, it was verified that in the presence of a strong liquid cross flow, independent of the D_{inj} used, the horizontal forces were dominant over the vertical forces.

The results from the assessment of D_{inj} influence in the bubbling dynamics were shown in Figure 5.4. The force comparison was categorized based on the principal forces for each direction. In the $\hat{y}$ direction, F_{SL} was compared to with both F_{Iy} and F_{Dy}. The attaching forces had a similar tendency, exhibiting comparable magnitude throughout the gas jet expansion time, although F_{Dy} had a more pronounced increase in magnitude near bubble detachment. As observed in Figure 5.4b. For D_{inj} = 0.27 and 0.52 mm, the slopes associated to the forces were similar. Increasing the D_{inj} up to 1.59 mm caused a more gradual variation in the force values.
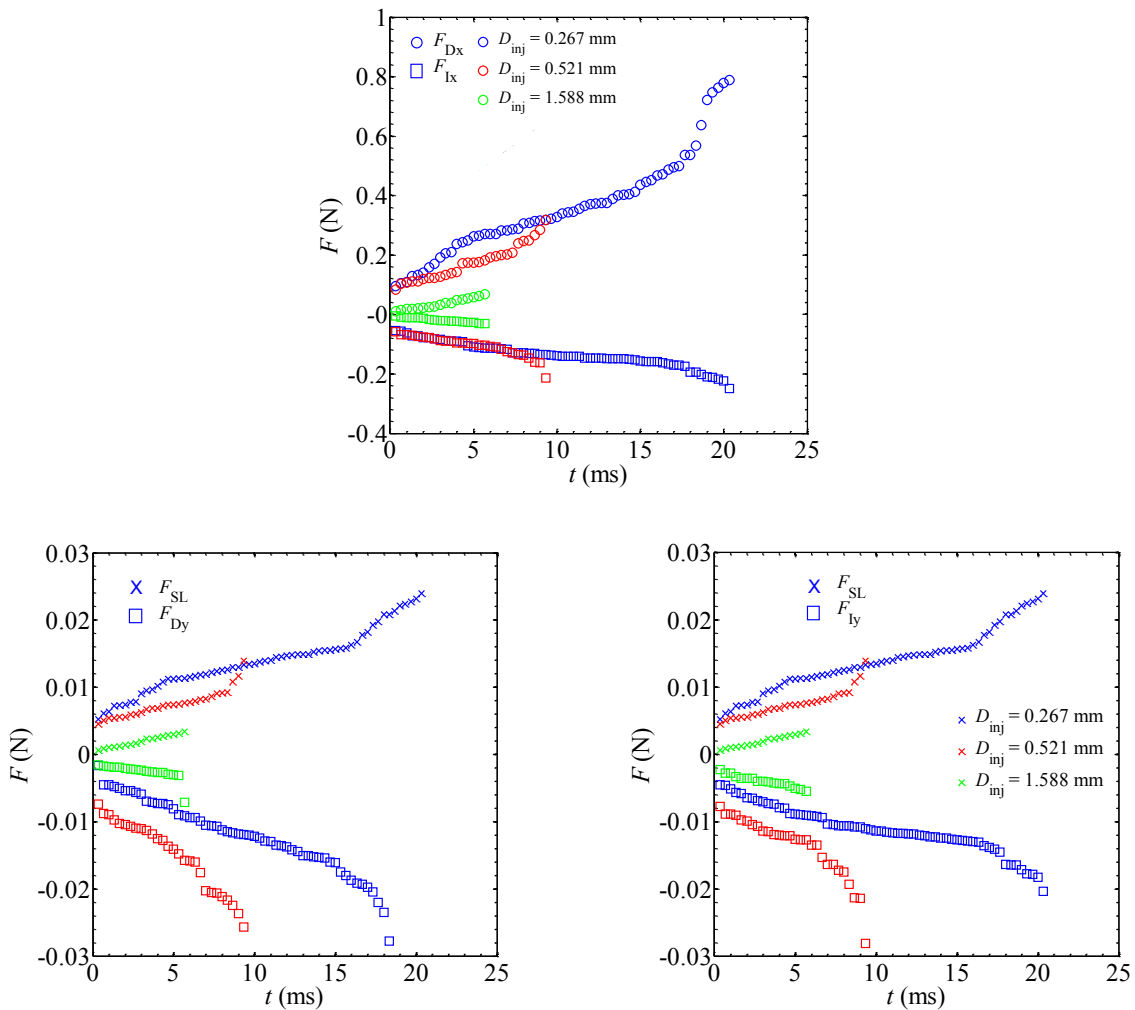
Figure 5.4.   Ratio of the dominant detaching force versus dominant attaching force as a function of time: a) horizontal forces. b) vertical forces: F_{SL} vs F_{Dy}. c) vertical forces: F_{SL} vs F_{Iy}. The graph depicts typical gas jet growth scenarios. The conditions corresponded to $M_G \approx 40.0 \times 10^{-3}$ g/s and $U_L \approx 3.1$ m/s. Near wall injection

Although none of the forces was implicitly governed by D_{inj}, this variable had a key influence in all the forces affecting the evolution of the gas jet. The results indicated that the use of a small D_{inj} delayed the breakup of the gas jet, hence increasing the growth time, as was shown in Figure 5.4. Increasing the dimension of D_{inj}, increased the frequency of detachment and decreased the volume of the gas jet. Conversely, a small D_{inj} translated into a delay of the detachment frequency. A small nozzle geometry translated into high U_G values, therefore high inertial forces (Fr_G numbers), which counteracted the effect of the liquid cross-flow to induce the gas jet breakup.

Nahra and Kamotani (2003) proposed that, though the force balance in the $\hat{x}$ and $\hat{y}$ directions was needed to estimate the bubble diameter at detachment, the momentum flux ratio between gas and liquid phases ($M''_{ratio} = \rho_G U_G^2 / \rho_L U_L^2$) was a key parameter in determining the detachment criteria for gas bubbles forming from an orifice in a liquid cross flow. They also reported that this parameter became more important as D_{inj} decreased, which explained the tendencies observed in Figure 5.4. A small D_{inj} caused large values of U_G, and therefore high M''_{ratio}. For large gas momentum flux $\left(M''_G = \rho_G U_G^2\right)$, the penetration of the gas jet in the channel was boosted, which hindered the separation of bubbles from the gas plume and allowed the gas jet to grow up to larger dimensions. This was inferred as the reason why for $D_{inj} = 0.27$ mm, the magnitude of the evolving gas jet forces had higher values than those estimated for $D_{inj} = 0.52$ mm and 1.59 mm.

5.5. Estimation of the Jet Breakup Location

The effects of U_G, D_{inj} and U_L on the averaged gas jet breakup location (x_{break}) were presented in Figure 5.5. The results considered the variation of U_L and U_G for a selected D_{inj} and nozzle location. The vertical bars indicated the x_{break} range, as determined from the experimental measurements. It was observed that at $U_L \approx 2.0$ m/s and independent of D_{inj} or the injector position, the jet breakup exhibited high variability, which was accentuated for high values of U_G. Kyriakides *et al.* (1997) found that high Re_G caused irregular formations of the gas stream. Weiland and Vlachos (2013) proposed that the combined effects of gas compressibility, internal turbulence of the gas jet and hydrodynamic instability were the phenomena behind the uneven breakup of a gas jet. In the present case, for the vast majority of the cases studied, gas phase compressibility was not an important factor. Hence, it was inferred that the high gas momentum flux and fully turbulent gas penetration, together with the unsteady drag between phases and liquid phase turbulence were the primary factors causing the randomness in x_{break}. Generally, when U_L was increased, x_{break} regularity increased, as indicated by a decline in the errors associated to each particular point (Figure 5.5). When $D_{inj} = 0.27$ mm, an increase in U_L caused the bubble detachment to occur closer to the inlet nozzle, particularly at $U_L \approx 5.30$ m/s, where x_{break} was confined between 9 and 23 mm, approximately. A similar behaviour was observed for $D_{inj} = 0.52$ mm. However, the results for $D_{inj} = 1.59$ mm did not follow the same trend, as observed in Figure 5.5c and 5.5f. Whereas an increase in U_G caused the jet disintegration to occur further downstream the nozzle, a higher U_L produced only a slight improvement in the x_{break} consistency. Also, for equally comparable values of U_G, a higher U_L induced a slightly more elongated x_{break}.
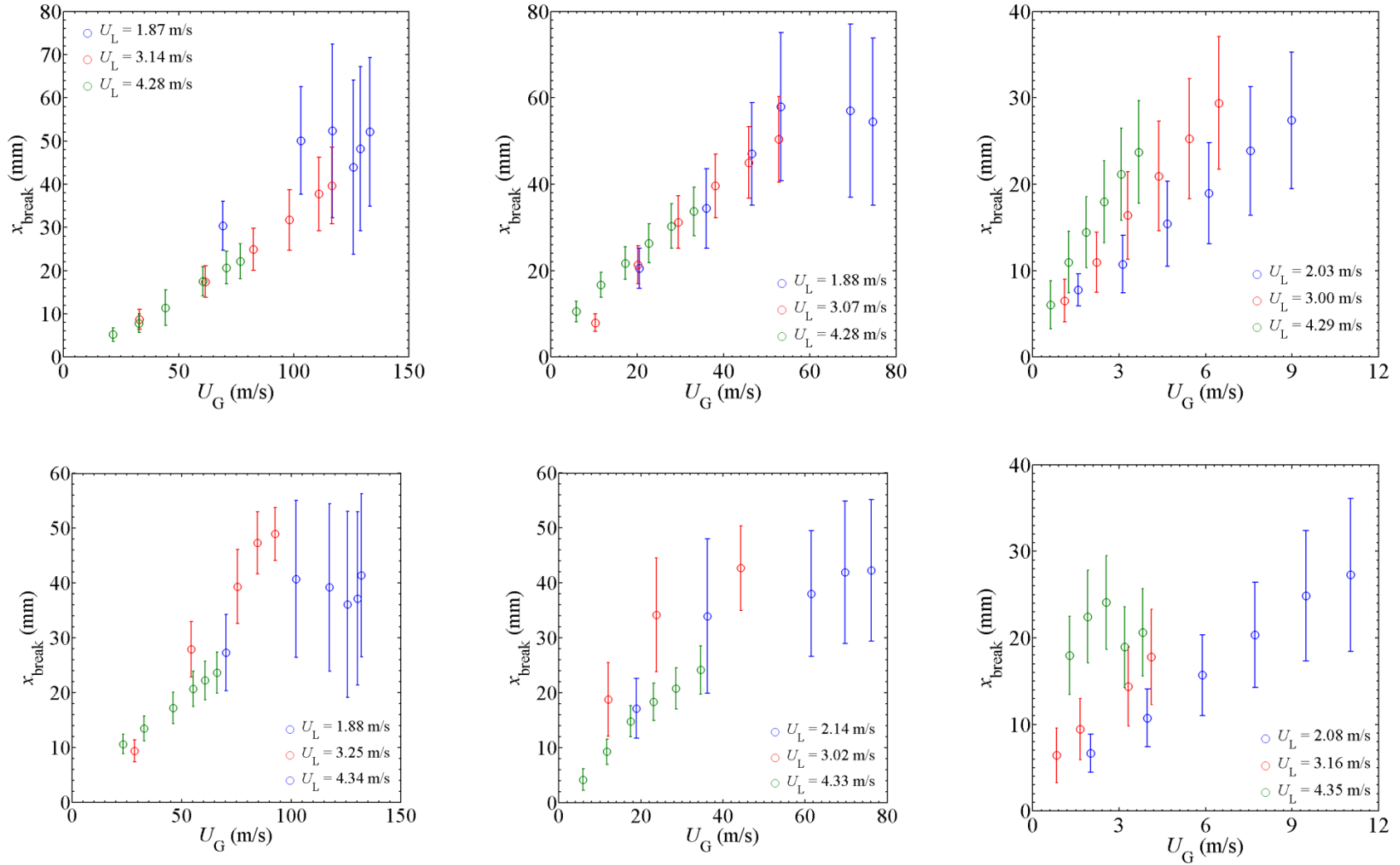
Figure 5.5.   Time-averaged jet breakup location in the horizontal dimension as a function of the gas injection velocity. The unsteadiness increases with higher U_G and decreases for higher U_L. a) Bottom wall, D_{inj} = 0.27 mm. b) Bottom wall, D_{inj} = 0.52 mm. c) Bottom wall, D_{inj} = 1.59 mm. d) Top wall, D_{inj} = 0.27 mm, e) Top wall, D_{inj} = 0.52 mm, f) Top wall, D_{inj} = 1.59 mm

A simple empirical correlation that estimates the averaged jet breakup location ($\bar{x}_{\text{break}}$) was derived from the experimental results shown in Figure 5.5. Taking into consideration the results of the force balance, the number of variables involved was simplified. The dominant forces, F_I and F_D, were related to the measured parameters which exert a key influence in the values for each force. Since F_I represents the expansion of the gas plume and the subsequent displacement of liquid, caused by the continuous injection of mass, M_G and D_{inj} were chosen as variables. These variables also present an intuitive measure of the gas phase centroid location and gas jet dimensions. F_D was related to Q_L, which linked the liquid velocity with the conduit dimensions. Physical properties of the fluids (ρ_G, μ_L) were included as well.

Taking these variables into consideration, dimensional analysis dictated that three dimensionless groups exist. Thus, the averaged dimensionless jet breakup location ($\chi_{\text{break}} = \bar{x}_{\text{break}}/D_H$) was defined as a function of two dimensionless parameters, (M''_{ratio}) and (Re_L), where equation (5.3) presents the correspondence between these numbers and χ_{break}, where the values for a, b and c were determined according to the expressions given in Table 5.2.

The results obtained from the comparison between χ_{break} and the empirical correlations are shown in Figure 5.6. As can be observed, for both top and bottom wall injection, the estimated results exhibit a remarkable agreement with the experimental data, while simultaneously including important physical effects such as the position of the gas injector and the liquid-cross flow magnitude. It is observed that χ_{break} has slightly higher values for bottom wall injection than top wall injection, which was expected based on the analysis and discussion presented in

previous sections about the effects of solid boundaries and the density difference between the phases.

$$\chi_{\text{break}} = a \left(M''_{\text{ratio}} \right)^b \left(Re_{\text{L}} \right)^c \qquad (5.3)$$

Table 5.2.　　Constant values for expression (5.3)

	Bottom wall			Top wall		
	a	b	c	a	b	c
χ_{break}	$0.26Eo_{\text{G}}^{0.60}$	0.41	0.41	$0.13Eo_{\text{G}}^{0.26}$	0.40	0.38
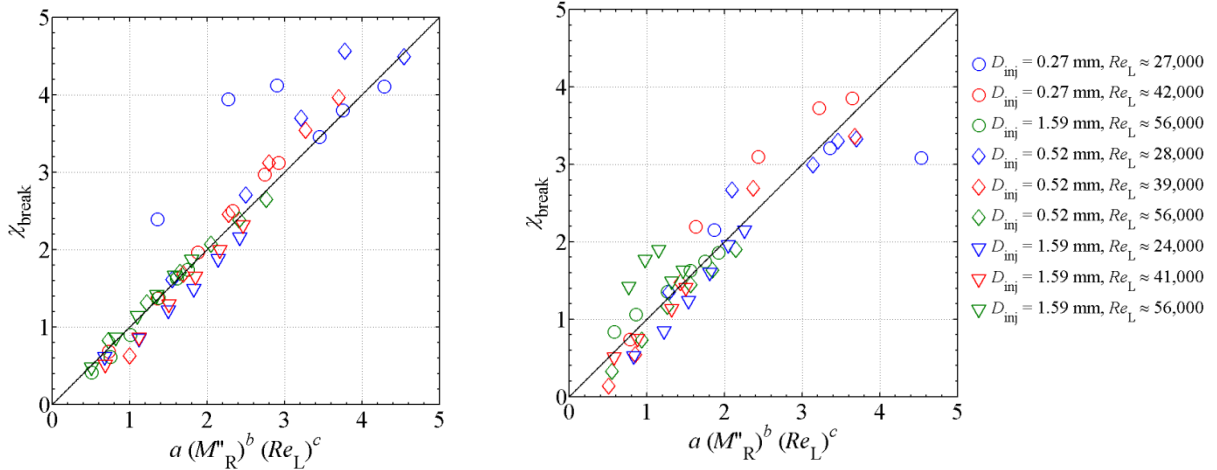
Figure 5.6.　　Estimation of the averaged dimensionless jet breakup location (χ_{break})

The averaged gas jet breakup correlations provided an accurate estimation of the position where detachment occurs. However, as was observed in Figure 5.5., at large M_{G} values the formation process becomes irregular and χ_{break} exhibits a broader spectrum, which reduces the accuracy of the empirical correlations. Hence, it was considered that a description of this phenomenon would be more precise by providing top ($\chi_{\text{break}}^{\text{upper}}$) and bottom ($\chi_{\text{break}}^{\text{lower}}$) limits to the ranges observed in Figure 5.5. Using the experimental data, correlations were proposed to delimit the boundaries, following a methodology similar to the one used for (χ_{break}). The coefficients obtained are

presented in Table 5.3 and can be substituted in equation 5.3 to estimate the maximum and minimum gas jet breakup length, which allows a better understanding of the expected χ_{break} range. The results obtained would yield accurately similar findings to those presented in Figure 5.6.

Table 5.3. Values used in the correlations for the estimation of upper and lower χ_{break} limits

	Bottom wall			Top wall		
	a	b	c	a	b	c
$\chi_{\text{break}}^{\text{upper}}$	$0.26Eo_{\text{G}}^{0.59}$	0.46	0.42	$0.16Eo_{\text{G}}^{0.23}$	0.42	0.36
$\chi_{\text{break}}^{\text{lower}}$	$0.23Eo_{\text{G}}^{0.60}$	0.35	0.39	$0.16Eo_{\text{G}}^{0.14}$	0.37	0.42

It was not possible to explore the validity of the proposed correlations under comparable operating and geometrical scenarios because of the scarcity of similar information in the literature. Although the occurrence of jetting formation in liquids has been shown by several authors, the focus has been on the identification of this regime. No information exists about the breakup point for this regime and, as previously discussed, most studies focus on the detachment location of individual bubbles.

5.6. Bubble detachment frequency

The bubbling frequency (f_{B}) was defined as the inverse of t_{growth}. The influence of the liquid dynamics, gas injection conditions and nozzle dimensions on f_{B} was evaluated. The results from this assessment were reported in Figure 5.7. For the vast majority of the scenarios, the higher bubbling frequencies were observed at lower M_{G} values. As the gas flow rate through the nozzle

increased, f_B diminished. Contrary to what occurs in discrete bubbling, it was inferred that under jetting conditions, an increase in M_G was associated to higher F_I, which caused the gas jet to grow and delayed bubble detachment. Therefore, f_B decreased. Also, it was observed that for similar M_G and U_L, the magnitude of f_B did not show marked variations with changes in D_{inj}, particularly for $U_L \approx 4.3$ m/s. which implied that even though the gas jet geometry was affected by the nozzle dimensions, f_B was not controlled by it.

For the same operational and geometrical configuration, f_B was not uniform, although it was located within a well defined interval. Similar to what occurs for gas jets in stagnant liquids (Weiland and Vlachos, 2013), the irregular formation process was attributed to the intrinsic unsteadiness of the gas injection mechanics when M_G induces a turbulent flow at the injector. Additionally, the existence of a turbulent liquid cross flow was considered as a contributing factor to the f_B variability. For each experimental case, a smoothed probability density estimate was used to determine the dominant bubbling frequency. Each reported f_B value represents the averaged frequency obtained from three individual cases at the same experimental conditions. A summary of the dominant f_B, along with the minimum (f_B^{min}) and maximum formation times (f_B^{max}) observed for $U_L \approx 2.0$ m/s can be seen in Table 5.4.
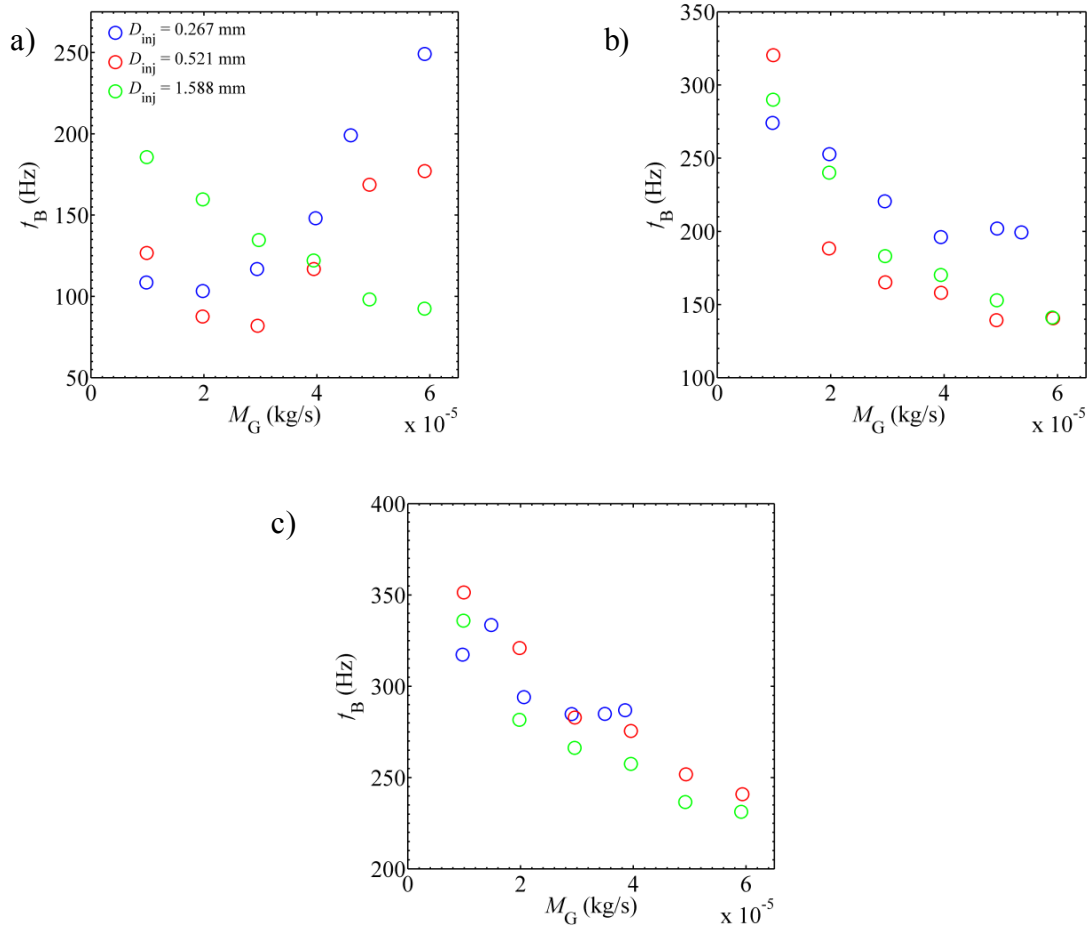
Figure 5.7. Effect of U_L, M_G and D_{inj} on the averaged frequency of bubble formation. a) $U_L = 2.0$ m/s, b) $U_L = 3.1$ m/s, c) $U_L = 4.3$ m/s

Table 5.4. Bubbling frequency range at $U_L = 2.0$ m/s

M_G	$D_{inj} = 0.27$ mm			$D_{inj} = 0.52$ mm			$D_{inj} = 1.59$ mm		
(kg/s x 10^{-6})	f_B^{min}	f_B	f_B^{max}	f_B^{min}	f_B	f_B^{max}	f_B^{min}	f_B	f_B^{max}
9.81	71	109	437	88	127	434	137	186	439
19.8	49	103	453	53	88	452	92	160	489
29.5	45	117	473	46	82	470	76	135	491
39.4	49	148	491	47	117	482	69	122	481
48.2	56	199	498	40	169	496	60	98	464
59.1	74	249	500	50	177	501	57	93	464

An interesting trend was noticed for D_{inj} = 0.27 and 0.52 mm when $U_L \approx 2.0$ m/s. Contrary to what was observed in the other configurations, when M_G was increased, f_B increased correspondingly, as was shown in Figure 5.7a. For D_{inj} = 0.27 mm, f_B had a pronounced slope, increasing rapidly from approximately 100 Hz up to 250 Hz. For D_{inj} = 0.52 mm, the slope experienced an initial decrease, as occurred with the other cases. However, after M_G exceeded 3×10^{-5} kg/s, f_B increased to 117 Hz and then up to 177 Hz at the end of the interval. The combination of low U_L and small D_{inj} translated into high M''_{ratio}, which allowed the gas plume to expand rapidly after injection. This caused a quick transition from an incipient jetting state towards an atomizing regime, where the bubble detachment occurs in an accelerated and unpredictable manner. Owing to the highly irregular breakup process, where the diameter of the separated bubbles has a wide distribution, f_B increased.

The measured f_B values showed a clear degree of dependence on U_L, M_G and D_{inj}. Following a methodology comparable to the one proposed for the experimental χ_{break} expressions, f_B was correlated to the same dimensionless parameters, with the added difference that the Eotvos number (Eo_G) was included in the correlations. The bubbling correlations were of the form given in expression (5.4), where f_{corr} represents the empirically determined bubbling frequency. The coefficients a_1 to a_4, are 8.75, -0.22, 0.26 and -0.58 respectively.

$$f_{corr} = a_1 \left(Fr_G \right)^{a_2} \left(Re_L \right)^{a_3} \left(Eo_G \right)^{a_4} \tag{5.4}$$

The measured f_B values were compared with the estimations obtained from correlation (5.4). The results, which were primarily valid for $U_L \geq 3.1$ m/s, were presented in Figure 5.8. The dotted lines represent a ± 20% deviation from the line that indicates a perfect correspondence between estimations and experimental data. As was observed, the majority of the values obtained from f_{corr} were located close to the line representing an exact correspondence with the measured values. The mean deviation between f_B and f_{corr} was 5.2%. The scatter of the predicted values was limited to -19.7% to +22.1%, which as observed occurred only on limited scenarios.

The results were compared with the expression presented by Iguchi *et al.* (1998). Although this expression produced satisfactory predictions of bubbling frequency in a cross-flow for the case study reported by the authors, when compared with the experimental data the difference with the experimental results where over +20% difference in a vast majority of the cases. The use of the expression proposed by Iguchi *et al.* (1998) indicated that f_B increased with an increase in M_G, which refers to the discrete bubbling case. It was inferred that the differences with the results of the current study could be created because of the different bubbling mechanics.
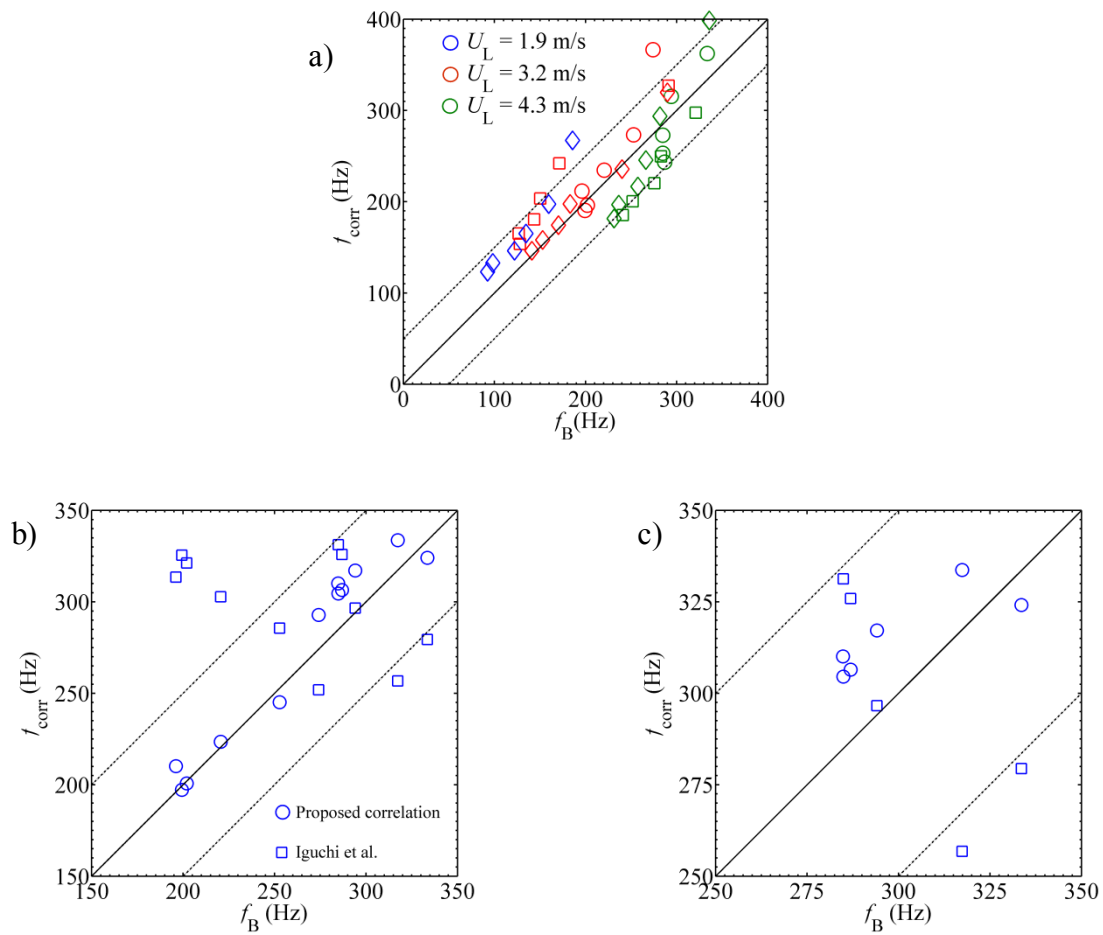
Figure 5.8. a) Comparison between experimental and correlation values for the bubbling frequency. Symbols: ○ D_{inj} = 0.27 mm, □ D_{inj} = 0.52 mm, ◊ D_{inj} = 1.59 mm. The contrast between the proposed correlation and the results obtained using the correlation proposed by Iguchi et al. (1998) was shown in b) U_L = 3.1 m/s and c) U_L = 4.3 m/s

5.7. Final Considerations

The force assessment during the gas jet evolution in a liquid cross-flow was conducted. This led to recognize which forces exert a dominant influence on the incipient gas jet. With a thorough understanding of the relevant parameters, it was possible to obtain empirical correlations that approximate within acceptable levels the dominant bubbling frequency and the averaged gas jet breakup location. A summary of the relevant observations obtained is presented next.

* The dominant forces were the inertial force (attaching) and the drag force (detaching). The forces in the horizontal direction were at least one order of magnitude higher than the ones in the vertical direction.

* Although the position of the gas injector, modifies the way that the buoyancy force acts on the gas jet, its magnitude was not considered relevant when compared to the inertial and drag forces. However, its contribution is minimal as the highest magnitude of F_B represents only 12% of the magnitude of F_{SL}.

* The combination of liquid cross-flow velocity, gas mass flow rate and nozzle diameter (or associated variables) decided the bubbling frequency and gas jet breakup location. No variable exerted an influence dominant enough as to disregard the others.

* When the liquid velocity diminished, the gas jet breakup location diminished as well. An increase in the liquid velocity also increased the bubbling frequency. Whenever possible, increasing the liquid velocity is recommended to obtain a higher bubbling frequency and smaller gas jets.

* An increase in the gas mass flow rate led to an increase in the inertial forces; hence the gas jets had enlarged volumes. This was more noticeable for smaller nozzle diameters.

* The gas jet breakup location was not regular. Instead it occurred within well defined ranges, which could be determined from the empirical correlations proposed. These expressions were a

first attempt to categorize this phenomenon and need further validation under different experimental conditions. However, they provided an accurate estimation of the region within the conduit where the gas jet disintegration occurs.

* Experimental correlations that estimate the bubbling frequency for $U_L \geq 3.0$ m/s were obtained. Limited expressions that determine the bubbling frequency were found and the existing ones refer to scenarios that do not take into account the possibility of gas jets and refer only to discrete, round bubbles. Hence when compared with the experimental data showed limited agreement. The proposed expressions constituted a novel approach to estimate the bubbling mechanics of gas jets in a cross flow.

* It was found that the F_τ was only a small portion of the magnitude of F_D. During the initial stages of the gas jet growth, F_τ was approximately equal to $0.25 F_{Dx}$. As the gas jet expanded, this ratio decreased. It was also found that as U_L increased, the influence of F_τ as a detaching force increased correspondingly, being equal to 8.8%, 10.4% and 12.7% of F_{Dx} for $U_L = 2.1, 3.1$ and 4.3 m/s respectively.

6. Flow characteristics upstream of the discharge nozzle and their link to the bubbling conditions

6.1. Background

As was discussed in Chapter 1, most studies investigating the internal flow in an effervescent atomizer focus on the visualization of the flow patterns inside the mixing chamber and transition between regimes (Ferreira *et al.*, 2001; Kim and Lee, 2001; Huang *et al.*, 2008; Jedelsky and Jicha, 2008; Ramamurthi et al., 2009). Varied degrees of success have been obtained in relating the external flow behavior with the flow pattern conditions inside the atomizer conduit (Buckner and Sojka, 1991; Chen and Lefevbre, 1994). Rahman *et al.* (2012) showed that the droplet diameter exhibits a dependence on the size of the bubbles upstream of the discharge nozzle.

A wealth of knowledge exists on the mechanics of bubble formation and the bubble evolution in closed conduits (Kulkarni and Joshi, 2005); however they were mostly developed for more basic processes unrelated to effervescent atomizer mechanics. The existing correlations for the prediction of the bubble size (Lefevbre, 1996; Forrester and Rielly, 1998) cannot be applied directly to effervescent atomizers, owing to the transient, accelerating nature of the flow inside them (Chin and Lefevbre, 1995).

The abovementioned works lead one to infer that for effervescent atomizers the bubbling conditions play a major role on the flow characteristics upstream of the nozzle, which influence

the external fluid mechanics of the effervescent atomizer (Chin and Lefevbre, 1993; Jedelsky and Jicha, 2006; Rahman *et al.*, 2012). Also, no studies exist on bubbling mechanics inside an effervescent atomizers and the link with the two-phase flow characteristics upstream of the nozzle.

The aim of this work is to explore the link between the gas injection process (Region I in an effervescent atomizer, Figure 1.1) and the nature of the flow upstream of the nozzle, by means of experimental visualization (Region III, Figure 1.1). Specifically, the morphology of the gas jet near the aerator will be studied and its influence on the bubble population distribution and geometry upstream of the discharge nozzle will be assessed. The maximum bubble diameter after detachment ($D_{99\ inj}$) will be correlated with the maximum bubble diameter upstream of the nozzle ($D_{99\ nozzle}$).

Also, the influence of the geometrical and operational bubbling conditions on the two-phase flow upstream of the nozzle will be evaluated. Flow features such as void fraction and bubble diameter distribution upstream the discharge nozzle were determined (Region III, Figure 1.1). Downstream processes have a strong dependency on the mechanisms inside an effervescent atomizer; it is clear that a meticulous analysis of the internal flow region will result in a better understanding of its performance.

6.2. Void fraction analysis

6.2.1. Local void fraction

The relationship between the α_{local} curves after bubble detachment and those observed upstream of the discharge nozzle are shown in Figure 6.1. The effects that the M_G and D_{inj} geometry have on the void fraction distribution along the channel were represented as well. A general assessment of the results depicted indicates how, for the same U_L and M_G quantities, the D_{inj} dimensions play a fundamental role on the gas-liquid distribution along the spanwise direction.
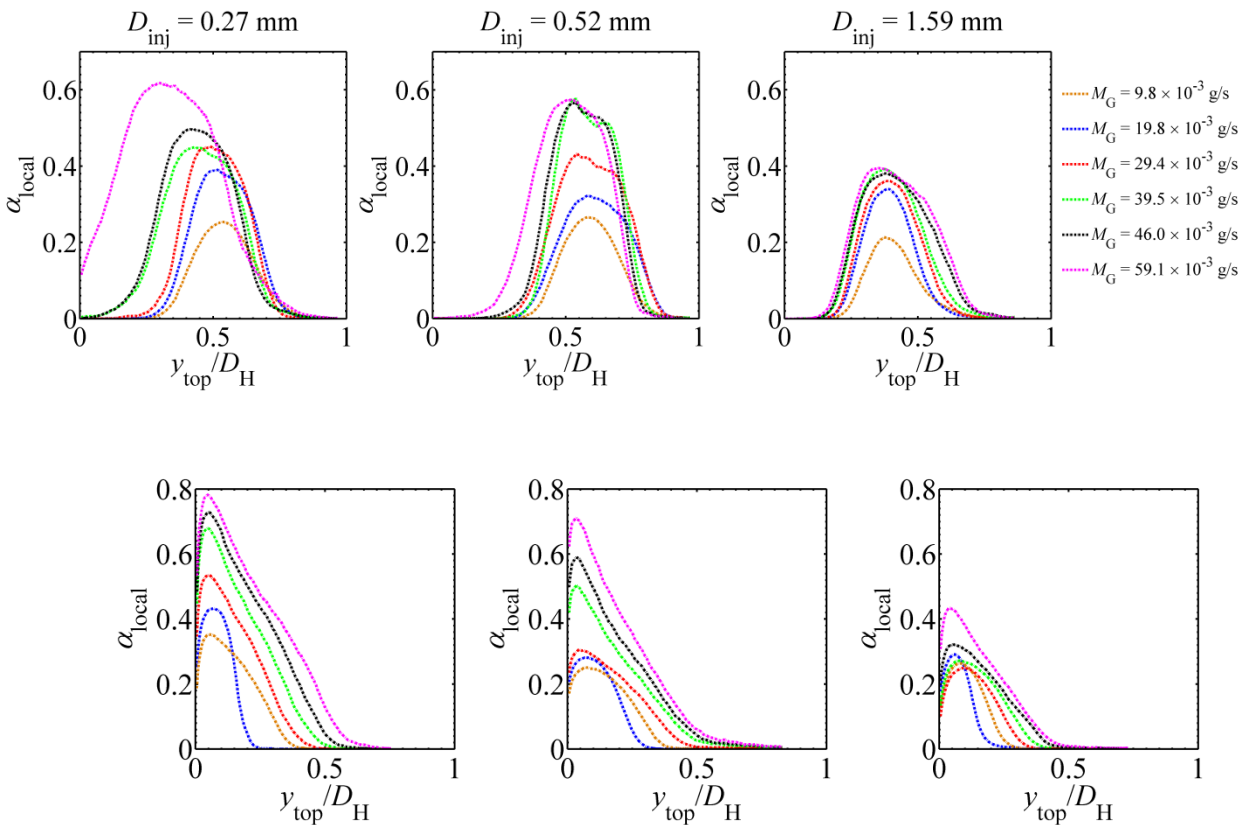
Figure 6.1. Comparison between the α_{local} curves at a distance $x/D_H = 4$ downstream the gas injector (top row) and $x/D_H = 2$ upstream of the entrance to the discharge nozzle (bottom row). The results correspond to $U_L = 1.9$ m/s and bottom wall injection

At the lowest M_G, the α_{local} curves near the gas injector had markedly similar behavior, independent of the D_{inj} used. In all cases, the maximum α_{local} was approximately similar to 0.21, and was located near the middle of the channel. However, for the smallest D_{inj}, 0.27 mm, the curve occupies a slightly broader vertical range than the one measured for the other nozzle geometries. For increasing values of M_G, this tendency is preserved.

The location of the injector in the bottom wall causes the α_{local} peaks to be positioned near the geometric center of the channel, between $y/D_H = 0.40$ and $y/D_H = 0.60$. The exception to this fact is $D_{inj} = 0.27$ mm and $M_G = 59.1 \times 10^{-3}$ g/s, where the max α_{local} value was found at $x/D_H \approx 0.30$. Owing to the combination of a high M_G and small D_{inj}, the conditions at the injection induce the formation of Taylor-like bubbles. It was inferred that this is the cause of the marked differences in the void fraction curve for these particular conditions.

The two-phase flow development up to the discharge region caused the buoyancy driven displacement of the gas phase towards the top channel wall, similar to what occurs in standard gas-liquid flow in horizontal pipes (Andreussi et al., 1999). The α_{local} tendencies after bubble detachment, as a function of the D_{inj}, had an obvious influence on the two-phase flow behaviour upstream the discharge nozzle. At both locations the maximum values were produced for the smallest D_{inj}. In general, for each experimental configuration, the α_{local} curves changed from maxima primarily located at $y/D_H \approx 0.50$ to void fraction maxima found at $y/D_H \approx 0.05$, causing a noticeable change in the shape of the void fraction distribution curve.

The results indicate that, under equal experimental conditions, a small D_{inj} causes higher gas dispersion as well as α_{local} magnitude in the conduit than that obtained for larger D_{inj} geometries. This was attributed to the fact that a small D_{inj} translated in higher inertial forces for the gas jet, which caused the formation of large gas bubbles. Due to the short residence time of the bubbles in the conduit before reaching the discharge nozzle, stable particle breakup conditions due to the effects of the liquid cross-flow was not possible. The results indicate how the conditions under which the bubbles were formed still have a strong effect on the void fraction distribution upstream the discharge nozzle.

As M_G increased, the α_{local} values along y_{top}/D_H increased proportionally. This indicated a higher dispersion probability of the gas phase along the vertical direction. The diameter of the bubbles in the conduit grows as U_{SG} increases. Hence, increasing the area occupied by the dispersed phase and the magnitude of α_{local} along the span wise direction. This was an expected result, due to the physics of two-phase flows.

6.2.2. Area void fraction

As was discussed previously, the orientation of the gas injector severely influences the gas phase distribution along the channel. Figure 6.2a displays the differences between the gas phase probability distribution in a region which encompasses the span-wise length of the channel at a distance 50 to 80 mm downstream the gas injector. Under equal experimental conditions, the lines indicate that top wall injection produces slightly higher α_{area} values than those obtained for bottom wall injection.

These differences, which were in average 1.8% between the two trends, were attributed to the effects of the buoyancy forces during the bubble formation process. The density difference between the phases caused the agglomeration of the gas phase near the top wall. It was deduced that this induced the formation of bubbles whose diameter is slightly higher than those produced from bottom injection. It also delayed the possibility of bubble breakup and therefore creating the differences in the averaged void fraction values observed (Hesketh *et al.*, 1991; Andreussi *et al.*, 1999). A contrast in the gas probability distribution between the two injector orientations was presented in Figure 6.2b, where it is clearly depicted the slightly higher gas concentration values caused by top wall injection.
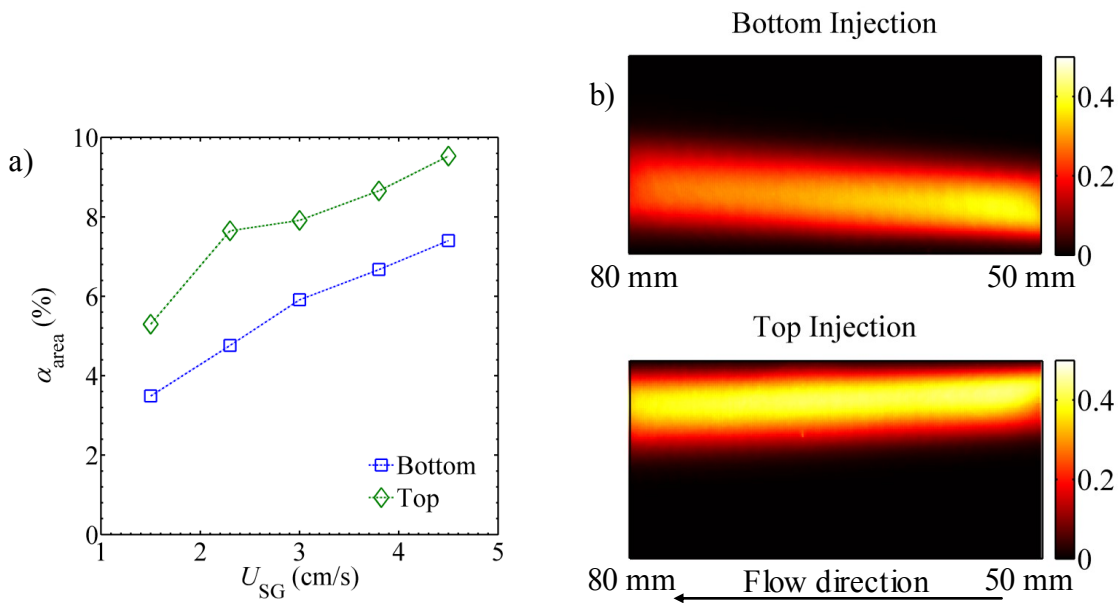
Figure 6.2. a) Effect of the injector location on α_{area} for U_L = 4.3 m/s and D_{inj} = 1.59 mm. b) Contrast between the phase probability contour for bottom and top wall injection. U_L = 4.3 m/s, D_{inj} = 1.59 mm and $U_{SG} \approx$ 4 cm/s

The α_{area} values in the vicinity of the injector region (bottom wall injection) were compared to the averaged void fraction upstream of the discharge nozzle. The results are reported in

Figure 6.3a and show the fractional α_{area} variations experienced by the two-phase flow during its evolution between the two locations. The trend indicates that for all U_{SG} values tested, the α_{area} values at the nozzle location have slightly lower magnitudes than those measured at the injector location. The void fraction differences between the two locations were attributed primarily to the combined effects of the liquid cross-flow induced bubble breakage and the gas stratification.

As the gas-liquid flow transitions towards the nozzle region, the initial bubbles separate into smaller particles. Simultaneously, the dispersed phase migrates towards the top wall. When reaching the upstream nozzle area, all the bubbles are already in the upper channel region, causing the agglomeration of smaller bubbles, the reduction of the gas phase dispersion and diminishing of the area-based void fraction. The results shown in Figure 6.3b indicate a higher concentration of the gas phase on a narrower region than what was measured in the injector area, which causes smaller α_{area} values before the gas-liquid flow is discharged.
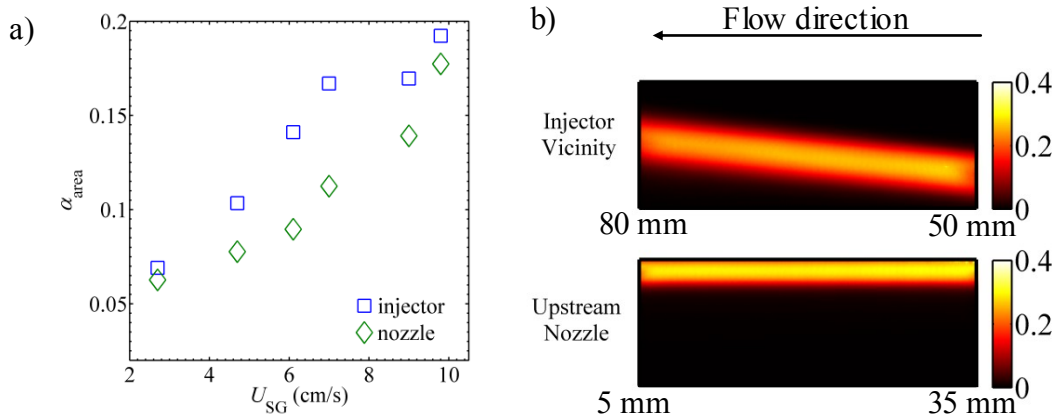
Figure 6.3.   a) Comparison between the α_{area} values at the injector and nozzle locations as a function of U_{SG} for $U_{\text{L}} = 1.9$ m/s and $D_{\text{inj}} = 0.52$ mm. b) Phase probability contour at the injector bottom and upstream the nozzle. $U_{\text{L}} = 1.9$ m/s, $D_{\text{inj}} = 0.52$ mm and $U_{\text{SG}} \approx 4$ cm/s

It was expected that, for the same U_L and geometrical configuration, increasing M_G would cause an increase in the percentage of the conduit area occupied by the gas phase. Figure 6.4 represented how M_G affects the time averaged probability of the dispersed phase for $U_L = 1.33$ m/s and $D_{inj} = 1.59$ mm. The contours encompassed a region between 5 and 35 mm upstream of the entrance to the discharge nozzle. The contour plot indicates how before the two-phase flow passes through the nozzle, it achieves a more uniform void fraction profile.
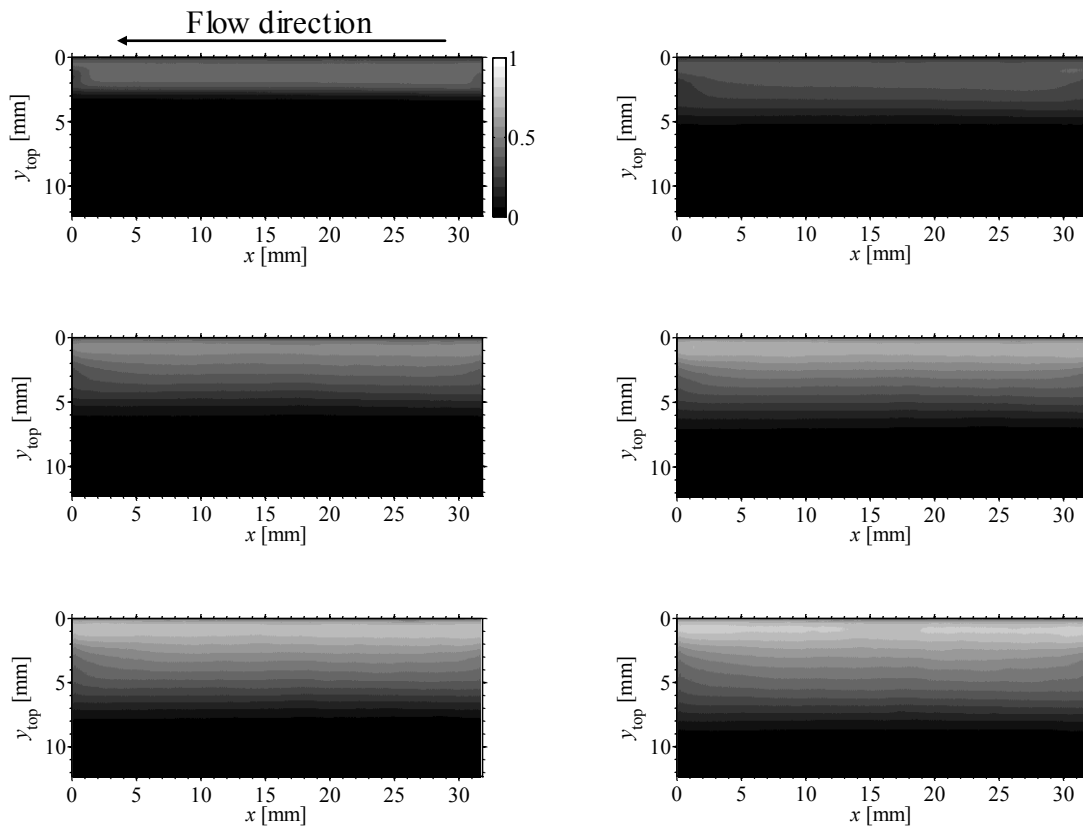
Figure 6.4.   Contour diagrams depicting the gas-liquid distribution between 5 to 35 mm upstream the discharge nozzle (approximately $40D_H$ downstream the injector). Left to right, top to bottom: $M_G = 9.8$, 19.8, 29.6, 39.1, 49.3 and 58.9×10^{-3} g/s. $D_{inj} = 0.59$ mm, $U_L = 1.3$ m/s

6.3. Gas jet and bubble diameter analysis

6.3.1. Gas jet morphology

The averaged dimensionless gas jet diameter (D_{equiv}/D_H) is defined as the mean value of an array of gas jet events, involving the growth and detachment cycle for a set of conditions. D_{equiv}/D_H describes the averaged equivalent diameter of the gas jet for a minimum of 250 expansion-disintegration cycles, considering the variation of the diameter between the minimum D_{equiv} (right after breakup) and maximum D_{equiv} (before disintegration occurs). This geometric length scale provided a proper characterization of the gas jet development. The scaling of D_{equiv} with the gas jet Froude number (Fr_G), injection diameter (D_{inj}), liquid cross-flow Reynolds (Re_L), and gas injector orientation on the averaged gas jet diameter was explored. Figure 6.5 presents a comprehensive review of the abovementioned variables, showing their effect on D_{equiv}/D_H.

The results showed that an increase in the Fr_G increases the D_{equiv}/D_H. For equal values of M_G injected through the nozzle; the use of a small D_{inj} resulted in a high U_G, and consequently in a high gas jet inertia. As the gas jet inertial forces grew in strength, both the minimum D_{equiv} (right after detachment) and maximum D_{equiv} (before bubble disintegration) increased. Hence, any related geometrical variables increased as well, implying that the gas jet expands further within the conduit before experiencing bubble separation. These findings exhibited analogies with the behaviour reported by Harby *et al.* (2014), where the geometric length scale of submerged gas jet increases with Fr_G for all D_{inj}.
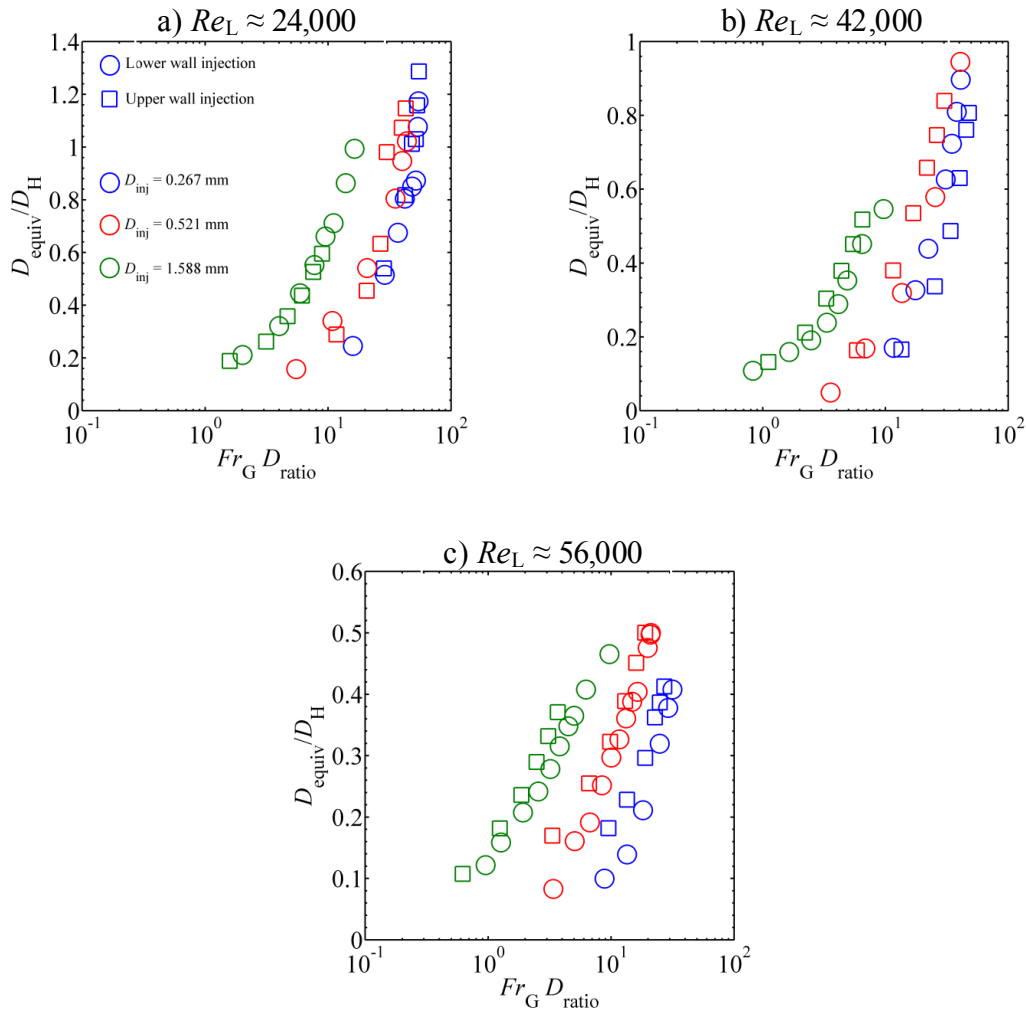
Figure 6.5.   Averaged dimensionless gas jet equivalent diameter versus the modified Froude number. a) $Re_L \approx 24,000$. b) $Re_L \approx 42,000$. c) $Re_L \approx 56,000$

Theoretically, the position of the gas nozzle, in either the upper or lower wall, causes differences in the buoyancy force, which acted as an attaching or detaching force based on the D_{inj} location. For upper wall injection (square symbol), D_{equiv}/D_H displayed slightly higher values than those measured for near wall injection (circle symbol). Despite the differences in D_{equiv}/D_H based on the injector location, for different gas injector orientations the D_{equiv}/D_H curves had very similar trends, which collapsed quite well unto each other under comparable Fr_G values, as indicated by a mean difference of 9.2% between them for all operational conditions tested. Other than the

effect of the buoyancy, the differences were attributed to the gas jet-wall interaction, which clearly played a role for far wall injection while being negligible for lower wall injection.

The liquid cross flow velocity also played a fundamental role in the evolution of the gas jet due to the combined effect of the momentum and turbulence. A low Re_L promotes the expansion of the gas jet. As expected, the highest dimensionless D_{equiv} were observed at Re_L = 24,000, where the gas jet could grow up to 1.2 times D_H. If the $Fr_G D_{ratio}$ value was kept constant, a continuous Re_L increase counteracted the expansion of the gas jet, resulting in decreased dimensions, as shown in Figure 6.5. At $Re_L \approx$ 56,000, D_{equiv}/D_H diminished by an approximate of 21% and 48% when compared to the lower Re_L magnitudes of 24,000 and 42,000 respectively.

Based on the behaviour exhibited by the averaged gas jet equivalent diameter and the operational and geometrical variables involved, a power-law based empirical correlation was developed. This relationship, expressed in equation (6.1), reproduced the physical implications of the studied variables in the morphology of the gas: An increase in Re_L reduced the gas jet dimensions whereas increasing Fr_G caused the expansion of the jet. Since D_{equiv}/D_H was found to be dependent on the gas nozzle diameter, its effect was also included in the correlations in the form of Eo_G. A slightly higher value of k_1 for upper wall injection was expected due to the small differences observed behaviour based on the position of the gas injector.

$$D_{equiv} \Big/ D_H = k_1 \left(Re_L^a \right) \left(Fr_G \right)^b \left(Eo_G \right)^c \qquad (6.1)$$

Table 6.1. Coefficient values for D_{equiv}/D_H correlation

Injector location	a	b	C	k_1
Lower wall				9.82
	-0.52	0.84	0.81	
Upper wall				9.18

Figure 6.6 presents the comparison between the values estimated by equation (6.1) and the experimental results. As shown, the correlations exhibit an acceptable level of certainty for D_{equiv}, given by the coefficient of determination values $R^2 = 0.94$ and $R^2 = 0.91$ for bottom (Figure 6.6a) and top (Figure 6.6b) wall injection respectively. The discrepancies between results and predictions were relatively small, around 2-7% at low D_{equiv} values. For D_{equiv}/D_H higher than 0.6, the scatter increased. Some outlier points over-predicted the gas jet diameter up to 25%. These percentual differences represent the mean absolute error between estimations and experimental results as defined by Chai and Drexler (2014).
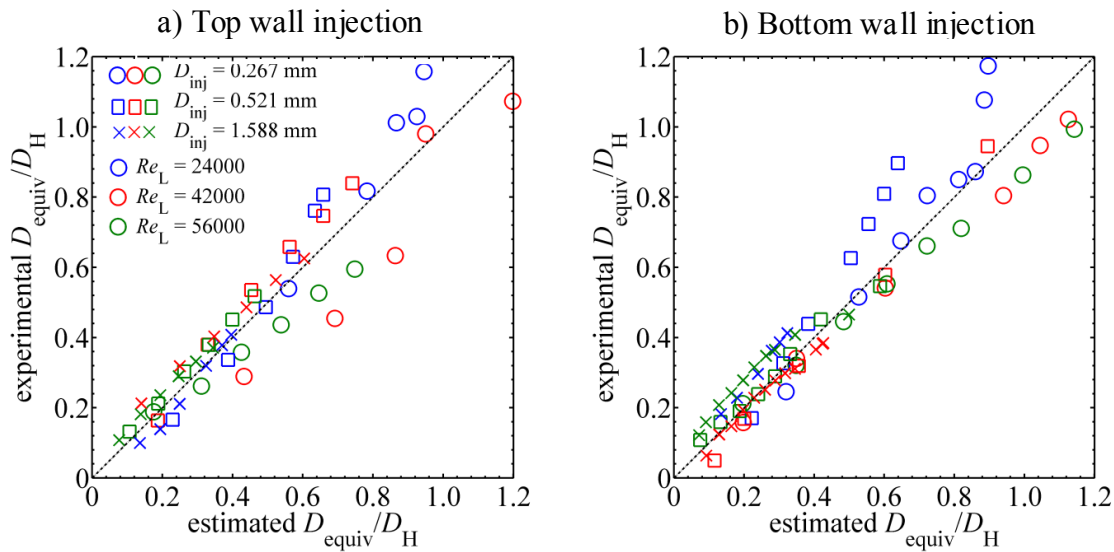
Figure 6.6. Contrast between the gas jet estimated from correlation (6.1) and the experimental data for: a) Top wall injection. b) Bottom wall injection

The higher variations were primarily observed at high Fr_G values and the lowest Re_L values, where the differences between the min-max values D_{equiv} of the gas jet exhibit a wide range, as was described in Section 5.3. This stochastic behaviour is inherent to gas injection in a liquid, where the turbulence of the gas phase and natural interphase instabilities cause less predictability of the gas jet morphology (Loth and Faeth, 1990; Harby *et al.*, 2014). Despite the higher turbulence intensity, when Re_L is increased, the liquid cross-flow momentum decreases the naturally unsteady break-up frequency of the turbulent gas jet, reducing the discrepancies between predictions and results.

6.3.2. Gas jet dimensions and its implications in the bubble diameter after detachment

The gas jet has a quasi-periodic behaviour, given by its continuous growth up to the point where bubble detachment occurs thanks to the influence of the liquid cross-flow. As demonstrated in the previous section, the operational and geometrical variables regulate the gas jet dimensions. The aim of this section is to determine the link connecting the growing gas jet dimensions and the diameter of the recently detached bubbles. Given the time-dependent nature of the gas injection phenomena, the bubble diameters were obtained statistically.

The association between the dimensionless D_{equiv} and D_{32} was represented in Figure 6.7, where D_{32} refers to the diameter of the main detached bubbles. The effects of D_{inj} and Re_L in the gas jet-bubble dynamics were also taken into consideration. D_{32} was made dimensionless by using D_H. It was found that as the gas jet became larger, the bubble diameter increased correspondingly,

following a linear correlation with D_{equiv}. This was an expected result because large gas jets counteract the liquid cross-flow effects for a longer time than smaller jets, allowing further expansion into the conduit and inducing the formation of higher D_{32} bubbles. It was also observed that as Re_L increased, D_{32}/D_H decreased correspondingly. For equal D_{equiv}/D_H values, an increase in Re_L from 24,000 to 42,000 caused an average decrease in D_{32}/D_H of approximately 15%. Similarly, incrementing Re_L from 42,000 to 56,000 incurred in a decrease of the dimensionless D_{32} of 22%. This was a likely outcome because a strong liquid cross-flow mitigates the expansion of the gas jet, causing premature gas jet disintegration and a smaller size for the detached bubbles.
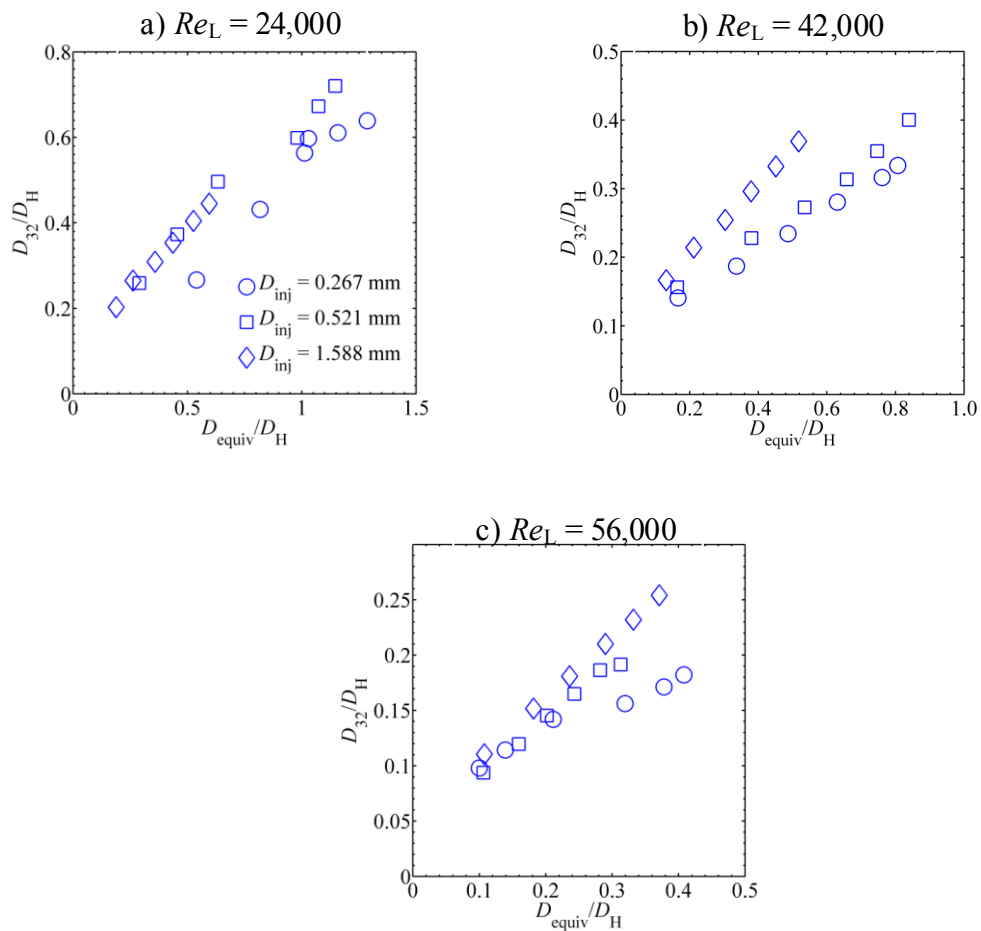
Figure 6.7.   Link between the averaged gas jet equivalent diameter and the dimensionless Sauter mean diameter as a function of Re_L and D_{inj}

For equal Re_L and D_{equiv} values, using the smallest D_{inj} produced a small D_{32}. For a large D_{inj}, the diameter of the detached bubbles became closer to that of the gas jet. Based on the linear correlation exhibited by the variables, the slope variation for each D_{inj} as a function of Re_L was presented in Table 6.2, where the reported value corresponds to the average slope k_2 obtained from a linear fit along with its associated error k_3. The results indicated that increasing Re_L reduces the correspondence between D_{32} and D_{equiv}. For the smaller D_{inj}, these variations were significant as indicated by a percentage decrease in k_2 approximately equal to 40 and 50% for $Re_L = 42,000$ and 56,000 respectively.

Table 6.2. Coefficients for the linear correlation
$D_{32}/D_H \approx k_2(D_{equiv}/D_H) + k_3$

| | D_{inj} (mm) | | | | | |
| | 0.27 | | 0.52 | | 1.59 | |
Re_L	k_2	k_3	k_2	k_3	k_2	k_3
24,000	0.50	0.11	0.53	0.06	0.58	0.10
42,000	0.30	0.08	0.35	0.08	0.52	0.10
56,000	0.25	0.08	0.27	0.04	0.54	0.05

It was observed that for changes in Re_L, the decrease in the k_2 coefficient for $D_{inj} = 1.59$ mm was almost negligible and had an average value approximately equal to 0.56. This indicated that for large nozzle geometries, the gas jet expansion decreased and a larger percentage of the gas jet would detach from the nozzle, resulting in bubble diameters with similar dimensions to those of the gas jet; hence a steadier and more predictable bubble formation regime. It was inferred that a small D_{inj} results in premature bubble detachment, where the bubbles break from the main gas core before achieving full expansion. Additionally, the effects of an enhanced gas jet momentum caused by the use of smaller nozzle geometries were considered as a contributing factor in the reduction of the averaged D_{32}. Lastly, an increase in Re_L decreased the disturbance of the D_{32}

correlation, represented by k_3. This was an additional and expected indication that an increase in the crossflow momentum induces a more stable bubble generation.

6.3.3. Maximum bubble diameter after detachment

The extent of the bubble diameter after detachment, and the influence of the evolving gas jet on this behaviour were observed. The maximum bubble diameter (D_{99}) was determined statistically and it was defined as the diameter where 99 percent of the population lies below this value. The maximum bubble diameter (D_{max}) was defined as the diameter of the largest measured bubble (D_{max}) within the conduit, based on the number distribution. The percentage differences between D_{99} and D_{max} were not greater than 10%. Therefore, D_{99} was considered as an adequate choice to represent the maximum bubble size.

The variation of D_{99} as a function of the gas jet equivalent diameter, the gas nozzle geometry and the liquid cross flow strength were represented in Figure 6.8. The results shown refer to diameter after the gas jet breakup occurs; that is in the detachment region as defined in Chapter 2. It is clear that the higher D_{equiv} is, the more likely it is to observe higher D_{99} diameters inside the mixing chamber. This was an expected conclusion since a larger average gas jet diameter is formed when the detaching gas forces allow the expansion of the gas plume into the conduit, delaying gas jet disintegration and resulting in the breakup of larger gas structures. This corroborates the findings presented in Section 6.3.2 which indicate a direct link between the gas jet geometry, represented by the averaged dimensionless D_{equiv} and the bubble size in the vicinity of the detachment area.
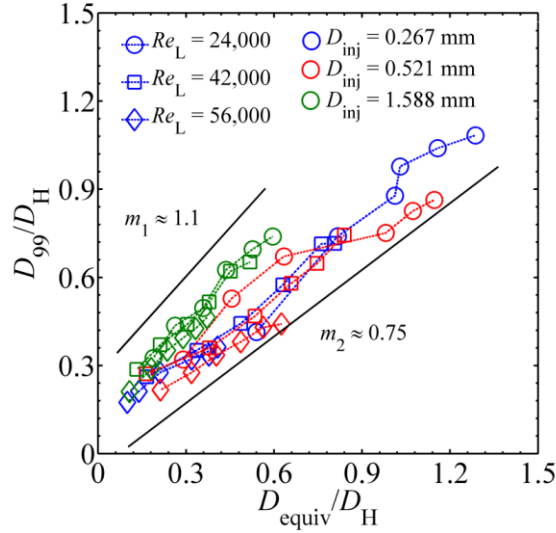
Figure 6.8.   Effects of D_{inj} and Re_L on the relationship between D_{equiv} and D_{99} near the injector region

The results in Figure 6.8 indicated that the dimensionless D_{99}/D_H values were encompassed between $0.75D_{equiv}/D_H$ and $1.1D_{equiv}/D_H$. When large nozzle geometries were used, the maximum bubble diameter is approximately similar in magnitude to the mean gas jet diameter values, as given by the slope lines, $m_1 \approx 1.1$. Physically, this meant that due to the decreased penetration of the gas jet, the growth and detachment process was more likely to lead to a full detachment of the gas jet. For smaller D_{inj}, the trends inclined towards the lower limit, $m_2 \approx 0.75$, which implied that the gas jet inertial forces oppose a full detachment and after the gas plume achieves full expansion, a small neck and gas core remain attached to the nozzle after breakup occurs.

As occurred with D_{32} and D_{equiv}, it was found that an increase in Re_L resulted in a decrease of D_{99}, independent of the nozzle geometry used. This was an anticipated outcome and was considered a consequence of the behaviour observed for previous bubble or gas jet features. A high Re_L reduced the expansion of the incipient gas jet in the conduit, which leads to a general

decrease of the detached bubble diameter, which includes D_{99}. Hence, a decrease in D_{99} was directly correlated with a decrease in D_{equiv}. Even though Re_{L} is a key parameter in the evolution of the gas jet core, under different Re_{L} values, the D_{99} versus D_{equiv} trend lines converge towards similar slopes, indicating that the incipient D_{99} depends primarily on the behaviour of the D_{equiv}.

The comparison between D_{99} and D_{32} after detachment was introduced in Figure 6.9. The evaluation involved the three D_{inj} tested under similar Re_{L} conditions. It is evident that for each Re_{L} case, the curves for the three nozzle geometries collapse unto each other, which indicated that the D_{99}/D_{32} ratio was possibly invariant with changes of D_{inj}. The results obtained were within acceptable levels to those reported for other bubbly flow systems, where the ratio D_{99}/D_{32} had values that were in the range of 1.67 to 3.33 (Razzaque *et al.*, 2003). Hesketh *et al.* (1987) found that D_{99}/D_{32} was approximately equal to 1.61, as obtained from a log-normal distribution approach. This finding indicates that under specific operational and geometrical conditions, data about D_{99} can be used to estimate a matching D_{32}, which is a key variable in the design of effervescent atomizers.

Variations of Re_{L} produced a small increase of the D_{99}/D_{32} ratio, from 1.51 at $Re_{\mathrm{L}} = 24{,}000$ to 1.80 at $Re_{\mathrm{L}} = 56{,}000$. Also, the range for both dimensionless D_{99} and D_{32} decreased for increasing Re_{L}. The underlying physical implications of these results suggest that two joint mechanisms are acting simultaneously to produce this effect. First, at high velocities, the liquid flow has a higher turbulent dissipation (ε), as given by the approximation $\varepsilon \sim U \quad D$. Under this high energy state, the continuous gas jet experiences a decreased expansion, breaks up more frequently, leading to a skew of D_{32} towards the minimum bubble size, causing the observed

increase of D_{99}/D_{32}. The second effect was the increased turbulence intensity for high U_L. The stronger liquid turbulence intensity contributes to a more random bubble detachment and a less uniform detachment size. Table 6.3 summarizes the empirical correlations that link D_{32} after with D_{99}, where the coefficient k_5 refers to the averaged error obtained from the expressions for each Re_L tested. As Re_L increased, the magnitude of the uncertainty diminished considerably.
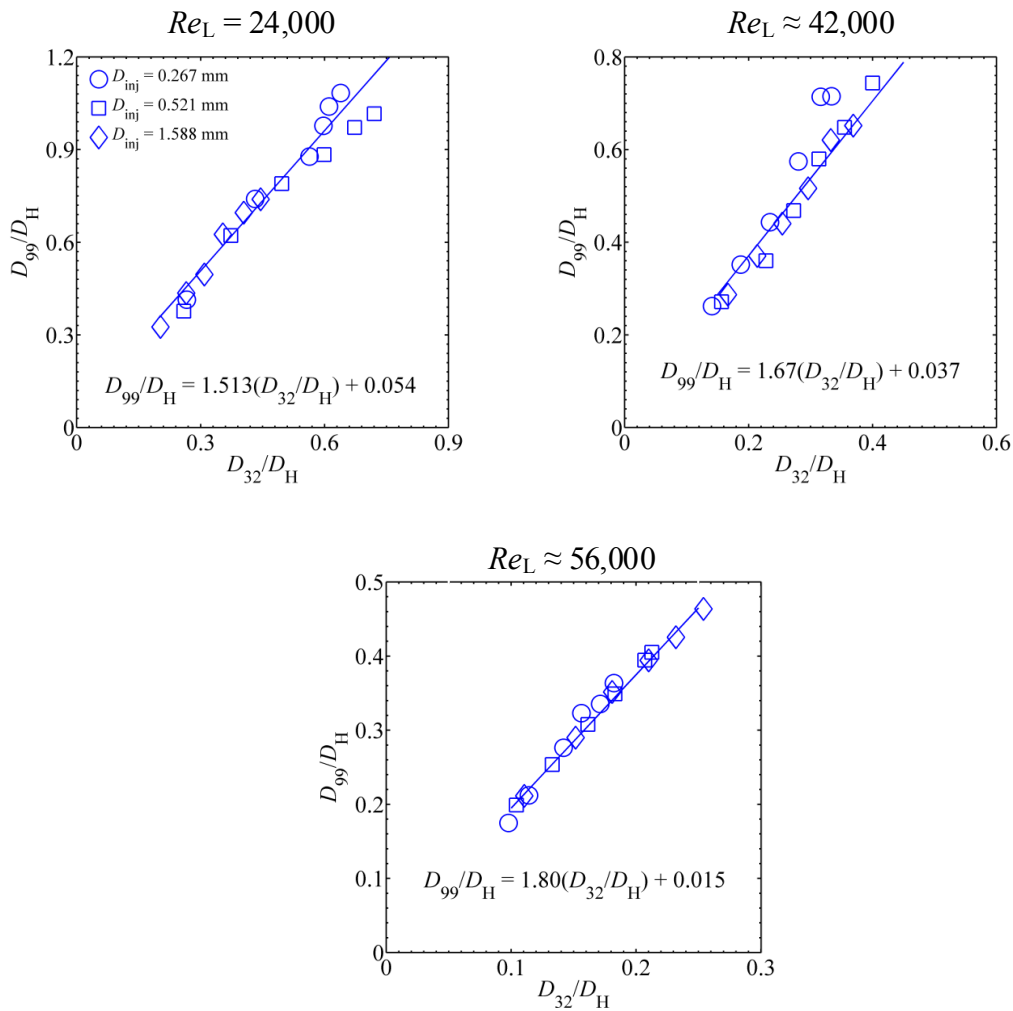
Figure 6.9.   Influence of Re_L and D_{inj} on the D_{99}/D_{32} ratio of bubble distribution functions near the gas injector

Table 6.3. Estimated values for the coefficients used in the linear correlation between D_{99} and D_{32}

$$D_{99}/D_H \approx k_4(D_{32}/D_H) + k_5$$

	Re_L		
	24,000	42,000	56,000
k_4	1.51	1.67	1.80
k_5	0.054	0.037	0.015

When combining the results from Tables 6.2 and 6.3, an experimental methodology to estimate D_{99} after bubble detachment as a function of the key dimensionless variables was proposed. This methodology considered that D_{99}/D_H was proportional to $0.9D_{equiv}/D_H$, based on the results of Figure 6.8. The results obtained from this approach are shown in Figure 6.10. The dimensionless D_{99}/D_H values, as a function of U_{SG}, were compared to the semi-empirical equation presented by Hesketh *et al.* (1987), Equation (6.2), where We_{crit} refers to the critical Weber number under which a bubble could maintain its volume before being subjected to breakup. It has been assigned a value between 1.05 and 1.10 (Andreussi *et al.*, 1999). The methodology is described next:

* Estimate the correlation between D_{99}/D_H and D_{32}/D_H (Table 6.3).

* Substitute the value of D_{32}/D_H into the appropriate value from Table 6.2. This step establishes a relation between D_{99}/D_H and D_{equiv}/D_H.

* Use equation (6.1) to determine D_{99}/D_H as a function of the fundamental dimensionless number Re_L, Fr_G and Eo_G. In this way it is possible to estimate the dimensionless D_{99} that can be observed in the mixing chamber of the atomizer in the region after the gas disintegration occurs.

$$D_{99} = 1.38 \left(We_{\text{crit}} \right)^{0.6} \left(\frac{\sigma^{0.6}}{\left(\rho_L^{0.3} \rho_G^{0.2} \right) \mu_L^{0.1}} \right)^{b} \left(\frac{D_H^{0.5}}{U_L^{1.1}} \right) \qquad (6.2)$$
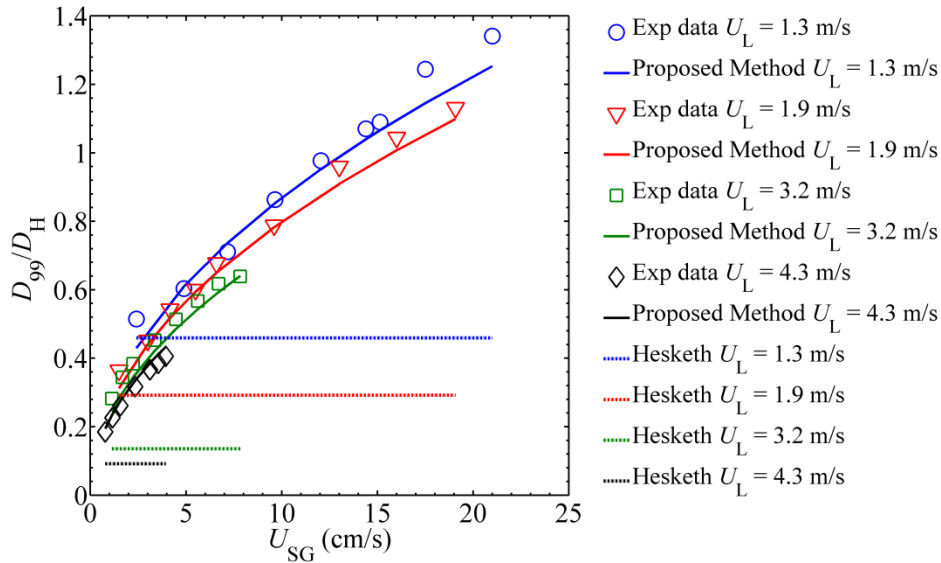
Figure 6.10.   Comparison between the correlation proposed by Hesketh et al. (1987) and the experimental results for $D_{\text{inj}} = 0.27$ mm

Equation (6.2) was developed following theoretical principles of bubble breakup. However, a simple assessment of the terms involved, indicates that it does not take into consideration that influence of the gas mass flow rate or superficial velocity on the diameter of the bubbles formed. While this does not constitute a fundamental issue for pipe flow, this is not the case for effervescent atomizers. As has been established in this work, the entrance conditions are of key importance for the bubbly flow morphology upstream of the discharge nozzle and more so for the incipient bubbly flow after the injector.

The results obtained in Figure 6.10 indicated that, despite its applicability for pipe flow analysis, Equation (6.2) does not provide an accurate estimation of the maximum bubble diameter

measured for the current application. Primarily, it does not take into account the variations in D_{99} created by an increase in or decrease in U_{SG}. As was shown in Figure 6.10, it estimates that for all U_{SG} values, D_{99}/D_H is a constant, while the data indicate a clear dependence on U_{SG}. Also, the different U_L values obtained do not correlate with the trends exhibited by the experimental data. Although modified versions of the equation were considered (Rahman *et al.*, 2012), they do not include any consideration about the gas phase kinematics, which would result in slightly improved, yet still inaccurate, predictions of the bubbly flow behavior measured.

6.4. Bubble size distribution

The percentage distribution functions of the geometrical bubble diameter ($D_B = D_{10}$) upstream of the discharge nozzle are shown in Figure 6.11. The results, obtained for all D_{inj} and $U_L = 1.3$ m/s, depict the effect of U_{SG} on the bubble distribution. As the superficial gas velocity increased, the population number of small sized bubbles increased correspondingly, as depicted in Figure 6.11a, where the fraction distribution raised from approximately 0.55 at $U_{SG} = 0.072$ m/s to slightly above 0.7 at $U_{SG} = 0.140$ m/s. Similar tendencies were observed for the other D_{inj}, Figure 6.11b and 6.11c, although an increase in U_{SG} caused a smaller fraction increase in the number of smaller bubbles than that observed for $D_{inj} = 0.27$ mm.
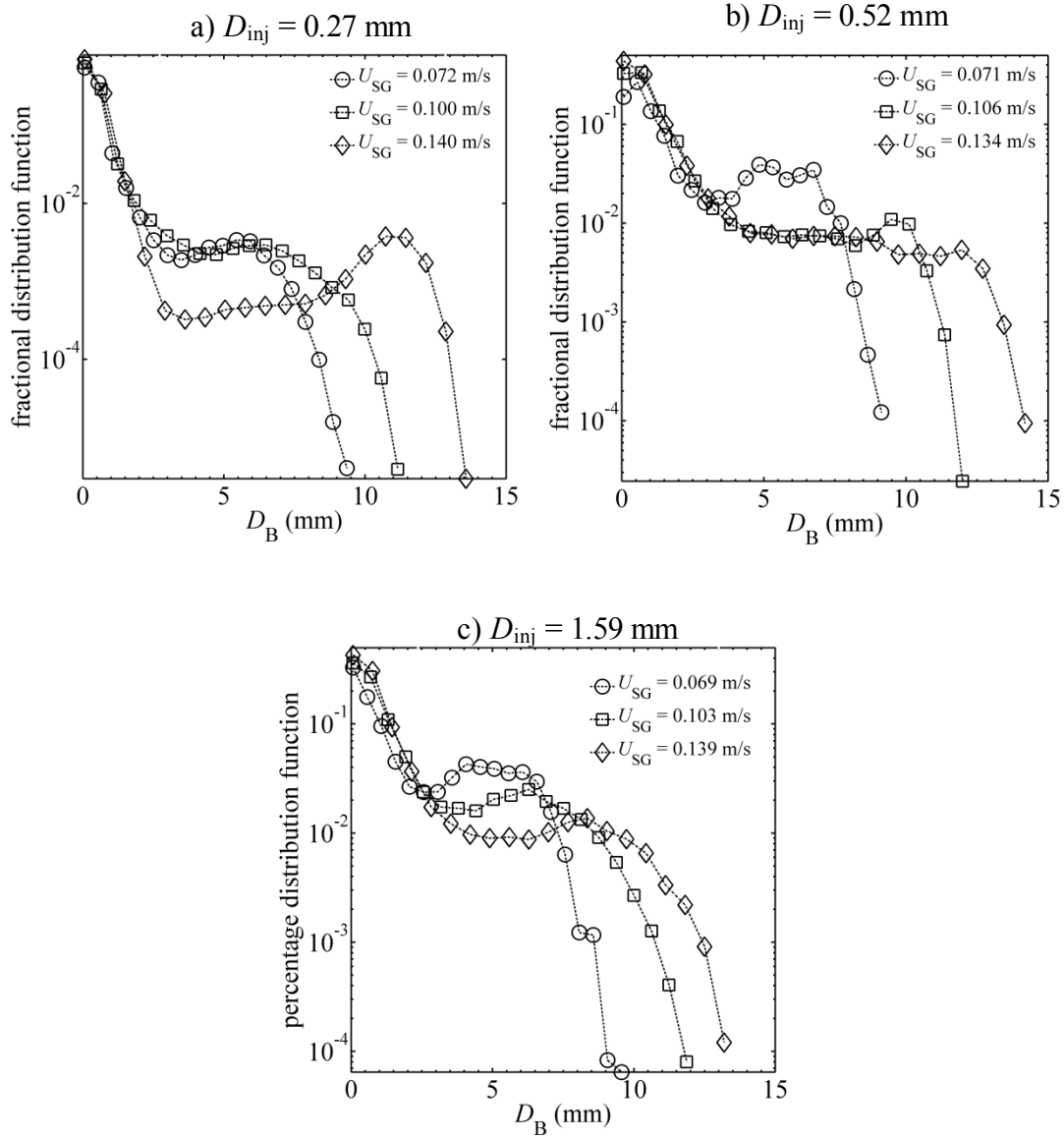
Figure 6.11. Effect of U_{SG} on the bubble distribution function for different D_{inj} at $U_L = 1.3$ m/s upstream of the discharge nozzle

Additional facts were observed from the results shown in Figure 6.11. Small differences between the distributions for $D_{inj} = 0.52$ mm and 1.59 mm occurred under similar operational conditions. It was inferred that even though the injection characteristics are key in an effervescent atomizer, at lower U_L the gas operational conditions exerted a more important influence in the control of D_B. This observation exhibited great similarity with the findings of Jedelsky *et al.* (2009), which

suggested that although the aeration diameter is important in the bubble diameter observed within the conduit, its influence cannot be considered individually but dependent on the range of other variables, such as liquid velocity and operation pressure.

While an increase in U_{SG} caused a higher number of small sized bubbles, it also induced the appearance of larger bubbles; therefore the bubble distribution became wider. For $U_{SG} \approx 0.139$ m/s, a broad scattering of the bubble diameter was observed. Whereas D_B was as high as approximately 1.1 times D_H, the highest bubble fraction corresponded to smaller bubbles.

The effect of the superficial velocities on the bubble distribution for the cases of higher U_L was studied as well. The results are shown in Figure 6.12 and depict how the cumulative percentage distribution upstream of the discharge nozzle changed with U_{SG} variations. At $U_L = 3.2$ m/s, a higher percentage of the bubbles was represented by the smaller particles, whose diameter was lower than 0.5 mm (microbubbles). This occurred for most of the U_{SG} conditions tested. It was also noticed that as U_{SG} was increased, the percentage of smaller bubbles increased as well. Independent of D_{inj}, when $U_{SG} \approx 4.45$ cm/s, the microbubble population was as high as 30% of the number total (Figure 6.12a and 6.12b). The marked shift towards the left axis, combined with the fast growth in the distribution function, implied that the population of smaller bubbles increased with U_{SG}. However, the results also indicated that the probability of larger bubbles within the channel increased as well.
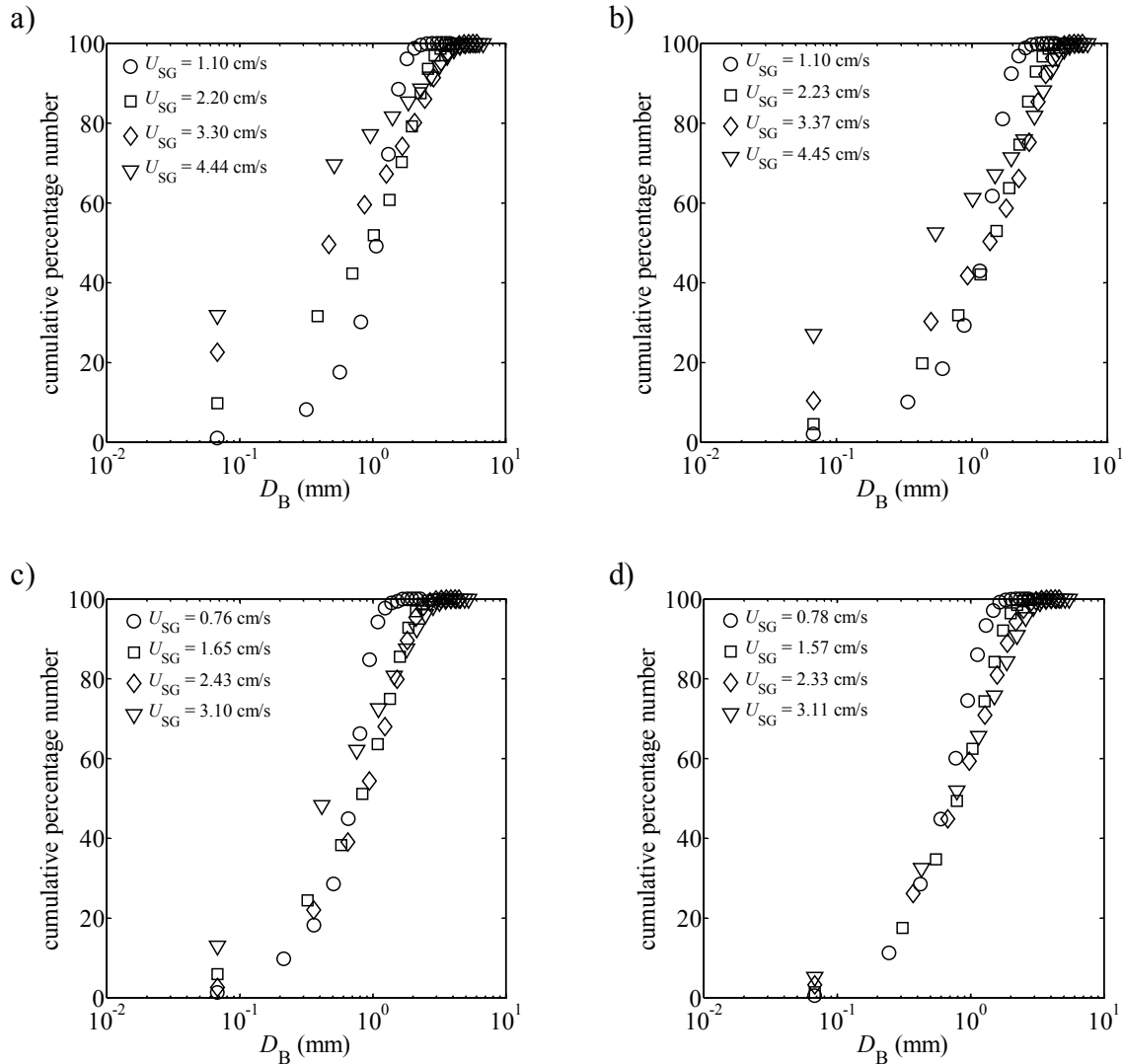
Figure 6.12. Cumulative percentage distribution of bubble diameter for different injection diameters and phase superficial velocities. a) $D_{inj} = 0.27$ mm, $U_L = 3.2$ m/s, b) $D_{inj} = 0.52$ mm, $U_L = 3.1$ m/s, c) $D_{inj} = 0.27$ mm, $U_L = 4.2$ m/s; d) $D_{inj} = 0.52$ mm, $U_L = 4.2$ m/s

For the majority of the experimental conditions reported (Figure 6.12a-c), at the highest U_{SG} the cumulative percentage function had a different tendency from the other functions, as indicated by the initial trends for the distributions. The results indicated that in most cases, between 45 to 64% of the bubbles were between 0.1 mm and 0.3 mm in diameter. The trend line exhibited a sharp growth up to the point where the percentage indicated that approximately 80% of the bubbles in the channel were smaller than 2 mm in diameter. Afterwards, the growth rate became less

163

pronounced, until reaching the maximum averaged bubble diameter measured where the growth was almost constant.

These findings match quite well with the observations near the injection region, where as U_{SG} increased, the size of the bubbles that detached from the gas plume increased as well. It was inferred that the high number of small bubbles observed upstream the nozzle resulted from the breakup of the incipient bubbles into smaller bubbles owing to the liquid crossflow effects. However, even though the bubble-liquid interaction caused the breakup and subsequent wider distribution of bubbles, large bubbles where present in the conduit right before the nozzle discharge. As observed in Figure 6.12, at $U_L = 3.2$ m/s, the vast majority of the particles within the conduit were smaller than 1 mm, even though it was possible to observe bubbles as large as approximately 8 mm.

For $U_L = 4.2$ m/s and for all U_{SG} values tested, the slope of the cumulative percentage functions had a very similar behaviour. Although at higher $U_{SG,}$ large bubbles survived within the conduit, the distributions presented a very similar scaling, both in trend as well as in the start and end points. These findings were interpreted as a decrease in the influence of the bubbling conditions on the bubble population behaviour for high U_{SL} values. At high liquid velocity, the flow possessed more energy, which reduced the diameter of the bubbles produced from the gas injection process. This resulted in a more stable D_B, less susceptible to break-up during its trajectory towards the nozzle, and a reduced presence of microbubbles within the conduit.

The cumulative distribution of D_B after bubble detachment from the injector/gas jet was compared to the cumulative distribution upstream of the nozzle exit. The resulting distributions were shown in Figure 6.13. The effects of U_{SG} on the bubble distribution were assessed. For that, the injection diameter $D_{inj} = 0.52$ mm and U_L were held constant, while the changes in the CDF for three different U_L values were studied. Near the injector region, the CDFs exhibited a noticeable shift towards the left, which indicated a high number of small bubbles ($D_B \leq 1$ mm) in this region.

This trend was observed at all U_{SG} values and was caused by two simultaneously occurring phenomenon: First, the turbulent interface stresses acting on the gas jet, which induces a premature detachment of small bubbles from the main gas plume. An increase in U_{SG}, which was directly related to an increase in M_G, enhanced the effect of both the interface stresses and the turbulent features of the gas jet, which produced a larger percentage of smaller bubbles. The second effect was the early and successive gas bubble breakup events, which although binary in nature did not equal to symmetrical break-up, and caused the appearance of a large number of small bubbles. As U_{SG} was increased, both effects were enhanced, as observed in Figure 6.13, where the percentage of smaller bubbles correspondingly increased with U_{SG}.
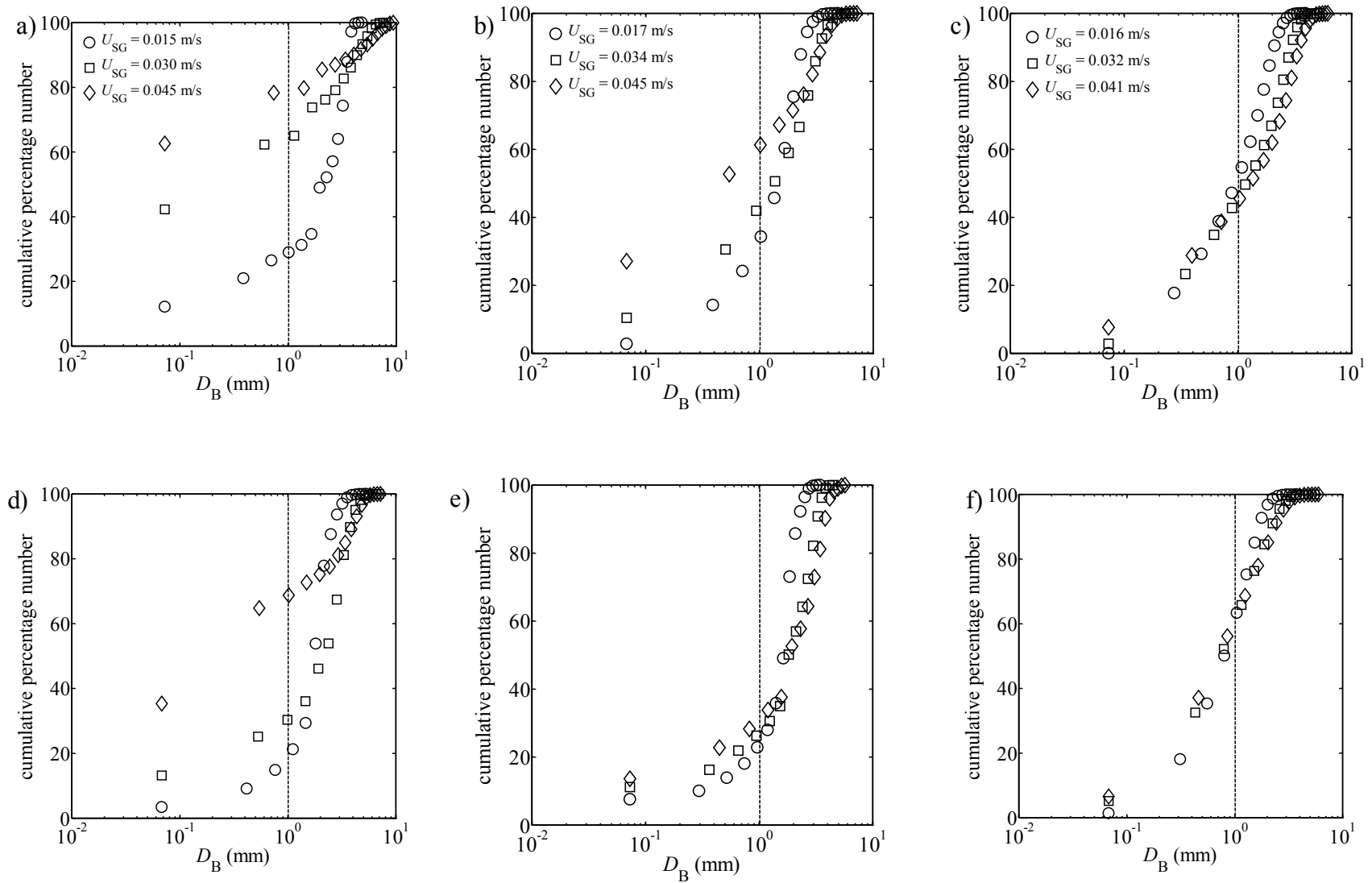
Figure 6.13. Effect of U_L on the D_B cumulative distribution at the gas injector (upper row) versus nozzle (lower row) for D_{inj} = 0.52mm and U_{SG} = 0.016, 0.030 and 0.045 m/s. a) and d) U_L = 1.9 m/s, b) and e) U_L = 3.2 m/s, c) and f) U_L = 4.2 m/s

The U_{SG} had a comparable effect on the distribution functions at both locations, particularly at the CDFs starting regions, where an increase in its magnitude caused a corresponding increment in the population of smaller bubbles. Qualitatively, the tendencies were preserved for the D_B distributions upstream of the discharge nozzle. However, for the same operational values, the percentage distribution of smaller bubbles upstream of the discharge nozzle decreased.

For $U_L = 1.9$ m/s, the number of small bubbles ($D_B < 1$ mm) incremented as U_{SG} was increased, reaching magnitudes approximately equal to 80% at the highest U_{SG} (Figure 6.13a). An equivalent behaviour was observed before the bubbly flow entered the discharge, but the population of small bubbles decreased to roughly 65%. Generally, the CDFs remained heavily shifted towards the left, indicating that even upstream the discharge nozzle, the small-sized bubbles would be numerous within the conduit. However, the percentage of larger sized bubbles either increased (Figure 6.13d-6.13e) or remained approximately constant (Figure 6.13f) as U_{SG} was increased.

It was evident that U_L played a strong role in the evolution of the bubble distribution. At lower liquid flow rates, U_{SG} exerted a clear influence on the D_B, as indicated by the differences in the CDF slopes (Figure 6.13a, 6.13d). As U_L increased, the distinction amongst trends decreased, until collapsing into a single, similar trend for $U_L = 4.2$ m/s (Figure 6.13c, 6.13f). The results indicated that the CDF trend after bubble detachment remained approximately similar upstream the nozzle discharge, which highlighted the importance of the gas injection conditions in the development of the bubbly flow. It was determined that U_L produced slightly narrower D_B distributions before the nozzle discharge, than those obtained right after bubble formation. The

turbulent stresses that acted on the bubble interface, particularly those for which D_B was equal or larger than the stable $D_{\max}$ (Hesketh *et al.*, 1987), caused bubble breakup.

At high U_L values, a decrease in the population of large bubbles occurred, which narrowed the CDF width. This also explained the slight decrease in the percentage of small bubbles in the channel. It was inferred that the microbubble population remained relatively constant. The high U_L values and short mixing chamber length would cause a small bubble residence time. When combined with the mildly strong liquid cross-flow, the possibility of bubble interaction and subsequent coalescence are reduced. However, the largest bubbles experienced breakup, causing smaller bubbles and increasing the percentage number of the middle sized bubbles. Consequently, a minor shift in the CDF towards this range was observed (Figure 6.13d-6.13f). Since the bubble size distribution became narrower, breakup dominated in the present experiments.

Finally, the previously shown results indicate that owing to the short distance between the injector and the nozzle, the conditions under which the bubbles are produced have a relevant role in the bubble morphology upstream of the discharge nozzle. Using a log-log scale and encompassing the range of U_L and U_{SG} values considered in this study, representative statistical diameters of the bubbly flow were evaluated at the two key positions within the conduit, near the injector and upstream the nozzle. The contrast of D_{99} and D_{32} between these locations is presented in Figure 6.14a and 6.14b respectively.
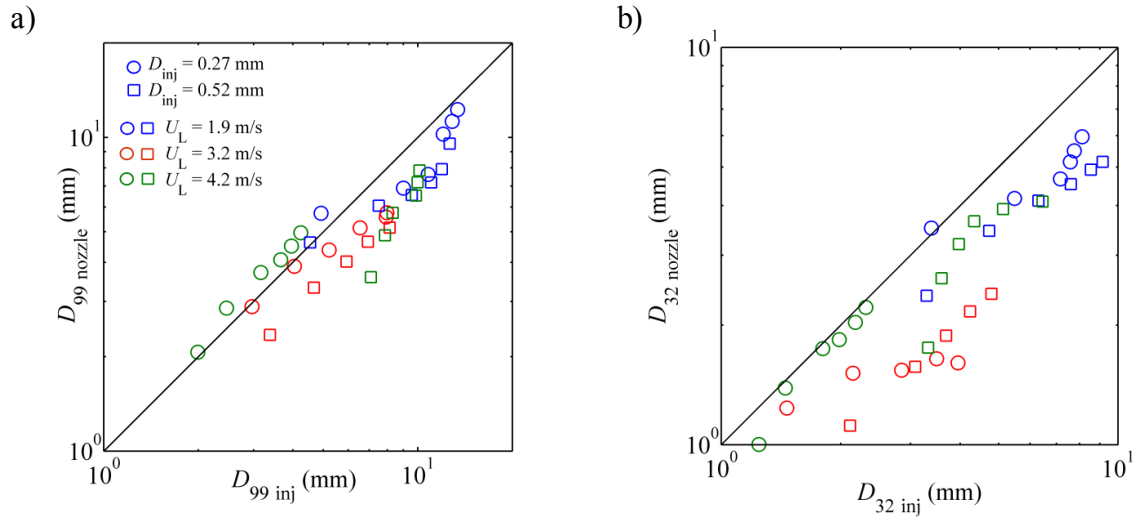
Figure 6.14. Contrast between key statistical bubble diameters at the injector and nozzle location: a) $D_{99@inj}$ vs $D_{99@nozzle}$. b) $D_{32@inj}$ vs $D_{32@nozzle}$

The assessment of D_{99} gave a clear picture of both the relevance of the injection conditions on the downstream processes as well as the gas-liquid interaction within the conduit. As previously reported, D_{99} measured after bubbles detach from the gas jets are larger than the theoretical, maximum stable bubble diameter (equation 6.2). Hence, the results shown in Figure 6.14a are an indication of bubble breakup during the flow transition between locations. In most cases, the correlation was $D_{99nozzle} \sim 0.66 - 0.77\ D_{99inj}$.

As can be seen in Figure 6.14a, there were cases where $D_{99\ nozzle}$ was almost equal to D_{99inj}. This occurred primarily for $D_{inj} = 0.27$ mm and $U_L = 4.2$ m/s. It was inferred that this was created by the combination of a high U_L and a diminished expansion of the gas jet. Hence, bubbles whose maximum diameters remain stable are formed. Although it is not explicitly shown, Figure 6.14a indicates that increasing values of U_{SG} result in a direct increase in the D_{99} of the bubbles observed within the conduit.

As can be seen in Figure 6.14b, for the vast majority of the experimental configurations, $D_{32nozzle}$ is lower than D_{32inj}. The results, which exhibit great correlation with the findings presented in Figure 6.13, show the occurrence of bubble breakup during the bubbly flow evolution. The $D_{32nozzle}$ ranges primarily between 0.60 to 0.75 times D_{32inj}, which is similar to the decrease observed for D_{99}. As was previously mentioned, the generalized decrease in D_{32} was caused by the cross-flow induced bubble disintegration. This implies that bubble breakup occurs along the majority of the diameter range, causing the appearance of a higher number of bubbles with a smaller diameter than measured near the injector.

6.5. Conclusion

The current study broadens the existing knowledge about the internal fluid mechanics of effervescent atomizers. Specifically, flow visualization was used to improve the understanding of the effect that fundamental variables have on the bubbly flow morphology: void fraction, Sauter and maximum bubble diameter and bubble diameter distribution. The novel methodology allowed for the assessment of the gas phase evolution along the conduit. It is one of the few reported attempts to describe in detail the characteristics of gas jets and bubbles formed under carefully controlled conditions that mimic an industrial setting. The link between the gas injection conditions, the diameter of the incipient bubbles and their transition towards the discharge nozzle was evaluated. The main conclusions obtained were:

* The assessment of the D_{inj}, U_L and M_G values highlighted the importance of the injection conditions upstream of the discharge nozzle. There was a definitive correlation between the gas-liquid flow behavior at both locations within the channel.

* Under similar experimental conditions, top wall gas injection translates into higher α_{local} values than those observed for bottom wall injection. This was caused by the horizontal orientation of the conduit and the buoyancy effects.

* For equal operating values, a small D_{inj} causes higher gas dispersion as well as α_{local} magnitude in than that obtained for larger D_{inj} geometries. This was caused by the higher inertial forces experienced by the gas jet.

* The α_{area} values at the nozzle location have slightly lower magnitudes than those measured at the injector location. The void fraction differences between the two locations were attributed primarily to the combined effects of the liquid cross-flow induced bubble breakage and the gas stratification.

* An empirical correlation that estimates the averaged gas jet equivalent diameter, as a function of Re_L, Fr_G and Eo_G was developed. The relationship reproduced the physical implications of the relevant dimensionless numbers, while estimating D_{equiv}/D_H with a mean error of 8%.

* Near the injector, the bubble size distributions measured in this study were characterized by a D_{99}/D_{32} that was independent of D_{inj} but depended on Re_L with values 1.51, 1.67 and 1.81 for $Re_L = 24,000$, 42,000 and 56,000 respectively.

* The comparison between the fundamental bubble diameters indicated that the link for D_{32} and D_{99} between two channel locations, after gas injection and upstream the discharge nozzle, did not have a 1:1 ratio. For both statistical parameters, the differences were in the range of $D_{@nozzle} \approx 0.60\text{-}0.77\, D_{@inj}$. The ratios D_{32}/D_{99} obtained for the injector remained relatively similar for the nozzle region.

* The results indicated that for the range of conditions tested in this work, the bubbly flow was subjected primarily to the effects of particle breakup owing to the contribution of the liquid cross flow. The $D_{99@nozzle}$ values obtained are an indication that even at a distance $x \approx 40 D_{H}$ downstream the gas injector, the maximum bubble diameter is not stable and the gas injection conditions still had a key role in the bubbly flow conditions.

* Although the use of correlations based on fully developed pipe flow could provide an estimation of D_{99} and D_{32}, they would not be able to reproduce the different physical mechanisms observed in an effervescent atomizer, as was shown here.

7. Bubble Formation Regimes during Gas Injection into a Liquid Cross Flow in a Conduit

7.1. Introduction

The purpose of this chapter is to examine, under controlled laboratory conditions, the effects that the physically meaningful gas mass flow rate (M_G), nozzle dimension (D_{inj}) and liquid cross-flow velocity (U_L) have on the bubble formation regime during the injection of gas into a liquid cross-flow in a horizontally-oriented conduit. These effects were represented in the form of fundamental dimensionless numbers, the Froude (Fr_G) and Eotvos (Eo_G) numbers of the gas phase and the liquid Reynolds number (Re_L), with the purpose of facilitating the generation of results and ease the way for comparison with other studies in this area. The specific focus of the experimental program is on the range of operating conditions that produces bubbly flow for air-water systems (Andreussi *et al.*, 1999). A series of bubble formation regime charts, based on Fr_G, Eo_G and Re_L have been introduced. As was suggested by previous authors (Sovani, 2001; Badam et al., 2007), the use of non-dimensional paramaters was introduced to facilitate the generation of results and to allow for future comparison with other studies. Where possible, data collected from the previous works are used to assess the general applicability of the flow regime transitions identified in this study. Empirical correlations developed by other researchers to predict bubble size after detachment (D_{32}) are evaluated using high-quality data collected in this study. The experimental results and analysis presented here provide an improved understanding of the mechanisms governing bubble formation and detachment. Of particular importance is the

identification of bubbling regimes and transitions using physically meaningful dimensionless numbers.

7.2. Previous studies on bubble regime identification

Very few researchers have acknowledged any bubble formation regime other than the single bubbling (SB) regime. Moreover, it is generally considered that the bubbles will form as discrete entities, even though it has been proven that there are at least two possible mechanisms of bubble formation: SB and jetting (J). The jetting regime is defined as the case where a continuous gas jet exists continuously at the injector and the formation of bubbles occurs through disintegration of the gas jet (Wace *et al.*, 1987). An inclusive summary of the existing studies dedicated to the characterization of bubbling regimes is presented in Table 7.1. This table compiles the test conditions, geometrical characteristics, fluids used and regimes observed by some of the authors that have presented results in the area. Sada *et al.* (1978) presented one of the first studies that proved the existence of different bubble formation regimes during gas injection into a vertical column of co-flowing liquid. It was determined that three types of bubble formation regimes occurred: single bubbling, coalescent bubbles and jetting. The bubble diameter after detachment (D_{32}) was the only criteria used to differentiate between bubbling regimes, limiting its applicability as a predictive tool. Sada *et al.* (1978) also reported that the parameters U_G, D_{inj} and U_L were dominant in defining the size of bubbles and/or types of bubbles formed. Using a simple balance of the detaching forces (buoyancy and drag) acting on a growing bubble, two empirical correlations that define D_{32} for the single bubbling and coalescent bubble regimes, as a function of bubble Froude number, were obtained.

Table 7.1.   Studies of bubble formation regimes in flowing liquids

Author(s)	Fluids used		Conduit description			Flow rate conditions, velocities and pressure	Regimes identified
	Gas	Liquid	Hydraulic diameter and geometry	D_{inj} (mm)	Orientation		
Sada *et al.* (1978)	Air Nitrogen	Water	$D_H = 50$ mm square cross section	0.86 3.05	Vertical	$Q_G = 0.33$ to 36.2 cm^3/s $Q_L = 0$ to 3040 cm^3/s $h_L = 91$ cm of water	*SB* Coalescing bubbles. *J*
Wace *et al.* (1987)	Air	Water	Rotary bubble generator (55 mm radius) Orifice location 40 mm from center	2, 3, 5, 8	Horizontal	$U_L = 0.1$ to 2.5 m/s $Q_G = 2$ to 20×10^{-6} m^3/min $h_L = 220$ mm of water	*SB* *J*
Rigby *et al.* (1995)	Air	Water	400 (depth) $\times$ 50 (wide) mm^2 rectangular duct Injection orifice located in a cylindrical impeller blade	2	Horizontal	$U_L = 0$ to 1.2 m/s $Q_G = 0$ to 140×10^{-6} m^3/s $U_G = 0$ to 45 m/s $h_L = 290$ mm of water	*SB* *P* Incipient *J* Stable continuous *J*
Forrester and Rielly (1998)	Air	Water	100 (height) $\times$ 20 (width) mm^2 rectangular duct $D_H = 33$ mm Injection orifice located on different geometries (cylinder, flat, concave)	1	Horizontal	$U_L = 1$ to 4 m/s $U_G = 2$ to 45 m/s $Q_G = 2$ to 35 cm^3/s	*SB* *P* *J* *C*
Sovani (2001)	Nitrogen	Water	Two width conduits used: 3.75 mm and 5.75 mm	0.178 0.330 0.508	Vertical	$U_G = 10$ to 500 cm/s $U_L = 4$ to 90 cm/s $P_L = 3.5$ to 40 MPa	*SB* *P* *PTJ* Varicose *J* Sinuous *J* Atomizing *J*

These expressions, Equations (7.1) and (7.2), along with correlations obtained by other researchers, were included in Table 7.2, which presents a summary of equations that allow the estimation of the bubble diameter according to the bubbling regime. However, two limitations were observed for expressions (7.1) and (7.2): first, they are not independent and require the use of additional equations to estimate the diameter of the initial bubbles (d_{B0}). Second, no clear criteria were presented for the differentiation between bubbling regimes, implying the use of direct observation of the bubble formation process, which is highly impractical. It is noticeable that Sada *et al.* (1978) did not consider the influence of U_G on the jetting regime even though they stated that this is a key variable that controls D_{32}.

Wace *et al.* (1987) investigated the range of U_L at which jetting detachment is replaced by single bubble formation. The experimental studies were performed using a rotating sparger inside a stagnant tank that simulated cross-flow conditions. They concluded that there are only two different mechanisms of bubble production in the presence of a cross-flow: single bubble and jetting. It was discussed that single bubble formation occurred if either U_L is similar to the natural bubble rise velocity, reported in their study as $\sim$ 0.3 m/s, or when U_L is very large, which reduces the gas jet diameter towards zero and caused single bubble formation at the orifice to occur. The jetting regime occurs when both U_L and U_G are high, which leads to the formation of a gas jet. No clear criterion was introduced to define what constitutes high U_G.

Table 7.2.   Existing correlations to estimate the bubble diameter according to the bubbling regime

Author(s)	Equation		Regime
Sada et al. (1978)	$\dfrac{D_{32}}{D_{inj}} = 1.55\left(NFr_B\right)^{0.2}$, where $NFr_B = \dfrac{U_G^2}{\left(gd_{B0} + 0.33U_L^2\right)}$	(7.1)	SB
	$\dfrac{D_{32}}{D_{inj}} = 2.5\left(NFr_B\right)^{0.2}\left(\dfrac{D_{inj}}{0.086}\right)^{0.1} - 3.5$, where D_{inj} in cm	(7.2)	Coalescing Bubbling
Kawase and Ulbretch (1981)	$V_B = (1.378)\dfrac{Q_G^{6/5}}{g^{3/5}}\left(1 - e^{-1/U_L^{0.242}}\right) + (0.489)\dfrac{Q_G^{3/2}}{U_L^{3/2}}\left(e^{-1/U_L^{0.242}}\right)$	(7.3)	SB
	Tested for $Q_G \leq 20$ cm^3/s		
Wace et al. (1987)	$D_{32} = 2.408\left(\dfrac{Q_G}{U_L}\right)^{0.5}$, where $Q_G = \left(\times 10^{-6}\ \text{m}^3/\text{s}\right), U_L = \left(\times 10^{-2}\ \text{m}/\text{s}\right)$	(7.4)	J
	Valid for $U_L \geq 0.5$ m/s		
Marshall (1990)	$U_G = (0.0208)D_{inj}^{-0.93} - (0.0109)D_{inj}^{-0.75}\left(U_L\right)$ 0.6 m/s $\leq U_L \leq 4.8$ m/s	(7.5)	Upper boundary for the P regime
Oguz and Prosperetti (1993)	$D_{32} = \left(1.135\times 10^{-3}\right)\left(\dfrac{Q_G}{U_L}\right)^{0.5}$, Q_G in $\left(\text{mm}^3/\text{s}\right)$ and U_L in $\left(\text{m}/\text{s}\right)$ $U_L \leq 2.0$ m/s	(7.6)	SB
Rigby et al. (1995)	$U_L = \left(2.19\times 10^{-2}\right)D_{inj}^{-0.93} - \left(2.25\times 10^{-2}\right)D_{inj}^{-0.75}\left(U_G\right)$ $U_L \leq 1.2$ m/s	(7.7)	Upper boundary for the SB regime
	$D_{32} = \left(\dfrac{8D_{inj}\sigma}{C_D U_L^2 \rho_L}\right)^{0.5}$	(7.8)	SB
Forrester and Rielly (1998)	$D_{32} = 0.5\left(D_{inj}^{0.826}\right)\left(\dfrac{U_G}{U_L}\right)^{0.36}$, $5\times 10^{-4}\text{m} \leq D_{inj} \leq 2\times 10^{-3}\text{m}, 2 \leq \left(U_G/U_L\right) \leq 58$	(7.9)	P

Using principles of Rayleigh instability theory, Wace *et al.* (1987) obtained a correlation (Equation 7.4) which predicts D_{32} under the jetting regime. This expression depends only on M_G and U_L, and establishes that the D_{32} depends on the gas jet diameter. Since the gas jet diameter is calculated from simple continuity, it was assumed that effects such as D_{inj} and fluid properties have no influence on D_{32} under the jetting regime. Neither the possible existence of sub-regimes within the jetting detachment scenario nor the existence of transitional regions between the regimes of formation was considered.

A complete characterization of the gas flow regimes that can occur in a liquid cross-flow was presented by Rigby *et al.* (1995). High-speed imaging was used to observe and distinguish the different bubbling scenarios for a gas injector located in a cylindrical object positioned in a rectangular water duct. It was concluded that there are at least four clearly differentiated regimes under which bubbles can form: Discrete bubbling, pulse bubbling (multiple pulse bubbling, penetrating pulse bubbling), incipient jetting and continuous jetting. The zones connecting the regimes were categorized as transitional regions, which may or may not appear depending on particular combinations of U_G and U_L. Using these variables, Rigby *et al.* (1995) introduced a gas dispersion map where the bubbling regimes were categorized.

Though the use of the fluid velocities provides a simple way to predetermine the possibility of bubble formation under a particular scenario, it does not take into consideration the importance that the fluid properties have on the mechanisms of bubble formation (Bowers, 1950; Sullivan *et al.*, 1964; Tsuge and Hibino, 1983). Also, the influence of D_{inj} on the boundaries between regimes was not fully assessed. It can be inferred from the results presented by Iguchi et

al. (1998) and Tan *et al.* (2000) that D_{inj} is an important variable during the growth and evolution of a gas jet interacting with a liquid in cross-flow. Marshall (1990) introduced a correlation that predicts the upper boundary for the generation of bubbles under the single bubbling regime (Equation 7.5). The proposed equation, which estimates the highest U_{G} at which discrete formation can be observed, considers the effect of D_{inj} and U_{G}.

Forrester and Rielly (1998) evaluated the mechanics of bubble formation regimes under the influence of a strong liquid cross-flow. Their focus was on the experimental study of bubble growth and detachment from submerged orifices located on objects of varied geometry: cylinders, flat plates and concave blades. Using high-speed imaging, the effects of U_{G}, U_{L} and inclination angle of the injector on bubble diameter were investigated. Following an approach similar to that of Rigby *et al.* (1995), they proposed gas dispersion maps for the profiles tested. For each one of these charts, four types of regimes were delimited based on a comparison of U_{L} versus U_{G}. The differentiation between regimes was made by evaluation of the images collected. The pulse and jetting sub-regimes were classified under more general categories, while a new regime, defined as cavity formation, was included. No transitional zones were defined. Furthermore, Forrester and Rielly (1998) compared their D_{32} measurements with correlations that estimate the bubble diameter based on the bubble formation regime.

Sovani (2001) assessed the effects of injecting a gas stream into a confined liquid flowing at a high pressure. The conditions under which the gas jet dispersion regimes occur were experimentally studied in a vertically oriented, narrow channel. For all the tests performed, the flow regime for the liquid phase was laminar and the velocity profile was fully developed. The

effects that the channel width (D_H), D_{inj}, operating pressure (P_L) and momentum flux ratio for the gas (MF_G'') and liquid (MF_L'') phases have on the bubbling modes were considered. Using photographic imaging, seven different cases under which gas particles can form were obtained: *SB*, *P*, pulse-to-jet transition (*PTJ*), varicose jet (*VJ*), sinuous jet (*SJ*) and atomizing jet (*AJ*). The last mode corresponds to the case where there is interaction between the gas stream and the far wall of the channel. After evaluating the relevant forces affecting the gas jet, Sovani (2001) selected MF_L'' and MF_G'' as the variables for the map coordinates in the abscissa and ordinate axes, respectively.

After careful evaluation of the literature concerning bubble formation regimes in a liquid cross-flow (Tables 7.1), it can be seen that very few studies consider bubbling modes other than the single bubbling regime. Even fewer studies provided a complete evaluation of the modes of bubble detachment from a gas jet in the presence of a flowing liquid (Table 7.2). It has been proven that the bubble formation regime controls the mean D_{32} and the bubble size distribution, which in turn affect parameters like the void fraction and bubble population. Rigby *et al.* (1995) and Forrester and Rielly (1998) present regime formation charts based on the fluid velocities, where the bubbling regions are clearly delimited. However, their studies were performed for gas injectors located in non-flat submerged profiles, where the possibility of flow separation and the interaction of the gas jet with curved surfaces dominate the bubble formation mechanics.

Few works have been devoted to the evaluation of the effects of injector geometry on the process of bubble formation. The use of fluid velocities to characterize flow regimes is a common practice, though the fluid physical properties play a critical role in the dynamics of bubble

formation. Hence, it can be concluded that the use of an approach based on dimensionless numbers, as proposed by Sovani (2001), provides a better comparison of the relevant forces controlling bubble formation.

7.3. Qualitative Categorization of the Process of Bubble Generation

The images were studied and categorized through visual examination of each frame to establish the bubbling regime. The bubble formation modes defined here were inspired by the studies of Rigby *et al.*, (1995), Forrester and Rielly (1998) and Sovani (2001). Despite studying similar physical processes, each one of the previously mentioned studies identified a different number of bubbling regimes, which was caused by the intrinsic subjectivity associated to the regime characterization methods. However, strong similarities exist between the various studies regarding the main regimes described (single bubbling, pulse and jetting) and their associated characteristics, which confirms the existence of different bubble formation modes. Building upon this, this section aims to illustrate the bubble formation regimes identified in the present study and describe the relevant characteristics associated to each of them.

7.3.1. Single Bubbling (SB)

The single bubbling regime refers to the production of individual bubbles of nearly spherical shape at quasi-uniform, regular intervals (Rigby *et al.*, 1995; Forrester and Rielly, 1998; Sovani, 2001). The single bubbling can be observed only at very low M_G values, causing the bubble size distribution to be monodisperse (Kyriakides *et al.*, 1997). In the single bubbling regime, a small

gas filament is formed in the vicinity of the injection orifice (Figure 7.1a). This gas thread-like structure grows, in length and diameter, until obtaining a tear-like shape because of the presence of the neck (Figure 7.1b and 7.1c). The bubble growth is limited by the detaching forces of the liquid cross-flow and severance occurs before full expansion. The bubble separates then from the gas filament and a new bubble is formed (Figure 7.1d and 7.1e). A filament remains at the end of the bubble, which transforms into a new bubble (Figure 7.1f). The change towards the next possible formation regime does not occur drastically; a transitional phase between the single bubbling and pulsating regime exists and it is clearly identifiable as it exhibits features associated with both regimes. This transitional region was categorized as single bubbling-to-pulsating (*SBP*).

a) $t = 0.00$ ms

b) $t = 2.33$ ms

c) $t = 4.33$ ms

d) $t = 5.67$ ms

e) $t = 6.00$ ms

f) $t = 6.33$ ms
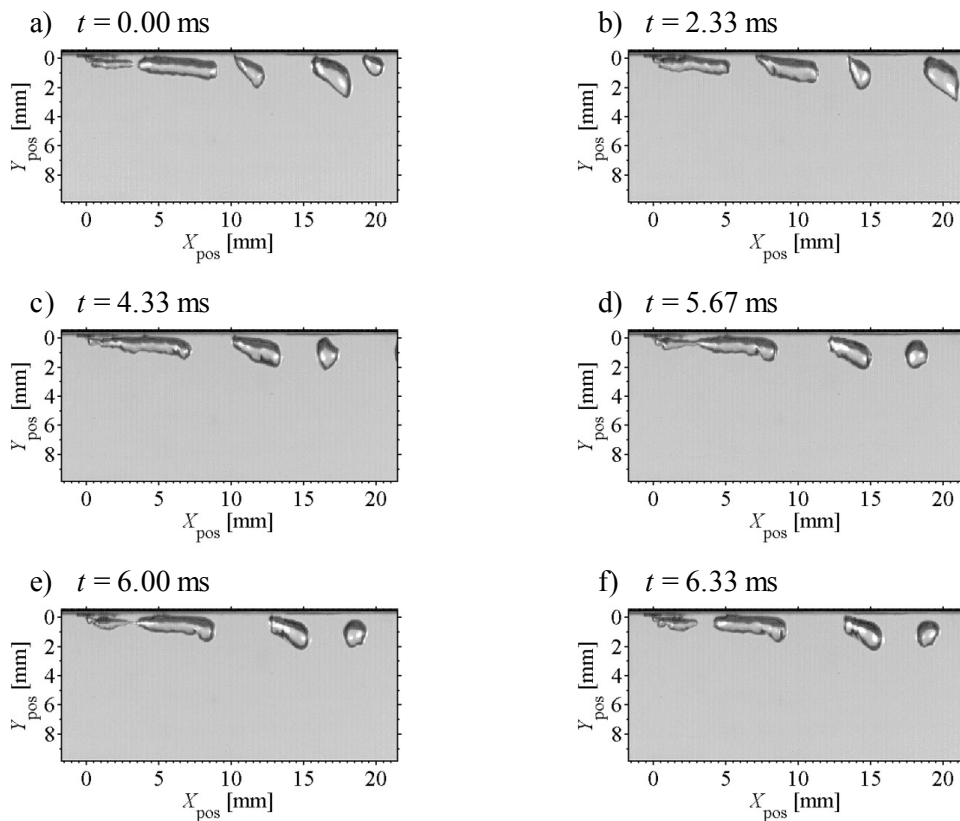
Figure 7.1.   Images depicting the *SB* formation regime. $D_{inj} = 0.27$ mm, $U_L = 1.9$ m/s, $U_G = 69$ m/s

7.3.2. Pulse Bubbling (*P*)

For a constant U_L, an increase in M_G over the value that delimits the single bubble regime, a transition towards the pulsating bubble formation regime occurs. The pulsating regime can be described as a chain of easily distinguishable gas lumps, a minimum of two and a maximum of four, interconnected by very small necks, which give the gas stream the appearance of a pulse (Sovani, 2001). Forrester and Rielly (1998) determined that in the pulsating regime, the bubbles agglomerate, appearing to run into each other, creating doublets and triplets. Rigby *et al.* (1995) determined that the pulsating regime can be divided into multiple pulse bubbling and penetrating pulse bubbling. However, in the current study no sub-regimes were observed within the pulse bubbling mode. The appearance of ripples in the gas structure creates small pockets trapped between the aft of a formed bubble and the fore of the gas jet, giving the gas stream a pulse-like shape (Figure 7.2). The internal recirculation of the gas, combined with the liquid effects, causes the closure of the small necks. In some cases the simultaneous closure of two gas pockets can produce bubbles whose diameters are at least an order of magnitude smaller than that of the bubbles formed from the gas pulse, as shown in Figure 7.2c.

As M_G is increased, the number of pulses increases and the gas stream takes on the form of an intermittent gas jet with noticeable disturbances. Sovani (2001) established the existence of an intermediary zone between the pulsating and jetting regimes where the gas stream penetration near D_{inj} is less affected by the cross-flow effects, resembling a plume of air. The present study verified the existence of a transitional region, defined as the Pulse-to-Jet (*PTJ*) regime, where the gas structure fluctuate randomly, resembling a succession of pulses or an incipient gas jet.

a) $t = 0.00$ ms

b) $t = 1.33$ ms

c) $t = 2.67$ ms

d) $t = 4.00$ ms

e) $t = 5.33$ ms

f) $t = 7.33$ ms
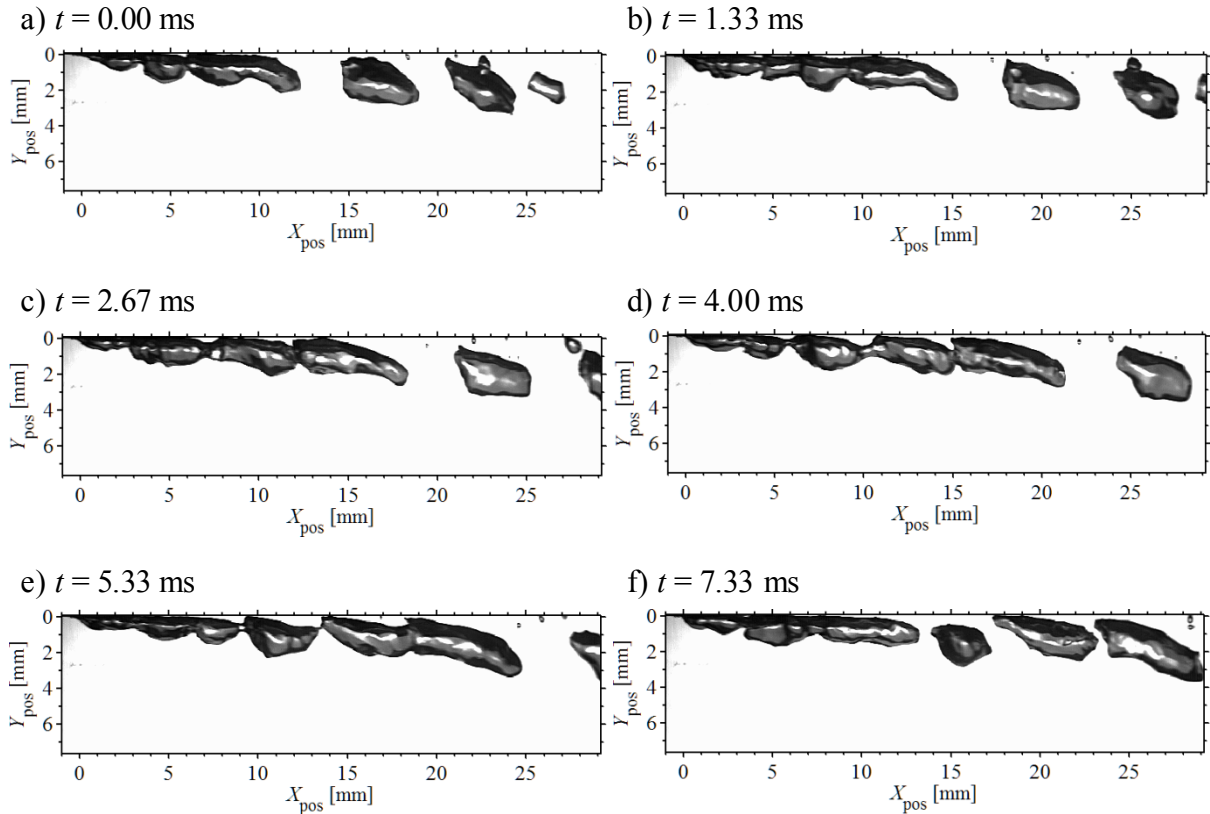
Figure 7.2.   Photographic representation of the P bubbling regime. D_{inj} = 1.59 mm, U_L = 3.1 m/s, U_G = 2.2 m/s

7.3.3. Jetting (J)

Once the PTJ regime is observed, a continuous increase in M_G while keeping U_L constant will lead to continuous jetting, where there is always a gas jet present inside the conduit. Wace et $al.$ (1987) defined this regime as that in which a cylinder of gas is subject to the effects of varicose instability and where gravitational effects are negligible. Rigby et $al.$ (1995) and Forrester and Rielly (1998) defined the jetting regime, in a qualitative manner, as the mode of bubbling in which a continuous gas jet emerges from D_{inj}, breaking up downstream the orifice in a chaotic manner. The authors of those studies suggest that in air-water systems, jetting occurs if U_G is at least one order of magnitude greater than U_L.

184

Similar to liquid jet breakup mechanics, Sovani (2001) considered the existence of three jetting regimes: varicose jet, sinuous jet and atomizing jet (*AJ*). For the purposes of this study, the sinuous and varicose sub-regimes jets defined by Sovani (2001) are grouped under a more qualitatively general category, referred to here as the Elongated Jet (*EJ*). The elongated jet regime can be described as a gas jet whose length is a few times the channel diameter, as can be observed in Figure 7.3.

The start of the elongated jet regime will be the point when there is a continuous presence of a gas jet, there are no distinguishable interconnected bubbles and where the bubble size distribution becomes broad. In the atomizing jet regime, the bubble formation regime is completely disorganized (Figure 7.4), the diameter of the detached bubbles deviates significantly from a spherical shape, the size distribution of the bubbles formed under this scenario can be wide and the morphology of the main gas core exhibits large geometry variations.

a) $t = 0.00$ ms
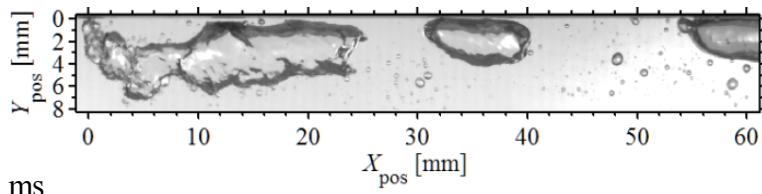
b) $t = 25.67$ ms
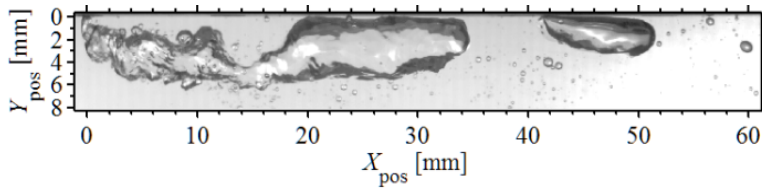
c) $t = 0.00$ ms
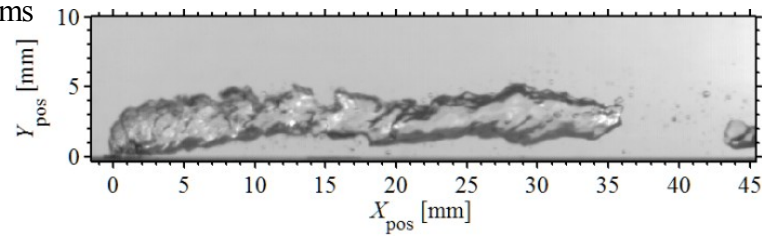
d) $t = 25.67$ ms
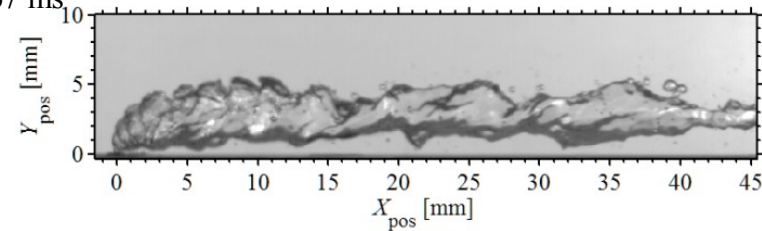
Figure 7.3.   *EJ* regime of bubble formation: a) and b) $D_{inj} = 0.52$ mm, $U_L = 1.1$ m/s, $U_G = 81$ m/s. c) and d) $D_{inj} = 1.59$ mm, $U_L = 3.1$ m/s, $U_G = 6.5$ m/s

b) $t = 50.00$ ms

c) $t = 90.00$ ms
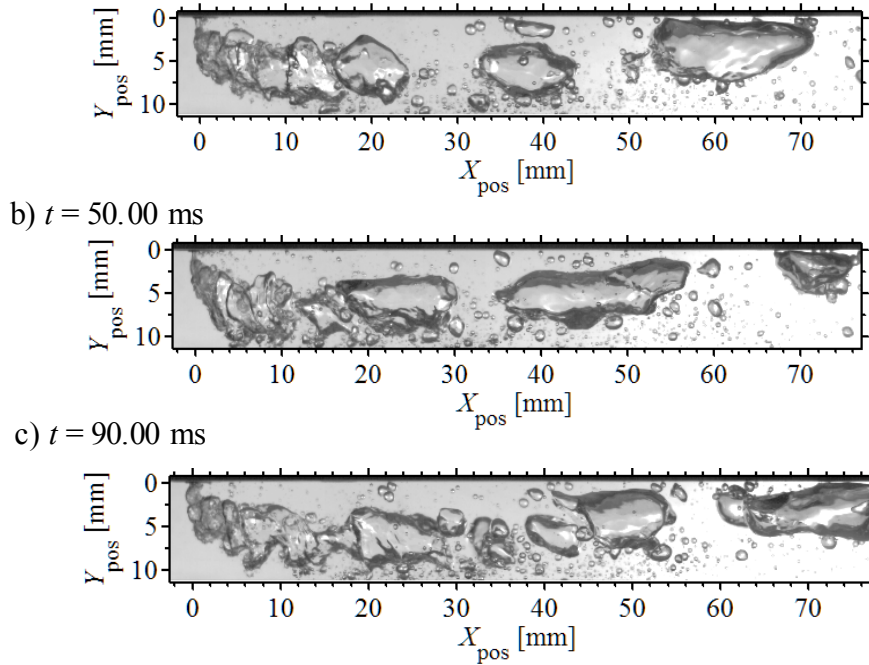
Figure 7.4.   *AJ* regime: $D_{inj} = 0.27$ mm, $U_L = 1.1$ m/s, $U_G = 132$ m/s

A set of values that describe the variations in the characteristics of the gas jet core depending on the bubbling regime are presented in Table 7.3. Starting in a single bubbling scenario, as M_G is increased the gas jet occupies a larger volume inside the conduit and transitions to the pulsating regime. A continuous increase of M_G causes the shifts from the pulsating regime towards a jetting mode, where the jet dimensions grow considerably, as can be noticed in the two-fold increase of the equivalent diameter (D_{equiv}), obtained from the projected area in the middle plane of the conduit. In the atomizing jet regime, the gas stream occupies a volume similar to that observed in the elongated jet but the mean breakup distance (x_{break}) has a wider range and the number of bubbles per area is significantly higher. Figure 7.5 compares the variations in the bubble distribution based on the bubbling regime observed.
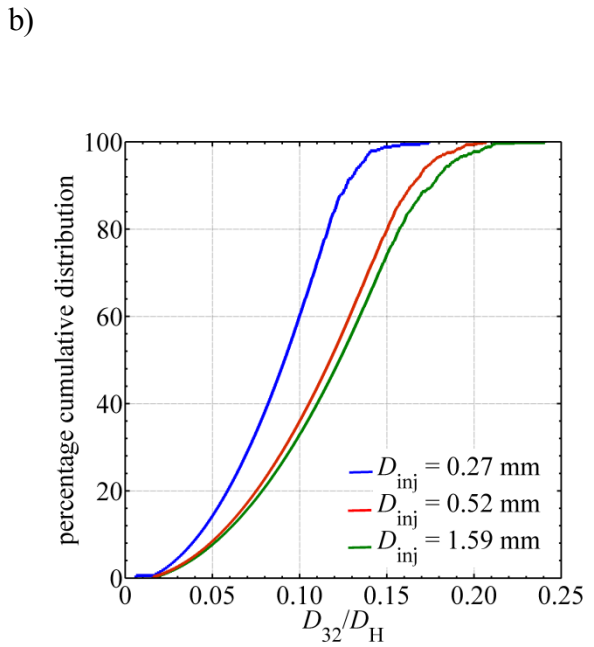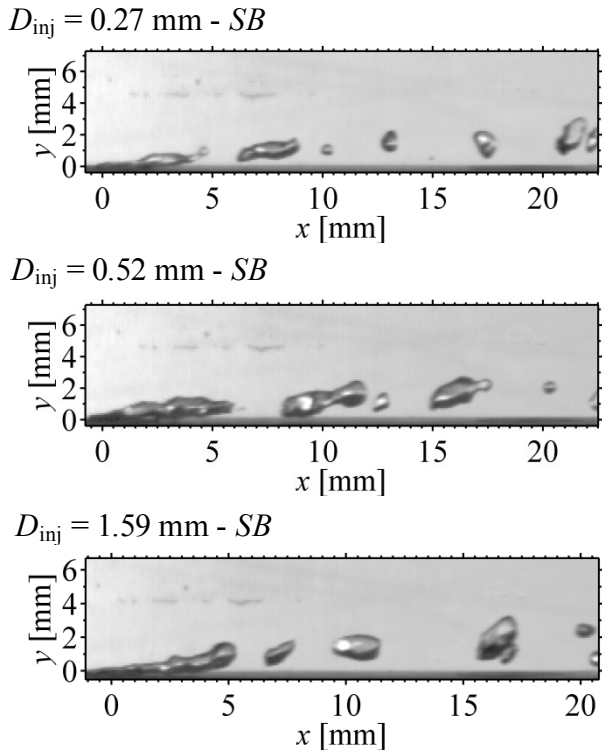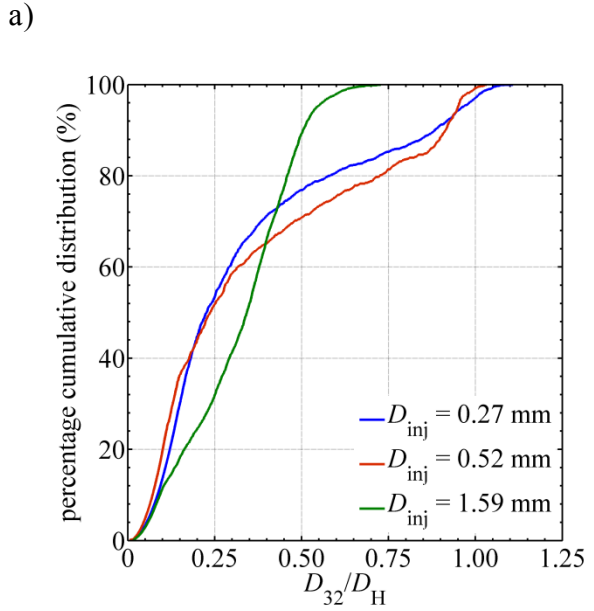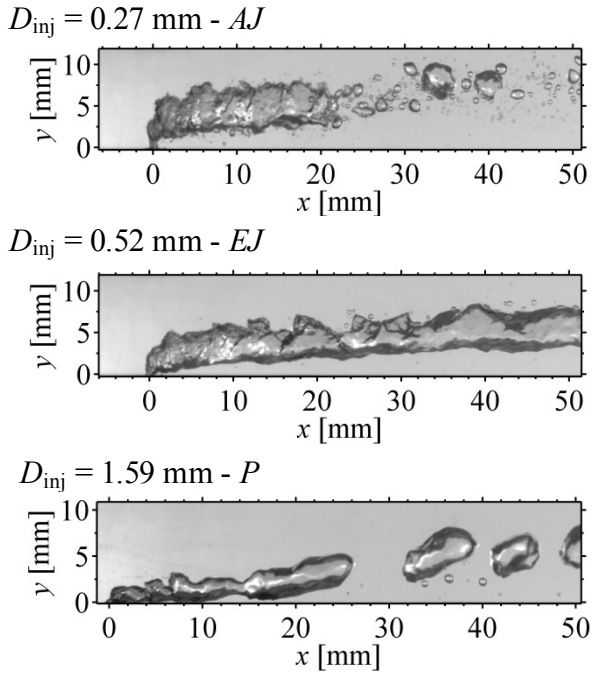
Figure 7.5. Effect of D_{inj} on the bubbling regime under comparable operating conditions: a) $U_L \approx 2.0$ m/s, $M_G \approx 59.1 \times 10^{-6}$ kg/s. b) $U_L \approx 4.3$ m/s, $M_G \approx 5.0 \times 10^{-6}$ kg/s

Table 7.3.   Morphological description of the gas stream for $D_{inj} = 0.27$ mm and $U_L = 1.9$ m/s

$M_G \times 10^{-3}$ (g/s)	Regime	D_{equiv} (mm)	x_{break} (mm)	Primary breakup/s	# bubbles/10 cm^2
9.80	SB	4.0	14.0 ± 1.5	502	12.2
19.8	SBP	4.3	17.9 ± 4.0	373	10.3
29.4	P	5.0	21.4 ± 3.1	271	11.4
39.5	PTJ	10.1	48.9 ± 8.8	103	9.9
46.0	EJ	14.2	64.1 ± 11.7	54	14.7
59.1	AJ	15.0	50.9 ± 20.2	57	61.7

7.4.   Results and Analysis

7.4.1. Bubble formation regime charts

The experimental results associated with the bubbling regimes described in the previous section are depicted as bubble regime maps in Figure 7.6. The regions identified in the maps were obtained through direct visualization of the bubbling regime at the injector region. Groups of at least 750 independent images were evaluated. Each experimental observation was performed three times for each set of conditions to guarantee the repeatability of the results presented.

The regions were defined based on the combination of dimensionless numbers used associated to each experiment conducted. Hence, the maps depict the regimes identified and the transition between regimes as a function of Eo_G and Fr_G under the range of Re_L values described in Tables 2.2-2.4. Because of the scattered nature of the results obtained, the boundaries between regions were obtained by means of a mathematical algorithm. This algorithm is a built-in Matlab function (Delaunay Triangulation-Interpolation) from which the proposed boundaries were obtained. The use of this numerical approach could induce the appearance of non-physical behaviour on the boundary curves, such as the presence of sharp corners. It was inferred that this could be caused by the sparsity of the experimental data. This could be improved or avoided by

considering additional Eo_G values. However, since the delimitations between zones are a result of an interpolation algorithm, it was assumed that they provide a repeatable prediction of the physical bubble formation behavior.

The results obtained here exhibit markedly similar trends with the results presented by Kyriakides *et al.* (1997) and Badam *et al.* (2007), where in general, the *SB* regime is observed at low Fr_G values, independent of the Re_L and Eo_G values. At any specific Eo_G value, the transition towards the pulsating regime was induced by an increase in the Fr_G, which in the current work occurs because of an increase in U_G. Similarly, for a particular Fr_G, an increase in Eo_G causes a transition from *SB* towards the transitional *SBP* region.

a)
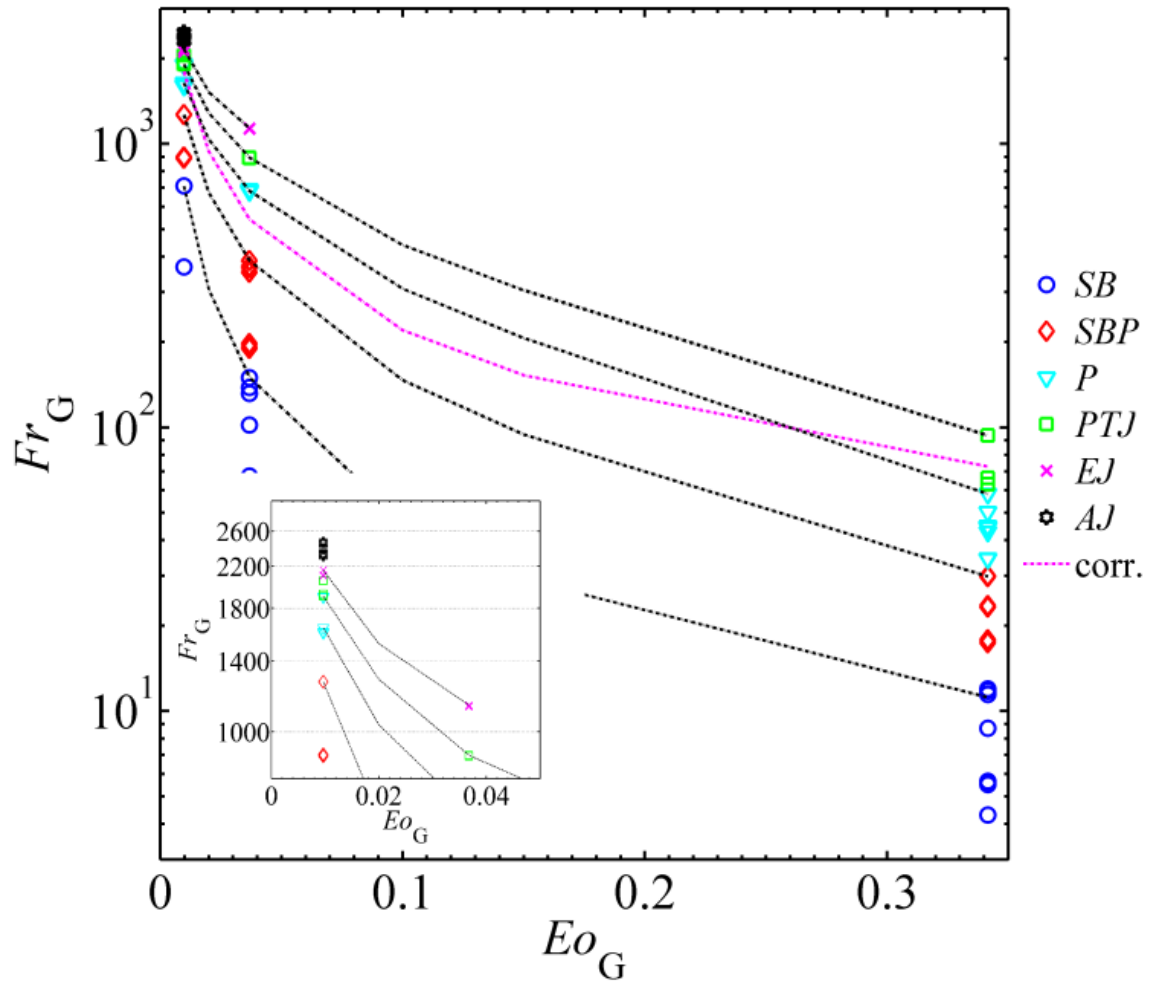
Figure 7.6.   Depiction of the transitional curves between bubbling formation regimes as a function of Eo_G versus Fr_G for different Re_L. a) $Re_L = 14{,}000\text{-}18{,}000$. The magenta line represents *MSBP* curves are based on correlation (Eq. 7.10).

b)
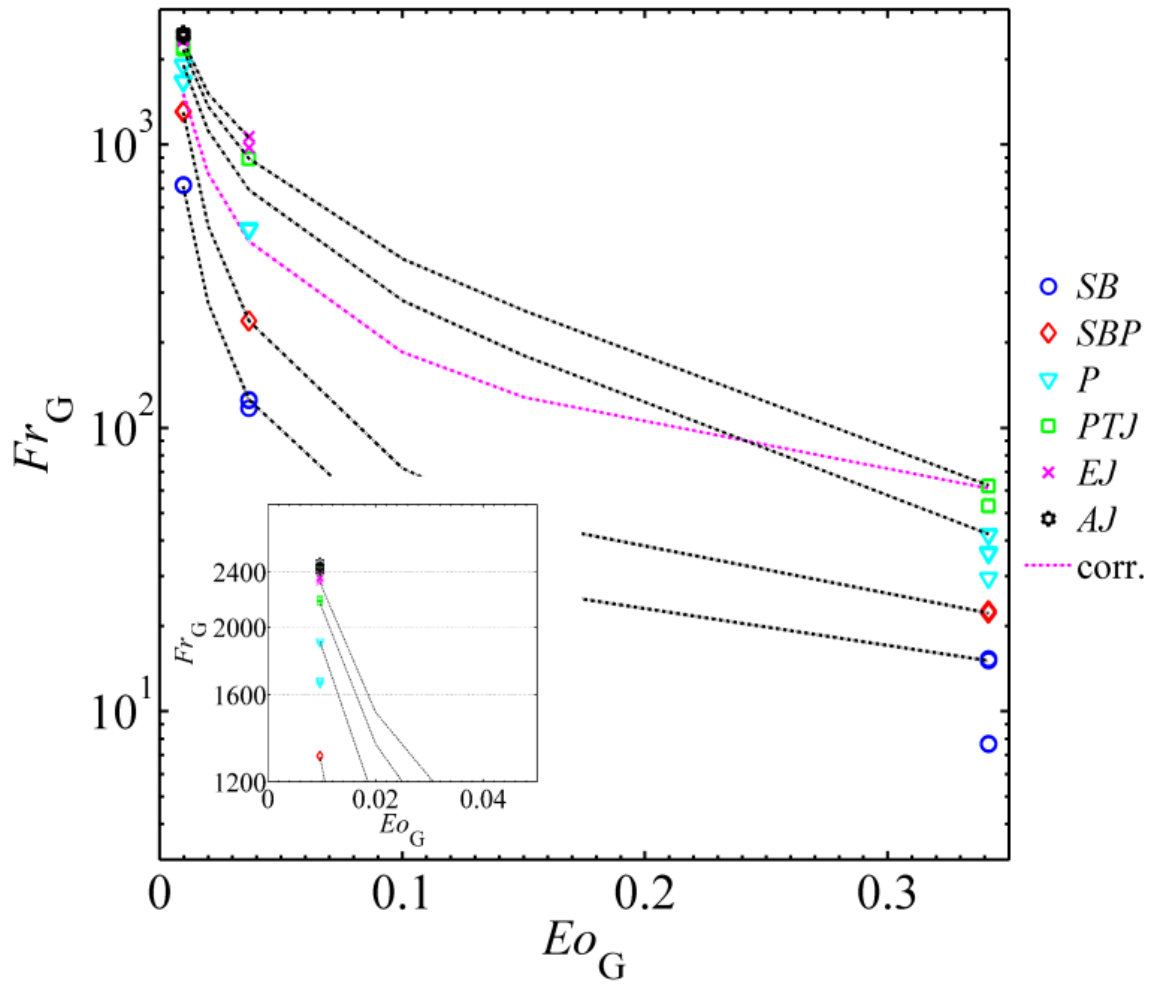
Figure 7.6.   Depiction of the transitional curves between bubbling formation regimes as a function of Eo_G versus Fr_G for different Re_L: b) Re_L = 24,000-28,000. *MSBP* curves are based on correlation. The magenta line represents *MSBP* curves are based on correlation (Eq. 7.10).

c)
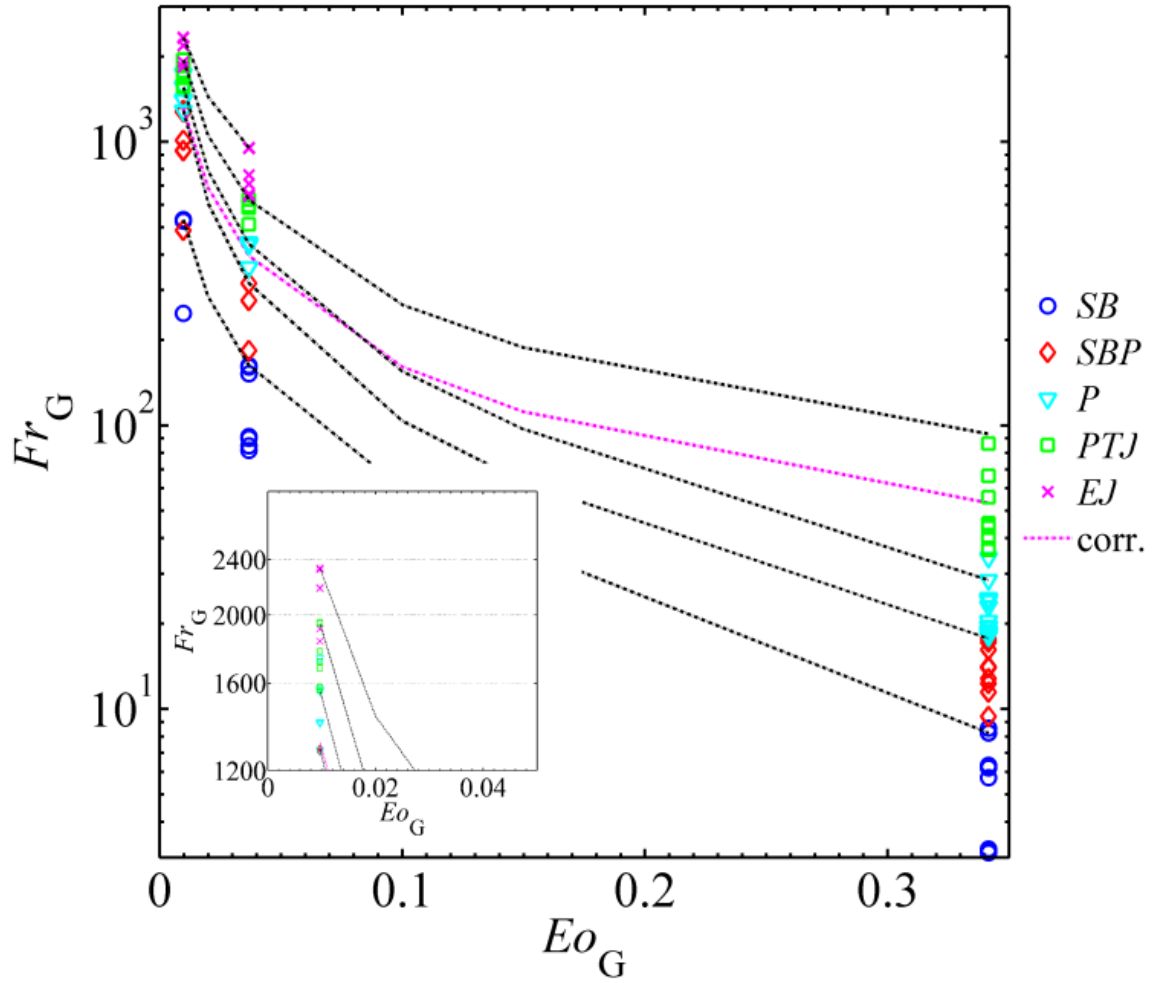
Figure 7.6. Depiction of the transitional curves between bubbling formation regimes as a function of Eo_G versus Fr_G for different Re_L. c) Re_L = 34,000-42,000. *MSBP* curves are based on correlation. The magenta line represents *MSBP* curves are based on correlation (Eq. 7.10).

d)
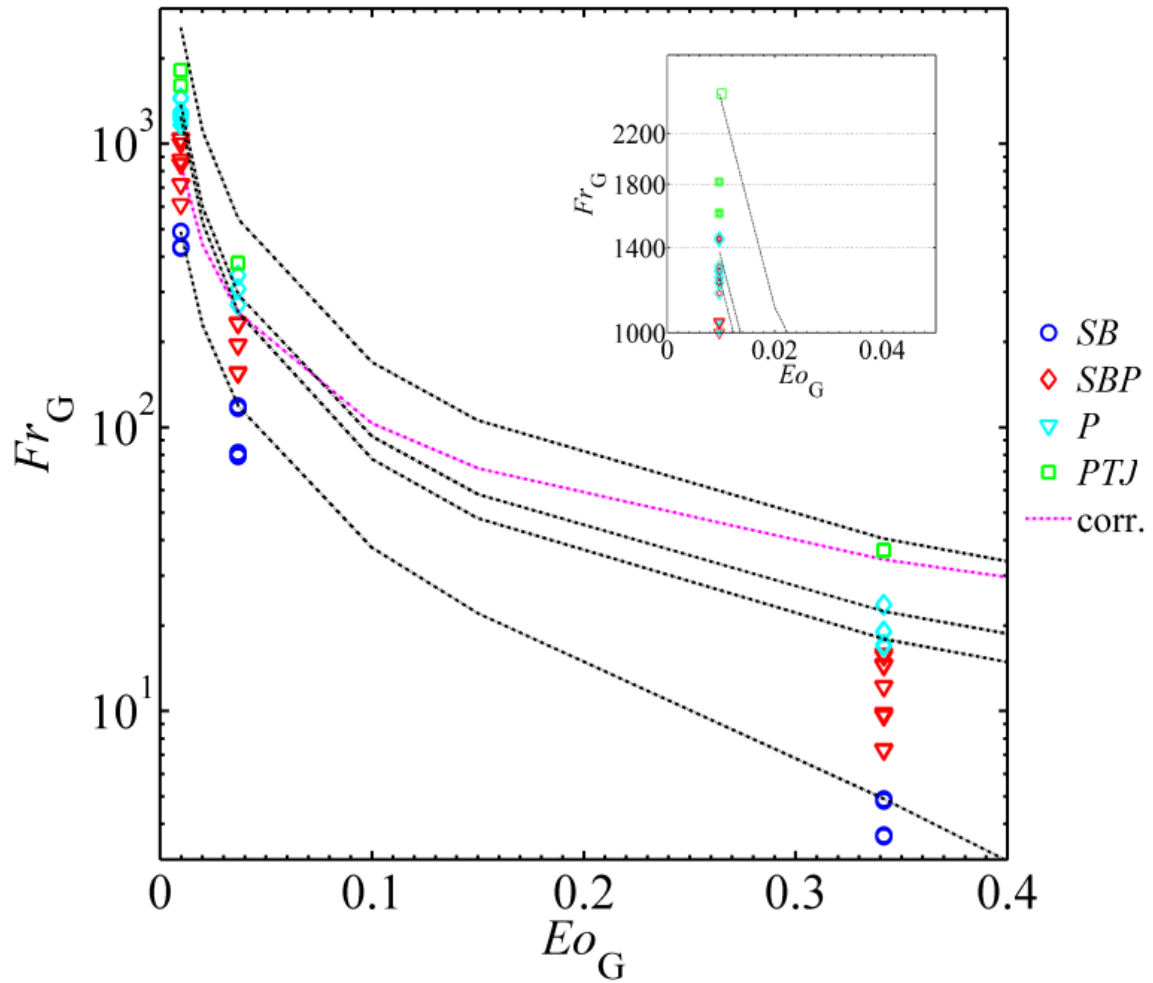
Figure 7.6. Depiction of the transitional curves between bubbling formation regimes as a function of Eo_G versus Fr_G for different Re_L. d) Re_L = 54,000-56,000. *MSBP* curves are based on correlation. The magenta line represents *MSBP* curves are based on correlation (Eq. 7.10).

Continuous increments in either Fr_G or Eo_G move the bubbling regime towards more chaotic modes. This is related to the fact that with increasing Fr_G, the inertial effects of the gas jet are enhanced, counteracting the detaching influence of the liquid cross flow and allowing the evolution of the gas towards the jetting modes. It was observed that increasing Re_L induced an increase in the Fr_G value at which jetting occurs, which agrees with the observations of Sada *et al.* (1978).

Under conditions where both Re_L and Fr_G were constant and Eo_G was increased (by increasing D_{inj}), a general trend toward more chaotic bubbling regimes was observed, which was in accord with previous experiments (Kyriakides *et al.*, 1997; Sovani, 2001; Badam *et al.*, 2007). This was an expected result, because it implies an increase in the gas influx required to maintain the balance between inertial and gravitational forces, which induces the switch towards the jetting modes.

The transitional characteristics between bubbling regimes were similar for every Re_L interval evaluated. As shown in Figure 7.6, an increase in Re_L did not cause marked variations in the observed boundaries between bubbling regimes. However, as Re_L was increased, a decrease in the number of bubbling modes was observed. The *AJ* regime occurred only at low Eo_G values and for Re_L lower than 24,000. For the range of Re_L between 34,000 and 42,000, the jetting regime occurred primarily as *EJ* and exclusively at high Fr_G values. Pure jetting scenarios were observed only for $Eo_G = 36.7 \times 10^{-3}$ and 9.70×10^{-3}, which corresponded to $D_{inj} = 0.27$ and 0.52 mm respectively. When Re_L was

between 54,000 and 56,000 no fully developed jetting occurred. Even at high Fr_G values, only a transitional PTJ regime was observed.

The maximum stable bubble formation point ($MSBP$) was defined as the highest Fr_G, for fixed Eo_G and Re_L values, under which a fully developed pulsating regime could exist. The results indicated that as Re_L was increased, $MSBP$ decreased. An empirical correlation based on the experimental results is proposed to estimate the $MSBP$. This correlation, given in equation (7.10), follows the same theoretical principles discussed by Forrester and Rielly (1998). It was observed that for every Re_L range tested, under a given Eo_G, there is a critical Fr_G corresponding to the $MSBP$, denoted Fr_α in Equation (7.10). Predictions obtained using through the use of this correlation are included in Figure 7.6. For all bubbling regimes located under this proposed boundary, the bubbles will form under conditions similar to those described for the pulsating regime. This implies a quasi-regular bubbling frequency and detached bubbles within a narrower diameter range than those observed in the jetting modes.

$$Fr_\alpha = 290 Re_L^{-0.25} Eo_G^{-0.9} \tag{7.10}$$

Little consideration has been given to the influence of the D_{inj}, which as inferred from the results presented in Figure 7.6, has a predominant effect on the bubbling regimes that occur within the conduit. The assessment of Marshall's correlation (Equation 7.5) did not provide accurate estimations of the single bubbling and pulsating formation regimes. The same

correlation implies that, for constant U_G, an increase in U_L will necessarily cause a shift towards the transitional or jetting regimes, which is the opposite of the trends shown in Figure 7.6.

Equation (7.10) is therefore an improved alternative for the calculation of the boundaries under which the *SB*, *SBP* and *P* regimes occur. The exclusive dependence on dimensionless variables provides a broader comparison of the relevant parameters affecting the bubbling process. However, the influence of these parameters on the bubbling regimes needs further validation since the experiments were conducted with an air/water system. It is concluded that the conditions under which the gas is injected, represented by Fr_G and Eo_G, would be a dominant factor in the various stages of bubble formation.

7.4.2. Estimation of the bubble diameter based on the bubble formation regime

A comparison between the D_{32} obtained from the bubbling regime-based predictive correlations described in Table 7.2, defined as D_{pred}, and the experimental findings was performed. The results, shown in Figure 7.7, assess the ratio between D_{pred} and D_{32} for selected correlations, as a function of U_G and U_L. As can be observed, there are significant discrepancies between the experimental D_{32} values and the D_{pred} results given by the correlations. In general, the correlations underestimated the bubble diameter results and as U_G increased, the discrepancies increased correspondingly, as indicated by the D_{pred}/D_{32} values shown in Figure 7.7.
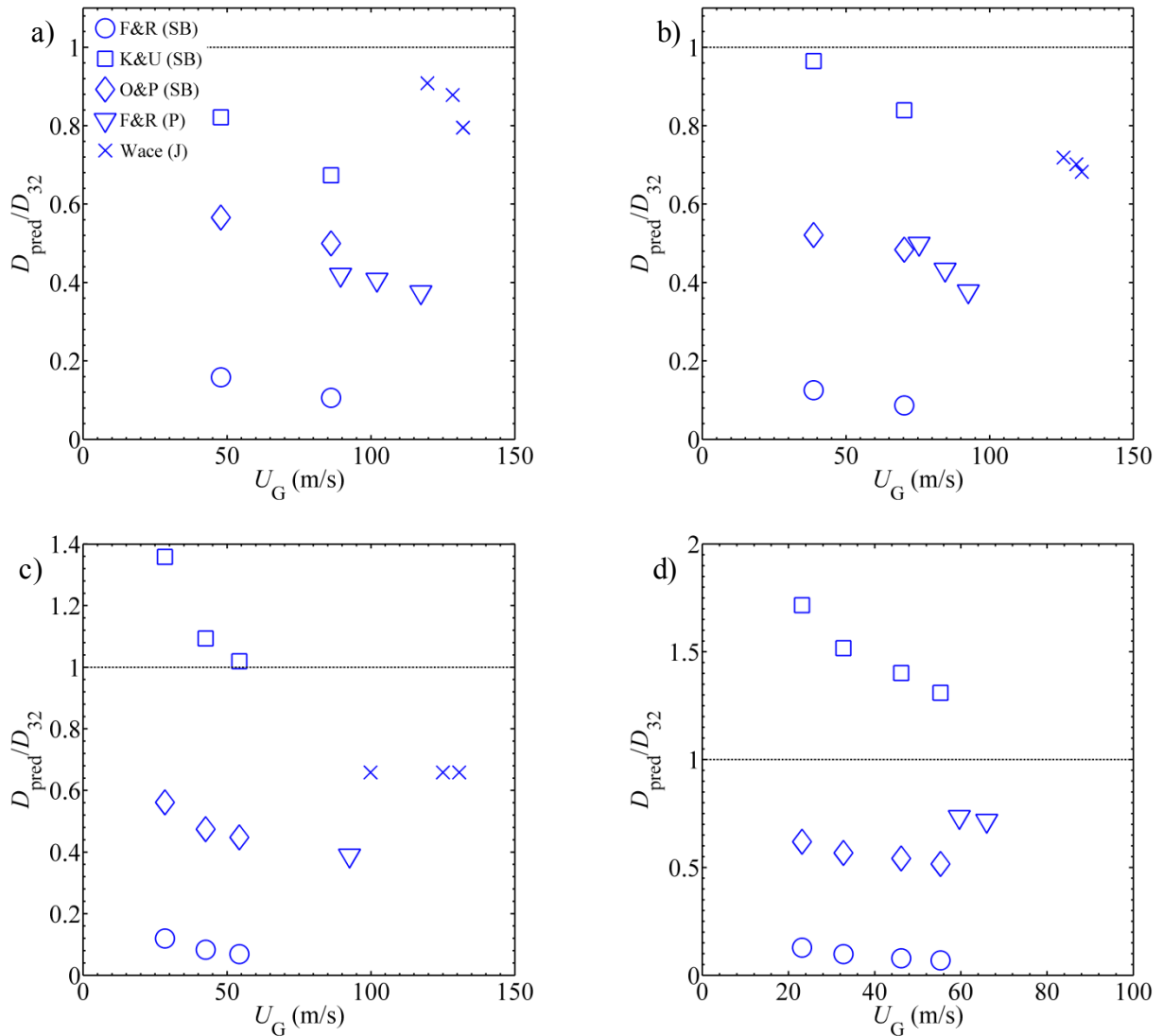
Figure 7.7. Comparison between the results obtained using the D_{32} regime-based predictive correlations (D_{pred}) and the experimental results for $D_{inj} = 0.27$ mm. a) $Re_L = 12{,}000$. b) $Re_L = 24{,}000$. c) $Re_L = 42{,}000$. d) $Re_L = 56{,}000$. F&R (SB) = Forrester and Riley, Equation (7.8), K&U (SB) = Kawase and Ulbretch, Equation (3), O&P (SB) = Oguz and Prosperetti, Equation (7.6), F&R (P) = Forrester and Riley, Equation (7.9), Wace (J) = Wace, Equation (7.4)

Forrester and Rielly's (1998) SB expression (Equation 7.8) disregarded the effects of U_G for

the SB regime, which did not adhere to the underlying physical implications derived from

the present study. This results in D_{pred} values which were at least four times lower than the experimental data. The expression proposed by Oguz and Prosperetti (1993) (Equation 7.6) gave better estimations than those obtained from Equation (8) results, although it still under predicted the D_{32} results for all operating conditions tested. Nahra and Kamotani (2003) argue that in the estimation of equation (7.6) not all the significant forces involved in the bubble formation process were considered; which could be a possible reason for the discrepancies obtained.

At low U_L, Equation (7.3), proposed by Kawase and Ulbretch (1981), under predicted D_{32}. For $U_L = 1.9$ m/s, the D_{pred}/D_{32} values improved significantly, giving results that ranged between $0.85 D_{pred}/D_{32}$ to $0.96 D_{pred}/D_{32}$. The trend reversed for higher U_L values, where Equation (7.6) gave results that overestimated the experimental data, with the largest disagreement observed at $U_L = 4.34$ m/s.

Equation 7.9, proposed by Forrester and Rielly (1998), was the only correlation that estimates D_{32} under the pulsating regime. For all the cases observed, the D_{32} predicted with the use of this equation are lower than those obtained from experimental measurements. The smallest D_{inj} used in this study does not fall within the range of applicability of the correlation. Hence the highest differences were obtained for this geometry. For the other D_{inj} values, an improvement in the D_{pred}/D_{32} ratio was obtained. Variations in the U_L did not play a significant role in the estimated data. The effects of regime transition were considered as one of the possible reasons for the divergence of results. It was concluded that equation (7.9) is not an effective tool for the estimation D_{32} under the P regime.

The results associated to the D_{32} of the bubbles detaching under the jetting mode are shown in Figure 7.7 as well. The predicted bubble diameter values were obtained using Equation (4), proposed by Wace *et al.* (1987). For a $D_{inj} = 0.27$ mm and independent of the magnitude of U_L, equation (7.4) produces D_{32} values lower than those obtained from the experiments. At lower U_L values the results match better the experimental findings. As U_L increased, D_{pred}/D_{32} decreased, indicating further discrepancies with the results. The tendency reversed for $D_{inj} = 0.52$, where the correlation overestimated the D_{32} values. When $U_L = 3.1$ m/s an almost exact agreement was observed.

Wace *et al.* reported that discrepancies were expected for $U_L < 2.0$ m/s. Finally, it was argued that Equation (4) does not consider the effects of D_{inj} on the D_{32}, which play a dominant role both on the bubble diameter as well as the bubbling mode. Also, the different dynamics governing the *EJ* and *AJ* regime, which are not accounted for in the equation, could be a factor in the disagreements observed.

7.5. Conclusions

The results obtained in the present work expand on the current knowledge about the dynamics of bubbling into a liquid cross-flow and the effects that the significant parameters have on this process. It is expected that these findings could be a significant contribution to understand the gas-liquid mechanics near the aerator inside an effervescent atomizer, which plays an important role in setting the characteristics of the two-phase flow being fed to the

discharge nozzle. While the results are not necessarily universal, as only one hydraulic diameter and only air-water were tested, it is expected that they could contribute appreciably in the development and improvement of numerical or theoretical bubbling models and to enhance the scarce knowledge about the internal flow in an effervescent atomizer.

As was mentioned in Table 1.3, the vast majority of the studies in the area of bubble formation into a liquid cross-flow assume that periodic, single bubbling occurs independent of the gas mass flow rate injection value. However, the bubbling maps obtained indicate that the mode under which bubbles form at the injector location is undoubtedly a function of three key effects: the strength of the liquid cross-flow, the magnitude of the gas mass flow rate and the nozzle dimension. For this study, dimensional analysis indicated that the effects of these parameters can be presented in the form of fundamental dimensionless numbers: Fr_G, Eo_G and Re_L. These maps could be used as an important tool in the design of effervescent atomizer for industrial applications or be a benchmark for further developments in this particular area. After this assessment, the following was concluded:

* Based on the magnitude of the Eo_G, Re_L and Fr_G, diverse bubble formation regimes can occur. The regimes found were: single bubbling, pulse bubbling and jetting, which consists of two sub-regimes, elongated jetting and atomizing jetting. It was determined that the shift between regimes does not occur instantly, hence two transition regions, single bubbling-pulse and pulse-to-jetting, were defined.

* The bubbling regimes were presented in a set of bubble regime maps Eo_G vs Fr_G, which are comparable to those presented in similar works. The contribution of the current study is the inclusion of the liquid cross-flow velocity, represented by Re_L, and its effects on the transition between bubbling modes. These maps show that the bubbling process does not depend exclusively on the gas mass flow rate, but the nozzle dimensions and liquid-cross flow velocity as well.

* A continuous increase in Fr_G causes a transition from the single bubbling regime towards the pulsating and jetting regimes respectively. The atomizing jetting regime was observed only at $Eo_G = 0.01$ and for $Re_L \leq 24{,}000$.

* The liquid cross-flow momentum is a key factor in the bubble formation under discrete modes (single bubbling and pulse bubbling). As Re_L was increased, the number of bubbling regimes decreased. At $Re_L = 56{,}000$, the bubbling regimes was limited to four bubbling modes, where the transitional pulse-to-jetting region was the evolved regime that could be observed.

* An increase in the Eo_G, which implied an increase in the nozzle diameter, induced a reduction in the number of regimes observed. When $Eo_G = 0.34$, a fully developed jetting mode was not observed, which indicated that the bubbling transitions do not depend exclusively on the gas mass flow rate, but the orifice dimensions as well.

* The evaluation of existing correlations that predict D_{32} as a function of the bubbling regime gave inadequate agreement with the experimental data. It was concluded that the main source of disparity was the assumption that a simplified momentum balance would mimic the complex process of bubble formation, without considering the effect that the nozzle dimensions or fluid properties have on the gas-liquid dynamics.

* The limited data existing in the literature about the bubbling regime charts, did not allow a direct comparison of the regime maps presented. The majority of the works focus on the development of mathematical models and experiments about the SB regime, which occurs under particular configurations of Fr_G and Re_L. Although the applicability of the SB regime is relevant, it might not be useful to industrial processes where larger Fr_G values are required.

8. Final Considerations

8.1. Summary of Conclusions

Few existing studies on the internal fluid mechanics of an effervescent atomizer have focused exclusively on adapting techniques from comparable scenarios, such as pipe flow, to the design of atomizers and the analysis of the atomization process. Moreover, the centre of attention has been on the study of flow patterns inside the conduit. While this is of practical interest, this kind of approach considers scenarios (annular flow, intermittent flow) that, as discussed by Chin and Lefevbre (1995) and Sovani *et al.* (2001), depart from the essence of effervescent atomization. Despite the relevancy of the gas injection conditions to the atomization process, scarce information exists about the bubble formation process under conditions which extend beyond the discrete bubble mode.

Therefore, the motivation of the current research was to study the fluid mechanics upstream of the discharge nozzle in an effervescent atomizer. Specifically, the focus was on expanding the current knowledge in what was categorized as regions (I) to (III) inside the atomizer: from the process of gas injection and bubble formation, to subsequent bubble development, to the evolution of the two-phase flow inside a confined space. In general terms, this was achieved by means of evaluating the effect that key design variables, such as nozzle diameter, liquid cross-flow velocity and gas injection velocity, have in the process of gas injection into a liquid cross-flow and on the bubble dynamics.

This study encompassed an integral method of evaluating the gas-liquid interaction as well as an assessment of the formation and evolution of bubbles within a horizontally-oriented conduit of square shape. A wide array of experimental conditions was covered. Three gas injector diameters (0.27 mm, 0.52 mm and 1.59 mm) were used; the liquid cross-flow velocities ranged from 1.3 m/s to 4.3 m/s and gas mass flow rates were encompassed between 0.5 to 3.0 SLPM. The findings presented can be of interest for a better understanding of the underlying physical mechanisms of gas-liquid mixing as well as for improving the efficiency of industrial atomizer applications. A summarized version of the conclusions obtained from each individual chapter is presented next:

* This study presented reliable evidence that the probability distribution of the gas phase within the liquid near the gas injector can be described by empirical correlations analogous to those used in canonical jets in counter flow. This methodology is a breakthrough contribution for gas jets in flowing liquids. Contrary to many other JICF scenarios, the correlations introduced in this study incorporate the effects of key dimensionless numbers related to GJILCF (Fr_G, Re_L and Eo_G). An assessment of standard JICF correlations gave highly unpredictable results, while the GJILCF correlations presented allow for a complete estimation of both the maximum probability distribution as well as the extent of the gas phase spreading in the liquid flow. The GJILCF expressions are power-law relations of the form:

$$\left(\frac{y}{D_{\text{channel}}} \right)_{\substack{\text{Centreline} \\ \text{Bottom wall}}} = 3.88 \left(Eo_{\text{G}} \right)^{0.18} \left(\frac{x}{D_{\text{channel}}} \right)^{3.10 Re_{\text{L}}^{-0.14}} \left(Fr_{\text{G}} \right)^{0.16} \left(Re_{\text{L}} \right)^{-0.38}$$

$$\left(\frac{y}{D_{\text{channel}}} \right)_{\substack{\text{Centreline} \\ \text{Top wall}}} = 0.32 \left(Eo_{\text{G}} \right)^{0.25} \left(\frac{x}{D_{\text{channel}}} \right)^{3.4 \times 10^{-6} Re_{\text{L}}^{1.1}} \left(Fr_{\text{G}} \right)^{0.26} \left(Re_{\text{L}} \right)^{-0.19}$$

$$\left(\frac{y}{D_{\text{channel}}} \right)_{\substack{\text{Borderline} \\ \text{Bottom wall}}} = 1.27 \left(Eo_{\text{G}} \right)^{0.24} \left(\frac{x}{D_{\text{channel}}} \right)^{2.50 Re_{\text{L}}^{-0.14}} \left(Fr_{\text{G}} \right)^{0.16} \left(Re_{\text{L}} \right)^{-0.23}$$

$$\left(\frac{y}{D_{\text{channel}}} \right)_{\substack{\text{Borderline} \\ \text{Top wall}}} = 0.19 \left(Eo_{\text{G}} \right)^{0.20} \left(\frac{x}{D_{\text{channel}}} \right)^{5.9 \times 10^{-4} Re_{\text{L}}^{0.59}} \left(Fr_{\text{G}} \right)^{0.30} \left(Re_{\text{L}} \right)^{-0.11}$$

It was found that for $Re_{\text{L}} \approx 24000$, the gas injection conditions played a dominating role on the trajectory of the incipient gas jet. As Re_{L} was increased, the effects of the liquid cross-flow became dominant for the gas plume mechanics near the injector, as was observed for $Re_{\text{L}} \approx 56000$. The results yielded reliable estimations for the wide array of experimental scenarios tested, as indicated by the relatively small mean errors. The knowledge of the gas-liquid mixing near the injector and possible interactions with the opposite wall are of practical interest for the design of effervescent atomizers.

* This study introduced an innovative method for the estimation of the different forces involved in the gas jet growth in a flowing liquid. This exploratory approach highlighted the high number of empiricisms and assumptions required to estimate the magnitude of the forces affecting the gas jet, particularly regarding the estimation of the hydrodynamic

coefficients. Despite the vast number of previous works on bubble formation dynamics in flowing liquids, very little agreement about the definition of the various forces involved on the growth and development of bubbles. It was concluded that assuming key parameters, such as the drag, lift and added mass coefficients, as constants would yield inaccurate estimations of key dynamic effects. Haider and Levenspiel (1989), Ishii and Hibiki (2010) and Kendoush (2006) presented the only expressions where C_D and C_M account for changes in the bubble volume.

* This study proved that the form-induced drag and the inertial force were the main detaching and attaching forces respectively. There is agreement with previous authors that consider the drag to be the principal detaching force. However, the surface tension is commonly assumed as the dominant cohesive effect and it was proven that this does not apply to gas jetting scenarios. Therefore, a simplified dynamic balance for the estimation of the gas jet growth is given by

$$F_D \approx F_I$$

$$\frac{1}{2}\rho_L C_D \sqrt{\left(\frac{d\mathbf{S}}{dt}-U_L\mathbf{x}\right)^2}\left(\frac{d\mathbf{S}}{dt}-U_L\mathbf{x}\right) \approx \frac{d}{dt}\left(\rho_G V_G \frac{d\mathbf{S}}{dt}\right)+\frac{d}{dt}\left[\rho_L C_M V_G \left(\frac{d\mathbf{S}}{dt}-U_L\mathbf{x}\right)\right]$$

where C_D and C_M are to be estimated instantaneously to account for the changes due to the gas jet growth. The magnitude of the forces on the horizontal dimension is at least an order magnitude higher than those in the vertical axis.

* The experimental analysis revealed that the gas jet breakup is not periodic. Both the bubbling frequency and the gas jet average length occurred irregularly but within well defined limits. It was determined that the averaged dimensionless gas jet length could be estimated from a power-law correlation of the form

$$\chi_{\text{break}} = aEo_{\text{G}}^{b} \left(M_{ratio}'' \right)^{c} \left(Re_{\text{L}} \right)^{d}$$

where the coefficients a, b, c and d depend on the location of the gas injector. Disregarding the outlier points, this correlation can predict the average χ_{break} with a mean absolute error of 8%. Similar expressions were obtained for the minimum and maximum χ_{break} values. At high liquid velocities, U_{L} = 4.3 m/s, and small D_{inj}, 0.27 and 0.52 mm, the jet breakup length oscillation decreases, limiting the range of values measured.

A comparable correlation was obtained for the estimation of the bubbling frequency for liquid cross-flow velocities above 3.1 m/s. The mean deviation between measurements and correlation was 5.2% with a maximum scatter of 22%, which occurred only for very limited conditions.

* This study proved that the diameter of the bubbles upstream of the nozzle is linked to the bubble dimensions after they separate from the gas jet. After detachment, the ratio D_{99}/D_{32} ranged from 1.5 to 1.8; values close to those reported by other researchers. The key statistical diameters (D_{99}, D_{32}) upstream of the discharge nozzle were between 0.60 to 0.75

times the diameters measured after detachment. The same D_{99}/D_{32} ratio was observed upstream of the nozzle which indicates that, even though bubble breakup occurs, the bubble diameter distribution preserves similarity with the near injector conditions.

It was also shown that the average diameter of the gas jet can be estimated with acceptable accuracy by a correlation based on fundamental dimensionless numbers of the form

$$D_{equiv}\Big/D_{\mathrm{H}} = k_1\left(Re_{\mathrm{L}}^{-0.52}\right)\left(Fr_{\mathrm{G}}\right)^{0.84}\left(Eo_{\mathrm{G}}\right)^{0.81}$$

where k_1 can take a value of 9.8 or 9.2 based on whether the injector position is on the top or bottom wall. Several correlations that estimate D_{32} and D_{99} based on Re_{L}, Fr_{G} and Eo_{G} were obtained. The D_{99} correlation was compared to the equation presented by Hesketh et al. (1987) and Andreussi et al. (1999). It was proven that pipe flow correlations do not fully account for the fluid dynamics inside an effervescent atomizer.

* Four clearly defined regimes of bubble formation were recognized: Single Bubbling, Pulse, Elongated Jetting and Atomizing Jetting. It was shown that the shift between regimes does not occur instantly and it is necessary to define transition regions. The bubbling modes depend not only on the operating conditions but also on the nozzle dimensions. Regime maps based on dimensionless numbers were proposed with the purpose of presenting innovative tools, specific for effervescent atomizers, which allow the identification of the regime of operation.

A correlation that provides a reliable limit between the maximum stable bubble formation and the jetting regimes was proposed. This correlation is the power-law expression

$$Fr_\alpha = 290 \left(Re_{\mathrm{L}}^{-0.25} \right) \left(Eo_{\mathrm{G}}^{-0.90} \right)$$

which indicates that for Fr_{G} numbers higher than Fr_α, the bubbling mode would occur as a jetting, where the bubble diameters are more difficult to control and estimate.

Lastly, it is considered of fundamental interest to highlight that even though the results obtained from the present work were presented in the form of empirical correlations based on dimensionless numbers, there was no "true" variation of the dimensionless parameters used. Since the hydraulic diameter of the chamber was constant and the liquid physical properties were not changed, a variation of the Re_{L} inherently referred to a change in the magnitude of U_{L}. Similarly, the changes in Fr_{G} could be primarily associated to a variation in the gas mass flow rate and the variations in the Eo_{G} refer to the changes in the nozzle injection dimensions.

Changes in the physical properties of the fluids used would have provided a more solid ground for correlations based on dimensionless parameters and the general applicability of the results obtained. However, presenting the empirical correlations as a function of dimensionless numbers was justified in the fact that it provides a better understanding about

the underlying physical phenomena involved as well as an easier way of assessing and extending the results obtained to future studies associated to GJILCF.

8.2. Applicability of the Results Obtained to the Spray Region in Effervescent Atomizers

As was argued in Chapter 1 of this thesis, the existing knowledge about the internal flow in an effervescent atomizer is scarce. It was proven that understanding the characteristics of the gas-liquid two-phase flow inside an effervescent atomizer is fundamental because the nature of the flow passed through the discharge nozzle will determine the performance in the spray region. Despite this, it has been a common misconception in the analysis of effervescent atomizers to treat the internal flow by following a "black box" approach of try to establish analogies with pipe flow behaviour.

Undoubtedly, the results obtained in this work could be of great interest for the effervescent atomization community, because as was discussed at several points during this work, they expand on a topic that has not been investigated rigorously before. Some of the specific contributions to the field of effervescent atomization are:

* It was proven that the characteristics under which the bubbles are formed have a fundamental influence in the characteristics of the flow that is fed to the discharge nozzle, which in turns controls the spray performance. Therefore, the spray dynamics are going to

be inherently affected by the bubbling dynamics. Key design parameters estimated in this study, such as D_{32} and D_{99}, still indicate a lasting effect of the bubbling dynamics on the gas-liquid flow.

Considering that the ligament formation at the exit nozzle and the subsequent droplet creation process are controlled by the size of bubbles passing through the discharge orifice, identifying how the bubbling characteristics affect the two-phase flow passing through the nozzle is essential for establishing a comprehensive model for effervescent atomization (Sovani et al., 2001). Although there is a wealth of information about the spray region, limited data is contained in the literature about bubble sizes in effervescent atomization.

The results obtained in this study represent an important contribution to this topic. The bubbling process was thoroughly quantified and linked to the gas-liquid flow that is being fed to the discharge orifice. The correlations, based on a simple presentation of the most relevant dynamic forces interacting at the gas injection region, connect the flow evolution between two fundamental areas inside the mixing chamber. Knowing the statistically relevant diameters after the disintegration of the gas jet (D_{32} and D_{99}) and how they are going to evolve at certain mixing length within the chamber could be of great applicability for the design of effervescent atomizers. Also, having an estimation of the averaged D_{32} and D_{99} passing through the nozzle is fundamental for the nozzle geometry design, specifically the exit diameter and the length. As was described in Chapter 1, there is a direct association between the D_{32} of the bubbles that are discharged and the performance of the spray.

* While the use of pipe flow regime maps constitutes the most commonly used approach to choose the parameters that indicate the existence of a bubbly flow inside the mixing chamber, it was determined that this is inherently incorrect. The flow inside an effervescent atomizer is transient, accelerating and without a doubt non-developed; a balance between breakup and coalescence is difficult to achieve because of the short flow development distance available in the atomizer.

Instead of utilizing fully developed pipe flow maps as a design tool, a more adequate approach would be the use of the bubbling regime maps introduced in Chapter 7. These maps correspond to bubble flow (Andreussi et al., 1999), which is an advantageous feature for effervescent atomizers. Interestingly, even though all the scenarios depicted in the maps introduced in Figure 7.6 correspond to a bubble flow, there is a markedly different behaviour between them. These characteristics are preserved along the flow transition towards, which reinforces the necessity of understanding the bubbling characteristics, as they affect the characteristics in the spray region.

The advantage of using bubbling maps over pipe flow regime maps is that they allow the estimation of the specific characteristics of bubbling. Instead of the general approach of what constitutes a bubble flow, it is possible to estimate the bubbling regime from the knowledge of key non-dimensional numbers associated to this type of application. While the result shown cannot claim generality, the use of non-dimensional parameters was used to simplify the results and to facilitate the comparison with other studies.

* The gas phase probability distribution in a liquid cross-flow, as shown in Chapter 3, is fundamental from an integral point of view to have a better understanding about the mixing between phases. Although this approach does not allow the estimation of specific information such as bubble diameter distribution, bubbling regime or specific features of the gas jet, it can be used in the design of effervescent atomizers to determine the possibility of interaction between multiple gas jets in a liquid cross-flow or the interaction of the gas jet with bubbles present in the conduit. Knowledge about the gas phase borderline trajectory allows the determination of the possible interaction between the gas stream and the opposite wall from which the gas is injected. By combining the centerline and borderline trajectories it is possible to estimate the extent of the gas phase dispersion along the channel and compare it with theoretical models and/or computational simulations.

8.3. Recommendations

* It is mandatory to conduct test under similar operating conditions but with different atomizer configurations, such as different development length, chamber diameter, nozzle location and number of injection ports. The dependence of the results presented on the atomizer geometry could be explored.

* The set of correlations proposed (gas jet dimensions, bubbling frequency, bubble diameter estimations) must be tested for experimental configurations different to the ones

used to verify for wider applicability. The testing with different operating fluids is recommended as well.

* It is imperative to estimate the magnitude of turbulence parameters related to the liquid cross-flow (intensity, energy dissipation rate) to determine experimentally their effect on the bubbling process.

* Exploring the advantages that other experimental techniques could add when compared to high-speed shadowgraphy is highly suggested. While the use of PIV does not allow a complete time-based approach, it can certainly contribute to a better understanding of the liquid flow field upstream of the injector as well as the coupling between phases during its transition towards the discharge nozzle. Full knowledge of the liquid flow velocity profile would provide invaluable benefits for the understanding of fundamental processes such as the hydrodynamic drag acting on the gas jet and the behavior of the gas-liquid interphase.

References

Akagi, Y., Okada, K., Kosaka, K., Takahashi, T., 1987. Liquid weeping accompanied by bubble formation at submerged orifices. Ind. Eng. Chem. Res. 26, 1546–1550.

Akbar, M.K., Plummer, D. a., Ghiaasiaan, S.M., 2003. On gas–liquid two-phase flow regimes in microchannels. Int. J. Multiph. Flow 29, 855–865.

Al-Hayes, R.A.M., Wonterton, R.H.S., 1981. Bubble Diameter on Detachment in Flowing Liquids. Int. J. Heat Mass Transf. 24, 223–230.

Amighi, A., Eslamian, M., Ashgriz, N., 2009. Trajectory of a Liquid Jet in High Pressure and High Temperature Subsonic Air Crossflow, in: ICLASS.

Andersson, R. & Andersson, B., 2006a. Modeling the Breakup of Fluid Particles in Turbulent Flows. Am. Inst. Chem. Eng. J. 52, 2031–2038.

Andersson, R. & Andersson, B., 2006b. On the Breakup of Fluid Particles in Turbulent Flows. AIChE J. 52, 2020–2030.

Andreopoulos, J., Rodi, W., 1984. Experimental investigation of jets in a crossflow. J. Fluid Mech. 138, 93–127.

Andreussi, P., Paglianti, A. & Sanchez S., F., 1999. Dispersed bubble flow in horizontal pipes. Chem. Eng. Sci. 54, 1101–1107.

Ashgriz, N., 2012. Atomization of a liquid jet in a crossflow 33, 33–46.

Azizi, F., Al Taweel, a. M., 2007. Population balance simulation of gas–liquid contacting. Chem. Eng. Sci. 62, 7436–7445.

Badam, V.K., Buwa, V., Durst, F., 2007. Experimental Investigations of Regimes of Bubble Formation on Submerged Orifices Under Constant Flow Condition. Can. J. Chem. Eng. J. Chem. Eng. 85, 257–267.

Bhunia, A., Pais, S.C., Kamotani, Y., Kim, I.-H., 1998. Bubble Formation in a Coflow Configuration in Normal and Reduced Gravity. AIChE J. 44, 1499–1509.

Bowers, R.H., 1955. The mechanics of bubble formation. J. Appl. Chem. 5, 542–548.

Brennen, C.E., 1995. Cavitation and Bubble Dynamics., 1st ed, Ultrasonics sonochemistry. Oxford University Press, New York, NY.

Brennen, C.E., 2005. Introduction to Multiphase Flow., 1st ed, Fundamentals of Multiphase Flows. Cambridge University Press, New York, NY.

Broadwell, J.E., Breidenthal, R.E., 1984. Structure and mixing of a transverse jet in incompressible flow. J. Fluid Mech. 148, 405–412.

Cai, Q., Shen, X., Shen, C., Dai, G., 2010. A simple method for identifying bubbling/jetting regimes transition from large submerged orifices using electrical capacitance tomography (ECT). Can. J. Chem. Eng. 88.

Chai, T., Draxler, R.R., 2014. Root mean square error (RMSE) or mean absolute error (MAE)? - Arguments against avoiding RMSE in the literature. Geosci. Model Dev. 7, 1247–1250.

Chakraborty, I., Biswas, G., Ghoshdastidar, P.S., 2011. Bubble generation in quiescent and co-flowing liquids. Int. J. Heat Mass Transf. 54, 4673–4688.

Chin, J.S., Lefebvre, A.H., 1995. A Design Procedure for Effervescent Atomizers. J. Eng. Gas Turbines Power 117, 266–271.

Chin, J. S. and Lefebvre, A.H., 1993. Flow Patterns in Internal Mixing, Twin-Fluid Atomizers. At. Sprays 3, 463–475.

Chow, C.Y., 1980. An Introduction to Computation Fluid Dynamics. Wiley, N.Y.

Crowe, C.T., 2006. Chapter 1: Basic Concepts and Definitions, in: Multiphase Flow Handbook.

Crowe, C.T., 2006. Multiphase Interactions, in: Group, T.& F. (Ed.), Multiphase Flow Handbook. CRC Press, Boca Raton, Florida.

Das, A.K., Das, P.K., Saha, P., 2011. Formation of bubbles at submerged orifices – Experimental investigation and theoretical prediction. Exp. Therm. Fluid Sci. 35, 618–627.

Diez, F.J., Torregrosa, M.M., Pothos, S., 2011. A Comparison Between Round Turbulent Jets and Particle-Laden Jets in Crossflow by Using Time-Resolved Stereoscopic Particle Image Velocimetry. J. Fluids Eng. 133, 091301.

Duhar, G., Colin, C., 2006. Dynamics of bubble growth and detachment in a viscous shear flow. Phys. Fluids 18, 077101.

Ferreira, G., Garcia, J., Barreras, F., Lozano, A, Lincheta, E., 2009. Design optimization of twin-fluid atomizers with an internal mixing chamber for heavy fuel oils. Fuel Process. Technol. 90, 270–278.

Forrester, S.E., Rielly, C.D., 1998. Bubble formation from cylindrical, flat and concave sections exposed to a strong liquid cross-flow. Chem. Eng. Sci. 53, 1517–1527.

Gavrilakis, S., 1992. Numerical simulation of low-Reynolds-number turbulent flow through a straight square duct. J. Fluid Mech. 244, 101–129.

Ghaemi, S., Rahimi, P., Nobes, D.S., 2010. Effect of Bubble Generation Characteristics on Effervescent Atomization at Low Gas-Liquid Ratio Operation. At. Sprays 20, 211–225.

Gutmark, E.J., Ibrahim, I.M., Murugappan, S., 2010. Dynamics of single and twin circular jets in cross flow. Exp. Fluids 50, 653–663.

Haider, A., Levenspiel, O., 1989. Drag Coefficient and Terminal Velocity of Spherical and Nonspherical Particles. Powder Technol. 58, 63–70.

Harby, K., Chiva, S., Muñoz-Cobo, J.L., 2014. An experimental investigation on the characteristics of submerged horizontal gas jets in liquid ambient. Exp. Therm. Fluid Sci. 53, 26–39.

Hesketh, R.P., Fraser Russell, T.W., Etchells, a. W., 1987. Bubble size in horizontal pipelines. AIChE J. 33, 663–667.

Hinze, J.O., 1955. Fundamentals of the hydrodynamic mechanism of splitting in dispersion processes. AIChE J. 1, 289–295.

Huang, X., Wang, X., Liao, G., 2008. Visualization of two phase flow inside an effervescent atomizer. J. Vis. 11, 299–308.

Iguchi, M., Terauchi, Y., Yokoya, S.-I., 1998. Effect of cross-flow on the frequency of bubble formation from a single-hole nozzle. Metall. Mater. Trans. B 29, 1219–1225.

Ishii, M., Hibiki, T., 2010. Thermo-Fluid Dynamics of Two-Phase Flow.

Ishii, M., Zuber, N., 1979. Drag Coefficient and Relative Velocity in Bubbly, Droplet or Particulate Flows. AIChE J. 25, 843–855.

Ishkintana, L.K., Bennington, C.P.J., 2010. Bubble shape, gas flow and gas-liquid mass transfer in pulp fibre suspensions. Can. J. Chem. Eng. 88, 322–328.

Jedelsky, J., Jicha, M., 2006. Unsteadiness in Effervescent Sprays - Measurement and Evaluation Using Combined PIV-PLIF Technique, in: 13th Int. Symp on Applications of Laser Techniques to Fluid Mechanics. Lisbon, Portugal, p. 12.

Jedelsky, J., Jicha, M., Slama, J., Otahal, J., 2009. Development of an Effervescent Atomizer for Industrial Burners. Energy & Fuels 23, 6121–6130. Jedelsky, J. & Jicha, M., 2008.

Kamotani, Y., Greber, I., 1974. Experiments on Confined Turbulent Jets in Cross Flow.

Kandakure, M.T., Patkar, V.C., Patwardhan, A.W., Patwardhan, J. a., 2009. Mixing with Jets in Cross-Flow. Ind. Eng. Chem. Res. 48, 6820–6829.

Kantarci, N., Borak, F., Ulgen, K.O., 2005. Bubble column reactors. Process Biochem. 40, 2263–2283.

Karagozian, A.R., 2010. Transverse jets and their control. Prog. Energy Combust. Sci. 36, 531–553.

Kawase, Y., Ulbrecht, J.J., 1981. Formation of drops and bubbles in flowing liquids. Ind. Eng. Chem. Process Des. Dev. 20, 636–640.

Kendoush, A., 2007. The virtual mass of an oblate-ellipsoidal bubble. Phys. Lett. A 366, 253–255.

Kikkert, G.A., 2006. Buoyant Jets with Two and Three-Dimensional Trajectories. University of Canterbury.

Kim, J.H., 1985. An Analytical Mixing Model for Buoyant Jet Injected Into Pipe Flow. J. Heat Transfer 107, 630–635.

Kim, J.Y., Lee, S.Y., 2001. Dependence of Spraying Performance on the Internal Flow Pattern in Effervescent Atomizers. At. Sprays 11, 735–756.

Klausner, J.F., Mei, R., Bernhard, D.M., Zeng, L.Z., 1993. Vapor bubble departure in forced convection boiling. Int. J. Heat Mass Transf. 36, 651–662.

Konstantinov, D.; Marsh, R.; Bowen, P. & Crayford, A., 2010. Effervescent Atomization for Industrial Energy-Technology Review. At. Sprays 20, 525–552.

Kulkarni, A. a., Joshi, J.B., 2005. Bubble Formation and Bubble Rise Velocity in Gas−Liquid Systems: A Review. Ind. Eng. Chem. Res. 44, 5873–5931.

Kyriakides, N.K., Kastrinakis, E.G., Nychas, S.G., Goulas, A., 1997. Bubbling from Nozzles Submerged in Water: Transitions Between Bubbling Regimes. Can. J. Chem. Eng. 75, 684–691.

Lefebvre, A.H., 1996. Some Recent Developments in Twin-Fluid Atomization. Part. Part. Syst. Charact. 13, 205–216.

Legendre, D., Magnaudet, J., 1998. The lift force on a spherical bubble in a viscous linear shear flow. J. Fluid Mech. 368, 81–126.

Liao, Y., Lucas, D., 2009. A literature review of theoretical models for drop and bubble breakup in turbulent dispersions. Chem. Eng. Sci. 64, 3389–3406.

Liu, C., Liang, B., Tang, S., Zhang, H., Min, E., 2010. A Theoretical Model for the Size Prediction of Single Bubbles Formed under Liquid Cross-flow. Chinese J. Chem. Eng. 18, 770–776.

Liu, Y., Lee, D.Y., Roy, T., Ishii, M., Buchanan, J.R., 2013. The development of two-phase flow structures in air–water planar bubble jets. Int. J. Multiph. Flow 56, 25–39.

Loth, E., Faeth, G.M., 1990. Structure of plane underexpanded air jets into water. AIChE J. 36, 818–826.

Loubière, K., Castaignede, V., Hebrard, G., Roustan, M., 2004. Bubble formation at a flexible orifice with liquid cross-flow. Chem. Eng. Process. 43, 717–725.

Machniewski, P.M., Bin, A.K., Evans, G.M., 2004. Bubble Formation at a Rotating Cylindrical Surface in Cross-Flowing Liquid. Can. J. Chem. Eng. 82, 442–449.

Magnaudet, J., 2003. Small inertial effects on a spherical bubble, drop or particle moving near a wall in a time-dependent linear flow. J. Fluid Mech. 485, 115–142.

Magnaudet, J., Takagi, S. & Legendre, D., 2003. Drag, deformation and lateral migration of a buoyant drop moving near a wall. J. Fluid Mech. 476, 115–157.

Marshall, S.H., 1990. Air bubble formation from an orifice with liquid cross-flow. University of Sydney.

Marshall, H. S., Chudacek, M.W.&, Bagster, D.F., 1993. A Model for Bubble Formation from an Orifice with Liquid Cross-Flow. Chem. Eng. Sci. 48, 2049 – 2059.

Mashayek, A., Ashgriz, N., 2011. Atomization of a Liquid Jet in a Crossflow, in: Ashgriz, N. (Ed.), Handbook of Atomization and Sprays. Springer, pp. 657–683.

Mazzitelli, I., 2003. Turbulent bubbly flow. PhD Thesis. University of Twente.

McCann, D.J., Prince, R.G.H., 1971. Regimes of bubbling at a submerged orifice. Chem. Eng. Sci. 26, 1505–1512.

Melling, A., Whitelaw, J.H., 1976. Turbulent flow in a rectangular duct. J. Fluid Mech. 78, 289–315.

Miyahara, T., Iwata, M. & Takahashi, T., 1984. Bubble Formation Pattern with Weeping at a Submerged Orifice. J. Chem. Eng. Japan 17, 592 – 597.

Muppidi, S., Mahesh, K., 2005. Study of trajectories of jets in crossflow using direct numerical simulations. J. Fluid Mech. 530, 81–100.

Nahra, H.K., Kamotani, Y., 2003. Prediction of bubble diameter at detachment from a wall orifice in liquid cross-flow under reduced and normal gravity conditions. Chem. Eng. Sci. 58, 55–69.

Nahra, Henry & Kamotani, Y., 2000. Bubble formation from wall orifice in liquid cross-flow under low gravity. Chem. Eng. Sci. 55, 4653–4665.

New, T.H., Lim, T.T., Luo, S.C., 2006. Effects of jet velocity profiles on a round jet in cross-flow. Exp. Fluids 40, 859–875.

Oguz, H.N., Prosperetti, A., 1993. Dynamics of bubble growth and detachment from a needle. J. Fluid Mech. 257, 111–145.

Ohl, C.D., Tijink, A., Prosperetti, A., 2003. The added mass of an expanding bubble. J. Fluid Mech. 482, 271–290.

Oryall, G.N., Brimacombe, J.K., 1976. The Physical Behavior of a Gas Jet Injected Horizontally into Liquid Metal. Metall. Trans. B. 7B, 391–403.

Pope, S.B., 2000. Turbulent Flows. Cambridge University Press.

Pratte, W.D., Baines, W.D., 1967. Profiles of the Round Turbulent Jet in a Cross Flow. J. Hydronautic Div. ASCE 92.

Ragucci, R., Bellofiore, A., Cavaliere, A., 2007. Trajectory and Momentum Coherence Breakdown of a Liquid Jet in High-Density Air Cross-Flow. At. Sprays 17, 47–70.

Rahman, M.A., Balzan, M., Heidrick, T., Fleck, B.A., 2012. Effects of the gas phase molecular weight and bubble size on effervescent atomization. Int. J. Multiph. Flow 38, 35–52.

Ramamurthi, K., Sarkar, U. K. & Raghunandan, B.N., 2009. Performance Characteristics of Effervescent Atomizer in Different Flow Regimes. At. Sprays 19, 41–56.

Razzaque, M.M., Afacan, A., Liu, S., Nandakumar, K., Masliyah, J., Sanders, R.S., 2003. Bubble size in coalescence dominant regime of turbulent air–water flow through horizontal pipes. Int. J. Multiph. Flow 29, 1451–1471.

Rigby, G.D., Evans, G.M., Jameson, G.J., 1995. Modelling of Gas Flow from a Submerged Orifice in Liquid Cross-Flow. Chem. Eng. Res. Des. 73a, 234–240.

Rudman, M., 1996. Simulation of the Near Field of a Jet in a Cross Flow, Exp. Thermal and Fluid Science, 1777, 134–141.

Sada, E., Yasunishi, A., Katoh, S., Nishioka, M., 1978. Bubble Formation in Flowing Liquid. Can. J. Chem. Eng. 56, 669–672.

Sallam, K. A., Aalburg, C., Faeth, G.M., 2004. Breakup of Round Nonturbulent Liquid Jets in Gaseous Crossflow. AIAA J. 42, 2529–2540.

Sato, M., Sadatomi, M., Sekoguchi, K., 1981. Momentum and Heat Transfer in Two-Phase Bubbly Flow. Int. J. Multiph. Flow 7.

Schetz, J.A., Fuhs, A.E., 1999. Fundamentals of Fluid Mechanics, 1st ed. Wiley-Interscience.

Sen, D., Balzan, M. A., Nobes, D.S., Fleck, B. A., 2014. Bubble formation and flow instability in an effervescent atomizer. J. Vis. 17, 113–122.

Silberman, E., 1957. Production of Bubbles by the Disintegration of Gas Jets in Liquid, in: Proceedings of the 5th Midwestern Conference on Fluid Mechanics. p. 263.

Smith, S.H., Mungal, M.G., 1998. Mixing, structure and scaling of the jet in crossflow. J. Fluid Mech. 357, 83–122.

Sovani, S.D., 2001. High pressure gas-liquid flow inside an effervescent diesel injector and its effects on spray characteristics. Purdue University.

Sullivan, S. L., J., Hardy, B.W., Holland, C.D., 1964. Formation of Air Bubbles at Orifices Submerged Beneath Liquids. Am. Inst. Chem. Eng. J. 10, 848–854.

Tan, R. B. H., Chen, W.B.& T.K.H., 2000. A non-spherical model for bubble formation with liquid cross-flow. Chem. Eng. Sci. 55, 6259–6267.

Thomas, R.M., 1981. Bubble Coalescence in Turbulent Flows. Int. J. Multiph. Flow 7, 709–717.

Thorat, B.N., Joshi, J.B., 2004. Regime transition in bubble columns: experimental and predictions. Exp. Therm. Fluid Sci. 28, 423–430.

Thorncroft, G.E., Klausner, J.F., Mei, R., 2001. Bubble forces and detachment models. Multiph. Sci. Technol. 13, 35–76.

Townsend, A.A., 1976. The Structure of Turbulent Shear Flow, 2nd. ed. Cambridge University Press.

Tsuge, H., Hibino, S.-I., 1983. Bubble Formation From an Orifice Submerged in Liquids. Chem. Eng. Commun. 22, 63–79.

Wace, P.F., Morrell, M.S., Woodrow, J., 1987. Bubble Formation in a Transverse Horizontal Liquid Flow. Chem. Eng. Commun. 62, 93–106.

Wallis, G.B., 1969. One-Dimensional Two-Phase Flow.

Weiland, C., Vlachos, P.P., 2013. Round gas jets submerged in water. Int. J. Multiph. Flow 48, 46–57.

White, F. M., 2005. Viscous Fluid Flow. 2nd Edition. McGraw Hill. Pp. 652.

Xiao, Y., Tang, H., Liang, D., Zhang, J., 2011. Numerical study of hydrodynamics of multiple tandem jets in cross flow. J. Hydrodyn. Ser. B 23, 806–813.

Yu, D., Ali, M.S., Lee, J.H.W., 2006. Multiple Tandem Jets in Cross-Flow. J. Hydraul. Eng. 132, 971–983.

Yuan, L.L., Street, R.L., 1998. Trajectory and entrainment of a round jet in crossflow. Phys. Fluids 10, 2323–2335.

Zhang, W., 2003. A model for bubble formation and weeping at a submerged orifice with liquid cross-flow. Chem. Eng. Sci. 58, 287–295.

Zhu, M.-Y., Sawada, I., Manabu, I., 1998. Physical Characteristics of a Horizontally Injected Gas Jet and Turbulent Flow in Metallurgical Vessels. ISIJ Int. 38, 411–420.

Zhukovskaya, O., 2012. Studies of Small Air Bubble Motion in Turbulent Pipe Flow. PhD Thesis, University of Calgary.

Appendix A. Uncertainty analysis associated to the imaging process

Due to the steps followed during the capture of the shadowgraphs and the image analysis process, a different number of uncertainties were introduced in the estimation of the different geometrical variables. The parameters of interest determined during this study were included in Table A.1, with its corresponding definition. The projected area (A_{proj}) and perimeter (*Per*) of the object within the image were calculated using the Matlab built-in tool *regionprops*.

Table A.1.   Definition of the geometrical parameters used in the characterization of the gas jets and bubbles

A_{proj} = total # pixels	(A.1)	$D_{\text{equiv}} = \sqrt{\dfrac{4A_{\text{proj}}}{\pi}}$	(A.2)
Per = distance around object border	(A.3)	$V_{\text{G}} = A_{\text{proj}}D_{\text{W}}$	(A.4)

Generally, the interest region had an associated field of view equal to 1000×168 pixels^2, which corresponded to an area approximately equal to $73 \times 12.5 = 912.5$ mm^2. The gas jets and bubbles were confined within this region; therefore all the objects identified by the imaging algorithm were necessarily of a size smaller than A_{FOV}. The error for any area related quantity was assigned a value of 1 pixel row or 1 pixel column. This was defined as the maximum area associated error or $(\mathrm{d}A_{\text{proj}})_{\text{max}}$ was defined according to equation (A.5) and as observed considered that the maximum area deviation was equal to $0.094A_{\text{FOV}}$.

$$(\mathrm{d}A_{\mathrm{proj}})_{\mathrm{max}} = (\text{max hor. length} + \text{max ver. length})\mathrm{mm}^2 = 85.5\ \mathrm{mm}^2 \qquad (\text{A.5})$$

Duhar and Colin (2006) proposed that the error associated to the image processing comprises the errors associated to the filtering operation, the binarisation process and due to the calibration. When added, this provided the total error associated to the projected area and was defined according to equation (A.6).

$$(\mathrm{d}A_{\mathrm{proj}})_{\mathrm{total}} = (\mathrm{d}A_{\mathrm{proj}})_{\mathrm{filtering}} + (\mathrm{d}A_{\mathrm{proj}})_{\mathrm{calibration}} + (\mathrm{d}A_{\mathrm{proj}})_{\mathrm{binarisation}} \qquad (\text{A.6})$$

The $(\mathrm{d}A_{\mathrm{proj}})_{\mathrm{binarisation}}$ was the uncertainty introduced by the binarisation process. This error involved the inversion of the image, the adjustment of its contrast by use of a background image and a threshold to produce a black and white image. In the inverted binary image, the white regions correspond to the dispersed phase and the black regions to the liquid phase. An adjustment process, based on the choice of a threshold (Th), was used to enhance the contrast within the image.

The threshold limit chosen had significant implications on the binary image produced, hence it was not assigned a fixed value, but was adjusted for each video processed, based on the intensity of each image. The maximum contrast value of the original image was fixed at 0.9, which meant that every value that exceeded this number would be converted to a white cell. The minimum contrast value of the original image ranged from 0.28 to 0.46.

This implied that every value within the image below this limit would be transformed to a black cell. The $(dA_{proj})_{binarisation}$ was defined according to equation A.7, where I_{max} and I_{min} refer to the maximum intensity values for the image, Th_2 and Th_1 are the threshold values used to delimit the adjusted image. $\sum_{i=Th_2} H(Th_2)$ and $\sum_{i=Th_1} H(Th_1)$ defined the number of pixels whose value is equal to Th_2 and Th_1 respectively. $\sum_{i=I_{min}}^{I_{max}} H(i)$ is the total number of pixels contained in the image.

$$(dA_{proj})_{binarisation} = \frac{\sum_{i=Th_2} H(Th_2) - \sum_{i=Th_1} H(Th_1)}{\sum_{i=I_{min}}^{I_{max}} H(i)} \times 100 \qquad (A.7)$$

The methodology used during the binary conversion of the image and estimation of the filtering error consisted of five steps, which were categorized as follows:

* Crop the original image (Figure A.1a) from (168 × 1280) pixels to (164 × 1000) pixels (Figure A.1b). This step was performed to subtract from the image the wall and avoid the presence of "bright spots" near the image ends created by the light diffusion process.

* Perform the subtraction of a steady background image and the inversion of the cropped image, which resulted in a modified negative of the cropped image (Figure A.1c).

* A threshold value was chosen to convert the image from a gray scale matrix to a binary-like assembly (Figures A.1d and A.1e). It is in this step where a threshold value was provided as an input. As mentioned, depending on the *Th* value chosen, the quality of adjusted image could vary. An initial threshold value (Th_1) was selected based on the results obtained from the intensity histogram of Figure A.1c.

* Using this estimate, the modified gray scale image was adjusted, resulting in a binary image (Figure A.1d). As observed, objects that were not part of the original image were created, resulting in noise. This implied that a new threshold value (Th_2) had to be chosen, which assured the removal of the introduced noise and the preservation of the original shape of the gas structures present within the image. The improved image was shown in Figure A.1e.

* The error of the binarisation operation was determined from the fine tuning followed during the choice of the adequate *Th*. The values for $\sum_{i=Th_2} H\left(Th_2\right)$ and $\sum_{i=Th_1} H\left(Th_1\right)$ were determined and the difference between them used to estimate the magnitude of $(dA_{proj})_{binarisation}$.
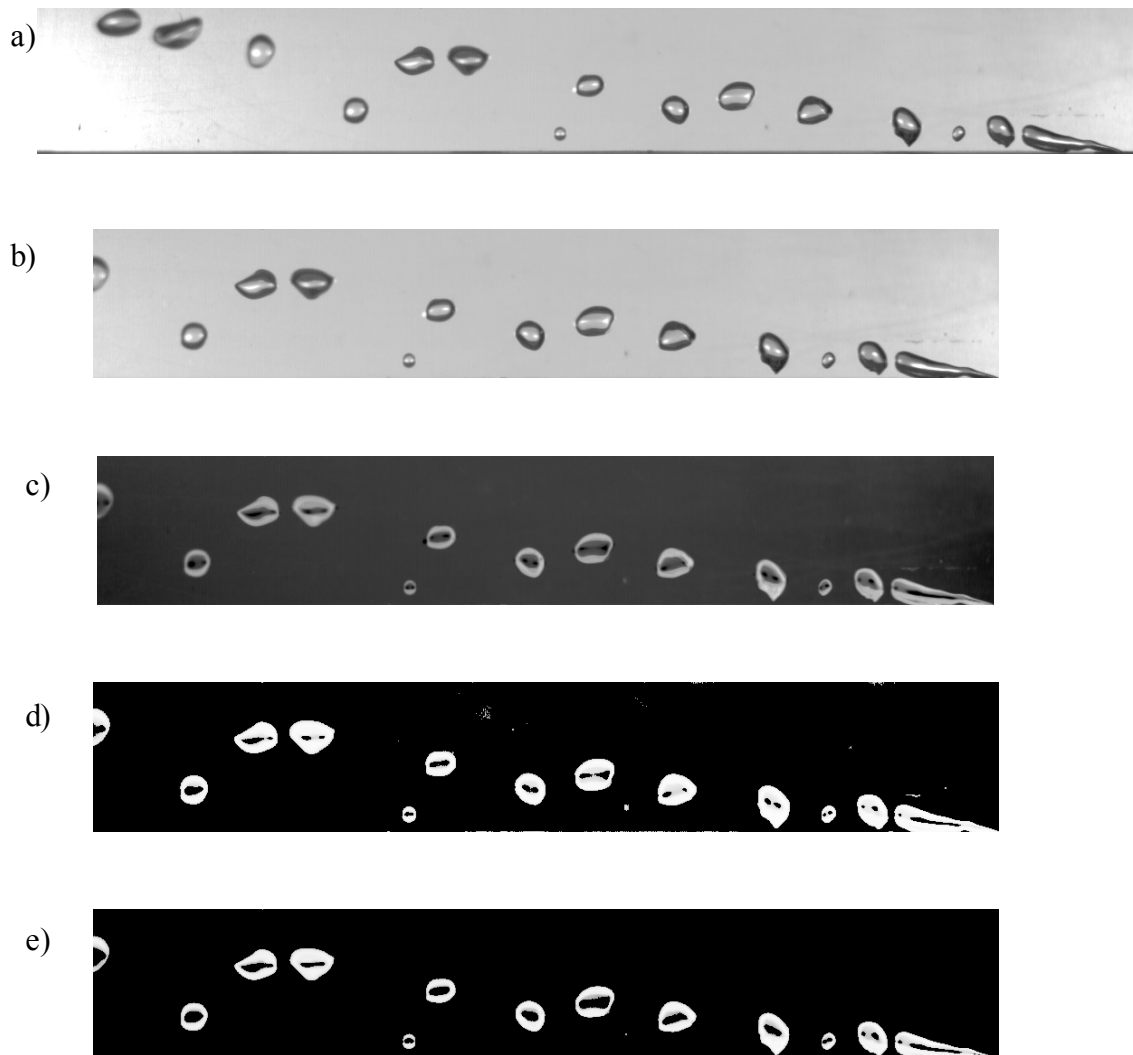
Figure A.1.   Description of the steps followed during the binarisation process of the image: a) Original image, b) Cropped image, c) Inverted image, d) First adjusted image, e) Improved adjusted image

If more than two *Th* values were selected, then the sum of the values encompassed between the min *Th* and max *Th* chosen was used. The methodology followed in the estimation of the binarisation error was similar to the technique followed by Liu (2009). The average $(dA_{proj})_{binarisation}$ obtained during this study oscillated between 0.25 and 0.7 %.
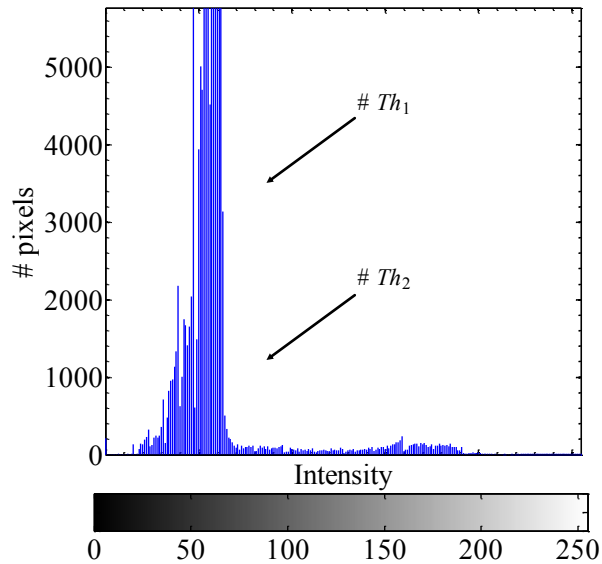
Figure A.2.   Intensity histogram associated to the inverted image used in the estimation of the threshold

The $(dA_{proj})_{filtering}$ was the error caused by the use of the dilation, filling, erosion and a structured squared filter. This was done with the purpose of filling any non-physical inner holes inside the objects and smoothing the object boundary. These holes were created by the light source reflection on the bubble surface. A sample of the changes introduced by the dilation and erosion processes was shown in Figure A.2. Duhar and Colin (2006) considered that the filtering operation errors where approximately equal to 0.1%, therefore they were negligible. In this study, a value of 0.5% was assigned to $(dA_{proj})_{filtering}$ and it was considered that it encompassed all the errors created by the morphological filtering operations. A sample of the dilation, filling and erosion steps for the adjusted image (Figure A.1e) were described in Figure A.3. The changes experienced by the objects within the image during each stage can be observed. The changes in the area and shape of the objects were minimal.

Figure A.3.   Description of the steps followed during the filtering process of the image: a) contrast adjusted image, b) dilated image, c) Filling of the black areas within the objects, d) eroded image

Next, a discussion about the calibration process was conducted. It was observed that the dimensions of the object had an impact in the magnitude of the calibration factor (CF) obtained. The CF was defined according to equation A.8. Nine circles, with diameters that ranged from 0.25 cm to 2.25 cm in diameter, were used to observe the variation in the magnitude of the CF. Using an image processing technique similar to the one described in this section, the D_{equiv} of each circle was obtained. The results were included in table A.2,

along with the real diameter of each object (D_r), the real perimeter (Per_r) and the CF associated.

$$CF = D_r/D_{equiv} \qquad\qquad (A.8)$$

Table A.2. Values of the real diameter, equivalent diameter, perimeter and calibration factor for the circular objects depicted in Figure A.4

	1	2	3	4	5	6	7	8	9
D_r (mm)	2.5	5	7.5	10	12.5	15	17.5	20	22.5
Per_r (mm)	7.9	15.7	23.6	31.4	39.3	47.1	55.0	62.8	70.7
D_{equiv} (pix)	10.5	19.8	29.3	38.7	48.2	57.6	67.0	76.5	86.0
Per (pix)	31.6	63.1	93.8	125.4	157.2	186.5	219.5	250.5	282.6
CF (mm/pix)	0.239	0.253	0.256	0.259	0.259	0.261	0.261	0.261	0.262

a)

b)

$$CF = 0.2227(D_{equiv}^{0.0383})$$
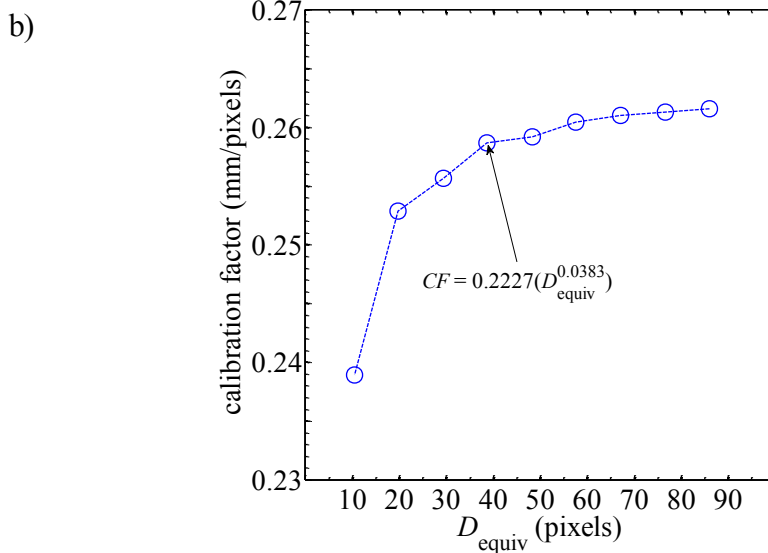
Figure A.4. Circular objects used to estimate the calibration factor. b) Variation of the calibration factor as a function of the D_{equiv}

The results depicted in Figure A.4 indicated that the calibration factor had a certain degree of variability based on the D_{equiv} used. As observed, if a smaller circular object was used as a reference (D_{equiv} = 10.46 pix), its associated calibration factor, CF_1, had a significant difference from the other results. However, when $D_{equiv} \geq 40$ pixels, the CF tendency reached a stable point. The percentual difference between CF_4 and CF_9 was equal to 1.16, which confirmed the minimal variation in the CF values after this point. A correlation (expression A.9) that allowed the estimation of CF as a function of D_{equiv} was obtained from the data of Figure A.4. This expression was a useful tool in the calculation of the CF produced by circular objects. It was inferred that to minimize the uncertainty in the calibration, a minimum of 40 pixels per object were required.

$$CF == 0.2227\left(D_{equiv}^{0.0383}\right) \tag{A.9}$$

To provide further insight about the effects of D_{equiv} on the estimation of the real dimensions of objects, an additional evaluation was performed. A group of selected CF values, CF_1, CF_5, CF_7, CF_8, CF_9, were used to convert the D_{equiv} values for each circle. The resulting values were compared to the real dimensions reported in Table A.1. The findings from the assessment were reported in Figure A.5. Using CF_1 to convert D_{equiv} into real dimensions gave results that deviated greatly from the expected solutions, according to the trend observed in Figure A.5. The mean error obtained by using CF_1 was equal to 7.7 %. The use of CF values corresponding to higher values of D_{equiv} gave significantly improved results with a percentual deviation approximately equal to 2.1%. As observed in Figure A.5, the tendency exhibited for the rest of CF evaluated was very similar.
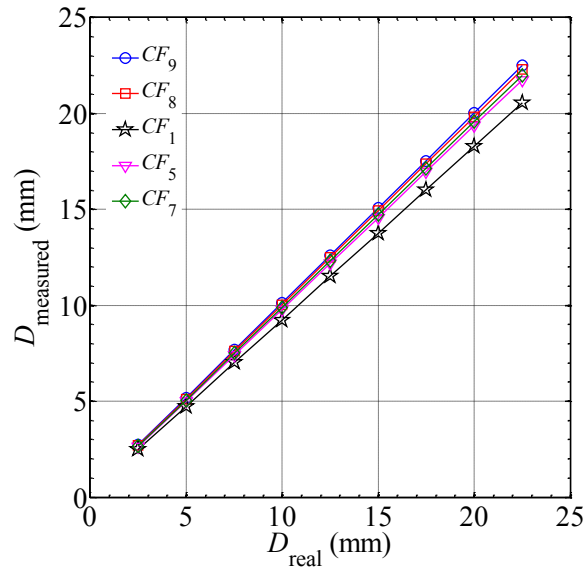
Figure A.5.   Comparison between real and measured diameters for selected *CF* values

An additional assessment for the conversion factor was performed. A factor, called *KF*, was

obtained from the ratio between the real perimeter (Per_r) and the perimeter obtained from

the analysis of image A.4a. The factor *KF* was defined according to equation (A.10) and the

results obtained were reported in table A.3. All the *KF* values were very similar, as

indicated by the small standard deviation of the *KF* vector, which was equal to 0.0012.

Table A.3.   Comparison between *CF* and *K*F

	1	2	3	4	5	6	7	8	9
D_r (mm)	2.5	5	7.5	10	12.5	15	17.5	20	22.5
KF (mm/pix)	0.2489	0.2489	0.2511	0.2505	0.2498	0.2527	0.2505	0.2509	0.2501
CF (mm/pix)	0.2389	0.2529	0.2556	0.2586	0.2592	0.2605	0.2610	0.2613	0.2616

The results of the contrast between *KF* and a selected calibration factor (CF_5) derived from

D_{equiv} were shown in Figure A.6. As indicated, both coefficients gave results very close to

the real values for $D_r \leq 10$ mm. After this point, the results for KF started to differ from the expected tendency. The maximum difference was obtained at $D_r = 22.5$ mm, where the KF under predicted by 0.96 mm. The mean deviation throughout the interval was 3.9%. When the coefficient CF_5 was used, the error was 0.5%. Hence, it was inferred that the use of calibration factors obtained from the D_{equiv} would result in improved results over factors derived from the perimeter.
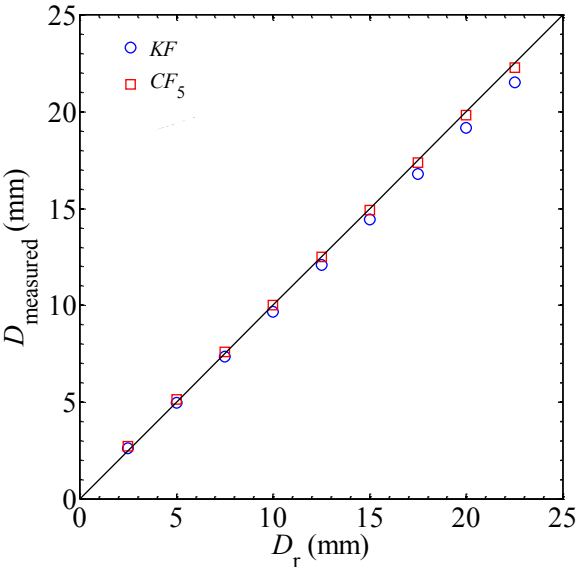
Figure A.6.   Comparison between the conversion factor obtained from D_{equiv} and the use of Per

The final factor involved in the estimation of $(dA_{proj})_{total}$ was extremely dependent on the previous discussion about the calibration factor. Based on the analysis performed, the uncertainty value associated to the calibration process was approximately equal to 1.1%. This value was obtained from the mean deviation found from the experiments. Hence, the total error derived from the calibration was estimated to be equal to 2.3% of the projected area:

$$(\mathrm{d}A_{\mathrm{proj}})_{\mathrm{total}} = (\mathrm{d}A_{\mathrm{proj}})_{\mathrm{filtering}} + (\mathrm{d}A_{\mathrm{proj}})_{\mathrm{calibration}} + (\mathrm{d}A_{\mathrm{proj}})_{\mathrm{binarisation}} \approx 0.5\% + 1.1\% + 0.7\% \approx$$

$$0.023 A_{\mathrm{proj}}$$

The uncertainty for D_{equiv}, $\mathrm{d}D_{\mathrm{equiv}}$, was calculated by differentiation of equation A.2. The expression obtained defined the error as a function of $(\mathrm{d}A_{\mathrm{proj}})$ as observed in equation A.10. Since the equivalent diameter was calculated from the projected area, it was expected that to obtain an expression that considers the uncertainty as a function of the parent variable A_{proj}.

$$\mathrm{d}D_{\mathrm{equiv}} = \mathrm{d}\left(\sqrt{\frac{4}{\pi} A_{\mathrm{proj}}}\right) \rightarrow$$

$$\mathrm{d}D_{\mathrm{equiv}} = 0.564 \frac{\left(\mathrm{d}A_{\mathrm{proj}}\right)_{\mathrm{total}}}{\left(A_{\mathrm{proj}}\right)^{1/2}} = 0.0130 \sqrt{A_{\mathrm{proj}}}$$

(A.10)

The perimeter was determined directly from the Matlab algorithm. Its value was calculated by counting the distance between each connecting pair of pixels along the border of the object. To avoid any inconsistency in the perimeter estimation, the boundary of the object had to be closed. Although, assigning to the error associated to Per ($\mathrm{d}Per_{\mathrm{rand}}$) a value equal to 1 pixel could have been considered as an adequate choice, a more thorough assessment was conducted. Using the values reported in Table A.2, the perimeter obtained from the images was compared to Per_{r}, which took into account possible deviations between real and calculated values based on the size of the object. The findings from this evaluation were reported in Figure A.7. The differences between Per_{r} and the calculated Per were relatively

small and had little variation along the range of diameters tested, with a mean deviation equal to 4.3%. The maximum variation was 4.8% above Perr while the minimum error was 3.3% over the real value. Other values of *CF* were tested and the results obtained had a similar tendency. The $dPer_{rand}$ was considered to be equal to the random 3.52% of the calculated perimeter or $dPer_{rand} = 0.0352Per$.

To estimate the $dPer_{bias}$, it was considered that the nature of the estimation process introduced an error equal to ± 1 pixel for each boundary, hence $dPer_{bias} \approx \pm 2$ pixels. Seeing as the mean calibration factor obtained during the experiments was approximately equal to 0.076 mm/pix, the error for $dPer_{bias}$ was approximately equal to 0.152 mm. Therefore, the total error for the perimeter involved the bias and random error and was estimated according to equation A.10. For very small objects ($Per \leq 3$ mm), the bias error would be dominant, while beyond this limit the random error would be the main source of uncertainty.

$$dPer = \sqrt{\left(dPer_{bias}\right)^2 + \left(dPer_{rand}\right)^2} = \sqrt{\left(0.152\right)^2 + \left(0.0352Per\right)^2}\, \text{mm} \qquad \text{(A.10)}$$
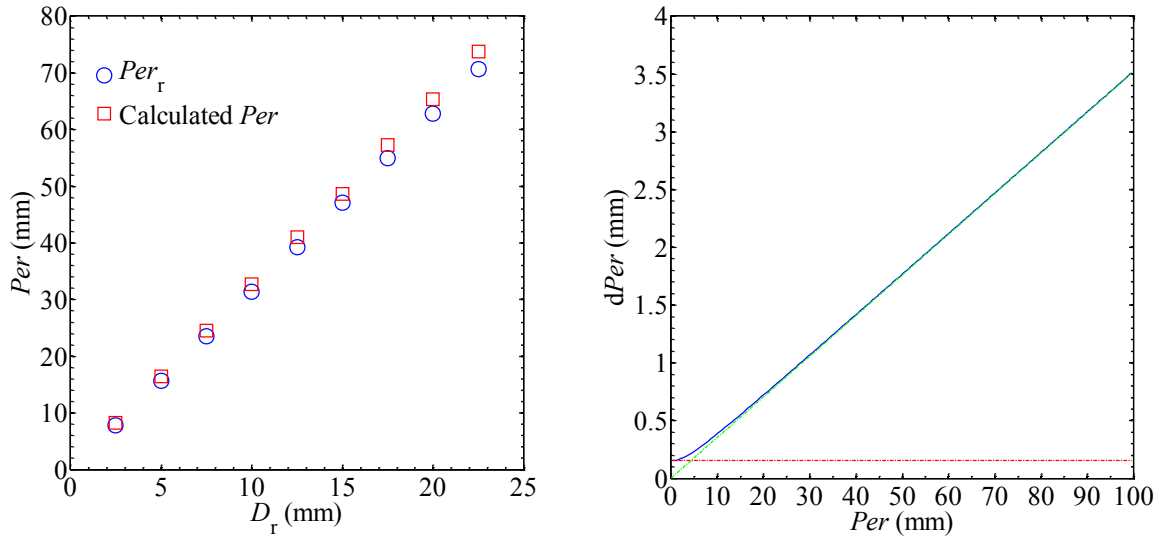
Figure A.7.   a) Comparison between the calculated perimeter, using CF_7, and the real perimeter of the circular objects. b) Contrast between the bias and random error as sources of uncertainty for the perimeter

The error related to the estimation of any variable involving the use of the volume, such as V_G or the buoyancy force, was determined to be a combination of the error of A_{proj} and the measured width of the object. Figure A.8 showed a rough representation of the width of any structure, which varied depending on the object analyzed, bubble or jet. For bubbles, the width was equal to the equivalent diameter of the bubbles. For the gas jet, the width was equal to the averaged distance between the upper and lower boundaries of the object. The range used to estimate this value was encompassed between $0.85X_{jet}$ and X_{jet}, where X_{jet} represented the length of the jet. Similar to the uncertainty analysis for the perimeter, it was considered that $dD_W \approx \pm 2$ pixels or $dD_W \approx 0.152$ mm. Therefore, the error estimation for the volume (dV_G) was determined using equation (A.11), which considered the uncertainties for both A_{proj} and D_W.

$$dV_G = A_{proj}\left(0.023D_W + 0.152\right)mm^3 \qquad (A.11)$$
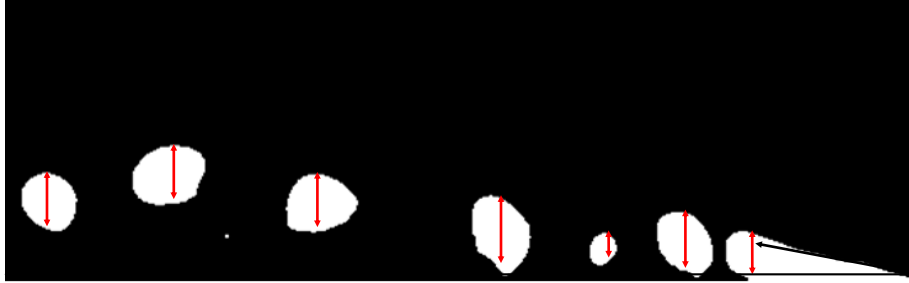
Figure A.8.   Description of the steps followed during the filtering process of the image: a) contrast adjusted image, b) dilated image, c) Filling of the black areas within the objects, d) eroded image

Equation (A.11) was appraised using the D_{equiv} values from Table A.2. The projected area was calculated using equation (A.2). The D_W of the object was assumed to be equal to D_{equiv}, which would be similar to the methodology followed in the estimation of D_W for objects in a liquid flow. The results of this assessment were presented in Figure A.9. The maximum percentual difference occurred for the smaller objects ($D_{equiv} \leq 20$ pixels), where dV_G was over 4.5% of V_G. As D_{equiv} increased, the discrepancies gradually decreased reaching a steady value that was approximately equal to $0.038V_G$. The mean deviation value was 4.2%.
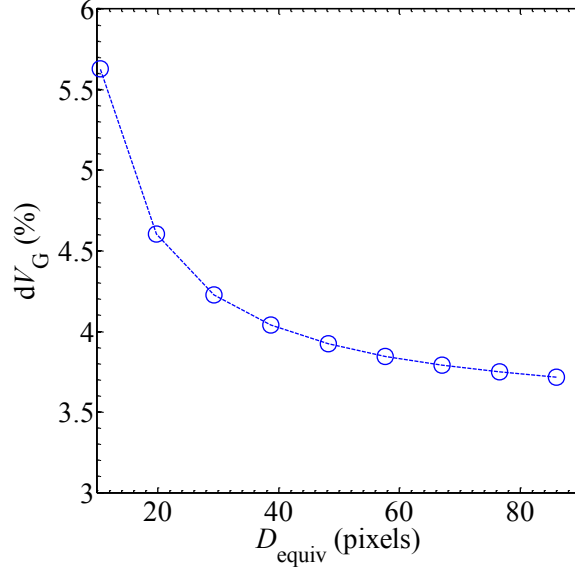
Figure A.9.   Assessment of the volume error (percentual)

To summarize, the uncertainties for the quantities reported in Table A.1 were determined as reported in Table A.4.

Table A.4.   Summary of the uncertainties for the geometrical quantities used during this study

$dA_{proj} = 0.023A_{proj}$ or 2.3% of the reported A_{proj} value	(A.12)
$dPer \sim 0.0352Per$ or 3.5% of the reported Per value	(A.13)
$D_{equiv} = 0.0130\sqrt{A_{proj}}$ or 1.3% of the reported $(A_{proj})^{0.5}$ value	(A.14)
$dV_G \sim 0.042V_G$ or 4.2% of the reported V_G value	(A.15)

Lastly, the uncertainty associated to a low resolution in the region close to the injection nozzle was assessed. Assuming an error of one pixel (~ 0.07 mm), the errors in the nozzle region are significant based on the following info:

D_{inj} (mm)	% error based on 1 pixel difference	% D_{inj}/D_H (vert)	% $D_{inj}/(4D_H)$ (horz)
0.27	25.9	2.1	0.5
0.52	13.5	4.1	1.0
1.59	4.4	12.5	3.1

If the interest is in the near injection region, certainly this comparison indicates that the error would be large, particularly for $D_{inj} = 0.27$ mm. However, the objectives of the current study were not focused on a detailed, in-depth analysis of the near injection region. An assessment of the primary objectives for each Chapter indicates this:

* Chapter 3: The gas phase probability distribution in a liquid cross-flow was measured along the spanwise direction of the channel (12.7 mm) and up to a distance of 51 mm in the stream wise distance. When comparing the extent of the nozzle dimension with the length and width of the area of interest, it is clear that the injection diameter represents only a very small fraction of either dimension independent of the D_{inj} used.

* Chapters 4-5: While there are forces that could be defined as a function of D_{inj}, they did not depend on an accurate estimation of the dimensions near the gas injector. The forces that depend in the dimensions of the gas jet (buoyancy, drag, lift, turbulence, inertial) are not significantly affected by a high accuracy in this region, as they depend on the projected dimensions and assumed width of the gas jet, which as previously shown, has dimensions that are much larger than those associated to the near nozzle vicinity. Also, the dimensions of the injection nozzle are negligible when compared to the averaged length of the gas jet.

* Chapter 6: The results obtained in this Chapter indicate that important morphological dimensions such as D_{equiv}, obtained from the projected area A_P, are orders of magnitude larger than the accuracy of D_{inj}, making it less necessary to focus on a detailed characterization of the field near the injection nozzle.

* Chapter 7: As shown in this chapter, the focus was on an integral approach of the bubbling dynamics, where an in-depth analysis of the injection nozzle does not expand on the knowledge presented and does not provide a better understanding of the transitions between bubble formation regimes.

The following figures present a comparison between the measured gas jet morphological property (A_P), the projected area of the gas jet in the focal plane of the image, with the area represented by the injection nozzle ($A_{inj} = 0.7854*D_{inj}{}^\wedge 2$). This assessment allows the estimation of how much of A_{inj} represents the results obtained for A_P. This serves as a proof that even though a higher resolution near the injection area, and for the measurements in general, would have been desirable, the results obtained are not severely affected by the resolution near the gas injection nozzle.
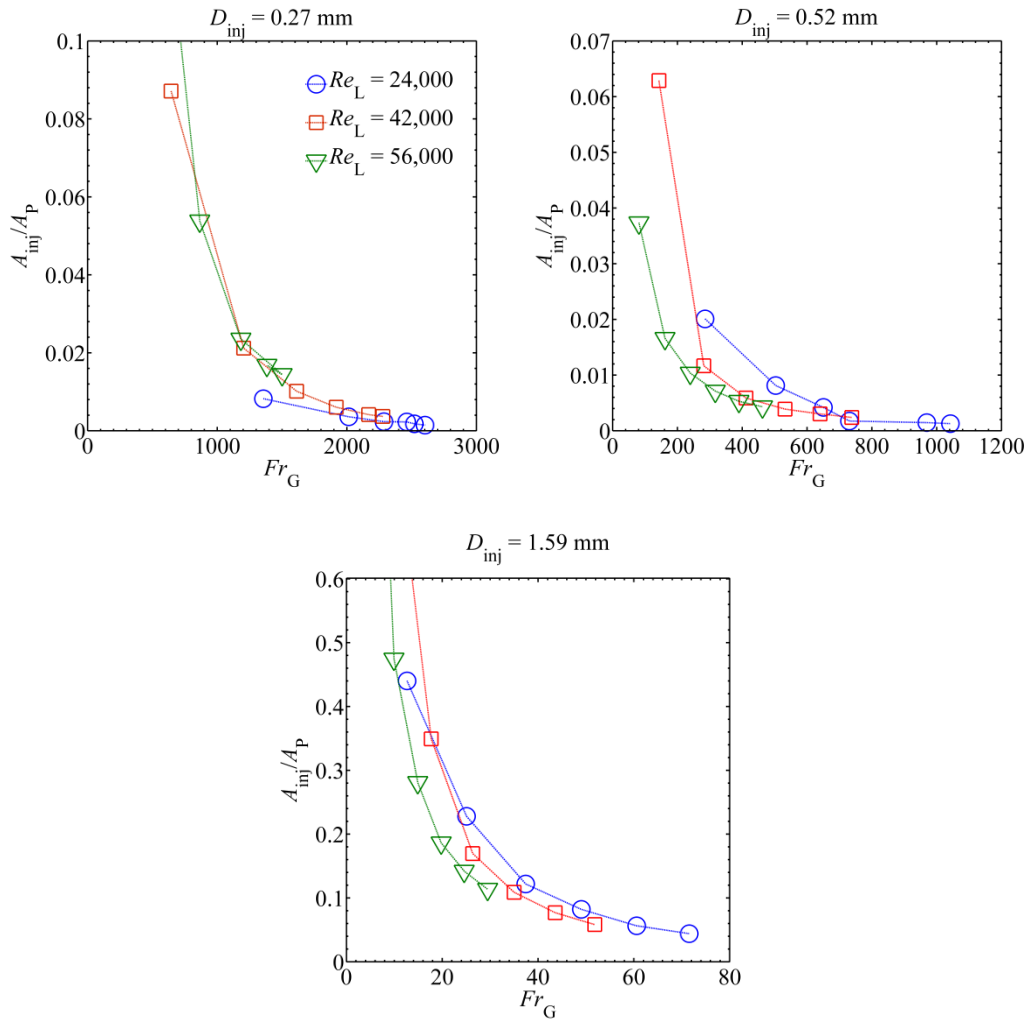
The results presented in the figures above indicate that for the vast majority of the scenarios, the magnitude of A_{inj} represents only a small percentage of the average area occupied by the gas jet. For $D_{inj} = 0.27$ and 0.52 mm, the ratios were very small, with A_{inj}/A_P magnitudes in the order of 0.1 or less for most scenarios. As A_{inj} was increased, it was expected that it would play a more relevant role but the results still indicate that for the vast majority of the results the dimensions of D_{inj} do not account for a significant percentage of A_P.

While having a detailed analysis of the dynamics of the gas jets could prove beneficial to understand some particular phenomena such as: formation of microbubbles, effects of the nozzle injection material on the bubbling process, estimation of the contact angle, advancing and receding angles in the vicinity of the nozzle; these processes are not the point of interest of the current work. Each one of these processes represents an interesting topic about the mechanics of bubble formation, but under the experimental conditions tested here, the contribution of them can be considered as a secondary objective that would not affect dramatically the results obtained.

Having a higher resolution in general would minimize the errors associated to the identification of the gas-liquid interface, but it was not necessary for the most important results obtained in the present work. Therefore, it can be concluded that the camera resolution selected was more than adequate to study the main region of the gas jet and the bubbles, as was described in sections 2.3-2.5. However, the resolution was not sufficient to study the vicinity of the injection nozzle, which was out of the scope of the thesis.

Another way of uncertainty estimation for volumetric estimations could be achieved by comparing the volumetric gas mass flow rate injected into the channel (Q_G) with the estimations obtained from the gas jet projected area (A_P) and the averaged width of the gas jet (D_W). Hence, the instantaneous volume of the gas jet was defined as $V_G = A_P * D_W$, where A_P is obtained according to the definition presented in Section 2.3.1 and D_W is estimated from the projected area as the averaged width of the gas along the streamwise direction. Due to the experimental technique employed, this assumption was required.

Although the use of a high-speed shadowgraph allowed for a very detailed estimation of the gas phase boundary, it is limited to plane measurements. Hence, the depth value can be obtained only thru the use of assumptions such as the one previously described. As was mentioned, D_W was calculated as the averaged value of the gas jet width at several locations, as shown in the next figure.
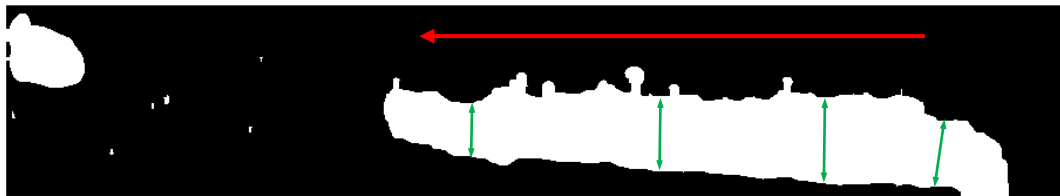
To perform the suggested assessment, a simple set of experimental results corresponding to $D_{inj} = 0.52$ mm and $U_L = 2.2$ m/s (Table 2.3) were used. Three M_G values, 9.8, 30.1 and 59.8 × 10^-3 g/s, were used. For each scenario a sample time interval of 1 ms was used. The averaged volume variation (ΔV) was the parameter used for comparison. The variation of ΔV as a function of time is presented in the next figure, which corresponds to the set of results used for $M_G = 59.8 \times$ 10^-3 g/s. The quasi-period behaviour associated to this phenomenon can be easily observed in the trend shown in the figure.
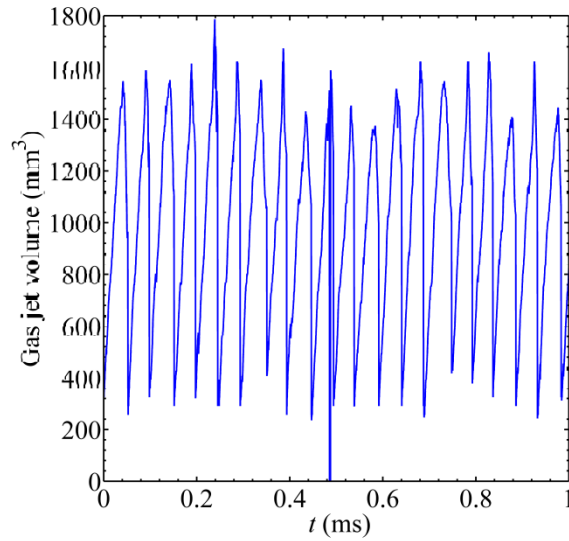
ΔV was defined as the variation between the minimum and maximum values within a growth-breakup. This was calculated for all the cycles. The results for each experimental set studied are introduced in the next table. The time that it took the gas jet to vary from these two values, which physically corresponds to the growth time, can be estimated in a similar manner. This time was defined as Δt. The variation associated to each variable was included in the table and it represents the random uncertainty inherent to this complex phenomenon.

Comparison between the experimental averaged volume variation for selected conditions and the set Q_G value

$M_G \times 10^{-3}$ (g/s)	Q_G (LPM)	ΔV (mm^3)	Δt (s)	Q_G imaging (LPM)	% diff$_{\text{imaging - exp}}$
9.8	0.29	33.8 ± 21.1	0.0060 ± 0.0024	0.34	+17.2
30.1	0.87	326.9 ± 84.5	0.0190 ± 0.0034	1.03	+18.7
59.8	1.78	1254.5 ± 99.8	0.0423 ± 0.0111	1.73	-2.9

The results indicate that for $M_G = 9.8$ and 30.1×10^{-3} g/s the imaging technique yields Q_G values larger than those given by the experimental measurement by approximately 18%. It was inferred that for the low M_G values, the reason for this overestimation was caused by the way D_W was estimated. Owing to the presence of a liquid cross flow, independent of M_G, the gas jet front will have a tear-like shape; with a roundish shape at the gas fore and a flattened contour at the back, as shown in the next figure.

It was conjectured that the algorithm used gives too much weight to the values at the gas jet fore, causing D_W to yield high values; hence the estimated ΔV values are higher than the ones obtained from Q_G. At low-medium M_G values, such as the scenario presented in the above figure, this causes the aft area of the gas jet to have a D_W than what is physically meaningful. Hence it can be argued that this is where the higher discrepancies in the gas jet volume estimations occur. At the higher M_G values, the gas jet shape losses its tear-like shape and resembles more a buff body object. As was observed in the first figure, this causes a more uniform width for the gas jet. Hence D_W gave ΔV results close to those obtained from Q_G, as shown by the 2.3% difference.

Certainly, the best approach to overcome this would be use simultaneous imaging measurements in another direction perpendicular to the one used during the experimental measurements. This would give the needed additional dimension to obtain a true estimation of the gas jet volume. If limited to the experimental setup used in this thesis, one possible way to overcome the deficiencies observed is to create an algorithm that instead of calculating D_W at several locations, performs an evaluation of the gas jet width along the perimeter of the gas jet and create a numerical algorithm that estimates the gas jet solid dimensions from the projected area.

Appendix B. Gas jet penetration and gas buoyancy lengths

Near the injector region in a GJILCF, the gas jet outer boundary remains relatively straight, owing to the effect of the gas jet momentum. At a certain vertical location, the liquid velocity induces a rapid change in the gas jet curvature, resulting in its alignment with the cross-flowing stream, an indication of the transition from region I towards region II (Figure 3.1, Chapter 3). In this work, the gas jet penetration length (y_P) was defined as the vertical location where the gas jet bending initiates.

Using the averaged jetting image, y_P was calculated as the first point where the reduction in the boundary growth between successive points in the streamwise direction becomes less than 2%. Because the process of gas injection in a flowing liquid produces unsteadiness in the gas jet boundary and undulations in the fluids interface, y_p was not a fixed magnitude and instead it fluctuated within a restricted range. Since y_P was determined from the summation of the instantaneous shadowgraphs, the values reported refer to the averaged location where the transition from a momentum driven region towards the buoyancy dominated regions begins.

After reaching the y_P point, the gas jet expansion in the vertical location continued, although driven primarily by the balance between buoyancy and liquid cross-flow, causing a slower growth of the gas jet boundary. The vertical location where the outer gas jet boundary achieved a quasi-stable location was defined as the buoyancy length (y_B), and

indicated the point where flow region (II) was fully established. Physically, this represented the averaged maximum position within the interrogation window where the gas phase could be found, as determined from the probability images. y_B was calculated as the first location where the averaged variation between 20 successive points in the horizontal variation became less than 2%.

An example of the estimation of y_P and y_B from the summation histograms is shown in Figure 3.1. The GJILCF behaviour depicted corresponded to $Fr_G = 2180$ and $Re_L \approx 41,000$ for $D_{inj} = 0.27$ mm. The color gradients within the figure indicated the time percentage throughout the test where the gas phase would occupy a specific Cartesian point. As observed, the y_P magnitudes for both injection locations were approximately similar, with values of $0.46D_{channel}$ and $0.52D_{channel}$ for bottom and top wall injection respectively. The horizontal location of y_P for bottom wall injection was $0.18D_{channel}$, while for top wall injection is $0.26D_{channel}$. The subtle differences in the y_P behaviour were attributed to effect of the buoyancy, which caused y_P to develop faster for bottom wall injection than top wall injection. The influence of the density difference between phases was more noticeable for y_B, where a stable point for the gas jet boundary was quickly achieved. The buoyancy length occurred approximately at the same horizontal position for both injector orientations.

For bottom wall injection the buoyancy force caused the displacement of the gas phase towards the opposite wall, while for top wall injection the stable horizontal line observed indicated that the buoyancy restricts the distribution of the gas jet to the region between $0.4D_{channel}$ and $1.0D_{channel}$. Although y_B remained relatively constant after $x/D_{channel} \approx 2$, a

small decrease in the boundary location was observed. This was interpreted as the point where the influence of the gas injection ends, starting the transition towards bubbly flow conditions (Start of flow region III, Figure 3.1).
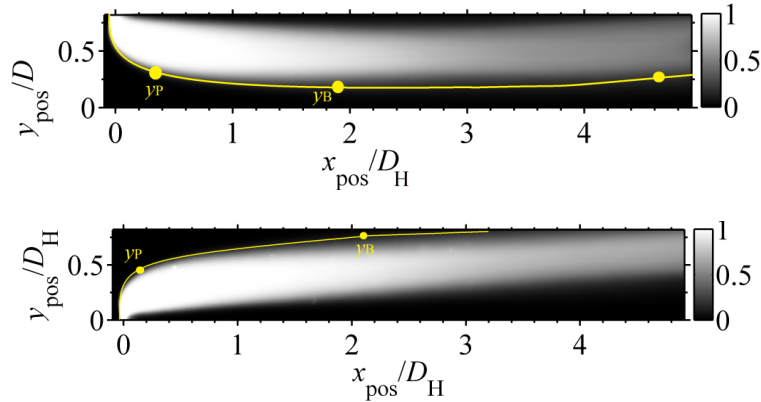
Figure B.1. Penetration (y_P) and buoyancy (y_B) length for a GJILCF at the same operational conditions ($Fr_G = 2180$, $Re_L = 41,000$, $D_{inj} = 0.27$mm) but different injector orientations

The trend y_P versus Fr_G was depicted in Figure B.2, where y_P was made dimensionless with D_{inj} and Fr_G was represented in a log axis. The data indicated that y_p/D_{inj} scaled with Fr_G and Re_L following a power law empirical correlation, as given in equation B.1. It was found that the coefficients a, b and c depended on the injector location. The values for the coefficients were given in Table B.1. For this correlation, the coefficient of determination was $R^2 = 0.88$ and $R^2 = 0.86$ for near and top wall injection respectively, which indicated an acceptable level of agreement with the experimental data.

$$\frac{y_P}{D_{inj}} = a\left(Eo_G\right)^b \left(Re_L\right)^c \left(Fr_G\right)^d \qquad (B.1)$$
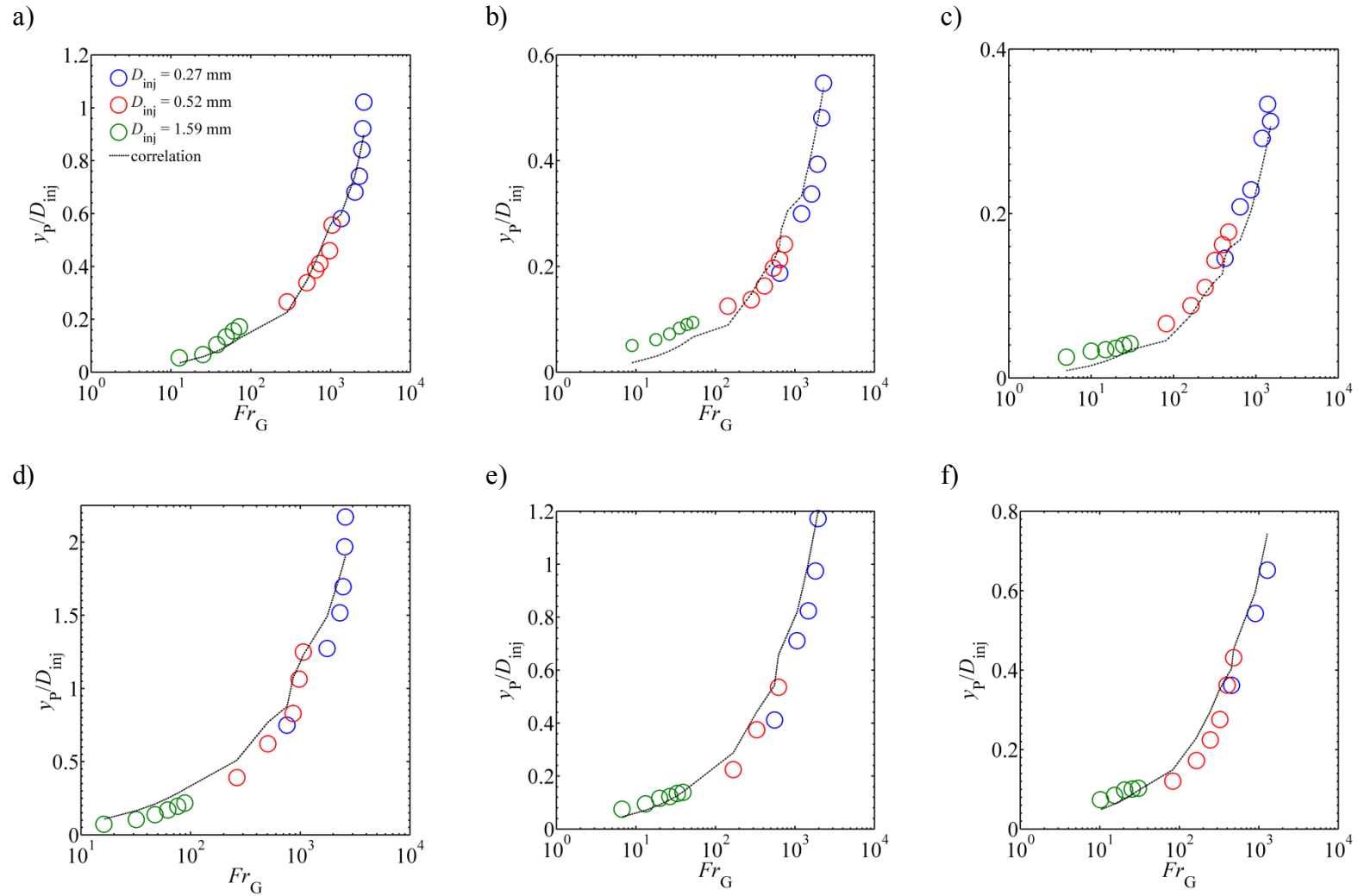
Figure B.2. Comparison between experimental data and empirical correlations estimating the penetration length y_P as a function of dimensionless parameters. Top row (Bottom wall injection): a) $Re_L = 24,000$, b) $Re_L = 42,000$, c) $Re_L = 56,000$. Bottom row (Top wall injection): d) $Re_L = 24,000$, e) $Re_L = 42,000$, f) $Re_L = 56,000$

Table B.1.   Coefficient values for y_P/D_{inj} correlation

Injector location	a	B	c	d
Bottom wall	21	0.21	-0.80	0.75
Top wall	980	0.21	-1.14	0.80

The proposed correlations took into consideration the physics of the problem at hand, where an increase in Fr_G enhanced the penetration of the gas jet in the injector vicinity, while an increase in Re_L decreased the spreading of the gas phase inside the conduit. The differences in the scaling of y_P/D_{inj} indicated that the injector orientation does play a key role in the initial behaviour of the gas jet. The slightly bottom values of the coefficients a and c for bottom wall injection correlated with the observed decreased dimensionless values described in Figure B.3.

The average relative error for the top wall injection correlation was 13% with a maximum difference of 25%, observed for $Fr_G \geq 2500$ and $Re_L \approx 24{,}000$. The sudden increase in the y_P trend was attributed to a transition towards chaotic jetting regimes, where the secondary bubble detachment occurs near the injection region. Similar results were obtained for the bottom wall injection case, where the averaged relative error for y_P/D_{inj} was 11%, with the highest difference observed at the highest values of Fr_G.

Under comparable operational conditions, the magnitude of y_P/D_{inj} varied based on the location of the gas injector. Bottom gas injection produced faster y_P development than when the injector was located in the top wall, as presented in Figure B.3. For bottom wall injection, the buoyancy forces caused the gas jet to experience fast alignment with the cross-flowing liquid, which translated into small y_P/D_{inj} values. For Re_L between 24,000 and 48,000, y_P/D_{inj} for far-wall

injection was approximately 0.7 times shorter than the values observed when the injector was located in the opposite wall. The results showed that as Re_L was increased to 56,000, which corresponded to the strongest liquid cross-flow; the position of the gas injector did not produce significant differences in the magnitude of y_P/D_{inj}. This indicated that as the liquid cross-flow momentum increased, the effects of the injector location would not be important in the behaviour of y_P/D_{inj}.

After the influence of the injection conditions on the GJILCF begins to dwell, its behaviour was primarily driven by the relative density between the gas and liquid phases. The trend exhibited by the buoyancy length y_B, which indicated the maximum penetration within the interrogation interval, was a clear indication of this effect. As is shown in Figure B.3, the values of y_B/D_{inj} for bottom wall injection are higher than those observed for equal values of Fr_G and when the gas injector was located on the opposite wall.
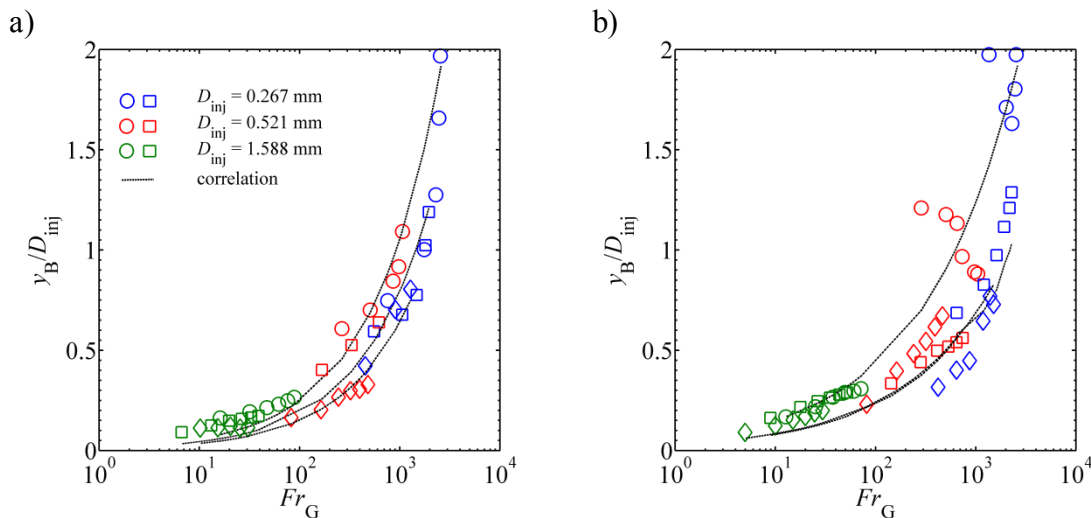
Figure B.3.   Evaluation of the dimensionless y_B correlation versus experimental data. a) Top wall injection. b) Bottom wall injection. ○ Re_L = 24000, □ Re_L = 42000, ◊ Re_L = 56000

When the gas inlet nozzle was located in the bottom wall, the density differences caused a displacement of the gas jet border towards the top of the channel. Similarly, the buoyancy caused the gas jet probability under the top wall injection scenario to be restricted to the top region of the conduit. If Fr_G is relatively high, the influence of the buoyancy caused the y_B/D_{inj} values to have a magnitude comparable to those of y_P/D_{inj}.

It was also found that for top wall injection, once y_B was achieved, its magnitude remained relatively constant throughout the interrogation window. Conversely, for bottom wall injection, the buoyancy caused y_B/D_{inj} to display a small growing tendency. Though after y_B was reached and its trend remained stable, the gas jet borderline experienced a small increase in its vertical location, displacing towards the channel top region. As occurred with y_P/D_{inj}, Re_L had an important contribution in the magnitude of y_B. As Re_L was increased, it counteracted the influence of the buoyancy, decreasing the y_B/D_{inj} location along the conduit. At $Re_L = 56,000$, y_B/D_{inj} values had comparable magnitudes for similar Fr_G, independent of the D_{inj} orientation.

A set of empirical correlations that estimate y_B/D_{inj} as a function of Re_L and Fr_G were obtained. These expressions, given by equation B.2 and Table B.2, considered the effect of the gas nozzle orientation on the y_B/D_{inj} trend. As observed in Figure B.3, the experimental data and empirical correlation curves collapsed remarkably well, as indicated by the coefficients of determination $R^2 = 0.91$ and $R^2 = 0.84$ for bottom and top wall injection respectively. Both expressions estimated that an increase of Fr_G would induce further gas penetration into the conduit, while increasing Re_L counteracted the buoyancy, causing the y_P/y_B ratio to diminish. The averaged

relative error between the correlation and the y_B/D_{inj} experimental was found to be 9.7% for the top wall injection and 11.0 % for bottom wall injection.

$$y_B\Big/D_{inj} = d\left(Eo_G\right)^e \left(Re_L\right)^f \left(Fr_G\right)^g$$ (B.2)

Table B.2.   Coefficient values for y_B/D_{inj} correlation

Injector location	D	E	f	g
Bottom wall	72	0.09	-0.69	0.47
Top wall	17	0.09	-0.66	0.63

The estimation of the penetration and buoyancy lengths provided a preliminary approach for the estimation of the centerline and borderline correlations presented in Chapter 3. The location for both points was used to estimate pathlines, as a function of $x/D_{channel}$ that estimate the centerline and borderline trajectories. With the purpose of refreshing the background related to this particular topic, a summary about the methodology used to determine equations 3.5-3.8 is be presented next:

- Compare existing correlations for JICF (Table 3.1), adapted to the GJILCF case, with the experimental results obtained. No general agreement was found.

- Most equations were of the form presented in equation (3.1). Based on this it was assumed that this functional form was inadequate to replicate the tendencies observed in a GJILCF.

- For most JICF scenarios, no dimensional analysis was conducted to determine the key variables involved. In this work, dimensional analysis was a fundamental step, as it allowed the inclusion of the most important parameters used for this particular scenario.

- Contrary to what was observed in Table 3.1, the form of the equations was based on the dimensional analysis and a simple, power-law type of correlation. This approach was chosen because it was simple, intuitive and was used for the analog case of LJIGCF.

- The only difference with was observed in the JICF scenarios is that the Re_L besides playing a key role in the y/D_H location also modifies the shape observed for each trajectory. This was considered as the major point that required to be reviewed.

The equations for the centreline/borderline were of the form

$$\left(\frac{y}{D_H}\right)_{Centreline} = a\left(Eo_G\right)^b \left(\frac{x}{D_H}\right)^{f\left(Re_L\right)} \left(Fr_G\right)^c \left(Re_L\right)^d$$

For the centerline, the $(x/D_{channel})$ exponents were of the form

Bottom $\qquad\qquad f\left(Re_L\right) = 3.10\, Re_L^{-0.14}$

Top $\qquad\qquad\quad f\left(Re_L\right) = 3.4 \times 10^{-6}\, Re_L^{1.1}$

While the forms presented for Re_L are not appealing, and it could be argued against them that the coefficients would not yield adequate variations for $f(Re_L)$ given the magnitude of the coefficients. The next figure shows the variations of $f(Re_L)$ in the range of Re_L values tested.

Centerline Coefficients

Bottom $f(Re_L) = 3.1(Re_L)^{-0.14}$

Top $f(Re_L) = 3.4\text{e-}6(Re_L)^{1.1}$
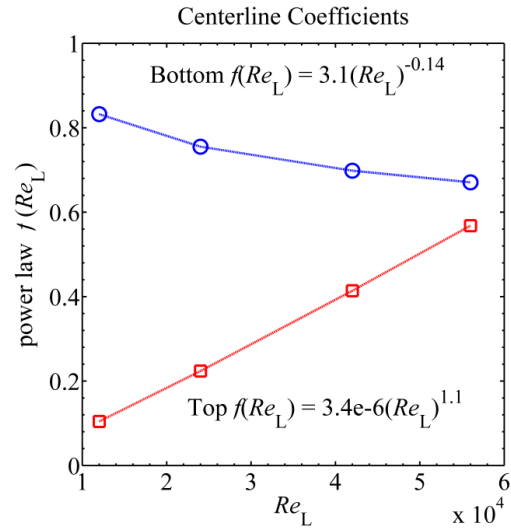
Based on the information shown in the figure above, it is clear that in both cases there is a variation caused by Re_L as to consider the use of a correlation. Physically, this implies that the Re_L not only reduces the vertical location of the gas jet centerline location, but also affects the dispersion shape. The next set of figures indicates how, even though the variations in $f(Re_L)$ might not look relevant, they do cause significant variations in the trend exhibited by $(x/D_H)^{f(Re_L)}$, which is the parameter that determines the form of the centerline trajectory.
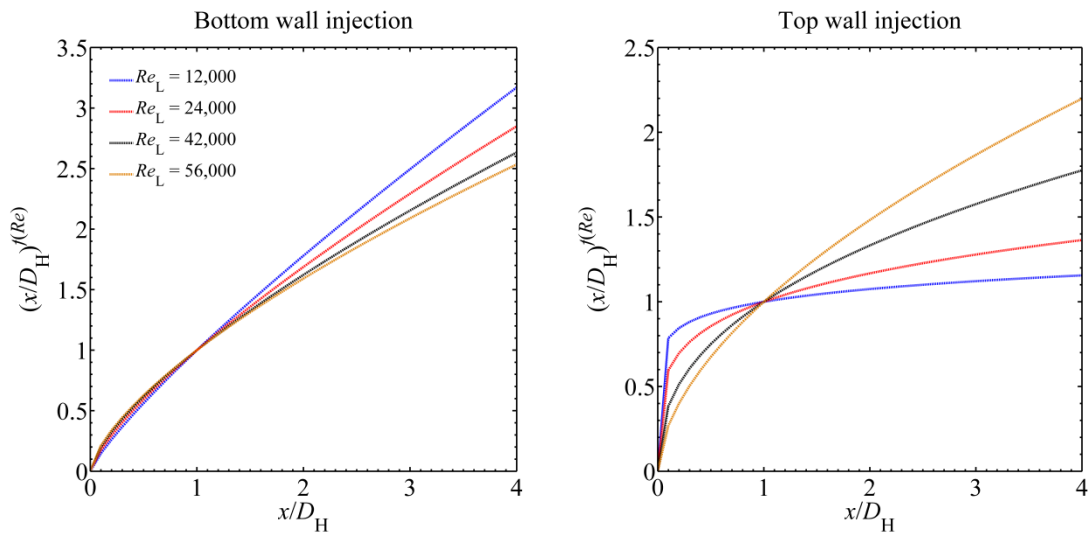
As can be seen in the above figures, the power-law factor plays a fundamental role in the shape of the (x/D_H) curve. While for the bottom wall injection the shape is very similar to the one observed in canonical JICF scenarios, for top wall injection the function adjusts particularly well to the fact that at low Re_L values there is sudden penetration of the gas jet with a sudden stabilization of the dispersion as the trajectory displaces along the streamwise direction. As the Re_L is increased, the trajectory is more similar to the ones observed for bottom wall injection.

While the information presented in this appendix refers only to the gas jet centerline correlations, the same analysis was conducted for the borderline correlations. The physical principles associated to the gas jet behaviour apply in an integral manner; therefore the empirical borderline correlations also have trendlines where the ($x/D_{channel}$) term has a power that is defined as a function of Re_L.

Appendix C. Additional Considerations about the Force Estimation

C.1. Comments about the Buoyancy Force

A common method of estimating F_B was to define the volume of the growing plume (V_G) analog to that of a spherical bubble, using the equivalent diameter (D_{equiv}) as the geometrical parameter. The buoyancy force obtained from this approach (F_{B1}) was obtained from equation (3.1). Although this definition was perfectly applicable for the case of spherical bubbles, it was inferred that F_{B1} miscalculates the buoyancy effects for elongated bubbles and gas jets. The experimental technique employed did not allow the direct calculation of the volume variations as a function of time; hence any estimation of the volume requires the extrapolation from the gas core projected area (A_P), which was obtained from the instantaneous shadowgraphs.

Based on this, two alternative definitions were explored: First, a shape factor C_k (equation C.2), as proposed by Clift et al. (1978), was used in estimating an extrapolated volume of the growing gas plume (V_{Gk}), as defined in Equation C.3. The buoyancy force estimated from this approach (F_{B2}) was defined in equation C.4. C_k allows the assessment of the gas core volume based on the breadth (D_w) and length (D_A) of A_P, as defined in Equation C.5. Since it was not possible to determine the thickness (w) of the gas structure, the extent of the plume was assumed symmetrical, implying that $w \approx D_w$. The coefficient k_e corresponds to an isometric particle with a volume equal to that of the uneven gas structure. Because the shape exhibited by the gas core is asymmetrical, resembling an elongated rounded structure, the value assigned to the coefficient k_e was equal to 0.56, which corresponded to a rounded particle with irregular shape (Clift et al.,

1978). The second approach was based on A_P, which allowed a better calculation of the volume from the shape of the gas plume. To determine V_G, as used in the previously discussed method, w was assumed equal to D_w. The buoyancy force estimated from this approach (F_B3) was defined in equation C.6.

$$F_\mathrm{B1} = \frac{\pi}{6}\left(\rho_\mathrm{L} - \rho_\mathrm{G}\right)D_\mathrm{equiv}^3 g\hat{\mathbf{y}} \qquad \text{(C.1)}$$

$$C_k = \frac{k_e}{\left(e_1\sqrt{e_2}\right)} \approx \frac{k_e}{\left(\sqrt{D_\mathrm{A}/D_\mathrm{W}}\right)} \qquad \text{(C.2)}$$

$$V_{\mathrm{G}k} = C_k D_\mathrm{equiv}^3 \qquad \text{(C.3)}$$

$$F_\mathrm{B2} = \left(\rho_\mathrm{L} - \rho_\mathrm{G}\right)gV_{\mathrm{G}k}\hat{\mathbf{y}} \qquad \text{(C.4)}$$

$$e_1 = \frac{D_\mathrm{W}}{w}, \quad e_2 = \frac{D_\mathrm{A}}{D_\mathrm{W}} \qquad \text{(C.5)}$$

$$F_\mathrm{B3} = \left(\rho_\mathrm{L} - \rho_\mathrm{G}\right)gA_\mathrm{Projected}D_\mathrm{w}\hat{\mathbf{y}} \qquad \text{(C.6)}$$

The differences in the magnitude of F_B, as obtained from the previously discussed approaches, were shown in Figure C.1. As was observed, using F_B1 to predict V_G gave results higher than the ones yielded by F_B2 and F_B3. It was inferred that, when V_G was estimated treating the gas structures as spherical particles, it caused an over calculation of the gas structure thickness. For the other methods, the magnitudes of F_B2 and F_B3 were similar, which indicated that either equation could be used in the estimation of the Arquimedes force. However, for this study, any calculation of V_G followed the methodology associated to equation (C.6). It was considered that it provided a clear delimitation of the volume, because the imaging algorithm allowed an accurate estimation of A_P. This was considered as an advantageous feature, because the use of empiricisms was limited. The only assumption was that of a symmetric growth in the perpendicular direction, $w \approx D_\mathrm{w}$, which is in line with an ample majority of the methods observed in the literature.

In general, the values of F_{B3} for the bottom wall injection were slightly higher than for the top wall injection, where the boundary limited the growth of the gas structure, resulting in slightly smaller volumes. Because of the density difference between the fluids, when the gas inlet was located in the lower wall, the gas core separated immediately from it and had a less marked influence of the solid boundary. However, the difference in the results obtained was within O(1) and minor differences in the operational parameters were also considered as a possible reason for the slight discrepancies.
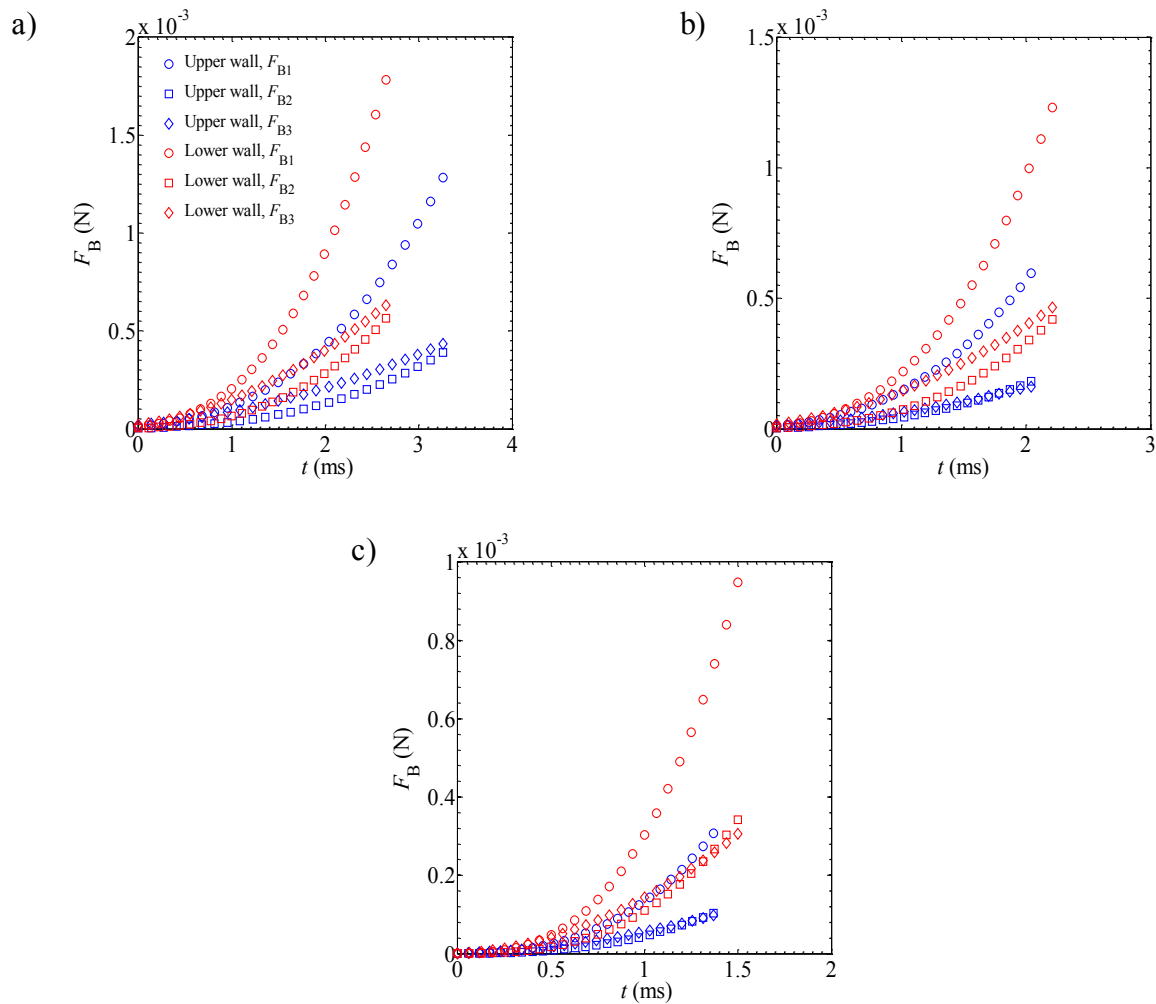
Figure C.1.   Estimation of the buoyancy force using various approaches for the gas volume. a) $D_{inj} = 0.27$ mm, b) $D_{inj} = 0.52$ mm, c) $D_{inj} = 1.59$ mm. The results depicted were obtained for $M_G = 9.24 \times 10^{-3}$ g/s and $U_L \approx 4.3$ m/s.

C.2. Considerations about the Surface Tension Force

A summarized description of the existing correlations for the estimation of the surface tension

force is presented in Table C.1.

Table C.1.　　Summary of existing correlations defining the surface tension force acting on a growing bubble

Author(s)	Definition of F_σ
Tan et al. (2000), Sovani (2001), Liu et al. (2010)	$F_{\sigma x} = \pi \sigma D_{inj} \cos(\theta)$ $\quad$ (C.7) $F_{\sigma y} = \pi \sigma D_{inj} \sin(\theta)$ $\quad$ (C.8)
Al-Hayes and Winterton (1981)	$F_\sigma = \left(\dfrac{58}{\theta + 5} + 0.14 \right) \pi D_{inj} \sigma \sin(\theta)\left(\cos(\beta) - \cos(\alpha)\right)$ $\quad$ (C.9)
Klausner et al. (1993) Loubiere et al. (2004) Duhar and Colin (2006)	$F_{\sigma x} = -1.25 D_{inj} \sigma \dfrac{\pi(\alpha - \beta)}{\pi^2 - (\alpha - \beta)^2}\left(\sin(\alpha) + \sin(\beta)\right)$ $\quad$ (C.10) $F_{\sigma y} = -D_{inj} \sigma \dfrac{\pi}{(\alpha - \beta)}\left(\cos(\alpha) - \cos(\beta)\right)$ $\quad$ (C.11)
Nahra and Kamotani (2003)	$F_{\sigma x} = 2 \displaystyle\int_{\pi/2}^{3\pi/2} D_{inj} \sigma \cos\left[\gamma(\varphi)\right]\sin(\varphi)d\varphi$ $\quad$ (C.12) $\left.\begin{array}{c} \\ \\ \\ \end{array}\right\}$ $F_{\sigma y} = 2 \displaystyle\int_{\pi/2}^{3\pi/2} D_{inj} \sigma \sin\left[\gamma(\varphi)\right]d\varphi$ $\quad$ (C.13) $\quad F_\sigma = f\left(\theta, D_{inj}\right)$ $\gamma(\varphi) = \left(a\varphi^2 + b\varphi + c\right)\hat{H}_{UnitStep}(\varphi - \kappa_0) + \beta\hat{H}_{UnitStep}(\varphi - \varphi_0)$ e.g. $F_{\sigma x} = 1.095\theta - 0.593\theta^2 \rightarrow D_{inj} = 0.15\,\text{cm}$

Some important observations were obtained from the assessment of the equations obtained from

previous works: All the correlations assumed that the neck region extended throughout the

injection orifice area, independent of the U_L and U_G effects. Generally, the results obtained in the

present study aligned with this consideration, although there were cases where the width of the

gas plume near the injector extended further than the D_{inj} region. Two images that proved this

statement were shown in Figure C.2, where the extent of the neck connecting the gas jet with the

inlet area extended to approximately two times D_{inj} for both far and near wall gas injection.
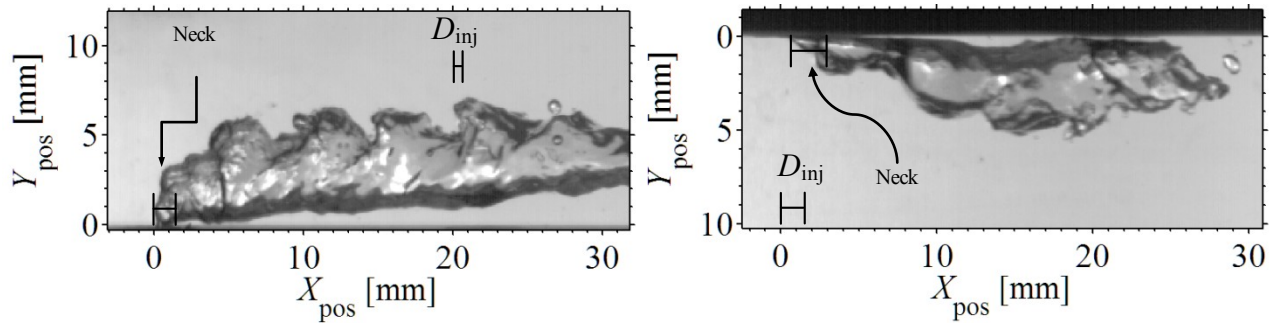
Figure C.2.   Width of the neck attaching the gas plume to the injection orifice. Left) D_{inj} = 0.52 mm, U_G = 74.5 m/s, U_L = 1.9 m/s. Right) D_{inj} = 1.59 mm, U_G = 13.9 m/s, U_L = 2.0 m/s. As observed, there were cases where the gas neck near the injector had an extension wider than the D_{inj}. A scaled reference value for D_{inj} was included within the pictures

As observed, the dimensions of the gas stem that linked the main core to the incipient, separating

bubble were smaller than the width of the gas structure. Kim et al. (1994) and

Bhunia et al. (1998) assumed that the neck collapsed when its length became equal to D_{inj}.

Experimental observations indicated that the neck length grew up to values larger than that

estimation. Figure C.3 showed the time evolution of a gas jet, exhibiting the formation and

closure mechanics of a gas neck, up to the point of bubble separation. It was found that in the

presence of a liquid cross-flow, the gas neck could grow up to six times the length of D_{inj}.
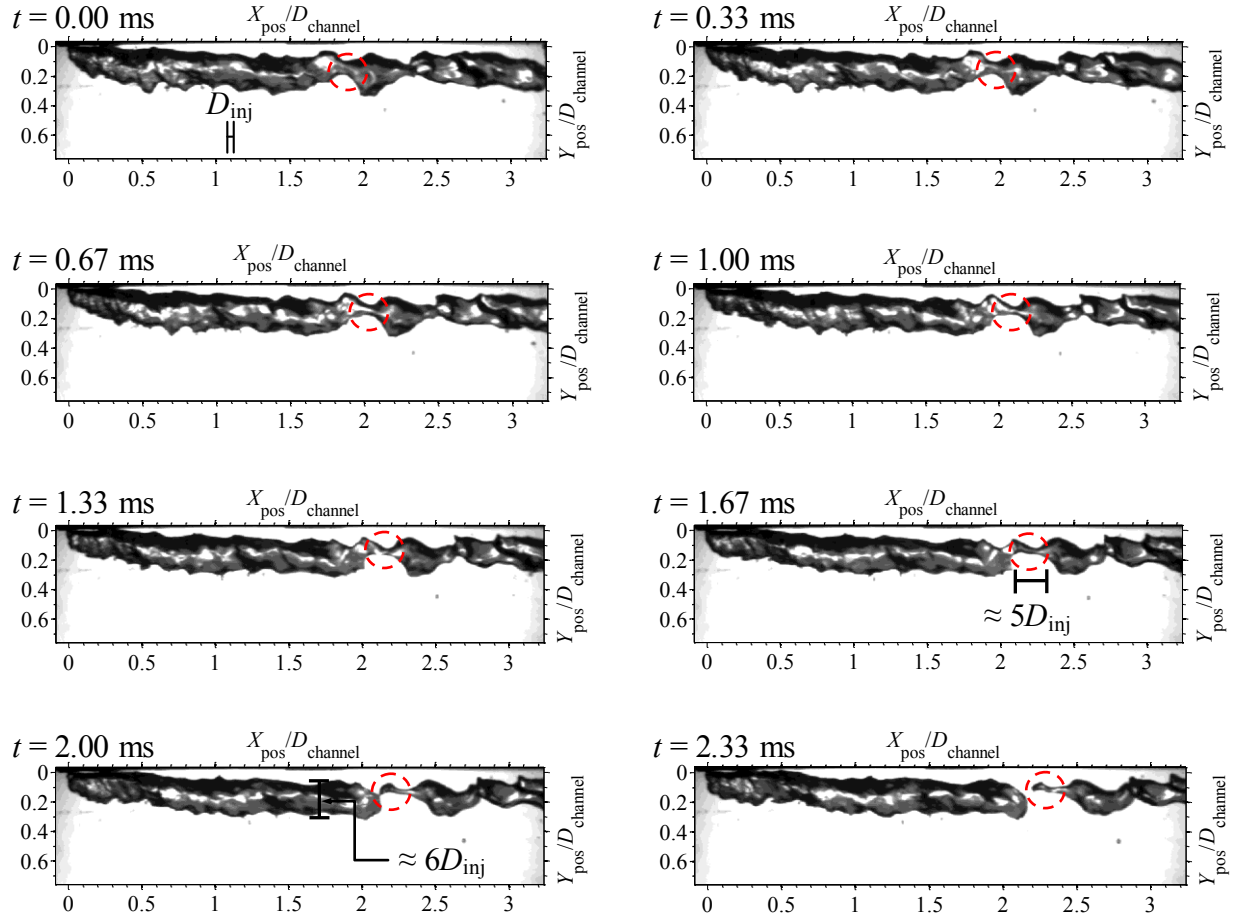
Figure C.3.   Formation and time evolution of the neck that connects the main gas core with the detaching gas lump. The neck length achieved a longitude approximately equal to $5D_{inj}$ and a width close to 1.8 D_{inj} before the separation occurs. The dotted circle in each image indicates the region of interest. $M_G = 9.24 \times 10^{-3}$ g/s, $U_L = 3.0$ m/s, $D_{inj} = 0.52$ mm. Upper wall injection

Due to the dependence of the surface tension expressions on the angles θ, θ_{adv} and θ_{red}, as defined in Figure 3.1, the influence of U_G and U_L on these parameters was studied. The results of this evaluation were included in Figure C.4, which showed the mean values of these angles as a function of the phase velocities. The increased penetration of the gas jet, as well as the volume increase, caused by an increase in U_G were able to counteract the liquid cross flow effects, producing a significant decrease on the advancing angle, as indicated in Figure C.4. For the lowest U_L, the values of α exhibited high variation as U_G changed. As the magnitude of U_L was

increased, the trend exhibited by α suggested a possible independence of this angle from U_L, given by the closeness of the data reported for $U_L \approx 3.1$ and 4.3 m/s respectively.
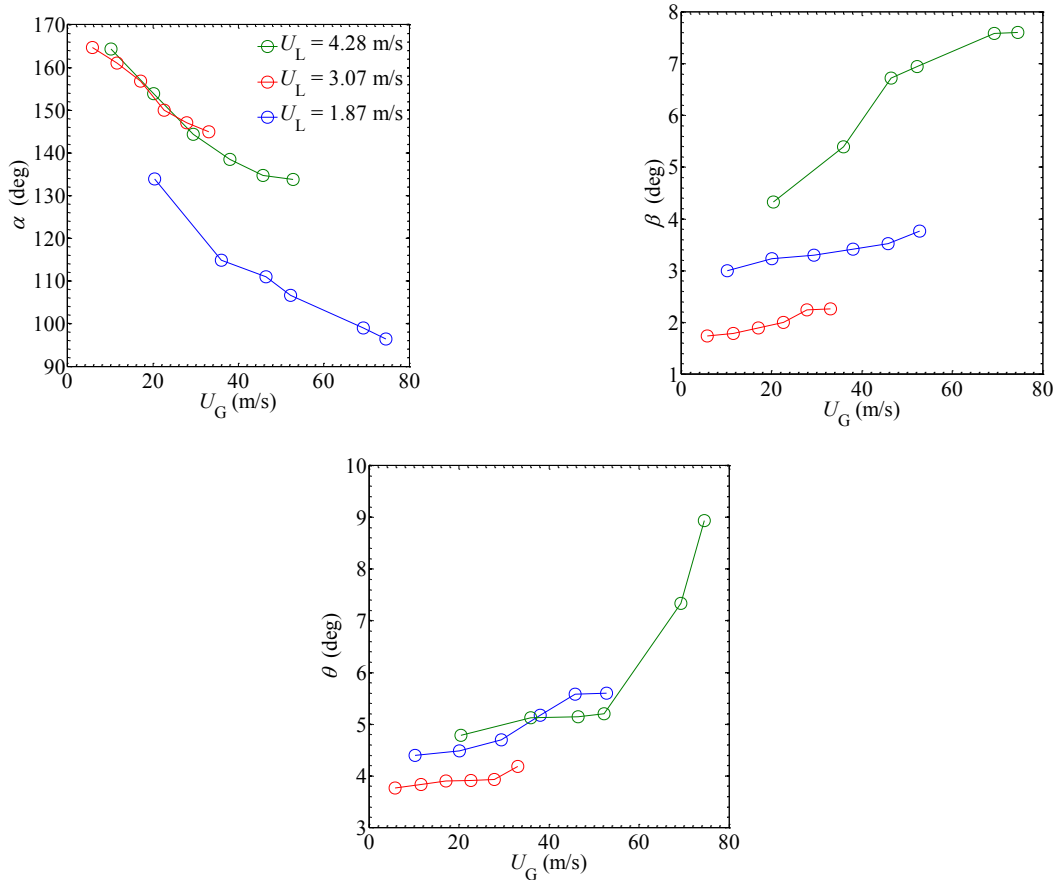
Figure C.4.   Mean values of the advancing (θ_{adv}), receding (θ_{red}) and inclination (θ) angles based on the injection (U_G) and liquid cross flow components (U_L). D_{inj} = 0.52 mm. The gas injector was located in the lower wall

As U_G was increased the β and θ angles experienced a small increment in their magnitude. Although the variation in the receding angle was more noticeable for U_L = 1.9 m/s, for the other liquid velocities the results were confined to a narrow interval, where the difference between minimum and maximum values was approximately 1.2°. For further increases in U_L, the magnitude of both β and θ experienced a considerable decrease, causing the receding angle to be

263

almost parallel to the injection wall. Increasing U_L from approximately 3.1 m/s to 4.3 m/s caused a mean decrease in the inclination angle of 27% and a 70% decline in the receding angle arc.

C.3. Comments about the Drag Force

Another common conjecture observed in the literature for the calculation of F_{Dy} was that, the effective velocity in this direction depends only on the displacement of the gas jet/bubble (Sovani, 2001; Nahra and Kamotani, 2003; Loubiere *et al.*, 2004), which was estimated from the change in the position of centroid for the gas structure, as shown in Figure C.5a. It was inferred that, in a closed channel, the obstruction produced by the gas plume induced the appearance of secondary flows in the vertical direction. Therefore, the liquid is forced to displace along the boundary of the gas structure, attaining a velocity component in the vertical direction that did not had before the interaction with the gas jet, as was hypothetically depicted in Figure C.5b. This could provide the liquid with a velocity in the spanwise direction that is generally unaccounted for. Consequently this may well affect the magnitude of F_{Dy} in an important way. Also, it could induce an acceleration of the liquid in the vicinity of the gas jet, which could have a higher velocity near the interaction region.

Liu *et al.* (2010) considered that the displacement of the gas plume centroid in the horizontal direction would always be smaller than U_L before the interaction between phases occurred. The results obtained indicated that the estimated values of dx/dt could surpass the values that U_L had before mixing with the gas. It was inferred that the liquid accelerated due to the presence of the gas plume in the conduit (Figure C.5b). Undoubtedly, the volume of the gas plume could play a

key role in this phenomenon. However, very little, if any, information about this topic was found in the literature and the experimental technique used did not allow the computation of this effect. Although it was considered that the assumptions generally used in previous works did not reproduce the fundamental complex dynamics of the fluids involved, they provided an acceptable approximation to be used in the calculation of the vertical component of the drag force.
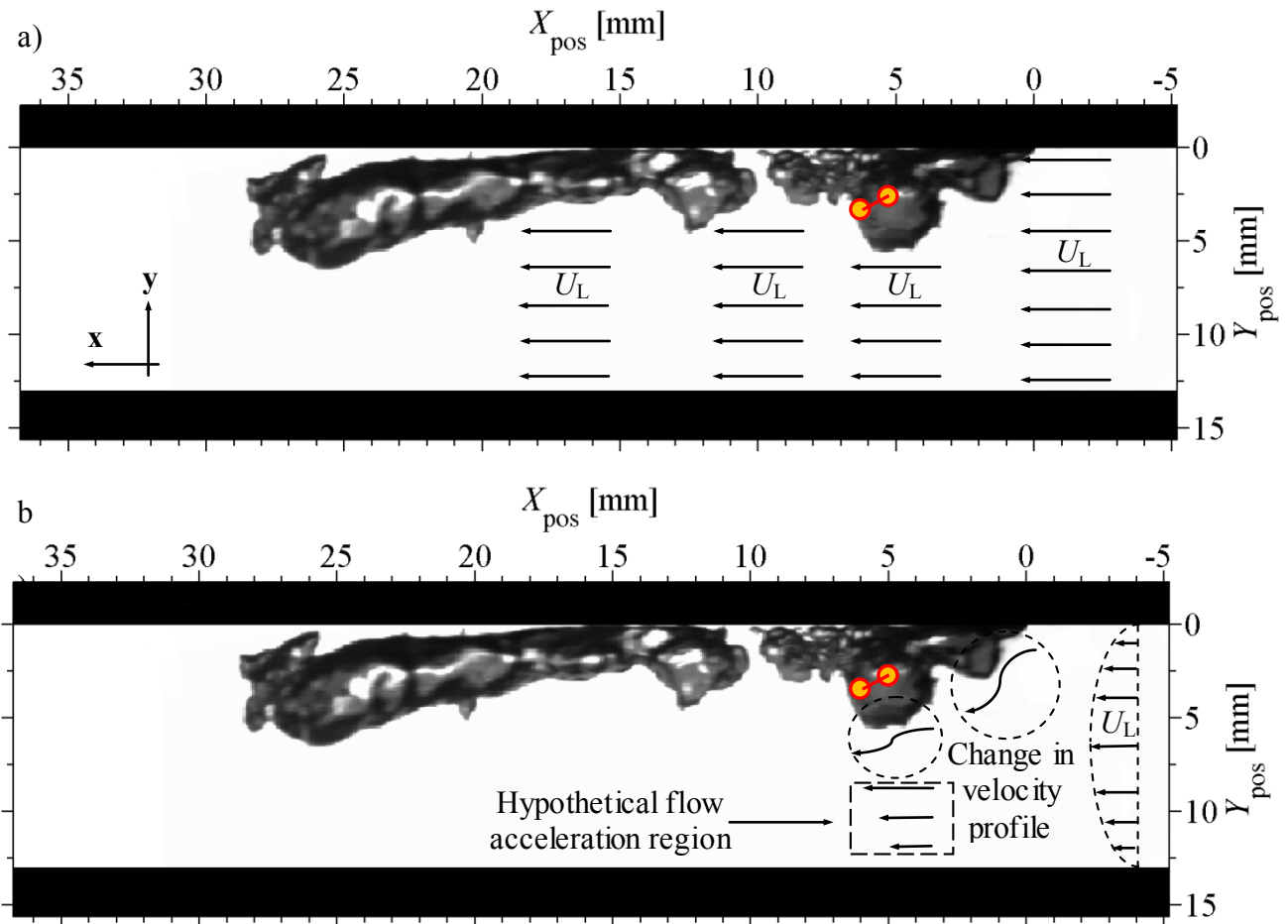
Figure C.5. a) Depiction of the commonly assumed one directional velocity profile used for the estimation of the drag force. The circles depict the hypothetical displacement of the centroid of the gas structure attached to the inlet. b) Portrayal of the change in the velocity profile caused by the presence of a gas jet inside the conduit, as indicated in the curved arrows inside the dotted circles. The liquid is forced to overcome the gas obstacle, obtaining a velocity component in the vertical direction. The flattened velocity profile implies a turbulent flow. D_{inj} = 0.27 mm, M_G = 19.3 × 10^{-2} g/s, U_L = 1.9 m/s

C.4. Considerations about the Lift Force

Both F_{SL} and F_D represent the effects of the shear stress caused by the velocity gradient acting on the bubble surface. No correlations were found in the literature that determine C_L for the interaction of non-spherical gas plumes with a liquid crossflow, hence the methodology followed in this study was similar to the scenario for single rounded bubbles. It was noticed that, similarly to the observations for C_D, C_L also varied with time, because of the change in dimensions experienced by the gas plume during its development. In the vertical direction, the lift force exerts an opposite effect to the drag: The drag force opposes the displacement of gas plume centroid, delaying the detachment in the spanwise direction, while F_{SL} helps in the separation of the gas plume from the wall. Klausner et al. (1993) determined that both effects were within a comparable order of magnitude; the lift force had a slightly higher magnitude than the drag force. Liu et al. (2010) determined that F_{SL} was the main detaching effect in the vertical direction while the drag force becomes negligible.

Thus, C_L was determined based on the instantaneous geometry of the gas jet and was not considered as a constant. Both C_L correlations were tested. Even though the expression proposed by Legendre and Magnaudet (1998) does not apply for all the range of Re_L tested during the current study, its behaviour was still assessed. The results obtained were presented in Figure C.6, taking into consideration the evolution of the gas plume from its early stages up to the point before bubble separation occurs. As observed, both correlations indicated that C_L is much smaller than C_D during the whole growth interval.
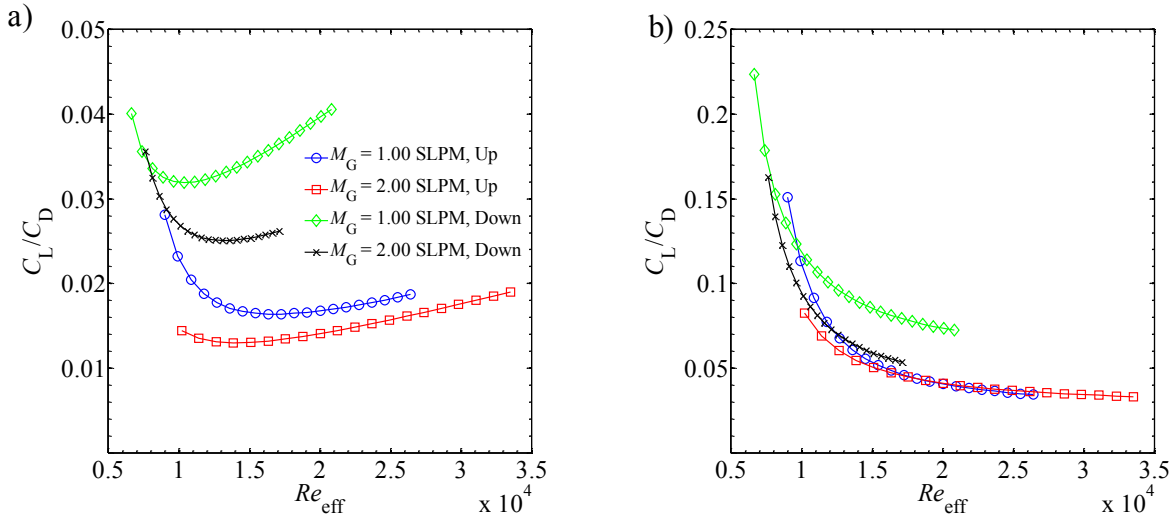
Figure C.6.   Ratio between the lift and drag coefficient as a function of the time-related effective Reynolds number: a) Klausner *et al*. (1993) definition. b) Legendre and Magnaudet definition. The results depicted were obtained for $Re_L \approx 42000$. $D_{inj} = 0.52$ mm. Lower wall injection

The C_L/C_D trend had a maximum when the gas plume had its lowest dimensions and as the gas jet grew, the proportion between coefficients decreased rapidly reaching a quasi-stable faction that ranged between $C_L/C_D \approx 0.04 - 0.08$. The C_L/C_D fraction had a maximum at the beginning of the gas core evolution, and then exhibited a fast decrease reaching a minimum point near the middle of the formation stage. After this, a slow increase in the coefficient ratio was observed. The ratio between coefficients had values that ranged between $C_L/C_D \approx 0.02 - 0.04$. For all the cases tested, the tendency was similar. Although the results shown in Figure C.6 indicated that the C_D is greater than C_L, the way the forces were defined appears to indicate that both of them could play an important role in the dynamics of bubble formation.

C.5. Comments about the Pressure Force

An estimation of the averaged pressure force magnitude and its variation as a function of U_G and D_{inj} was shown in Figure C.7. It was observed that for similar hydrodynamic effects (liquid

pressure and velocity), as the D_{inj} increased F_P increased as well. A larger D_{inj} created a wider injection area, which evidently caused an increase of F_P. Even if an increase in D_{inj} caused a decrease in the D_{equiv}, the increase in the orifice area overcame this factor and produced higher values for F_P. The lowest D_{inj} produced a pressure force that remained almost constant with an increase in the gas flow through the injector. Although the mean effects were considered here, it was understood that the pressure force contribution was time dependent, since it was a function of D_{equiv} which increased with time during the formation interval.
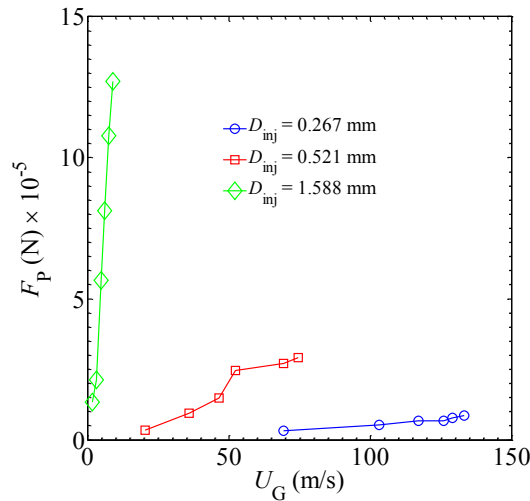
Figure C.7.   Effect of the D_{inj} on the magnitude of the averaged pressure force as a function of the injection velocity. An increase in D_{inj} enhanced the F_P effects. The results depicted correspond to a $Re_L \approx 24000$ and lower wall injection

C.6. Thoughts on the Turbulent Induced Force

The Kolmogorov scale (η), defined according to equation (C.12), determines the smallest eddies that can exist before being dissipated by viscosity. The Taylor microscale (λ) refers to the length of small eddies where the turbulence is isotropic. This scale characterized the intermediate, dissipative scales which constituted the inertial sub-range. λ was determined from equation

(C.13) (Pope, 2000). *Λ* scale was considered as a representation of the largest possible turbulent structures that could be found within the turbulent flow. These structures have a large velocity fluctuation and a low frequency. For fully developed duct flow, the integral length scale is considered to be a fraction of the hydraulic diameter, generally comprehended between 3 to 10% (Townsend, 1976; Thomas, 1981; Zhukovskaya, 2012). For the purposes of this study, the integral length scale was assumed to be equal to the maximum percentage reported in the literature, i. e. $Λ \approx 0.1D_{\text{channel}}$.

$$\eta = \left(\frac{v^3}{\varepsilon} \right)^{\frac{1}{4}} \qquad (C.12) \qquad\qquad \lambda = \left(\frac{10v\kappa}{\varepsilon} \right)^{\frac{1}{2}} \qquad (C.13)$$

$$\bar{\varepsilon} = \frac{2f\bar{U}_{\text{L}}^3}{D_{\text{channel}}} \qquad (C.14) \qquad\qquad \kappa = \frac{1}{2}\left(u_{\text{x}}'^2 + u_{\text{y}}'^2 + u_{\text{z}}'^2 \right) \qquad (C.15)$$

As was observed, the turbulent length scales were identified with the turbulence dissipation rate (ε) and the turbulent kinetic energy (κ), defined in equations (C.14) and (C.15) respectively. Hesketh et al. (1987) proposed that, for pipe flow, the average dissipation rate ($\bar{\varepsilon}$) could be defined as a function of the friction factor, as was shown in equation C.14. They also proposed that in a pipeline the local energy dissipation rate is equal to the average energy dissipation. Hence, this assumption was used to obtain the value of ε.

The kinetic energy κ depended on the turbulence intensity (*I*). For fully developed pipe flow, the turbulence intensity at the core can be estimated according to expression (C.16), where the Reynolds number was defined based on the hydraulic diameter of the conduit. Using this correlation, it was estimated that the turbulence intensity oscillated between $0.041U_{\text{L}}$ to 0.048

U_L for the range of Re_L comprehended from 14000 to 56000. Melling and Whitelaw (1976) obtained that in a square-like conduit the turbulence fluctuations were not fully isotropic. At a streamwise position $x/D_\text{channel} \approx 36$ and $Re_\text{L} \approx 42000$, the maximum values of the fluctuating components measured were $u'_\text{x} \approx 0.08$, $u'_\text{y} = u'_\text{z} \approx 0.06$. At this position, the $U_\text{center}/U_\text{L}$ ratio obtained a quasi-steady value ≈ 1.21. When substituted in equation (C.16), these values provided an estimation of I based on the liquid bulk velocity which was approximately equal to 0.12. Zhukovskaya (2012) reported that the turbulent intensity in a conduit oscillated between 25 to 17% for Re_L between 53000 to 78000. Zhukovskaya (2012) determined that in a square conduit the turbulence intensity was a function of the Reynolds number of the liquid and was given by the expression (C.17). Equations (C.18) and (C.19) were used to estimate the characteristic velocity and relaxation time of the eddies respectively. It was inferred that the same equations were applicable to the Taylor and Kolmogorov scales.

$$I = 0.16\,Re_\text{L}^{-\frac{1}{8}} \qquad \text{(C.16)} \qquad\qquad I = 5575\,Re_\text{L}^{-0.92} \qquad \text{(C.17)}$$

$$u_\Lambda = (\varepsilon\Lambda)^{\frac{1}{3}} \qquad \text{(C.18)} \qquad\qquad t_\Lambda = \Lambda/u_\Lambda = \frac{\Lambda^{\frac{2}{3}}}{\varepsilon^{\frac{1}{3}}} \qquad \text{(C.19)}$$

Due to the variety of results found in the literature, the approach used to estimate the influence of the turbulence length scales on the bubble formation considered two turbulence intensity scenarios. For a given value of the Re_L, medium ($I = 5\%$) and high turbulence intensity ($I = 25\%$) possibilities were tested, as indicated by equations (C.16) and (C.17). The lower intensity situation ($I < 1\%$) was not considered as this is an unlikely possibility for a standard fully developed flow in a conduit. The chosen values for I were studied for two values of Re_L (≈ 24000 and 55000) and the findings obtained were presented in Tables C.2 to C.5.

Isotropic turbulence was assumed, although it was understood that this might not be a proper representation of the physics of the problem.

Table C.2. Estimation of the ratio between the turbulence length scales at a high intensity ($I = 25\%$) versus the mean equivalent diameter of the gas structure. $D_{inj} = 0.27$ mm

Re_L	$Re_G \times 10^{-3}$	D_{equiv} (mm)	D_{equiv}/η	D_{equiv}/λ	D_{equiv}/Λ
	1.7	6.9	493.5	98.0	5.4
	5.2	10.4	746.8	148.3	8.2
24200	7.7	12.9	924.5	183.6	10.1
	10.3	13.1	941.0	186.9	10.3
	12.0	14.7	1058.3	210.1	11.6
	15.5	16.3	1175.5	233.4	12.9

Table C.3. Estimation of the ratio between the turbulence length scales at a medium intensity ($I = 5\%$) versus the mean equivalent diameter of the gas structure. $D_{inj} = 0.27$ mm

Re_L	$Re_G \times 10^{-3}$	D_{equiv} (mm)	D_{equiv}/η	D_{equiv}/λ	D_{equiv}/Λ
	1.7	6.9	879.5	137.8	5.4
	5.2	10.4	1330.8	208.4	8.2
24200	7.7	12.9	1647.4	258.0	10.1
	10.3	13.1	1676.9	262.7	10.3
	12.0	14.7	1885.9	295.4	11.6
	15.5	16.3	2094.9	328.1	12.9

Table C.4. Estimation of the ratio between the turbulence length scales at a high intensity ($I = 25\%$) versus the mean equivalent diameter of the gas structure. $D_{inj} = 0.27$ mm

Re_L	$Re_G \times 10^{-3}$	D_{equiv} (mm)	D_{equiv}/η	D_{equiv}/λ	D_{equiv}/Λ
	2.5	1.3	91.4	18.1	1.0
	3.9	1.8	127.3	25.3	1.4
55500	5.4	2.7	192.8	38.3	2.1
	7.6	4.1	292.1	58.0	3.2
	9.1	5.2	372.7	74.0	4.1
	10.1	4.8	345.3	68.6	3.8

Table C.5. Estimation of the ratio between the turbulence length scales at a medium intensity ($I = 5\%$) versus the mean equivalent diameter of the gas structure. $D_{inj} = 0.27$ mm

Re_L	Re_G	D_{equiv} (mm)	D_{equiv}/η	D_{equiv}/λ	D_{equiv}/Λ
	2.5	1.3	162.8	25.5	1.0
	3.9	1.8	226.9	35.5	1.4
55520	5.4	2.7	343.6	53.8	2.1
	7.6	4.1	520.5	81.5	3.2
	9.1	5.2	664.1	104.0	4.1
	10.1	4.8	615.4	96.4	3.8

The results indicated that, independent of the magnitude of the turbulence intensity and/or the Re_L, D_{equiv} was at least an order of magnitude higher than both η and λ. The energy containing eddies were the only structures whose length scale was constantly within an order of magnitude comparable to that of the gas plume. Hence, only these eddies could be to ones capable of producing a significant alteration during the growth and evolution of the gas core. The smaller turbulent structures could create micro scale deformations at the gas interface which look like small ripples. The energy contained in the small eddies is rapidly dissipated and does not contribute significantly to the bubble breakup (Andersson and Andersson, 2006). An analog behaviour was assumed to occur for the Taylor eddies, although the magnitude of the deformations would be more noticeable and could even contribute to the internal flow within the gas plume. The size of the viscous length scale was much smaller than D_{equiv}, hence it was concluded that its contribution to bubble formation process was not relevant. Overall, it was observed that for the vast majority of the cases, the mean D_{equiv} of the gas plume were higher than all the turbulence length scales, hence turbulence could affect the formation process only at the integral scale dimensions.

The time scale associated to eddies of size Λ (t_Λ) was obtained from equation C.19. The estimated mean growth time for the gas plume (t_{growth}) was reported in Tables 3.8 and 3.9. The turbulence Stokes number (St_Λ) was defined as the ratio of t_{growth} versus t_Λ, as seen in Equation (C.20) (Ishii and Hibiki, 2010). The turbulence effects were compared to the growth effects considering the previously described Re_L and I scenarios. St_Λ was higher than 1 for all the cases, which implied that during the growth process, the gas plume had little time to respond to the turbulence fluctuations (Crowe, 2006). It was inferred that, even though the turbulence was

considered the main cause for possible irregularities in the formation frequency, the mechanics of gas injection were not solely dominated by the energy-containing eddies.

$$St_\Lambda = \left(t_{growth} \middle/ t_\Lambda \right) \tag{C.20}$$

Table C.6. Estimation of the ratio between the turbulence time scales at a medium intensity ($I = 5, 25\%$) versus the associated time constant of the gas structure. $D_{inj} = 0.27$ mm

Re_L	$Re_G \times 10^3$	D_{equiv} (mm)	t_{growth} (ms)	t_Λ (ms)	St_Λ
	1.7	6.9	6.8	1.8	3.8
	5.2	10.4	12.8	1.8	7.1
24200	7.7	12.9	16.6	1.8	9.1
	10.3	13.1	16.3	1.8	9.0
	12.0	14.7	16.3	1.8	9.0
	15.5	16.3	12.9	1.8	7.1

Table C.7. Estimation of the ratio between the turbulence time scales at a medium intensity ($I = 5, 25\%$) versus the associated time constant of the gas structure. $D_{inj} = 0.27$ mm

Re_L	$Re_G \times 10^3$	D_{equiv} (mm)	t_{growth} (ms)	t_Λ (ms)	St_Λ
	2.5	1.3	1.6	0.8	2.0
	3.9	1.8	1.7	0.8	2.0
55500	5.4	2.7	2.6	0.8	3.2
	7.6	4.1	2.5	0.8	3.0
	9.1	5.2	2.8	0.8	3.4
	10.1	4.8	2.7	0.8	3.2

Conclusive information about the interaction between a developing gas plume/bubble, produced by nozzle injection and in the presence of a turbulent liquid cross flow was not found in the literature. However, it was understood that a turbulent field would interact with the growing gas jet. Because of the lack of specific information for the problem at hand, an analogy was established with the very similar case of bubble/drop breakup. Liao and Lucas (2009) presented a comprehensive review about the mechanisms involved in the disintegration of a fluid particle in a turbulent dispersion. Based on the information reported in the literature, at least eight possible

particle breakup criteria were identified, of whom five were caused by turbulence. These phenomena were summarized in Table C.8.

Table C.8.　Classification of fluid particle breakup mechanisms. Adapted from Liao and Lucas (2009)

Turbulent fluctuation and collision	Non-Turbulent
The turbulent kinetic energy of the particles has to be greater than a critical energy value.	Interfacial instability.
The velocity fluctuation over the particle surface must be above a critical value.	Viscous shear forces.
The turbulent kinetic energy of "hitting" eddies exceeds a critical energy value.	Shearing-off process.
The inertial force of interacting turbulent eddies must be greater than the interfacial force associated to the smallest particle produced by breakup.	
The combined effect of the eddies (turbulent kinetic energy + inertial force) must overcome the particle interfacial force and a critical energy value.	

Important considerations highly applicable to the present study, owing to the similarity in the phenomena observed, were derived from the work of Liao and Lucas (2009). They were presented with the purpose of highlighting the existing difficulties in predicting the breakup dynamics of a bubble in a turbulent field and were included next:

* Key parameters, like the critical energy needed for breakup, were arbitrarily defined by each author.

* For larger fluid particles, the relative velocity at the interface has a significant contribution in the shearing-off process and in the generation of interfacial instabilities. It was reported that for air-water flows, the shearing process was dominated by the gas velocity profile inside the bubble.

* Effects, such as the Kelvin-Helmholtz and Rayleigh-Taylor instabilities, were commonly disregarded in the presence of a turbulent field.

* The viscous force and relative velocity between phases were neglected in favour of the turbulent flow field. Generally, no validation was provided.

* The complexity of the breakup phenomenon have made impossible to obtain a unified criteria that evaluates all the possible mechanisms involved.

* Most breakup models focus solely on the turbulence mechanics, which are far from understood, and have been mostly verified only for ideal cases of individual bubbles and under specific conditions.

Appendix D. Additional Bubble Formation Regime Charts Based on Dimensionless Variables

D.1. Reynolds number based formation maps

All the scenarios illustrated in Figure 7.1 through 7.4 are associated with a fully turbulent regime for the liquid phase. With regards to the gas phase, based on the development length associated to each one of the injection diameters used, provides more than the rule-of-thumb $50D_{inj}$ required for a turbulent gas jet. For lower values of the injection velocity, the Re_G indicates a laminar regime. Nonetheless, the development length for this case is above the recommended $150D_{inj}$. A lower value of D_{inj} leads to higher values of the gas injection velocity, hence increasing the Re_G and producing a more turbulent regime. Successive increases in the injection diameter from $D_{inj} = 0.27$ mm to $D_{inj} = 0.52$ mm and $D_{inj} = 1.59$ mm produce a decrease in the range of the gas Reynolds number 50% and 75% respectively.

In agreement with Kyriakides et al. (1997), it was observed that, independent of the D_{inj}, the single bubbling regimes are analogous for the various regions delimited in the maps. At lower liquid cross-flow velocity values, therefore at lower Re_L, the transition between regimes occurs faster. Increasing the Re_L delays the switchover between bubbling scenarios. This trend is independent of D_{inj}, as can be observed in Figure D.1 Increasing the value of D_{inj} from 0.27 mm to 1.59 mm, approximately six times, reduces the number of observable regimes (from six to four) and completely eliminates the possibility of chaotic bubble formation for the range of parameters tested here (Figure D.1c). A higher injection diameter predominantly induces the

formation of bubbles under the single bubble regime, pulse regime or the transitional region SBP.
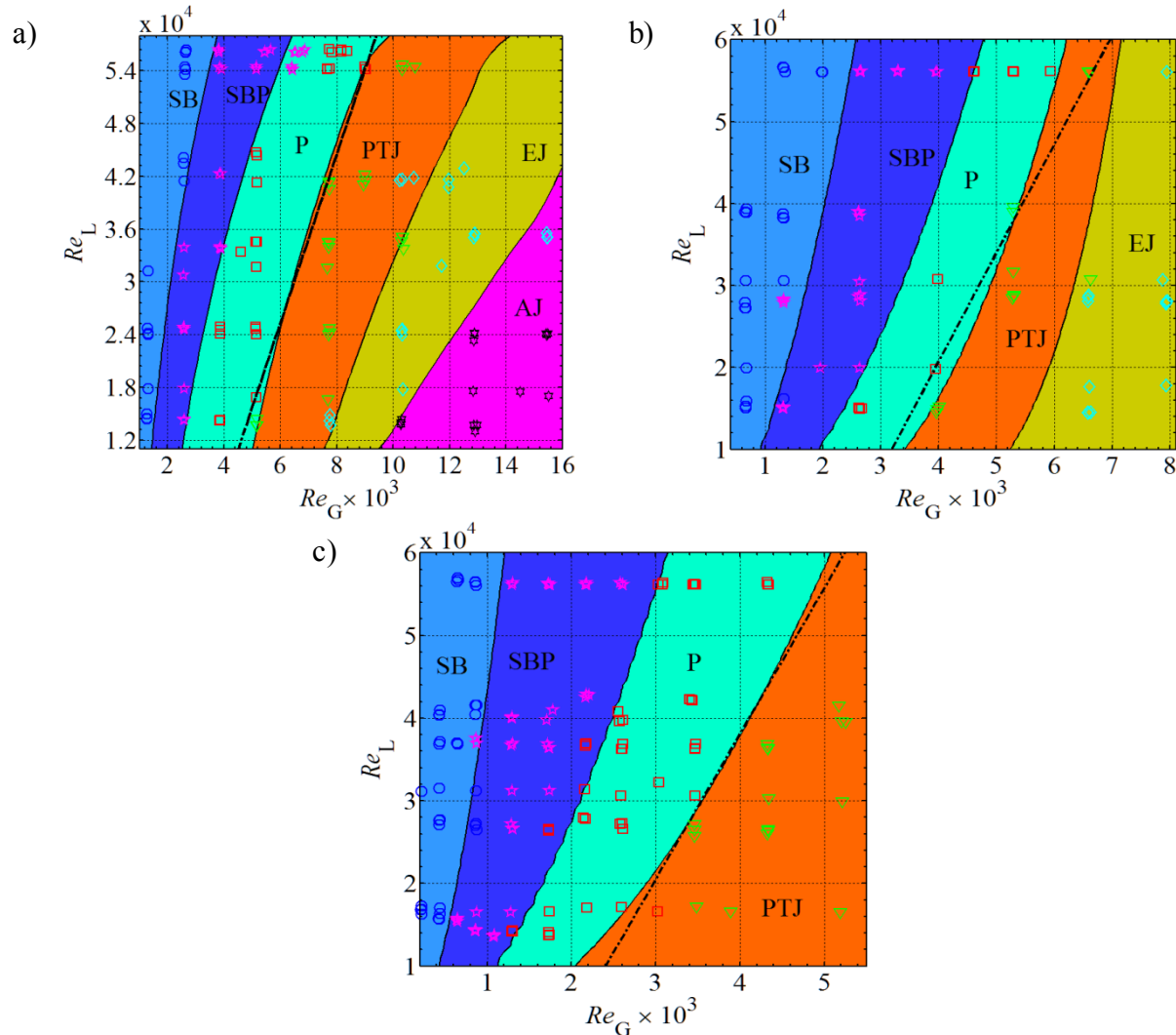
Figure D.1   Bubble formation map based on dimensionless numbers (Re_G-Re_L) for: a) D_{inj} = 0.27 mm. b) D_{inj} = 0.52 mm. c) D_{inj} = 1.59 mm

In the work of Kyriakides et al. (1997), it was determined that the Reynolds number at the gas inlet is the physical mechanism driving the transition between bubbling regimes. This effect is noticeable in Figure D.1a and D.1b, where the transition towards the developed jetting regime occurs when the Re_G is within the range of can be considered a fully turbulent gas jet. For the

disordered regimes, such as *AJ*, the gas disperses multiple times before the detachment of what can be considered a main gas core occurs, producing a broad distribution of bubble diameters.

It is possible to establish an analogy between the turbulence evolution of a submerged gas jet and its single phase counterpart, which sets the internal turbulence of the gas phase as the driving factor behind the perturbations of the jet boundary (Weiland & Vlachos, 2013). During the atomizing bubbling mode, in the vicinity of the gas inlet, the small turbulent structures of the jet generate early breakup. Although it might be argued that they do not possess enough energy to overcome the surface tension forces, due to their higher frequency, they are capable of deform the gas-liquid interface more rapidly than larger vortices (Sovani, 2001). This fast perturbation induces a recirculation of the gas inside the jet and creates small pockets, which, when combined with the detaching effects of the liquid cross flow, induce the formation of small-sized bubbles (Andersson & Andersson, 2006).

This can be considered as a secondary detachment, because the loosening of the small particles does not affect significantly the morphology and behavior of the gas core. Based on the results shown in Figure 7.4c, it is clear that the first bubbles formed in this region will have a small diameter. As stated by Brennen (2005), further downstream from the injection, the energy contained in the small turbulent structures associated to the gas phase, decays faster than the energy transported by the larger structures. Hence, the size of the disturbances created in the interface grows correspondingly, leading to bubbles with a larger diameter. The largest turbulent eddies present in the gas phase will be the last ones to disappear due to having higher energy, and they will be responsible for creating bubbles whose size is of the same order of magnitude of

the jet diameter, and as observed in Figure 7.4b, will be generated at the point where the jet breaks completely. This can be considered as a primary detachment, due to loosening of a sizeable gas lump, which allows the re-growth of the jet and starts the cycle anew. A wider array of turbulent structures is present in the gas jet that leads to atomization, hence a larger bubble size distribution will be observed.

Using an approach similar to the one taken by Akagi et al (1987), Marshall (1990) and Rigby et al. (1995), it is possible to propose an experimental relationship that defines the maximum Re_G, as a function of the liquid phase Reynolds number, under which a purely ordered regime occurs. The correlation was defined as a function of the diameter ratios considered in this experiment (Equation D.1), and the results obtained were represented in the regime maps shown in Figure D.1, where the dotted black line represents the proposed boundaries. Based on the Reynolds numbers of the gas and liquid phase, if the value obtained from the correlation, defined as $Re_{disordered}$, is higher than Re_G, then the regime will be in any of the ordered formation patterns; the opposite implies a chaotic regime.

$$Re_{disordered} = \left(0.028 Re_L + 905\right) D_{ratio}^{0.34} \tag{D.1}$$

If the gas phase momentum is high, it will have enough momentum to overcome the bending effect imposed by the liquid phase and penetrate further into the conduit. When exposed to higher values of the local liquid velocity, it is assumed that there will be an additional effect causing the jet disintegration: the liquid turbulent eddies whose size are smaller than the jet width will collide with the gas stream, imposing an internal flow in the gas, causing a reordering

which induces the formation of separated structures within the jet, similar to the bubble breakup criteria described by Andersson & Andersson (2006). If the combined detaching effects are able to overcome the surface tension effects, the bubbles will form and detach. However, if Re_G is high but the small eddies do not possess the energy necessary to cause a breakup; a lower number of initial bubbles will form, if any. The high energy vortices create noticeable disturbances in the interface (Brennen, 2005; Weiland & Vlachos, 2013). If no early detachment occurs, the small eddies lose their energy and the larger vortices control the process of bubble detachment which will occur predominantly at x_{break}. This scenario describes the elongated jet regime.

High values of Re_G induce jetting regimes. At high ratios Re_G/Re_L it is more feasible to observe an elongated and/or atomizing jet inside the conduit. An increase in the momentum ratio between the phases is required in order to achieve a fully developed jet regime. At lower values of Re_L, a dominant EJ can be observed at $Re_G \approx 8000$, while at higher values of Re_L, the minimum required Re_G oscillates around 13500. As expected, the atomizing jet occurs only in a limited region of map, requiring the Re_G to have a minimum value of 9600, and completely disappearing as a possible regime when $Re_L \approx 44000$. The experimental data obtained lead to a correlation which defines minimum value of the gas Reynolds number required for the appearance of an atomizing jet, defined as Re_{AJ} in equation (D.2).

$$Re_{AJ} \geq 0.2(Re_L) + 7200, \quad \text{for } Re_L \leq 4.5 \times 10^4 \tag{D.2}$$

Contrary to the conditions required for the dominant jetting regimes, in the single bubble regime the Re_G is mostly laminar. Increasing the magnitude of the injection diameter decreases the shift from a *SB* regime to a transitional phase. For a similar value of Re_G, a higher D_{inj} triggers the changeover towards the transitional and pulsating regimes. A higher Re_L delays the evolution towards a pulsating regime. For a $Re_G = 2000$ and $Re_L = 25000$, a $D_{inj} = 0.27$ mm will produce a regime located near the boundary that gives rise to the transitional scenario, increasing the diameter to $D_{inj} = 0.52$ mm with the regime being located into the *SBP* region, while for the highest injection diameter, $D_{inj} = 1.59$ mm the same point will be located close to the limit of the pulsating regime (Figure D.1).

For the same value of the gas Reynolds number, doubling the value of Re_L, will move the proposed formation scenarios to a dominant *SB* (lowest and mid D_{inj}) or well into the *SBP* region (Highest D_{inj}). Increasing Re_L raises the detaching effect, increasing the frequency of formation and decreasing the bubble diameter, all features associated to the SB regime. Increasing the D_{inj}, diminishes the gas injection velocity, which in turn decreases the Re_G.

D.2. Weber number based bubble formation maps

The transition between regimes can also be evaluated by comparison of the balance between surface tension/inertia effects associated to the gas phase and the inertial/viscous effects of the liquid phase. Increasing D_{inj} modifies considerably the effect that the surface tension forces have on the formation regime. Assuming a constant mass flow rate and surface tension coefficient, while neglecting the compressibility effects, the We_G can be considered to be inversely

proportional to D_{inj}^3. Although the density experiences some degree of variation, for the range of conditions evaluated, the range of deviation is not enough to consider the Mach number as a dominant parameter.
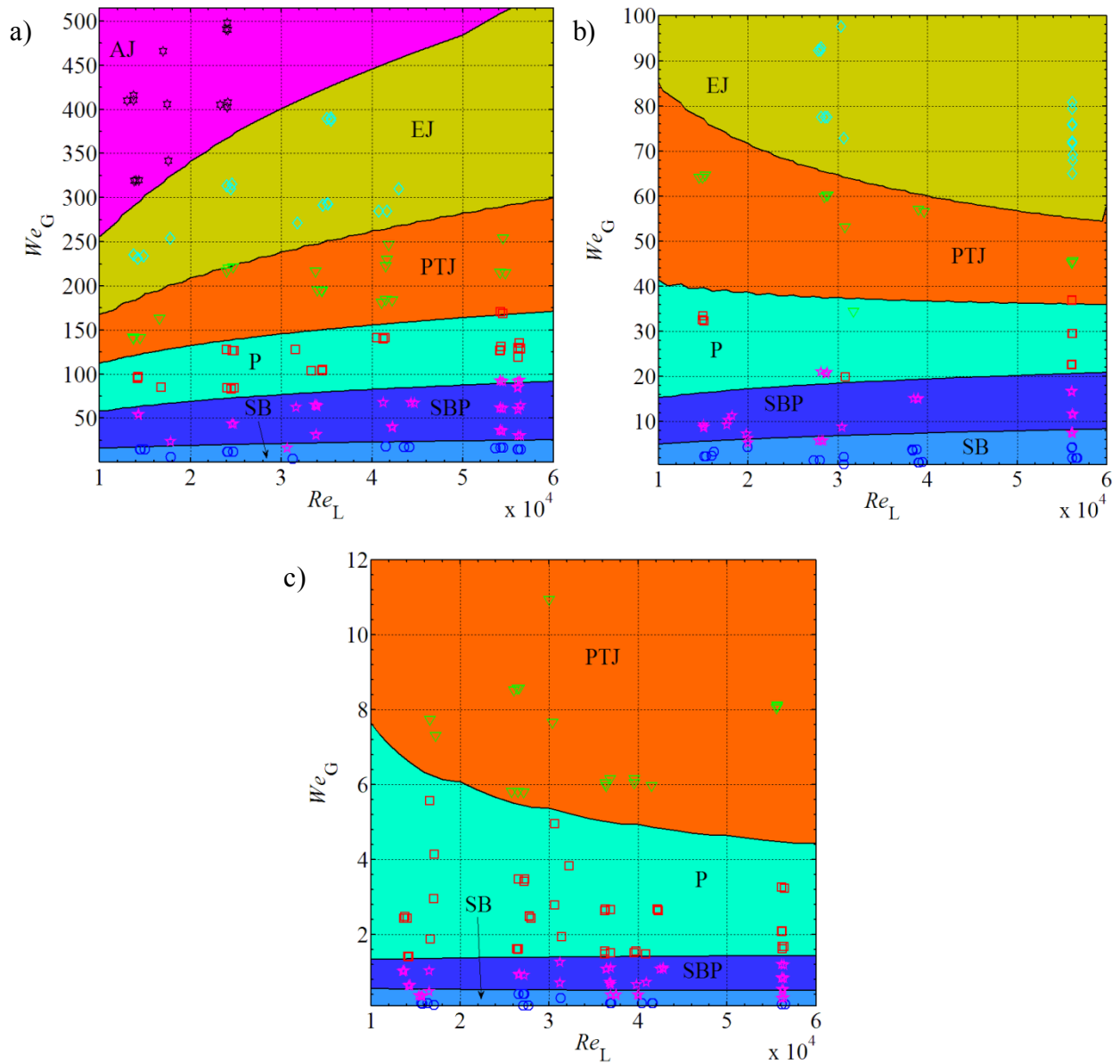
Figure D.2. Bubble formation map based on dimensionless numbers (We_G-Re_L) for: a) $D_{inj} = 0.27$ mm. b) $D_{inj} = 0.52$ mm. c) $D_{inj} = 1.59$ mm

Independent of the injection diameter and Re_L value, the SB region is located at low values of the gas Weber number, indicating that, as expected, surface tension forces play an important role in the establishment of the ordered regime. Combined with the small gas momentum values associated with this regime, bubbles whose growth and detachment occur very close to the gas inlet location occur; a feature characteristic of the SB regime. For a $1/D_{ratio} = 48$ and $1/D_{ratio} = 24$, an increase in Re_L induces a slight increase of the magnitude of We_G at which the transition occurs, as observed in Figure D.2 where the continuous lines represent the proposed boundaries between the individual bubble and transitional zones.

If $1/D_{ratio} = 8$, the switchover occurs at an almost constant value of $We_G \approx 0.525$, for the range of Re_L considered. Only when the momentum of the laminar gas flow exiting the inlet pipe is able to reach a magnitude higher than 50% of the attaching forces associated to the surface tension $\left(\rho_G U_G^2 D_{inj}^2 > 0.5 \sigma D_{inj} \right)$, is possible to observe a mixed formation regime. For this particular case, the liquid phase momentum and its turbulence associated effects have very little influence in controlling the process of bubble formation. The tilting created by liquid momentum and/or the turbulent eddies whose size is larger than the equivalent bubble diameter is the only noticeable effect associated with the liquid phase. When the D_{ratio} is high, the gas stream penetration is significantly reduced. Due to the cross-flow velocity, the bubble spreads over the orifice, increasing its contact area (Duhar & Colin, 2006). This region appears to increase proportionally with the detaching forces, which creates the relatively constant Weber number (Figure D.2c).

The trend exhibited by the *SB* and transitional *SBP* regions is similar for each one of the injection diameters studied. A slow increase in the limiting We_G value as Re_L increases, with a less

pronounced increment as D_{inj} is increased (Figure D.2). However, the tendency changes for the other zones: For a $D_{\text{ratio}} = 0.0210$, the shift between regions occurs at higher We_{G} numbers when the liquid velocity increases. The high ratio between the fixating and disconnecting effects in the gas phase might indicate that the mechanisms of bubble formation for this geometry show relative independence of surface tension effects. Based on the behavior shown, at low D_{ratio}, increasing the Re_{L} induces an enhancement in the gas jet contact area, strengthening the effects that oppose bubble separation from the gas jet.

The atomizing regime sub-region is located within the limits or $Re_{\text{L}} \leq 2.5 \times 10^4$ and $We_{\text{G}} > 300$ (Figure D.2a). The high ratio between gas inertial forces versus attaching forces indicates an injection mechanism dominated by the gas momentum effects, with little contribution from the surface tension. The high injection velocity produces a rapid penetration of the gas into the channel, which enters at an almost vertical angle. The contact region between the gas and the inlet orifice is relatively small. As explained before, only the highest energy eddies of the gaseous phase are capable of overcoming the surface tension and create small bubbles near the injection area, right before the tilting of the jet occurs.

Once the liquid momentum forces the bending of the gas stream, the decay of high frequency turbulent vortices has occurred, and only the larger vortices will be able to overcome the influence of the connecting forces. After the primary detachment occurs, the surface tension appears to decrease, giving rise to several phenomena: The influence of the gas recirculation during the jet allows the smaller vortices to overcome the surface tension and create smaller sized bubbles. A premature breakup of the large gas volume can also occur, in part due to the

effect of the liquid phase turbulent eddies, which induce an internal recirculation inside the recently detached bubble before the wobbly movement associated with the gas turbulence is dissipated. It also might be possible that, multiple necks exist, which close and form particles thanks to the contribution of the liquid phase turbulence. All of these are plausible explanations for the large bubble size distribution.

For a D_{inj} = 0.52 mm, at lower values of Re_L, an elevated We_G number is required for the switchover between the P, PTJ and EJ zones. As Re_L increases, the limiting We_G decreases. This effect is particularly noticeable for the pure jetting region. With the increase in the D_{inj}, the surface tension effects are increased, and the turbulence/inertial effects of the gas phase are not able to produce an atomizing regime. When Re_L = 10000, the EJ occurs for $We_G \geq 85$, while at the maximum Re_L studied, the elongated jet can be observed at $We_G \geq 54$; a decrease of 36.5% in the inertial effects is required in order to achieve the same regime. If the We_G is held constant and the Re_L value is incremented, the gas stream experiences an increased drag (Marshall et al., 1993; Sovani, 2001; Thorncroft et al., 2001; Nahra & Kamotani, 2003). This shifts the regime from a possible transitional phase to a pure jetting zone (Figure D.2b). A similar situation occurs when D_{inj} = 1.59 mm, but with the important difference that in this case the change involves the pulse to jet transitional region (Figure D.2c).

In order to evaluate the applicability of the maps presented, the straightforward choice is a comparison with previously existing maps from the literature. However, for the set of conditions studied, a direct comparison is not feasible. From the few existing studies that have been oriented to the categorization of the bubbling regimes in a cross-flow, only Rigby et al. (1995), Forrester

& Riley (1998) and Sovani (2001) present charts that delimit the different bubbling zones. The first two works focused principally on evaluating the effects of impeller blade geometries. Little consideration was given to the influence of the D_{inj}, which as inferred from the results presented in Figures D.1 and D.2, has a predominant effect on the bubbling regimes that occur within the conduit. Also, the use of different velocity ranges and the choice of maps based on dimensional variables present additional difficulties to the task of establishing an appropriate comparison.

According to Sovani (2001), the use of velocity maps yields results similar to those based on dimensionless variables, such as Reynolds numbers or Weber numbers associated to the phases, provided that the fluid properties remain constant. The experimental conditions for Rigby et al. (1995) and Forrester and Riley (1998) indicate constant liquid pressure. However, no consideration was given to the effect that an increase on the gas or liquid mass flow rate has on the gas density. Based on the experimental findings of the current study, modifications of the fluid flow rates induce slight variations in the gas density. Even though the density variations observed were within less than an order of magnitude, the ρ_G changes could have a non-negligible contribution to the Re_G and We_G.

Sovani (2001) is the only existing study that considers the use of Weber number based bubbling maps. Still, the existing operational and geometrical differences between his study and the current one, observable in the values reported in Tables 7.1 and 7.2, present daunting difficulties that make impossible to compare the results obtained from both maps beyond a quantitative assessment (Table 2). The experimental correlation developed by Marshall (1990), could not be directly applied to the regime charts presented, due to the different physical phenomena

considered. Also, it implies that, for constant values of the gas velocity, an increase in the liquid cross-flow velocity will necessarily trigger the shift towards the disordered regime, which is the opposite of what has been shown in Figures D.1 and D.2.
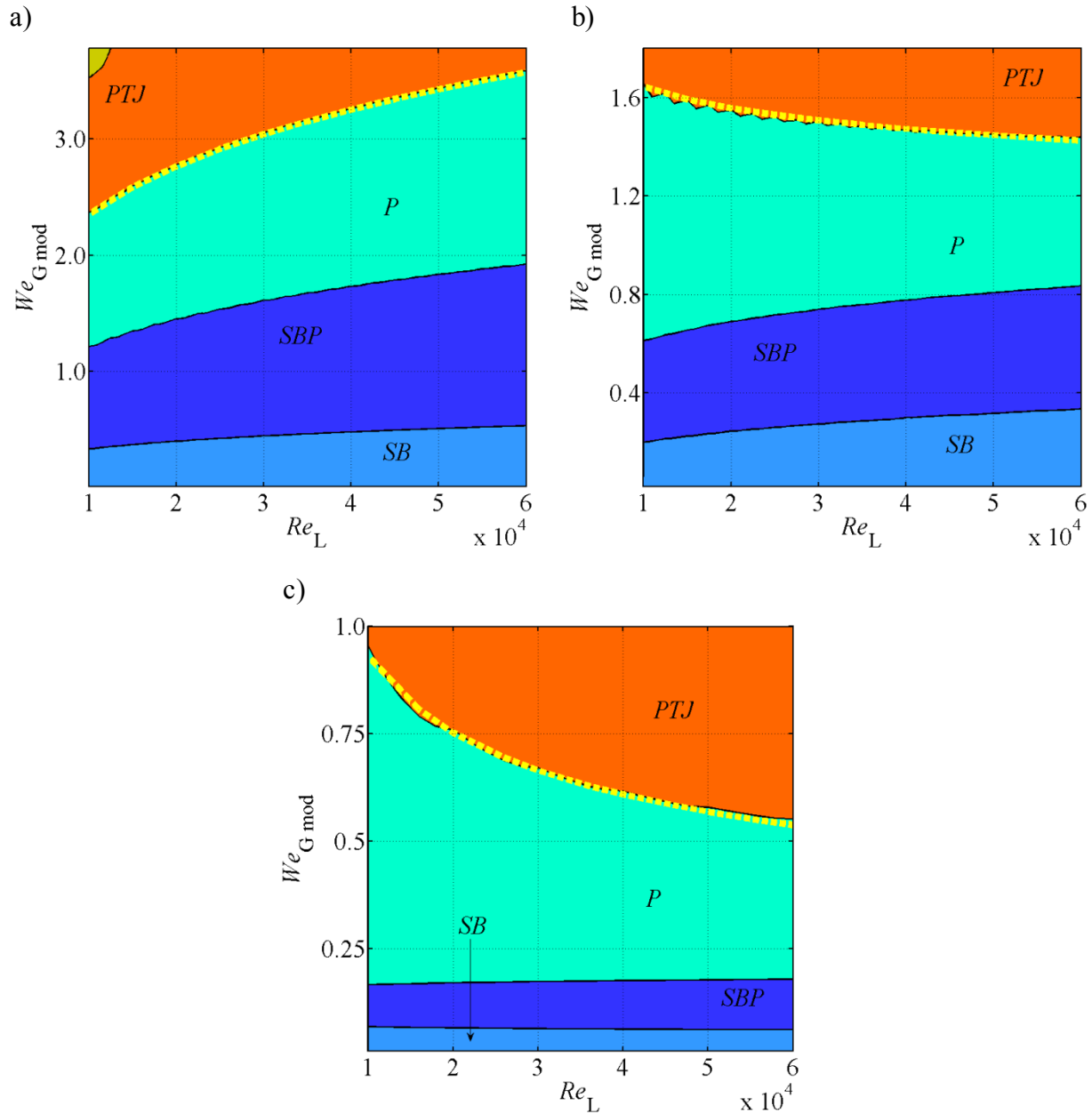
Figure D.3. Bubble formation map based on dimensionless numbers (We_G-Re_L) for: a) D_{inj} = 0.27 mm. b) D_{inj} = 0.52 mm. c) D_{inj} = 1.59mm.

Appendix E. Additional Void Fraction Discussion

A thorough description of the void fraction analysis was given in Section 2.3.3. However, the void fraction can also be defined as a function of the phase superficial velocities, as given by equation (E.1), where U_{SG} and U_{SL} are the superficial velocity of the gas and liquid phases, ρ_G and ρ_L are the gas and liquid densities, S is the slip ratio, q is the flow quality (GLR) and U_G and U_L are the gas and liquid phase velocities.

$$\alpha_{area} = \frac{U_{SG}}{U_{SG} + U_L} = \frac{\rho_L q}{S\rho_G(1-q) + \rho_L q} \tag{E.1}$$

$$U_{SG} = \frac{M_G}{\rho_G A} \qquad U_L = \frac{M_L}{\rho_L A} \tag{E.2}$$

$$S = \frac{U_G}{U_L} = \frac{U_G(1-\alpha_{area})}{U_L \alpha_{area}} = \frac{\rho_L q(1-\alpha_{area})}{\rho_G(1-q)\alpha_{area}} \tag{E.3}$$

$$U_{GU} = \frac{Q_G}{A}\alpha_{area} \qquad U_{GU} = \frac{Q_L}{A}(1-\alpha_{area}) \tag{E.4}$$

Usually, the slip ratio is higher than unity for most flows except when the flows are gravity driven, where $S < 1$. As observed, to estimate the aforementioned variables it is necessary to use a closure model which considers the differences between the phase velocities. These models vary from simple one-dimensional methods, to empirically determined correlations and elaborated phenomenological models.

One example of such methods is the drift flux model, where the void fraction is determined based on a Lagrangian physical interpretation of the gas-liquid interaction inside the conduit

(Wallis, 1969). The drift flux describes the gas volumetric rate of gas passing through a unit plane perpendicular to the channel axis which is itself moving with the flow at a velocity U_{GU}. A general expression used in the estimation of the drift flux void fraction is shown in equation (E.5), where C_o is an empirically determined coefficient; U_{GU} is the weighed mean drift velocity, ρ_M is the mixture density and U_M is the mixture velocity. The variables U_{GU} and C_o are estimated from expressions (E.6) and (E.7).

$$\alpha_{area} = \frac{q}{\rho_G}\left[C_o\left(\frac{q}{\rho_G}+\frac{1-q}{\rho_L}\right)+\frac{U_{GU}}{\rho_M U_M}\right]^{-1} \tag{E.5}$$

$$C_o = 1+c(1-q); \quad c=0.12 \tag{E.6}$$

$$U_{GU} = 1.18(1-q)\left[\frac{g\sigma(\rho_L-\rho_G)}{\rho_L^2}\right]^{1/4} \tag{E.7}$$

Although the abovementioned methodology or similar ones have been thoroughly used in pipe flow scenario with acceptable results, its adaptability to effervescent atomizers is not guaranteed. For example, a simple assessment of the equations indicates that when the void fraction is estimated by this method, it does not take into consideration the conditions under which the two-phase is produced. As has been proven before in this study and will be seen next, even under the same operating conditions, the influence of the gas formation conditions has a fundamental role on the gas-liquid dynamics.

Figure E.1 shows a hypothetical picture, likely to occur in two-phase flow scenarios, that describes how information about the void fraction can be misleading in the categorization of the

flow inside a conduit. The figure describes two different gas-liquid flow scenarios with an instantaneous $\alpha_{local} \approx 0.24$. The left diagram depicts a dispersed bubbles flow while the right schematic represents an elongated bubble flow. Even though the void fraction value for both cases is the same, it is clear that the coupling between the phases and the bubbly flow behaviour will be different, which reinforces the importance of understanding the conditions under which the bubbly flow is produced.
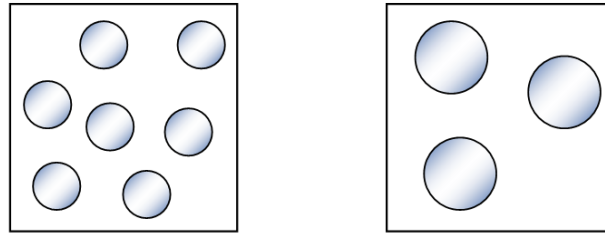
Figure E.1.   Depiction of two bubbly flow configurations under the same instantaneous void fraction value $\alpha_{local} \approx 0.24$

An example based on the two experimental scenarios is used to provide further clarification about the previous discussion. It depicts the α_{area} and statistical bubble diameter values obtained from two different D_{inj} values, 0.52 and 1.59 mm, under the same operating conditions. The results are depicted in Table E.1 and Figure E.2, where still images of the scenarios compared are included, along with a visual representation of the time-averaged void fraction. A contrast between the population based, bubble diameter CDF was included, to represent the differences in the bubbly flow statistical values caused by D_{inj}.

Under similar operating conditions, any α_{area} values estimated from the empirical correlations yield results which do not fully correspond to the developing flow inside an atomizer. The α_{area}

estimated from equation (E.5) gives an approximate value of 0.026, which does not adhere to any of the estimations obtained from experimental data.

Table E.1. Comparison between bubbly flow characteristics for different D_{inj} under the same operating conditions

D_{inj} (mm)	M_G ($\times 10^{-3}$ g/s)	U_L (m/s)	ρ_G (kg/m^3)	$GLR \times 10^{-4}$	U_{SG} (m/s)	α_{area}
0.52	49.2	3.1	4.4	1.00	0.07	0.07
1.59	49.3	3.0	4.5	1.02	0.07	0.02
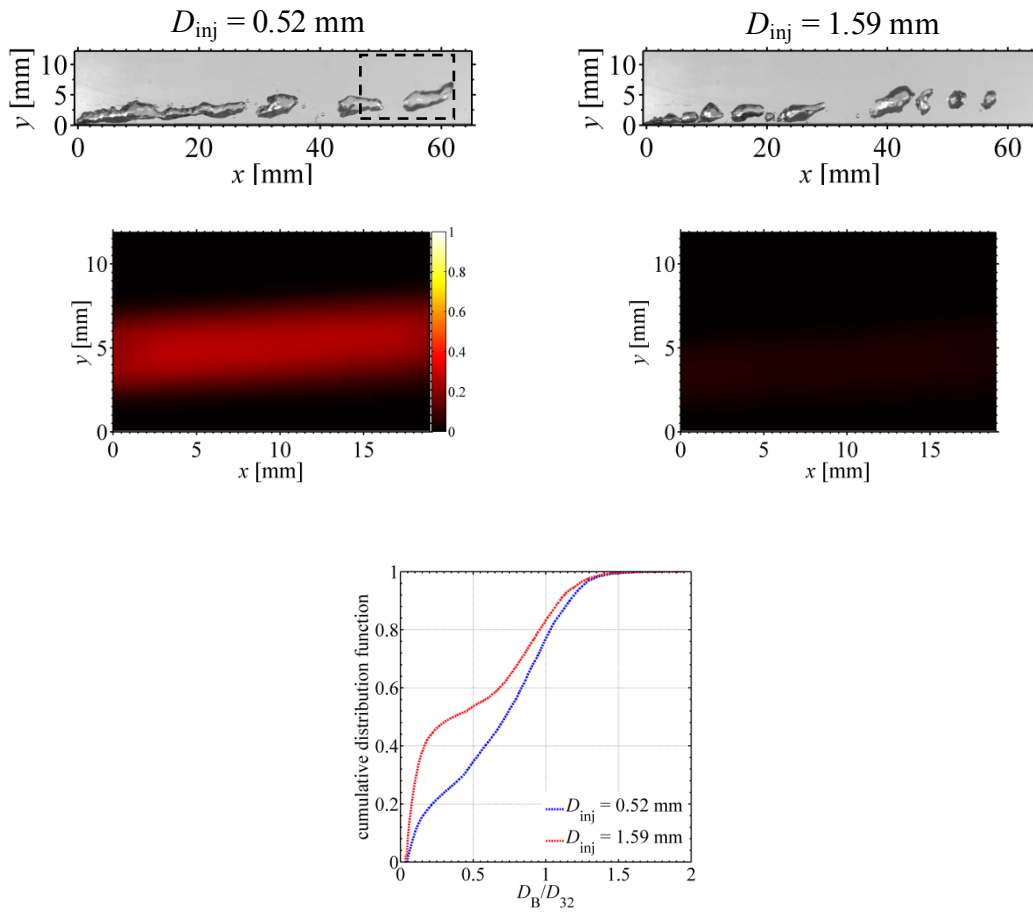
Figure E.2. Effects of the D_{inj} on the experimental α_{area} and the population based cumulative distribution for $U_L = 3.1$ m/s and $M_G = 49.2 \times 10^{-3}$ g/s

It is important to remark that despite equal values of M_G, U_L and ρ_G, the area based void fraction between the two cases are different. Hence, the influence of D_{inj} in the gas-liquid interaction

extends beyond the gas injection region and plays a fundamental role in the bubble geometry and gas phase distribution within the liquid. It was inferred that the differences in the void fraction values were caused by slightly larger bubbles being detached from the gas jet, as can be seen in the photographs included in Figure E.2, which depict the case studies being compared. The population distribution included presents clear proof of the previous statement. As can be seen, when using D_{inj} = 1.59 mm a higher percentage of small bubbles (D_B/D_{32} < 0.5) occurs when compared with the distribution obtained from D_{inj} = 0.52 mm. As explained, the larger bubbles would have a higher residence time within the interrogation window, causing higher α_{area} values.

Further clarification about the effects of the selected operating and geometric variables on the void fraction will be provided in the following sections, with emphasis on the individual contribution of each parameters and how they affected the phase distribution within the conduit.

E.1. Effect of the injector location

The density difference between the gas and liquid phases has a central role in the two-phase flow dynamics. Owing to the horizontal orientation of the conduit, it is expected that the position of the gas injector influences the dispersed phase distribution in the liquid, particularly in the vicinity of the gas nozzle and immediately after bubble detachment. A comparison between the effects of the injector location on the α_{local} distribution along the span-wise direction is shown in Figure E.3. The void-fraction was measured at a distance x/D_H = 4 downstream the gas nozzle. As was expected, under comparable operating and geometric conditions, top wall gas injection

causes higher α_{local} values than those observed for bottom wall injection, which validates the above mentioned statement.
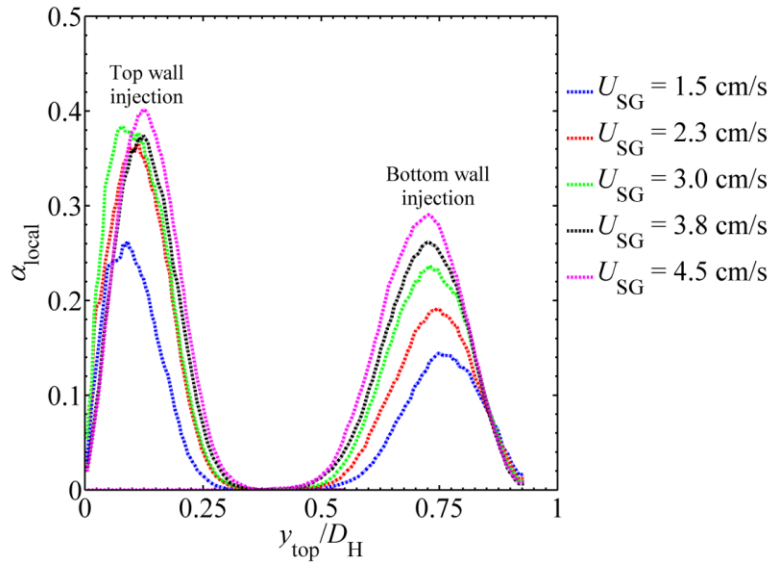
Figure E.3.   Effect of the injector location on the local void fraction for U_L = 4.3 m/s and D_{inj} = 1.59 mm

Independent of the U_{SG} magnitude, top wall gas injection causes α_{local} to exhibit narrower trends with higher peaks than those obtained from bottom wall injection, where the tendency is to have a wider distribution of the gas phase along the conduit. Under top wall injection, when $U_{\text{SG}} \geq 1.5$ cm/s the curves had a very similar behavior with the α_{local} maximum ranging between 0.35 and 0.4. For the opposite nozzle location scenario, a continuous increase in U_{SG} values translated into an increment of the maximum α_{local} peak. As depicted in Figure E.3, incrementing U_{SG} from 1.5 cm/s to 2.3 cm/s cause an increase in max α_{local} equal to 25%. Successive increments in U_{SG} caused less marked variations in the peak values, with increases of 18%, 10% and 9% for U_{SG} = 3.0, 3.8 and 4.5 cm/s respectively.

It was observed that at the horizontal location chosen, the α_{local} profiles are not symmetric with respect to their peak value. For top wall injection, the curves have an averaged width equal to $0.34D_H$ while the peaks were primarily located at $y/D_H \approx 0.13$. On the other hand, for bottom wall injection the curves had an averaged width that started at $0.52\ y_{\text{top}}/D_H$ and ended at 0.94 y_{top}/D_H with a peak located approximately at $0.75\ y_{\text{top}}/D_H$.

In a horizontal conduit the buoyancy forces cause an uneven dispersed phase distribution, displacing the gas towards the upper region of the conduit. The results obtained for top wall injection depict this clearly, causing the contracted α_{local} curves. The effects of the liquid cross-flow counteract the buoyancy forces, causing the displacement of the α_{local} maxima towards the conduit center. It is expected that at lower U_L values, the α_{local} peaks locate closer to the top wall. For bottom wall injection the residence time of the gas phase has not been enough for the buoyancy forces to overcome the turbulence dispersive liquid forces, causing the gas phase to remain on the lower part of the conduit.

For lower U_L values than the one reported in Figure E.3, it is expected a faster transitioning of the gas phase towards the upper channel area. Similarly, it is expected that as the two-phase flow transitions towards the discharge nozzle, the density difference will cause an upward gas migration, causing a possible independence of the gas-liquid on the injection conditions.

E.2. Effect of U_L

The influence of D_{inj} and U_L on α_{local} at a distance $x = 2$ cm upstream of the nozzle was reported in Figure E.4. For all the conditions tested, the results indicated an asymmetric distribution of α_{local} along the vertical direction. These findings are similar to the observations of Sato *et al.* (1981) and Andreussi *et al.* (1999), where independent of the D_{inj}, U_L or U_{SG} used; the α_{local} curves exhibited a clear peak near the top channel wall. As was expected, the magnitude of α_{local} within the channel decreased as U_L was increased.
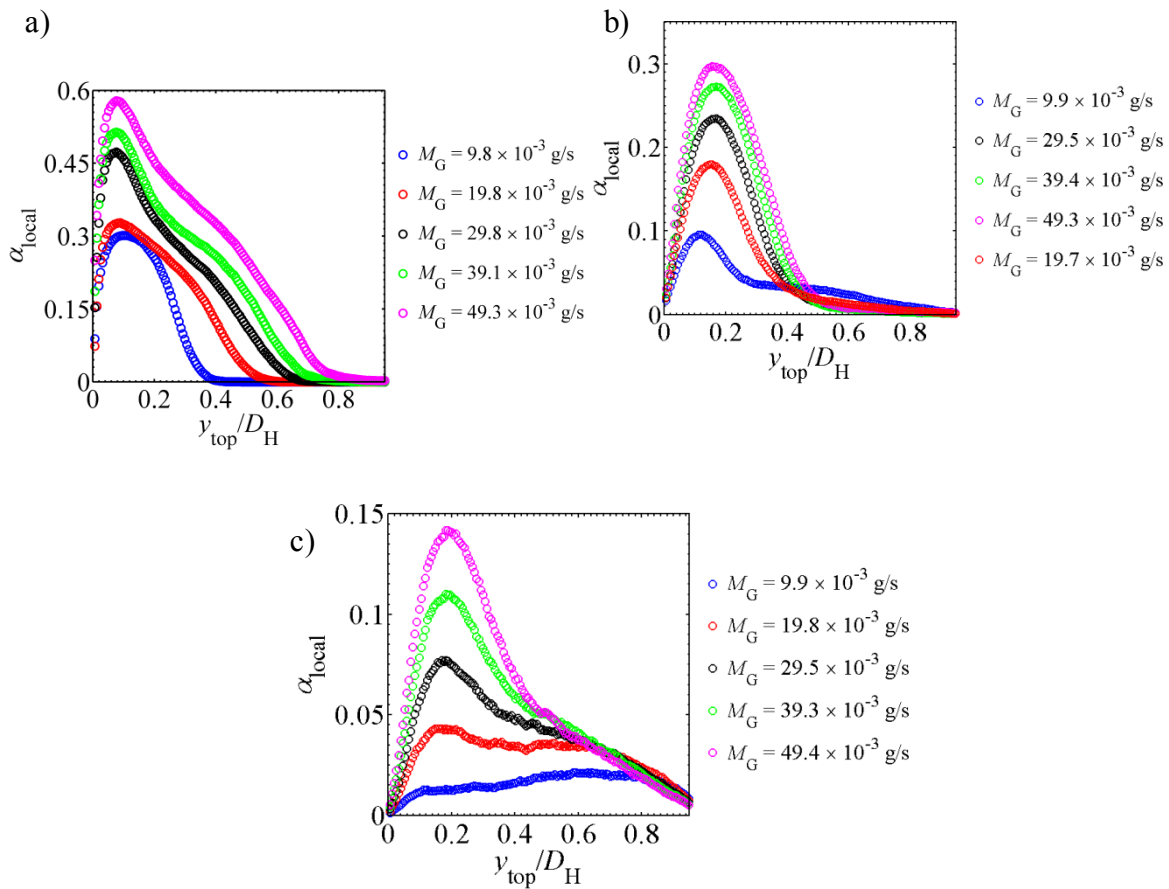
Figure E.4. Effect of U_L on α_{local} at a distance $x = 2$ cm upstream of the discharge nozzle entrance for $D_{inj} = 0.52$ mm. a) $U_L = 1.9$ m/s, b) $U_L = 3.1$ m/s, c) $U_L = 4.3$ m/s

For the vast majority of the scenarios, the α_{local} maximum was encompassed between $0.05y_{\text{top}}/D_{\text{H}}$ and $0.22y_{\text{top}}/D_{\text{H}}$. The only exception to this behaviour occurred for $M_{\text{G}} = 9.9 \times 10^{-3}$ g/s and $U_{\text{L}} = 4.3$ m/s, where the maximum value was located at $y_{\text{top}}/D_{\text{H}} = 0.8$. For this particular experimental configuration, due to the M_{G} value, the bubbles produced are of small size, which decreases the magnitude of the buoyancy forces. When combined with a high liquid cross-flow velocity, the dispersive forces cause an even distribution of the gas phase throughout the conduit.

As was shown in Figure E.4a, at $U_{\text{L}} = 1.9$ m/s the void fraction curves had similar shapes. For all M_{G} values tested, the curves start from a non-zero value at the wall interface and quickly achieve a maximum α_{local} at a distance $y_{\text{top}}/D_{\text{H}} \leq 0.10$. After this point, which ranged between $0.4y_{\text{top}}/D_{\text{H}}$ and $0.8y_{\text{top}}/D_{\text{H}}$ depending on M_{G}, the curves had a gradual decrease until α_{local} reached a zero value. As the liquid cross-flow velocity increased from $U_{\text{L}} = 1.9$ m/s to 3.3 m/s, the curve behavior changed. Besides the expected decrease in the maximum void fraction values, other important changes were observed. Stronger dispersive forces, caused by a higher liquid cross-flow velocity, induced the peak displacement towards the channel center, being located at $y_{\text{top}}/D_{\text{H}} \approx 0.20$, save for the lowest M_{G} value. Also, a more steep decrease in the α_{local} trend line was observed. All the curves started from an almost null value at the solid interface and reached the zero gas probability case after $y_{\text{top}}/D_{\text{H}} \geq 0.60$.

Lastly, for $U_{\text{L}} = 4.3$ m/s, the max α_{local} value was achieved at a similar distance to that observed for the previous U_{L}, $y_{\text{top}}/D_{\text{H}} \approx 0.20$. However, other differences were found. The scattering of the gas phase along the conduit was more uniform, as shown in Figure E.4c. For equal M_{G} values, the magnitude of the curve height decreased to approximately half of the value observed for the

previous U_L value. Once this point was reached, the slope decreased slowly until reaching $\alpha_\text{local} \approx 0.02$. Lastly, it was observed how for $M_\text{G} \leq 30 \times 10^{-3}$ g/s, the high U_L caused the flattening of the void fraction profiles, being the physical implication of this a more uniform dispersion of the gas phase along the spanwise direction.

Appendix F. Considerations about flow development in square conduits

There were experimental reasons behind the choice of a square conduit. Primarily, a conduit with flat side walls was used to eliminate optical distortion. Since the motivation of the study required the gas injector to be located at the walls, an appropriate assessment of the conditions near this area would be severely affected by the pipe curvature. To avoid the effects of aspect ratio/channel dimensions, a square conduit was used.

However, besides the obvious differences in the shape created in the imaging process, there are distinctions in the flow field, such as the presence of secondary flows and entrance length development. To estimate the effects of flow development in a square conduit, several correlations were considered. For the case of laminar flows, several correlations exist. These equations can be found in Table 28.7, from the Handbook of Fluid Dynamics (page 28-73). However, for the case of developing turbulent flow in conduits, no definitive agreement about the correct approach was found in the literature. Schetz and Fuhs (1999) considered two possibilities:

a) The entrance length is defined as the distance where the wall shear stress and therefore, the pressure gradient reaches a fully developed value. This results in an entrance length approximately equal to 15 hydraulic diameters (D_H).

b) The entrance length is defined as the length required for the fully developed profiles of the mean and turbulence variables to be independent of the inlet condition. Under this consideration, the entrance length can exceed 140 D_H.

As observed, the differences between the two cases yield markedly different criteria about the entrance length in a square conduit. Solid theoretical grounds exist to support the validity of either criterion. Following the shear stress criterion, the entrance length is approximately equal to 19.1 cm, which indicates a developed liquid upstream of the gas inlet. However, the second criterion indicates that a minimum distance of 220 cm is required, which clearly exceeds the total length of the experimental conduit.

Establishing analogies with pipe flow theory was also considered. According to White (2005), the development length in a turbulent pipe flow can be estimated using the expression $L_{dev} = 4.4 D_H Re_L^{1/6}$. Substituting the experimental conditions used in this experiment, the development length is between 30.0 to 34.6 cm, which is well under the 36 cm location for the gas inlet. Therefore, two criteria indicate that the liquid flow is fully developed before interacting with the gas jet.

Melling and Whitelaw (1976) observed that the main differences between developing pipe flow and developing rectangular flow is the presence of secondary flows at the conduit edges. Also, as occurs with circular conduits, the effect of inlet conditions has a significant impact on the flow behaviour at considerable distances downstream the conduit entrance.

About the existence of secondary flows, some authors (Melling and Whitelaw, 1976; Gavrilakis, 1992) have observed that in a turbulent square conduit flow, the maximum values of the secondary velocity are approximately equal to 2% of the bulk velocity, which occur at the corner walls. The secondary flows affect the wall shear stress distribution. However, it was considered that the primary contribution of the liquid cross-flow to the gas phase distribution was caused by the mean bulk velocity rather than the secondary flows.

Despite the obvious scientific interest about secondary flows in square conduits, the purpose of this paper was on the estimation of a different phenomenon. Based on the relatively small value of the secondary flows, it was estimated that their contribution to the gas-liquid interaction could be disregarded when compared to the primary flows.

Appendix G. Matlab algorithms and methodology used to process the images

G.1. Jet Analysis Algorithm

```matlab
%% IMAGE ANALYSIS ALGORITHM V 1.4
% Analysis of the jet region - Contour plots of the probability of finding
% a bubble in the vicinity of the jet area

%% Step 0: Clean the space/screen
clear all
close all
set(0,'DefaultFigureWindowStyle','docked')
format short
clc


filenames_video = dir('*.avi');

name_video = {filenames_video.name};

for ij = 1:length(name_video)
%% Step 1: Obtain the images from original video and create new video

% Construct multimedia object from original video
original_video          = VideoReader(name_video{ij});
original_number_frames  = original_video.NumberOfFrames;
original_size_vector    = [original_video.Width original_video.Height];
original_height         = original_size_vector(1);
original_width          = original_size_vector(2);
original_format         = original_video.VideoFormat;

% Frames per second used
fps = 3000;

% Set the number of frames to be read
number_frames = 25;

counter = floor(original_number_frames/number_frames);


image_cell = cell(counter, 1);

jet_data  = cell(counter,1);
jet_raw   = cell(counter,11);

area_property_estimation = 1;

jet_info = struct('axis',[], 'diameter', [],'centricity', [], 'centroidx', [],  'centroidy',
[],...
                'centertot', [], 'velocity', [], 'angle', [], 'number', [], 'width',[],
'perimeter', []);


for k = 1:counter

frames_read = read(original_video, [(k-1)*number_frames+1 k*number_frames]);
```

```matlab
% Preallocate new video in MATLAB format
new_video(1 : number_frames) = struct('cdata', zeros(original_height, original_width, 3, ...
'uint8'),...
                                      'colormap', []);

    % Create a matlab movie by reading one frame at a time
    for n = 1 : number_frames
        new_video(n).cdata    = frames_read(:,:,:,n);
        new_video(n).colormap = [];
    end

% Define the crop vector

crop_vector = [330 1 900 163];
size_vector = [crop_vector(3) crop_vector(4)];

%% Step 2: Image processing

% Initialize image
image_base = zeros([crop_vector(4)+1, crop_vector(3)+1]);
image_1    = double(image_base);

for m = 1:number_frames

                % Grab frame
                image_1O  = new_video(m).cdata;
                image_1C  = imcrop(image_1O, crop_vector);

                % Convert from RGB24 to gray
%                 image_1G    = rgb2gray(image_1C);

                % Invert image
                image_1I  = max(max(image_1C)) - image_1C;

                 % Adjust the image contrast
                image_1A    = imadjust(image_1I, [0.26; 0.9], [0; 1], 0.05);

                % Threshold the image
                level = 0.05;
%                 level        = graythresh(image_1A);

                % Convert to BW
                image_1B    = im2bw(image_1A, level);

                % Add a false line above/below the image to create closed objects
%                 image_1T = [zeros(1,length(image_1B)); image_1B];
                image_1T = [image_1B; zeros(1,length(image_1B))];

                % Create a filter - Strel
                SE = strel('square',6);

                % Dilate the image
                image_dilat = imdilate(image_1T,SE);

                % Fill the image
                image_1F     = imfill(image_dilat,'holes');

                % Erode the image
                image_1FF = imerode(image_1F,SE);

                % Eliminate objects whose area is smaller than 6 pixels
                image_2   = bwareaopen(image_1FF, 6);

%                 [B,L] = bwboundaries(image_2,'noholes');
%                 imshow(image_2);hold on;
%                 for klm = 1:length(B)
%                         boundary = B{klm};
%                         plot(boundary(:,2), boundary(:,1), 'r', 'LineWidth', 1)
%                 end
%
```

```matlab
                % Return image to its original size
                [ms,ns] = size(image_2);
                image_1P = image_2(2:ms,1:ns);

                % Determine if the image is going to be processed
                if max(max(image_1P)) == 0
                    area_property_estimation = 0;
                else
                    area_property_estimation = 1;
                end

                % Process the image
                % Find jet properties
                        if area_property_estimation ~= 0

                            % jet_values = regionprops(image_1P, 'EquivDiameter',
'Eccentricity','MajorAxisLength');
                            jet_values    = regionprops(rot90(rot90(image_1P)),
'EquivDiameter',
'Eccentricity','MajorAxisLength','Centroid','Orientation','MinorAxisLength','Perimeter');

                            % Jet Diameter
                            jet_diam      = jet_values(1).EquivDiameter;

                            % Jet Centricity
                            jet_cent      = jet_values(1).Eccentricity;

                            % Jet Axis
                            jet_axis      = jet_values(1).MajorAxisLength;

                            % Jet Width
                            jet_width     = jet_values(1).MinorAxisLength;

                            % Jet Centroid
                            jet_centroid  = jet_values(1).Centroid;

                            % Jet Orientation
                            jet_angle     = jet_values(1).Orientation;

                            % Jet Perimeter
                            jet_perimeter = jet_values(1).Perimeter;

                            % # of objects
                            number_objects = bwconncomp(image_1P);

                            % Store the info on the structure
                            jet_info(m).axis       = jet_axis;
                            jet_info(m).diameter   = jet_diam;
                            jet_info(m).centricity = jet_cent;
                            jet_info(m).centroidx  = jet_centroid(1);
                            jet_info(m).centroidy  = jet_centroid(2);
                            jet_info(m).centertot  = sqrt((jet_info(m).centroidx)^2 +
(jet_info(m).centroidy)^2);
                            jet_info(m).angle      = jet_angle;
                            jet_info(m).number     = number_objects.NumObjects;
                            jet_info(m).width      = jet_width;
                            jet_info(m).perimeter  = jet_perimeter;

                            if m >= 2 && (jet_info(m).centertot > jet_info(m-1).centertot)
                                jet_info(m).velocity = (jet_info(m).centertot - jet_info(m-
1).centertot);
                            end

                        end

                image_1 = (image_1) + im2double(image_1P);
```

303

```matlab
end

                                jet_axis     = [jet_info.axis];
                                jet_cent     = [jet_info.centricity];
                                jet_diam     = [jet_info.diameter];
                                jet_centroidx = [jet_info.centroidx];
                                jet_centroidy = [jet_info.centroidy];
                                jet_centertot = [jet_info.centertot];
                                jet_velocity  = [jet_info.velocity];
                                jet_angle     = [jet_info.angle];
                                jet_number    = [jet_info.number];
                                jet_width     = [jet_info.width];
                                jet_perimeter = [jet_info.perimeter];

                                avg_jet_diam       = mean(jet_diam);
                                avg_jet_axis       = mean(jet_axis);
                                avg_jet_centricity = mean(jet_cent);
                                avg_jet_centroidx  = mean(jet_centroidx);
                                avg_jet_centroidy  = mean(jet_centroidy);
                                avg_jet_centertot  = mean(jet_centertot);
                                avg_jet_velocity   = mean(jet_velocity);
                                avg_jet_angle      = mean(jet_angle);
                                avg_jet_number     = mean(jet_number);
                                avg_jet_width      = mean(jet_width);
                                avg_jet_perimeter  = mean(jet_perimeter);


                    jet_data(k,1)   = {[avg_jet_diam avg_jet_axis avg_jet_centricity
avg_jet_centertot avg_jet_velocity avg_jet_angle avg_jet_width avg_jet_perimeter]};
                    jet_raw(k,1)    = {jet_axis};
                    jet_raw(k,2)    = {jet_cent};
                    jet_raw(k,3)    = {jet_diam};
                    jet_raw(k,4)    = {jet_centroidx};
                    jet_raw(k,5)    = {jet_centroidy};
                    jet_raw(k,6)    = {jet_centertot};
                    jet_raw(k,7)    = {jet_velocity};
                    jet_raw(k,8)    = {jet_angle};
                    jet_raw(k,9)    = {jet_number};
                    jet_raw(k,10)   = {jet_width};
                    jet_raw(k,11)   = {jet_perimeter};

                    avg_image = image_1 * (1/number_frames);

                    image_cell(k,1) = {avg_image};


clear frames_read new_video

end

%% Step 3: Mean values

% Mean value of the images in the array
image_zero  = zeros([crop_vector(4)+1, crop_vector(3)+1]);
image_start = double(image_zero);

% Convert the cell into a matrix
total_jet_data = cell2mat(jet_data);

% Bubble diameter
tot_avgjet_diam  = mean(total_jet_data(:,1));
tot_avgjet_axis  = mean(total_jet_data(:,2));
tot_avgjet_cent  = mean(total_jet_data(:,3));
tot_avgjet_velo  = mean(total_jet_data(:,5));
tot_avgjet_width = mean(total_jet_data(:,7));

for k = 1:counter

    image_start = image_start + cell2mat(image_cell(k,1));
```

```matlab
end

    final_image = image_start * (1/counter);


%% Step 4: Display the results


%% Step 5: Obtain a pure binary image from the final result

binary_image = final_image;
threshold = 0.05;
indices_matrix = find(final_image < threshold);
for i = 1:length(indices_matrix)
    kk = indices_matrix(i);
    binary_image(kk) = 0;
end

[ver_length, hor_length] = size(final_image);
total_elements = hor_length*ver_length;

for i = 1:total_elements

    if binary_image(i) <= threshold
        binary_image(i) = 0;
    else
        binary_image(i) = 1;
    end

end


% Jet axis length analysis

k = length(jet_raw);
index_i = 1;

jet_axis_matrix = [];

while index_i <= k
    jet_axis_matrix = [jet_axis_matrix cell2mat(jet_raw(index_i,1))];
    index_i        = index_i + 1;
end

delta_time = 1/fps;
time_vector = 0:delta_time:(k*m-1)*delta_time;

data = sort(jet_axis_matrix);
mod_data = linspace(min(data),max(data),20);

% Geometric mean
Mean_JG  = exp(sum(log(jet_axis_matrix))/length(jet_axis_matrix));

% Arithmetic mean
Mean_JA  = mean(jet_axis_matrix);

% Statistical parameters of the distribution
A = mean(jet_axis_matrix);
B = std(jet_axis_matrix);
E = cov(jet_axis_matrix);

pdf_values = zeros(2,length(mod_data)-1);

for ii = 2:length(mod_data)

        numbers      = find(data >= mod_data(ii-1) & data < mod_data(ii));

        jet_axis_val = zeros(1,length(numbers));

        for jj = 1:length(numbers)
```

```matlab
        jet_axis_val(jj) = data(numbers(jj));

    end


    avg_numbers = mean(jet_axis_val);
    pdf_values(1,ii) = avg_numbers;                                 % First row  = Average
diameter of the particles within the interval
    pdf_values(2,ii) = length(numbers);                             % Second row = Number of
particles contained in the interval

end


    % "Standard" pdf values
    X          = pdf_values(1,:);
    pdf_values = pdf_values(2,:);

    % Normalized pdf
    norm_pdf_values = pdf_values./sum(pdf_values);

    % Normalized cdf
    cdf_values = zeros(1,length(norm_pdf_values));
    cdf_values(1) = norm_pdf_values(1);

%       cdf_values(2:length(cdf_values)) = norm_pdf_values(2:length(cdf_values)) +
cdf_values((2:length(cdf_values))-1);

    for kk = 2:length(cdf_values)
        cdf_values(kk) = norm_pdf_values(kk) + cdf_values(kk-1);
    end


    % Normal probability density function
    N = pdf('Normal',data,A,B);

    % Normal Cumulative distribution function
    C = cdf('Normal',data,A,B,E);

    % Log-normal PDF
    V     = var(jet_axis_matrix);
    mu    = log((A^2)/sqrt(V+A^2));
    sigma = sqrt(log(V/(A^2)+1));
    L     = pdf('lognormal',data,log(A),sqrt(E));


    X0 = linspace(0,max(data),length(N));



savefile = char(['jet_contour_' name_video{ij} '.mat']);

save(savefile)

clearvars -except name_video
close all
end
```

G.2. Sample algorithm to automate the process of data collection and analysis

```matlab
clear
clc

filenames_data = dir('bubble_contour*.mat');

name_data = {filenames_data.name};

NNN = length(name_data)/3;

for k = 1:length(name_data)

    A_name = name_data{k};

    B_name = textscan(A_name, '%15c %d %c %d %8c');

    load(A_name);

    var_a = char(['tot_avgbub_dia_3_4_' num2str(B_name{2}) '_' num2str(B_name{4})]);

    var_b = char(['tot_avgbub_num_3_4_' num2str(B_name{2}) '_' num2str(B_name{4})]);

    var_c = char(['tot_avgbub_vfr_3_4_' num2str(B_name{2}) '_' num2str(B_name{4})]);

    var_d = char(['tot_avgbub_vfrr_3_4_' num2str(B_name{2}) '_' num2str(B_name{4})]);

    var_e = char(['final_image_3_4_' num2str(B_name{2}) '_' num2str(B_name{4})]);

    var_f = char(['statistical_diameters_3_4_' num2str(B_name{2}) '_' num2str(B_name{4})]);

    var_g = char(['size_vector_3_4_' num2str(B_name{2}) '_' num2str(B_name{4})]);

    var_h = char(['X_pdf_3_4_' num2str(B_name{2}) '_' num2str(B_name{4})]);

    var_i = char(['pdf_3_4_' num2str(B_name{2}) '_' num2str(B_name{4})]);

    var_j = char(['npdf_3_4_' num2str(B_name{2}) '_' num2str(B_name{4})]);

    var_k = char(['cdf_3_4_' num2str(B_name{2}) '_' num2str(B_name{4})]);


    eval([var_a '=tot_avgbub_dia']);

    eval([var_b '=tot_avgbub_num']);

    eval([var_c '=tot_avgbub_vfr']);

    eval([var_d '=tot_avgbub_vfrr']);

    eval([var_e '=final_image']);

    eval([var_f '=[Mean_D20 Mean_D30 Mean_D32 tot_avgbub_dia Mean_DG A]']);

    eval([var_g '=size_vector']);

    eval([var_h '=X']);

    eval([var_i '=pdf_values']);

    eval([var_j '=norm_pdf_values']);

    eval([var_k '=cdf_values']);


    clc
```

```matlab
    clearvars -except tot_avgbub_dia_3* tot_avgbub_num_3* tot_avgbub_vfr_3* tot_avgbub_vfrr_3*
final_image_3* statistical_diameters_3*...
               X_pdf_3* pdf_3* npdf_3* cdf_3* name_data NNN

end

clearvars name_data


bubble_matrix_data_3_4 = zeros(NNN,9);

bubble_num_3_4          = zeros(1,NNN);
bubble_diam_3_4         = zeros(1,NNN);
bubble_vfr_3_4          = zeros(1,NNN);

statistical_matrix_3_4 = zeros(NNN,18);

statistical_vector_3_4 = zeros(1,6);


for i = 1:NNN

    for j = 1:3


        bubble_matrix_data_3_4(i,j)   = eval(char(['tot_avgbub_dia_3_4_' num2str(i) '_'
num2str(j)]));
        bubble_matrix_data_3_4(i,j+3) = eval(char(['tot_avgbub_num_3_4_' num2str(i) '_'
num2str(j)]));
        bubble_matrix_data_3_4(i,j+6) = eval(char(['tot_avgbub_vfr_3_4_' num2str(i) '_'
num2str(j)]));

        A_stat = eval(char(['statistical_diameters_3_4_' num2str(i) '_' num2str(j)]));

        statistical_matrix_3_4(i,j)    = A_stat(1);
        statistical_matrix_3_4(i,j+3)  = A_stat(2);
        statistical_matrix_3_4(i,j+6)  = A_stat(3);
        statistical_matrix_3_4(i,j+9)  = A_stat(4);
        statistical_matrix_3_4(i,j+12) = A_stat(5);
        statistical_matrix_3_4(i,j+15) = A_stat(6);


    end

        bubble_num_3_4(i)  = mean(bubble_matrix_data_3_4(i,4:6));
        bubble_diam_3_4(i) = mean(bubble_matrix_data_3_4(i,1:3));
        bubble_vfr_3_4(i)  = mean(bubble_matrix_data_3_4(i,7:9));

        statistical_vector_3_4(i,1) = mean(statistical_matrix_3_4(i,1:3));
        statistical_vector_3_4(i,2) = mean(statistical_matrix_3_4(i,4:6));
        statistical_vector_3_4(i,3) = mean(statistical_matrix_3_4(i,7:9));
        statistical_vector_3_4(i,4) = mean(statistical_matrix_3_4(i,10:12));
        statistical_vector_3_4(i,5) = mean(statistical_matrix_3_4(i,13:15));
        statistical_vector_3_4(i,6) = mean(statistical_matrix_3_4(i,16:18));
end

clearvars i j A_stat
```

G.3. Algorithm to estimate the centerline trajectory

```matlab
clear all
close all
set(0,'DefaultFigureWindowStyle','docked')
format short
clc

% Calibration factor
Cf = 0.0519;

filenames = dir('jet_contour*.mat');

name_var = {filenames.name};

traj_cell     = cell(length(name_var),9);
traj_cell_tot = cell(length(name_var)/3,2);

for ijk = 1:length(name_var)

load(name_var{ijk})

            XYZ = flipud(final_image);
%             XYZ = (final_image);
            [y_bw, x_bw] = size(XYZ);
            x_cut = find(XYZ(1,:) > 0.1,1);
            XYZ = imcrop(XYZ, [x_cut 1 x_bw-x_cut y_bw]);
            [y_bw, x_bw] = size(XYZ);

            minmax_st = struct('maxpos', zeros(1,x_bw), 'pos', zeros(1,x_bw));

            for i = 1:x_bw

                minmax_st(i).maxpos     = max(XYZ(:,i));
                    if max(XYZ(:,i)) ~= 0
                        minmax_st(i).pos        = find(XYZ(:,i) == max(XYZ(:,i)));

                            if length(minmax_st(i).pos) > 1
                                minmax_st(i).pos = min(minmax_st(i).pos);
                            end
                    else
                        minmax_st(i).pos        = 0;
                    end
            end

            position_vector = [minmax_st.pos];


            X_pos           = 1:length(position_vector);

            intensity_vector = [minmax_st.maxpos];


            traj_cell{ijk,1} = X_pos;
            traj_cell{ijk,2} = position_vector;
            traj_cell{ijk,3} = intensity_vector;
            traj_cell{ijk,4} = A*Cf/12.7;
            traj_cell{ijk,5} = [y_bw,x_bw];
            traj_cell{ijk,6} = X_pos*Cf/12.7;
            traj_cell{ijk,7} = (position_vector)*Cf/12.7;
            traj_cell{ijk,8} = XYZ;
            traj_cell{ijk,9} = tot_avgjet_axis;


            clearvars -except traj_cell name_var Cf filenames

end
```

```matlab
for xxx = 1:length(name_var)/3

    temp_cell = cell(3,2);

    length_cell = cell(3,1);

    for yyy = 1:3

        index = 3*(xxx-1) + yyy;

        temp_cell{yyy,1} = traj_cell{index,6};
        temp_cell{yyy,2} = traj_cell{index,7};

        length_cell{yyy,1} = length(temp_cell{yyy,1});

    end


    if length_cell{1} ~= length_cell{2} || length_cell{1} ~= length_cell{3}

        length_cell = cell2mat(length_cell);
        min_val    = min(length_cell);

        traj_cell_tot{xxx,1} = (temp_cell{1,1}(1:min_val) + temp_cell{2,1}(1:min_val) +
temp_cell{3,1}(1:min_val))/3;
        traj_cell_tot{xxx,2} = (temp_cell{1,2}(1:min_val) + temp_cell{2,2}(1:min_val) +
temp_cell{3,2}(1:min_val))/3;

    else

        traj_cell_tot{xxx,1} = (temp_cell{1,1} + temp_cell{2,1} + temp_cell{3,1})/3;
        traj_cell_tot{xxx,2} = (temp_cell{1,2} + temp_cell{2,2} + temp_cell{3,2})/3;

    end

end

clearvars -except traj_cell traj_cell_tot
```

G.4. Algorithms used for the estimation of the dynamics effects acting on a gas jet in a liquid cross-flow

```matlab
% Centroid position

image_index_16c = [2682 2699];

AB = cell2mat([jet_raw(:,4)']);
AB = AB(image_index_16c(1):image_index_16c(2))*0.0680*1e-3;

X_16c = sort(AB);

AB = cell2mat([jet_raw(:,5)']);
AB = AB(image_index_16c(1):image_index_16c(2))*0.0680*1e-3;

Y_16c = sort(AB);

AB = cell2mat([jet_raw(:,6)']);
AB = AB(image_index_16c(1):image_index_16c(2))*0.0680*1e-3;

XY_16c = sort(AB);

% Jet width

AB = cell2mat([jet_raw(:,10)']);
AB = AB(image_index_16c(1):image_index_16c(2))*0.0680*1e-3;

Dw_16c = sort(AB);

% Jet perimeter

AB = cell2mat([jet_raw(:,11)']);
AB = AB(image_index_16c(1):image_index_16c(2))*0.0680*1e-3;

P_16c = sort(AB);

% Jet Diameter

AB = cell2mat([jet_raw(:,3)']);
AB = AB(image_index_16c(1):image_index_16c(2))*0.0680*1e-3;

Db_16c = sort(AB);

Ab_16c = 0.7854*(Db_16c.^2);

% Estimated surface
Ap_16c = P_16c.*Dw_16c;

% Circularity
sphe_16c = ((3.1416)*(Db_16c))./P_16c;

% Gas core diameter from the surface
Dg_16c = sqrt(2*Ap_16c/3.1416);

% Time vector
time_16c = (0:(1/3000):(length(AB)-1)*(1/3000));

% Properties
rhoL_16c = 994;
rhoG_16c = 3.16;
MG_16c  = 0.000009851;
Dinj_16c = 1.588e-3;
UG_16c = MG_16c/(rhoG_16c*0.7854*Dinj_16c*Dinj_16c);
sigma = 0.072;
```

```
R = 0.287;
T_16c = 24.9+273.15;
PL_16c = 261.7*1e3;
UL_16c = 2.01;
miuL = (9.772e-4);
epsilon = 32.2;
PG_16c = 270.0*1e3;


%% Vertical

% Buoyancy
FB_y16c = (rhoL_16c - rhoG_16c)*9.81*Ab_16c(2:length(Ab_16c)).*Dw_16c(2:length(Dw_16c));

% Momentum
FM_y16c = rhoG_16c*0.7854*Dinj_16c*Dinj_16c*UG_16c*UG_16c;

FM_y16c = FM_y16c*ones(1,length(time_16c)-1);

% Inertial - Added mass

for i = 2:length(Ab_16c)

        dAdt_16c(i-1)    = (Ab_16c(i) - Ab_16c(i-1))./(time_16c(i) - time_16c(i-1));
        dDdt_16c(i-1)    = (Db_16c(i) - Db_16c(i-1))./(time_16c(i) - time_16c(i-1));
        dDDdtt_16c(i-1)  = ((Db_16c(i) - Db_16c(i-1))./(time_16c(i) - time_16c(i-
1)))./(time_16c(i) - time_16c(i-1));
        Ub_16c(i-1)      = (XY_16c(i) - XY_16c(i-1))./(time_16c(i) - time_16c(i-1));
        dydt_16c(i-1)    = (Y_16c(i) - Y_16c(i-1))./(time_16c(i) - time_16c(i-1));
        dxdt_16c(i-1)    = (X_16c(i) - X_16c(i-1))./(time_16c(i) - time_16c(i-1));
        dyydtt_16c(i-1)  = ((Y_16c(i) - Y_16c(i-1))./(time_16c(i) - time_16c(i-
1)))./(time_16c(i) - time_16c(i-1));
        dxxdtt_16c(i-1)  = ((X_16c(i) - X_16c(i-1))./(time_16c(i) - time_16c(i-
1)))./(time_16c(i) - time_16c(i-1));

end

Cm_16c = (3*(dDdt_16c.^2)./(Ub_16c.^2)) + 0.5;
% Cm = Cm(5:length(Cm)-5);
% Cm = mean(Cm);

FI_y16ca = ((rhoG_16c + rhoL_16c*Cm_16c).*Dw_16c(2:length(Ab_16c))).*dAdt_16c.*mean(dydt_16c);
FI_y16cb = ((rhoG_16c +
rhoL_16c*Cm_16c).*Dw_16c(2:length(Ab_16c))).*Ab_16c(2:length(Ab_16c)).*mean(dyydtt_16c);

FI_y16c = FI_y16ca + FI_y16cb;

% Surface tension

AB = cell2mat([jet_raw(:,8)']);
AB = AB(image_index_16c(1):image_index_16c(2));

angle_16c = AB;

FS_y16c = sigma.*Dw_16c.*sind(-angle_16c);

FS_y16c = FS_y16c(2:length(FS_y16c));

% Pressure
% Contact pressure
FP_y16c = 0.7854*((sigma./Db_16c)).*(Dinj_16c.^2);

Mo = 9.81*(miuL^4)/(rhoL_16c*sigma^3);
alpha = 8.6 + 0.425*log(Mo);

dP_16c = alpha*rhoL_16c*(1.5*(dDdt_16c.^2) + 1.2*0.5*UL_16c*UL_16c +
Db_16c(2:length(Db_16c)).*dDDdtt_16c);

PB_16c = MG_16c*R*T_16c./(0.5236*Ab_16c.*Dw_16c);

FP_y16c = FP_y16c(2:length(FP_y16c));
```

```matlab
% FP_y16c = (9/32)*3.1416*rhoL*UL*UL*Dinj*Dinj;

FP_16c  = (PG_16c - PL_16c)*0.7854*(1.588*0.001*1.588*0.001);

for i = 2:length(Ab_16c)

        Ueff_16c(i-1) = sqrt( (dxdt_16c(i-1)-UL_16c)^2 + dydt_16c(i-1)^2);
        Re_16c(i-1)   = rhoL_16c*Ueff_16c(i-1)*Db_16c(i-1)/(9.772e-4);
        ReB_16c(i-1)  = rhoL_16c*UL_16c.*Db_16c(i-1)/(9.772e-4);

end

        Ap_16c = Ap_16c(2:length(Ap_16c));
        sphe_16c = sphe_16c(2:length(sphe_16c));



Cd1 = (24./Re_16c).* (1 + exp(2.3288 - 6.4581.*sphe_16c + 2.4486.*sphe_16c.^2)).*(Re_16c.^(0.0964
+ 0.5565*sphe_16c));

Cd2 = (Re_16c).* (exp(4.905 - 13.8944*sphe_16c + 18.4222*sphe_16c.^2 - 10.2599*sphe_16c.^3))./(
Re_16c + exp(1.4681 + 12.2584*sphe_16c - 20.7322*sphe_16c.^2 + 15.8855*sphe_16c.^3) );

Cd_16c = (Cd1 + Cd2);

kenh = 1.00;

FD_y16c = (0.5*rhoL_16c*Ap_16c.*Cd_16c.*Ueff_16c.*(dydt_16c));

% Lift
Cl_16c = 0.5*(1 + 16*ReB_16c(1,:).^(-1))./(1 + 29*ReB_16c(1,:).^(-1));

dudy_16c = UL_16c./Dw_16c;

Kl_16c = ( 3.877*( (Db_16c(1,2:length(Db_16c)-1)/UL_16c)*mean(dudy_16c(1,2:length(Db_16c)-
1))).^(0.5) ) + (Re_16c(2:length(Db_16c)-1).^(-2) + (0.344* ( (Db_16c(1,2:length(Db_16c)-
1)/UL_16c)*mean(dudy_16c(1,2:length(Db_16c)-1))).^(0.5)        ).^4   ).^(0.25);

FL_y16c = (0.5*rhoL_16c*Ueff_16c.*Ueff_16c.*Cl_16c.*Ap_16c(2:length(Ap_16c)));

% Turbulence
Ftau_y16 = 2*rhoL_16c*((epsilon*0.0127*0.1)^(2/3))*(D2_16c.*Per_16c);

%
% % Total Y
% plot(time_16c(2:length(time_16c)),FB_y16c,'ob',
time_16c(2:length(time_16c)),FM_y16c,'sr',...
%     time_16c(2:length(time_16c)),FP_y16c,'dg',
time_16c(2:length(time_16c)),sort(FL_y16c),'hy',...
%     time_16c(2:length(time_16c)),-sort(FI_y16c),'xk', time_16c(2:length(time_16c)),-
FS_y16c,'pm',...
%     time_16c(2:length(time_16c)),-sort(FD_y16c),'vc', 'MarkerSize',12,'LineWidth',2); axis
square
% xlabel('\itt\rm (ms)');
% ylabel('\itF\rm (N)');

% legend(['F_B';'F_M';'F_P';'F_S_L';'F_I_y';'F_\sigma_y';'F_D_y']);

% % Attaching
% plot(time(2:length(time)),sort(FI_y16c),'xk',time(2:length(time)),FS_y16c,'.m',...
% time(2:length(time)),sort(FD_y16c),'vc'); axis square

Fatt_y16c = FI_y16c + FS_y16c + FD_y16c;

%
%
% % Detaching
% plot(time(2:length(time)),FB_y16c,'ob',time(2:length(time)),FM_y16c,'sr',...
% time(2:length(time)),FP_y16c,'dg',time(2:length(time)),sort(FL_y16c),'hy'); axis square

Fdet_y16c = FB_y16c + FM_y16c + FP_y16c + FL_y16c;
```

```matlab
%% Horizontal

% Inertial - Added mass

FI_x16ca = ((rhoG_16c + rhoL_16c*Cm_16c).*Dw_16c(2:length(Ab_16c))).*dAdt_16c.*mean(dxdt_16c);
FI_x16cb = ((rhoG_16c +
rhoL_16c*Cm_16c).*Dw_16c(2:length(Ab_16c))).*Ab_16c(2:length(Ab_16c)).*mean(dxxdtt_16c);
FI_x16cc = rhoL_16c*UL_16c*Cm_16c.*Dw_16c(2:length(Ab_16c)).*dAdt_16c;

% FI_x16c = FI_x16ca + FI_x16cb;
FI_x16c = FI_x16ca + FI_x16cb - FI_x16cc;

% Surface tension

FS_x16c = sigma.*Dw_16c.*cosd(-angle_16c);

FS_x16c = FS_x16c(2:length(FS_x16c));

% Drag

FD_x16c = (kenh*0.5*rhoL_16c*Ap_16c.*Cd_16c.*Ueff_16c.*(UL_16c - dxdt_16c));
%
% % Horizontal
% plot(time_16c(2:length(time_16c)),-sort(FI_x16c),'xk',time_16c(2:length(time_16c)),-
FS_x16c,'pm',...
% time_16c(2:length(time_16c)),sort(FD_x16c),'vc','MarkerSize',12,'LineWidth',2); axis square
% xlabel('\itt\rm (ms)');
% ylabel('\itF\rm (N)');

Fatt_x16c = FI_x16c  + FS_x16c;
Fdet_x16c = Ftau_y16 + FD_x16c;

% Total
% plot(time(2:length(time)),sort(Fatt_x16c),'ob',time(2:length(time)),sort(FD_x16c),'sr'); axis
square
%
clearvars -except X_* Y_* XY_* Dw_* P_* Db_* Ap_* Ab_* sphe_* Dg_* time_* rhoG_* rhoL_* MG_* T_*
Dinj_* UG_*...
                PL_* UL_* dAdt_* dDdt_* dDDdtt_* Ub_* dxdt_* dydt_* dyydtt_* dxxdtt_* Cm_* F*
Cd_*...
                Fatt_* Fdet_* PB_* Re_* ReB_* Ueff_* Cl_* angle_* dudy_* image_index_*

clear time_vector
```